



Contract Number: 622177

## Deliverable n°4.4

### FE and TEM results

Work Package 4

Project Acronym	Modern2020
Project Title	Development and Demonstration of Monitoring Strategies and Technologies for Geological Disposal
Start date of project	01/06/2015
Duration	48 Months
Lead Beneficiary	NAGRA
Contributor(s)	Amberg Infraestructuras,
Contractual Delivery Date	31/05/2019
Actual Delivery Date	31/07/2019
Reporting period 3:	01/06/2018 - 31/05/2019
Version	FINAL

*Project co-funded by the European Commission under the Euratom Research and Training Programme on Nuclear Energy within the Horizon 2020 Framework Programme*

Dissemination Level	
PU	Public
PP	Restricted to other programme participants (including the Commission Services)
RE	Restricted to a group specified by the partners of the Modern2020 project
CO	Confidential, only for partners of the Modern2020 project and EC



History chart			
Type of revision	Document name	Partner	Date
Draft version FE	Draft_MoDeRn_2020-WP4_20190228_ftb	Nagra	Mars 2019
Final version FE	D4_4_FE_NAB 19-32	Nagra	June 2019
Draft version TEM	NAB 19-33.docx.	Amberg	June 2019
Final version TEM	D4_4_TEM_NAB 19-33	Nagra	July 2019

#### Reviewed by

This report has been reviewed according to the Modern2020 Quality Plan and the Deliverables Review Procedure therein. Formal review according to a Review Plan has been undertaken by Jan Verstricht (WP4 leader) and documented in Review Statements

#### Approved by

This report has been approved by:

- Jan Verstricht, Work Package 4 Leader, *08.08.2019*
- Johan Bertrand, the Modern2020 Project Co-ordinator (on behalf of the Modern2020 Project Executive Board), *19.08.2019*



## Table of content

---

1. PARTIE I: Full-Scale Emplacement Experiment (NAGRA)
2. PARTIE II : Test and Evaluation of Monitoring Systems (TEM)



## 1. PARTIE I: Full-Scale Emplacement Experiment (NAGRA)

---



# Arbeitsbericht NAB 19-32

## Modern2020 WP4.4 Full-Scale Emplacement (FE) Experiment, Mont Terri (Switzerland) – Field realisation

August 2019

H.R. Fisch, B. Firat Lüthi,  
A. Reinicke & T. Sakaki

### KEYWORDS

Modern2020, Work package 4.4, Full-Scale Emplacement,  
FE-Experiment, Demonstration experiment, FE-Data,  
Measurements, DTS, Temperature, TDR, Fibre optics,  
Rock laboratory, Mont Terri (Switzerland)

**National Cooperative  
for the Disposal of  
Radioactive Waste**

Hardstrasse 73  
P.O. Box 280  
5430 Wettingen  
Switzerland  
Tel. +41 56 437 11 11  
[www.nagra.ch](http://www.nagra.ch)

Nagra Arbeitsberichte ("Working Reports") present the results of work in progress that have not necessarily been subject to a comprehensive review. They are intended to provide rapid dissemination of current information.

"Copyright © 2019 by Nagra, Wettingen (Switzerland) / All rights reserved.

All parts of this work are protected by copyright. Any utilisation outwith the remit of the copyright law is unlawful and liable to prosecution. This applies in particular to translations, storage and processing in electronic systems and programs, microfilms, reproductions, etc."

## Executive summary

Heat transport and deformation processes within engineered barrier systems (EBS) of deep geological repositories for radioactive waste disposal play a central role in safety analyses. Monitoring these processes requires precise *in-situ* methods for measurement of temperature and strain on a scale of decimetre to hundreds of metres or even kilometres. Fibre optic monitoring systems for measuring temperature and strain distribution are offering a reasonable spatial resolution for this measuring range. They are promising emerging technologies that are widely used already in geotechnical, hydrologic and structural health monitoring. To gain experience with these distributed fibre optic sensing methods under repository like conditions, to demonstrate their feasibility for monitoring in these conditions, and to evaluate their performance, distributed fibre optic monitoring systems were installed in the Full-Scale Emplacement (FE) experiment at the Mont Terri Underground Rock Laboratory in Switzerland. Based on the Swiss disposal concept the FE-Experiment simulates the construction, emplacement, backfilling, and post-closure thermo-hydro-mechanical (THM) evolution of a spent fuel (SF) / vitrified high-level waste (HLW) repository tunnel in a realistic manner. The main aim of this experiment is to investigate SF / HLW repository-induced THM coupled effects in the host rock as well as in the EBS, which consists besides the canisters of a granulated bentonite mixture and bentonite blocks, by means of a full-scale multiple heater test.

The FE experiment serves in work package WP 4 of Modern 2020 – Demonstration of monitoring implementation at repository like conditions – as field demonstration of sensors and the evaluation of their applicability and their implementation into real monitoring plans, as well as for the assessment of relevant field tests.

The entire experiment implementation (in a 50 m long tunnel with approx. 3 m diameter) as well as the post-closure THM evolution is monitored using a network of several hundred sensors (standard state-of-the-art point sensors, prototype sensor systems and advanced fibre optic sensor technologies). The sensors are installed in the near- and far-field of the host rock, on the tunnel lining, in the EBS, and on the heaters. The two implemented fibre optic systems are distributed temperature sensing (DTS) based on Raman backscattering and distributed temperature and strain sensing (DTSS) based Brillouin and Rayleigh scattering. Both systems have different resolutions and accuracies and therewith different advantages. Several fibre optic cables of different manufacturers, which are installed on the tunnel wall within the EBS as well as in boreholes, are connected to the interrogator units via multiplexers. The instrumentation set-up allows us to compare different cables and different fibre optic measurement principles. Furthermore, prototype time-domain reflectometry (TDR) probes have also been installed in the rock and in the granular bentonite material (GBM) to monitor the water content evolution.

This report focuses on the demonstration and evaluation of the DTS with fibre optic monitoring technology as well as the prototype time-domain reflectometry (TDR) measurements for water content calculation. The lessons-learned and findings of different aspects of the instrumentation and the four years of experimental monitoring have been documented in this report. Within this context, following topics will be covered for the fibre optic for DTS: - instrumentation concept - installation - protection during tunnelling and backfilling works - calibration - data analysis, visualization and management - comparison and evaluation of the different DTS measurement systems as well as the comparison of the DTS measurements with conventional point sensors for temperature. In addition to the technical aspects, data and results from the four years of experimental heating phase will be presented. The DTS data reveal detailed insights in the spatial and temporal varying temperature distribution in the host rock and EBS. Furthermore, the custom-made sensor design, calibration, installation, measurement technique and results of four years of water content monitoring utilizing TDR will be discussed in the report.



## Table of Content

Executive summary .....	I
Table of Content.....	III
List of Tables.....	VI
List of Figures .....	VII
Acronyms and abbreviations.....	XI
<b>1 Introduction .....</b>	<b>1</b>
1.1 Modern 2020 Project .....	1
1.2 Work package 4.....	2
1.3 Structure of the report.....	3
<b>2 Swiss radioactive waste disposal concept.....</b>	<b>5</b>
2.1 Full-Scale Emplacement (FE) experiment.....	7
2.1.1 Experiment aims .....	7
2.1.2 Experiment layout.....	7
2.2 Project history since LUCOEX .....	8
2.2.1 Selection of the monitoring techniques and equipment.....	9
<b>3 Monitoring technologies.....</b>	<b>11</b>
3.1 Distributed temperature sensing (DTS) and conventional point temperature sensors .....	11
3.1.1 DTS Working principle .....	11
3.1.2 Fibre optic (FO) cables installed in the FE tunnel .....	12
3.1.3 FO cables installed in boreholes A10 and A11 .....	14
3.1.4 Conventional point temperature sensors in the FE tunnel wall .....	15
3.2 Time-Domain Reflectometry (TDR) .....	18
3.2.1 Working principle.....	18
3.2.2 TDR rock probes.....	19
3.2.2.1 Rock probe design for Opalinus Clay.....	19
3.2.2.2 Installation of rock probes .....	20
3.2.3 TDR probes in granular bentonite .....	21
3.2.3.1 Bentonite probe design .....	21
3.2.3.2 Installation of bentonite probes .....	21
<b>4 FE Data collection and handling .....</b>	<b>23</b>
4.1 Data acquisition systems (FE-DAS) and FE information system (FEIS).....	23
4.2 Technical background and data pipeline structure .....	24

<b>5</b>	<b>FE Data analysis .....</b>	<b>25</b>
5.1	DTS data.....	25
5.1.1	Setting parameters and specifications of the used DTS units.....	25
5.1.2	Identification of FO measurement positions in 3D space.....	28
5.1.2.1	Challenges specific to DTS .....	28
5.1.2.2	Methods applied .....	28
5.1.2.3	Further adjustments of cable meter positions .....	29
5.1.2.4	Instrument-specific adjustments of measuring positions.....	30
5.1.2.5	Cable position results based on fingerprinting and further shift optimization.....	30
5.1.3	Signal analysis .....	32
5.1.4	Effects of changes in fibre quality over time.....	32
5.1.4.1	Example showing the effect of varying signal-loss .....	33
5.1.4.2	Detection of signal quality.....	35
5.1.4.3	OTDR measurements for the localisation of signal losses .....	36
5.1.5	DTS Calibration.....	36
5.1.5.1	Design specifications.....	36
5.1.5.2	Set-up of the calibration system .....	38
5.1.5.3	Dynamic calibration formula.....	42
5.1.5.4	Verification of calculated temperatures (RMSE) .....	43
5.1.6	Comparison of calibration results between Smartec and Silixa.....	44
5.1.6.1	General comments on the graphs of this sub-chapter.....	44
5.1.6.2	Calibration results for Brugg Standard cable.....	45
5.1.6.3	Calibration results for Brugg Heatable cable.....	48
5.1.6.4	Calibration results for AFL cable using Smartec and Silixa units.....	50
5.1.6.5	Calibration results for A11A10 cable using Smartec and Silixa units.....	52
5.1.6.6	Discussion of results .....	53
5.1.7	Temperature analysis DTS versus point-type sensors in FE tunnel .....	53
5.1.7.1	Temperature profiles of the FE tunnel and point-type sensors.....	55
5.1.7.2	Comparison of Brugg Standard Temperature FO measurements versus point-type T-sensors .....	56
5.1.7.3	Comparison of Brugg Heatable FO measurements versus point-type T sensors .....	58
5.1.7.4	Comparison of DTS on AFL cable versus point-type T-sensors.....	61
5.1.7.5	Comparison of AFL versus Brugg Standard cable .....	62
5.1.8	Comparison of DTS versus point-type T-sensors.....	65
5.1.8.1	Comparison of temperatures in Borehole BFEA010.....	65
5.1.8.2	Comparison of temperatures in Borehole BFEA011 .....	66
5.1.8.3	Discussion of results .....	67

5.1.9	Temperature evolution in the FE tunnel from 2014 until 2018 .....	70
5.1.9.1	Time series of point-type temperature sensors .....	70
5.1.9.2	Thermal maps of FE tunnel heater section based on DTS data .....	71
5.1.9.3	Discussion of results .....	75
5.1.10	Temperature evolution in ISS section from 2014 to 2018.....	75
5.1.11	Temperature evolution in the BFEA011 borehole from 2014 to 2018.....	77
5.1.12	Change of FO calibration parameters .....	79
5.1.12.1	Overview of additional parameters checked for possible correlation.....	80
5.1.12.2	Short-term irregularities (spikes) of C- and $\gamma$ -parameters.....	81
5.1.12.3	Abrupt trend-change of the C-parameter .....	81
5.1.12.4	Discussion of results .....	82
<b>6</b>	<b>TDR data .....</b>	<b>85</b>
6.1.	TDR probe verification.....	85
6.1.1.	Verification of rock probes .....	85
6.1.2	Verification of bentonite probes .....	87
6.2.	Travel time analysis of TDR measurements.....	87
6.3	Analysis of TDR measurements .....	88
6.3.1	Water content calibration.....	88
6.3.2	Cable length calibration.....	90
6.3.3	Correction to the reference probe .....	91
6.3.4.1	TDR trace acquisition under varied water content .....	93
6.3.4.2	TDR trace acquisition under varied temperature .....	95
6.3.5	Calibration for bentonite.....	99
6.4	Water content.....	102
6.5	Summary and results.....	106
<b>7</b>	<b>Conclusions.....</b>	<b>107</b>
7.1	Fibre optic monitoring .....	107
7.1.1	Installation and documentation.....	107
7.1.2	FO cable selection.....	107
7.1.3	Dynamic (real-time) calibration .....	107
7.1.4	Selection of interrogator .....	108
7.1.5	Monitoring of cable quality by means of OTDR measurements .....	108
7.1.6	Data processing and visualization .....	108
7.2	TDR monitoring .....	109
<b>8</b>	<b>References.....</b>	<b>111</b>

## List of Tables

Tab. 2-1:	Summary of measurements and sensors installed on the tunnel wall and in the bentonite buffer close to the tunnel wall.....	9
Tab. 2-2:	Summary of measurements and sensors installed in the host rock.....	10
Tab. 2-3:	Summary of measurements and sensors installed in/on the heaters and in the surrounding bentonite (GBM and pedestals).....	10
Tab. 3-1:	FO cables installed for FE experiment .....	13
Tab. 3-2:	List of Pt1000 sensors installed on the tunnel wall (plotted in this chapter and sorted according to the tunnel section in which they were installed). .....	16
Tab. 5-1:	FO cables, DTS devices and channel settings .....	25
Tab. 5-2:	DTS devices - Technical specifications.....	26
Tab. 5-3:	Final cable fingerprinting for FO cables measured by two different DTS devices.....	31
Tab. 5-4:	Final cable fingerprinting for Brugg Heatable FO cable in the ISS section. ....	32
Tab. 5-5:	Step-loss at 850 nm and 1350 nm.....	36
Tab. 5-6:	Cable meter lengths in baths as-built (field assessment / as given by FEIS).....	40
Tab. 5-7:	Cable meter lengths in baths theoretically usable for calibration (Smartec). ....	40
Tab. 5-8:	Number of measuring points in baths used for dynamic calibration (Smartec).....	40
Tab. 5-9:	Comparisons of DTS versus point-type sensors at various times & configurations. ....	54
Tab. 5-10:	Clock face positions and corresponding circumference values used for thermal map interpolation.....	72
Tab. 5-11:	Start and end positions of G2, G4 and G6 loops and corresponding cable meters after fingerprinting. ....	75
Tab. 6-1:	Relative permittivity of verification material for FE TDR sensors .....	85
Tab. 6-2:	Feeding coaxial cable length (including multiplexer path).....	90
Tab. 6-3:	Schematic sketch of the transformations from individual measured travel time to material specific volumetric water content.....	92
Tab. 6-4:	Material characterization from FE TDR borehole samples (located in Opalinus Clay and shotcrete) to identify parameter range for calibration campaign.....	93
Tab. 6-5:	Variations in water content and temperature during Opalinus Clay calibration campaign.....	94
Tab. 6-6:	FE bentonite TDR calibration data generation .....	99

## List of Figures

Fig. 1-1:	The Modern2020 Project work plan is structured into six work packages (WP's).....	2
Fig. 2-1:	Possible layout for a deep geological repository for SF / HLW and long-lived ILW in Opalinus Clay.....	6
Fig. 2-2:	Experimental layout with the FE cavern and FE tunnel main parts shown but without backfill.....	7
Fig. 2-3:	Experimental layout with FE/GM coordinate systems - FE local coordinates of main sections and corresponding gallery meters.....	8
Fig. 2-4:	Project history of the FE-part of WP4.4 and predecessor project. ....	8
Fig. 3-1:	Various types of backscatter.....	11
Fig. 3-2:	Fibre optic cables that are installed in the FE-Tunnel .....	12
Fig. 3-3:	Schematic sketch of FO cables measured by Smartec, Neubrex or by both units .....	14
Fig. 3-4:	Location of boreholes BFEA010 and BFEA011 (from Morel, 2013).....	14
Fig. 3-5:	Configuration of measurement position in boreholes a) BFEA010 and b) BFEA011 .....	15
Fig. 3-6:	Location of the 53 Pt1000 sensors installed on the tunnel wall and on holders attached to the tunnel wall - Side view of FE tunnel.....	15
Fig. 3-7:	Location of the 53 Pt1000 sensors installed on the tunnel wall and on holders attached to the tunnel wall - Cross-sectional view looking from the FE cavern to the deep end of the FE tunnel.....	16
Fig. 3-8:	Location of relative humidity and corresponding temperature sensors - Side view of FE tunnel.....	17
Fig. 3-9:	Location of relative humidity and corresponding temperature sensors - Cross-sectional view - looking from the FE cavern to the deep end of the FE tunnel. ....	17
Fig. 3-10:	Position of the water content TDR probes.....	18
Fig. 3-11:	Basic working mechanism of the TDR devices in soil moisture content determinations. ....	19
Fig. 3-13:	Left: vertical inverted “Y” configuration (with probes perpendicular/parallel to bedding); Right: Rock probe after confirming the grout return.....	20
Fig. 3-14:	Customized TDR bentonite probe for “hot” sections using a single TDR sensor module. The temperature sensor is located in the white block in the yellow circle. ....	21
Fig. 4-1:	Illustration of the DAS's installed in the FE-A niche (left) and workflow for data collection from all DASs (right). ....	23
Fig. 4-2:	Data Pipeline schematic of the FE information system (FEIS) .....	24
Fig. 5-1:	Specifications of two different interrogators installed in FE experiment - above: Neubrex; below: Smartec.....	27

Fig. 5-2:	Fingerprinting: punctual heating of FO cable at geodetically surveyed locations.....	29
Fig. 5-3:	Assignment of cable meter distance to measured temperature value. ....	30
Fig. 5-4:	Effect of abruptly changing Stokes/anti-Stokes ratios on DTS instrument temperatures shown in time-series graph.....	34
Fig. 5-5:	Effect of abruptly changing Stokes/anti-Stokes ratios on DTS instrument temperatures shown in DTS profile graph.....	34
Fig. 5-6:	Irregular patterns in a coloured heat plume plot .....	35
Fig. 5-7:	Single-ended configuration of permanent calibration system. ....	38
Fig. 5-8:	Arrangement of cables in the calibration baths. ....	39
Fig. 5-9:	Heated bath (left) and ambient temperature bath (right) without cover .....	41
Fig. 5-10:	Calibration baths and components.....	41
Fig. 5-11:	Brugg Standard cable - Results of calibration using Smartec and Silixa shown for entire cable.....	46
Fig. 5-12:	Brugg Standard cable - Temperature peaks related to cable sections parallel and across heaters. ....	47
Fig. 5-13:	Brugg Standard cable - Smartec and Silixa calibrated temperatures across CB1 and CB2.....	47
Fig. 5-14:	Brugg Heatable - Results of calibration using Smartec and Silixa shown for entire cable.....	49
Fig. 5-15:	Detailed view of temperature differences between Silixa and Smartec.....	50
Fig. 5-16:	AFL cable: results of calibration using Smartec and Silixa shown for entire cable.....	51
Fig. 5-17:	A11A10 cable: results of calibration using Smartec and Silixa shown for entire cable.....	52
Fig. 5-18:	DTS compared to point-type temperatures at various stages of the project (2014 -2018). ....	55
Fig. 5-19:	Examples of labelled plot markers indicating sensor name and its distance to the FO cable.....	56
Fig. 5-20:	Brugg Std cable, Sections I-J & K-L: point T-data vs DTS measurements.....	57
Fig. 5-21:	Brugg Std cable, Sections I-J & K-L: point T-data vs DTS measurements (2).....	58
Fig. 5-22:	Entire Brugg Heatable cable measured using the Silixa device (average of 30 runs shown).....	59
Fig. 5-23:	Brugg Heatable cable, Sections A-B & J-K: point T-data vs DTS data (1). ....	60
Fig. 5-24:	Brugg Heatable cable, Sections A-B & J-K: point T-data vs DTS data (2). ....	60
Fig. 5-25:	AFL - Entire cable measured using the Silixa device (average of 30 runs shown).....	61
Fig. 5-26:	AFL cable, Sections A-B & C-D: point T-data vs DTS measurements. ....	62

Fig. 5-27:	Clock face position of selected cables sections shown at gallery cross-section GM25.....	63
Fig. 5-28:	Routing of Brugg Standard cable (Section A-B) and AFL cable (Section C-D) in FE tunnel at 07:00 position. ....	63
Fig. 5-29:	Brugg Standard Section O-P and AFL Section A-B - Silixa DTS vs Point T-data. ....	64
Fig. 5-30:	Brugg Standard Section A-B and AFL Section C-D - Silixa DTS vs Point T-data. ....	64
Fig. 5-31:	BFEA010 - Comparison of 40 thermistor values with DTS data using Smartec and Silixa. ....	68
Fig. 5-32:	BFEA011 - Comparison of 40 thermistor values with DTS data using Smartec and Silixa. ....	69
Fig. 5-33:	Evolution of the temperatures at bottom and top side of each heater (2014 - 2018). ....	70
Fig. 5-34:	Evolution of the temperatures at the heaters and at the tunnel wall (2014 – 2018).....	71
Fig. 5-35:	Temperature evolution along the tunnel recorded by DTS-FO cables in 2015. ....	73
Fig. 5-36:	Temperature evolution along the tunnel recorded by DTS-FO cables between 2016 -2018. ....	74
Fig. 5-37:	ISS Loop positions G2, G4 and G6 along the Brugg Heatable cable.....	76
Fig. 5-38:	Evolution of temperatures in the Interjacent Sealing Section (ISS) (December 2014 – December 2018).....	76
Fig. 5-39:	Temperatures (Smartec) on 01.07.2017 as loop plots at G2, G4 and G6 of ISS.....	77
Fig. 5-40:	Borehole A11 - DTS and point-type T sensor temperatures 2014 - 2018. ....	78
Fig. 5-41:	Detail from previous graph Fig. 5-40. ....	78
Fig. 5-42:	Static T-corrections applied to DTS data Dec. 2014 to March 2018.....	79
Fig. 5-43:	Schematic sketch of the calibration system and potential factors influencing the quality of measurement.....	80
Fig. 5-44:	Calibration parameters - RMSE, T-values of niche, interrogator and calibration baths (May - Nov. 2018).....	83
Fig. 5-45:	Calibration parameters - RMSE and cable temperatures (May - Nov. 2018).....	84
Fig. 6-1:	Transformation between travel time and rel. permittivity for FE TDR sensors of rock probe BFEB017. ....	86
Fig. 6-2:	Transformation function between travel time and relative permittivity for FE TDR sensor BFEB017_SEA_01 including measurement tolerance as a result of multiple measurements.....	86
Fig. 6-3:	Transformation between travel time and rel. permittivity for FE TDR bentonite probes. The initial field data (just before heaters were started) are also plotted to the function. ....	87
Fig. 6-4:	Example of the travel time analysis of the TDR signal (Schlaeger & Sakaki, 2017).....	88

Fig. 6-5:	Travel time of TDR probes at rock sensor BFEB017 - TDRs 01-04 are located in Opalinus Clay.....	89
Fig. 6-6:	Travel time of TDR probes in bentonite.....	89
Fig. 6-7:	Effect of the feeding coaxial cable length on the TDR traces (dry Opalinus Clay). .....	91
Fig. 6-8:	Reference sensor used for material calibration.....	92
Fig. 6-9:	Reference calibration sensor installed in the calibration block. ....	94
Fig. 6-10:	TDR traces obtained for dry Opalinus Clay block under varied temperatures.....	95
Fig. 6-11:	Relative dielectric permittivity of water depending on temperature .....	96
Fig. 6-12:	Empirical determination of a temperature to travel time relation for Sensor BFEB017_SEA_01 - Rock was assumed to have remained saturated. ....	97
Fig. 6-13:	Linear relation between temperature and travel time for dry Opalinus Clay.....	97
Fig. 6-14:	Alpha-mixing model for sensor BFEB017_SEA_01 to describe relation between reference travel time and volumetric water content using additional temperature information (Sensor BFEB017_SEA_01). ....	98
Fig. 6-15:	Volumetric water content calculation using the initial data used for calibration (showing full saturation; Sensor BFEB017_SEA_01) .....	99
Fig. 6-16:	Comparison of TDR traces in bentonite with different water content (Cable length = 25 m - Temperatures 18°C (a) and 60°C (b)).....	100
Fig. 6-17:	Linear regression of transformation parameters $a$ (a), $b$ (b) and $c$ (c) within the exponential travel time to water content transformation. ....	101
Fig. 6-18:	Exponential model for sensor FE_SEA_001 to describe relation between reference travel time and volumetric water content using additional temperature information. ....	102
Fig. 6-19:	Water content at TDR probes at rock sensor BFEB017 - TDRs 01-04 are in Opalinus Clay (Jan. 2014 – Jun. 2018). ....	103
Fig. 6-20:	Water content at TDR probes at rock sensor BFEB018 (Jan. 2014 – Jun. 2018).....	103
Fig. 6-21:	Water content at TDR probes at rock sensor BFEB019 (Jan. 2014 – Jun. 2018).....	104
Fig. 6-22:	Water content at TDR probes at rock sensor BFEB020 (Jan. 2014 – Jun. 2018).....	104
Fig. 6-23:	Water content at TDR probes at rock sensor BFEB021 (Jan. 2014 – Jun. 2018).....	105
Fig. 6-24:	Water content at TDR probes at rock sensor BFEB022 (Jan. 2014 – Jun. 2018).....	105
Fig. 6-25:	Water content at TDR probes at bentonite sensor FE_SEA (Jan. 2014 – Jun. 2018).....	106

## Acronyms and abbreviations

Symbol	Description	Unit
<i>Notations</i>		
$C$	Dimensionless coefficient of the incident laser of the DTS	
$C_{22}$	Modified Rayleigh frequency-temperature conversion coefficient	
$\Delta\alpha$	Differential attenuation rate	dB/m
$Dt$	Sampling time (averaging time)	s
$dx$	Sampling resolution (m)	m
$\Delta\nu_R$	Rayleigh frequency shift	
$R(z)$	Natural logarithm of the ratio $P_s/P_{as}$	
$T / \Delta T$	Temperature / Temperature difference	°C
$\gamma$	Fibre material and DTS instrument coefficient	
<i>Commonly used abbreviations</i>		
A-DTS	Active distributed temperature sensing	
CB1 / CB2	Calibration bath 1 (ambient T) / calibration bath 2 (heated)	
CM / GM	Cable metre / Gallery metre	
DAS	Data acquisition system	
DTS	Distributed temperature sensing	
EBS	Engineered barrier system	
EC	European commission	
FE	Full-scale Emplacement	
FEIS	FE Information System	
FO	Fibre optic	
G2/G4/G6	Gap 2/Gap 4/Gap 6 between steel arches at ISS	
GBM	Granulated bentonite mixture	
GTS	Grimsel Test Site	
H1/H2/H3	Heater 1 (deep end of the FE tunnel) / Heater 2 (middle) / Heater 3 (close to plug)	
HLW	High-level waste	
ISS	Interjacent sealing section	
L/ILW	Low- and intermediate-level waste	
Modern	Monitoring developments for safe repository operation and staged closure	
OTDR	Optical time-domain reflectometry	
PA12	Polyamide 12, the outer Polymer sheath material of the FO cable	
$P_s / P_{as}$	Power of Stokes and anti-Stokes	
PT1000	Platinum resistance thermometers	
R&D	Research and development	
RD&D	Research, development and demonstration	
RMSE	Root mean square error	
TDR	Time-domain reflectometry	
TEM	Test and evaluation of monitoring techniques	
THM	Thermo-hydro-mechanical	
ULTIMA-S	Raman DTS unit, Silixa Ltd., UK	
WP	Work-package	



# 1 Introduction

## 1.1 Modern 2020 Project

The Development and Demonstration of Monitoring Strategies and Technologies for Geological Disposal (Modern2020) Project is a European Commission (EC) project funded by Euratom research and training program 2014-2018 together with European nuclear waste management organizations (WMOs). Twenty-eight WMOs and research and consultancy organizations from twelve countries are participating in the project since June 2015 till May 2019 (Modern2020, 2016).

Based on the findings of the Monitoring Developments for Safe Repository Operation and Staged Closure Project (Modern Project; White, 2014), Modern2020 aims to provide an efficient operational monitoring program for developing and implementing a repository. The project intends to address the issues that are related to strategy, technology, demonstration and practical implementation and societal concerns and stakeholder involvements, focusing on the monitoring of the near-field during repository operational phases (Modern2020, 2018a).

To accomplish the objectives of the Modern 2020 project, the work is divided comprehensively and coherently into six interrelated workpackages (WP; Modern2020, 2018a).

- WP 1 - Coordination and management of the consortium: “provides an effective, smooth and high-quality implementation of the project, communication and integration between the partners, monitoring of the project progress and outputs, maintaining information up-to-date on the project’s website, and efficient financial administration according to the official European Commission guidelines”.
- WP 2 - Monitoring program design basis, monitoring strategies and decision making: “defines the requirements on monitoring systems in terms of the parameters that should be monitored in optimized monitoring programs with explicit links to the safety case and the wider scientific program which will include consideration of decision making requirements, monitoring strategies, screening of preliminary monitoring parameter lists, and performance measures and response plans.”
- WP 3 - Research and development of relevant monitoring technologies: “provides solutions for the critical gaps identified in Modern project. Improvement and combining the wireless data transmission systems (WDT), research on power supply sources, new sensors, developing new techniques and probes, refinement and improvement of the most promising geophysical methods, establishing a common methodology for the qualification of the monitoring system components for repository use.”
- WP 4 – Demonstration of monitoring implementation at repository like conditions: “summarizes the field demonstrations of sensors as well as their applicability and their implementation into real monitoring plans, assessment of relevant field tests and establishment of an implementation manual” (see Chapter 1.2).
- WP 5 - Effectively engaging local citizen stakeholders in research and development (R&D) / research, development and demonstration (RD&D) on monitoring for geological disposal: “discusses the societal concerns and the expectations from stakeholders in more concrete ways in the lights of the findings from Modern Project.”
- WP 6 - Modern2020 Dissemination: “combines the findings and knowledge from each WP to distribute and disseminate knowledge and results, and to enhance the impact of the project and achieve a high-level of engagement.”

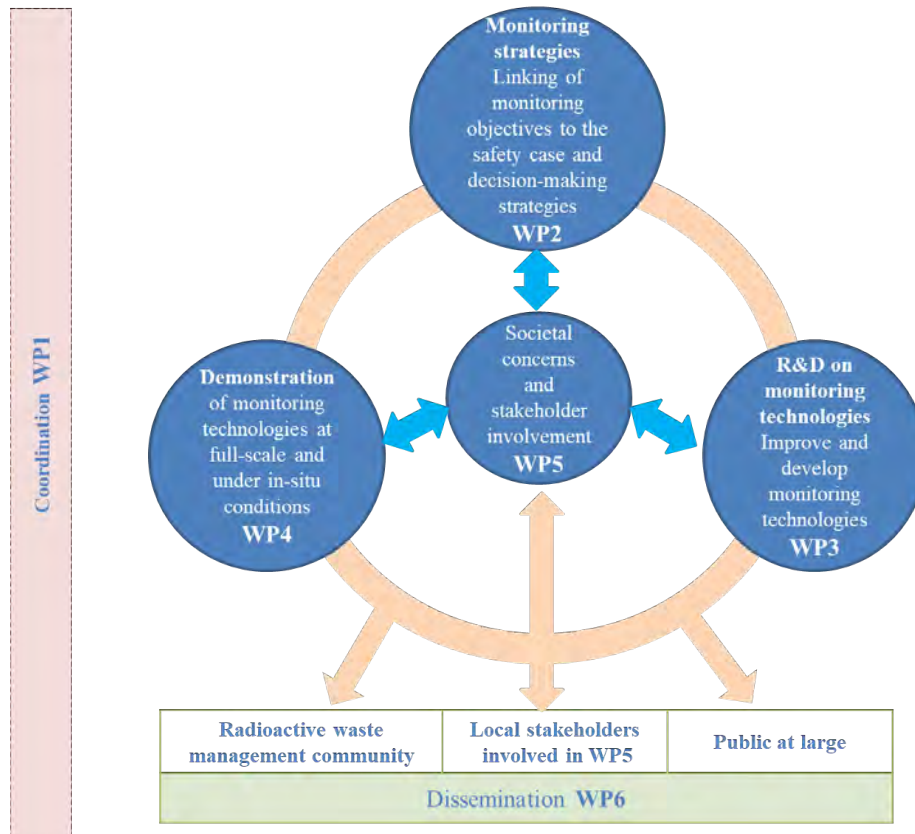


Fig. 1-1: The Modern2020 Project work plan is structured into six work packages (WP's)  
(Source: <http://www.modern2020.eu/activities.html>)

## 1.2 Work package 4

The work package 4 (WP4) aims to explain the practical implementation of monitoring techniques at repository like conditions. To demonstrate the integrated monitoring parameters and techniques, it is important to consider the application of individual techniques and systems utilizing various technologies. Therefore, under the framework of WP 4 the objectives are defined as following (Modern2020, 2018b):

- Demonstration of the developments of the new technologies under *in-situ* conditions in Finnish, Swedish French and Swiss concepts.
- Demonstration of the developments of a monitoring system design utilizing multiple technologies and linked to a specific safety case.
- Utilization of the existing near-field monitoring experience to provide guidance on monitoring system design.

The focus of NAGRA in this phase of the project is the demonstration and evaluation of the fibre optic (FO) monitoring technology for distributed temperature sensing (DTS) and the prototype time-domain reflectometry (TDR) sensors under repository like conditions and as well as the comparison of these systems with conventional standard sensing systems. This task will also include a continuation and assessment of the performance of geophysical techniques (tomographical imaging) as well as acoustic and wireless monitoring with Test and Evaluation of

Monitoring techniques (TEM) set-up at the Grimsel Test Site (GTS), which is documented in separate report (Tuñón Valladares et al., 2019).

The whole work is funded by the Swiss Confederation – namely the State Secretariat for Education, Research and Innovation (SERI) - in the framework of Horizon2020 Euratom programme (Euratom research and training programme 2014 - 2018 under a grant agreement No. 662177). The opinions expressed and arguments employed herein do not necessarily reflect the official views of the Swiss Government.

### **1.3 Structure of the report**

After the introduction into the project, a short outline of the Swiss radioactive waste disposal concept is given and the connection with the Full-Scale Emplacement (FE) experiment is described as well as the outline of the FE-Experiment (Chapter 2).

The working principles of the distributed temperature sensing (DTS) and time-domain reflectometry (TDR) monitoring technologies and their implementation as well as the implemented conventional measurement devices in the FE experiment are presented in throughout Chapter 3.

The collection of the data and the FE database is explained in Chapter 4.

Distributed temperature sensing (DTS) data measured with fibre optics (FO's) are analysed in Chapter 5. In general, the signal analysis, specifications comparisons of different DTS interrogators, the measurements before and after calibration as well as comparison to the conventional temperature probes etc. are shown throughout this chapter.

TDR data analysis and calibration techniques and final analysis of the water content calibration and the calculated water content data are shown in Chapter 6.

The conclusions for the FO and TDR are drawn and the lessons learnt from the monitoring in FE experiment is discussed in the conclusions Chapter 7.



## 2 Swiss radioactive waste disposal concept

The Swiss waste disposal programme (Nagra, 2008a) as approved by the Swiss Federal Government in 2013 foresees the disposal of spent fuel (SF) / vitrified high-level waste (HLW) and solidified long-lived intermediate-level waste (ILW) in a deep geological repository. In compliance with the existing legal framework, the repository concept comprises a 1 km x 2 km arrangement of waste emplacement tunnels (Fig. 2-1; Nagra, 2019). It is currently envisaged that the ILW repository will start operation in 2050 and the HLW repository in 2060 (Nagra, 2016) and current work is therefore focusing on the development of the conceptual design of the deep geological repository.

The disposal concept envisages that SF / HLW carbon steel waste canisters would be emplaced horizontally in a centred position on bentonite block pedestals in 800-m-long disposal tunnels, comprising 700 m for waste emplacement, a 40-m-long tunnel plug and a 60-m-long branch tunnel for operations during emplacement. In the section used for waste emplacement, the tunnels would be supported by shotcrete to allow operations to proceed safely and to provide tunnel stability prior to the saturation of the tunnel backfill.

Following the emplacement of each canister and pedestal, the tunnel around the canister would be backfilled with a granulated bentonite material (GBM) buffer. The canister emplacement and backfilling procedure would be repeated progressively from the far end of the tunnel to the tunnel plug. Between every tenth canister, an Interjacent Sealing Section (ISS), consisting of bentonite blocks would be emplaced to limit solute transport along the backfilled tunnel. The ISS would be supported by steel arches. The pedestals, GBM and ISS jointly comprise the bentonite buffer, which is part of the engineered barrier system (EBS), and thus also part of the multi-barrier concept contributing to the isolation and containment of the waste (Nagra, 2002).

Within the emplacement tunnels for long-lived ILW, steel drums incorporated into concrete emplacement containers would be stacked on a concrete slab forming the floor of the tunnels, with cementitious mortar used to fill the void spaces around the drums and around the emplacement containers.

Candidate host rocks in Switzerland were evaluated within the framework of the ongoing site selection process governed by the so-called Sectoral Plan for Deep Geological Repositories. In 2008, Nagra proposed selection of the Opalinus Clay as the host rock for the deep geological repository for HLW (Nagra, 2008b). The Federal Government approved Nagra's proposal in 2011.

The Full-Scale Emplacement (FE) Experiment at the Mont Terri Underground Rock Laboratory simulates aspects of the construction, waste emplacement, backfilling and early-stage evolution of a SF / HLW repository tunnel in a clay-rich formation (Opalinus Clay), using heaters in place of SF / HLW canisters (Müller et al., 2017). The entire experiment implementation and the post-emplacement THM evolution is monitored using several hundred sensors. Some monitoring of gas concentration was also undertaken. The sensors are distributed in the near-field and far-field host rock, on the tunnel lining, in the buffer and tunnel plug, and on the heaters.

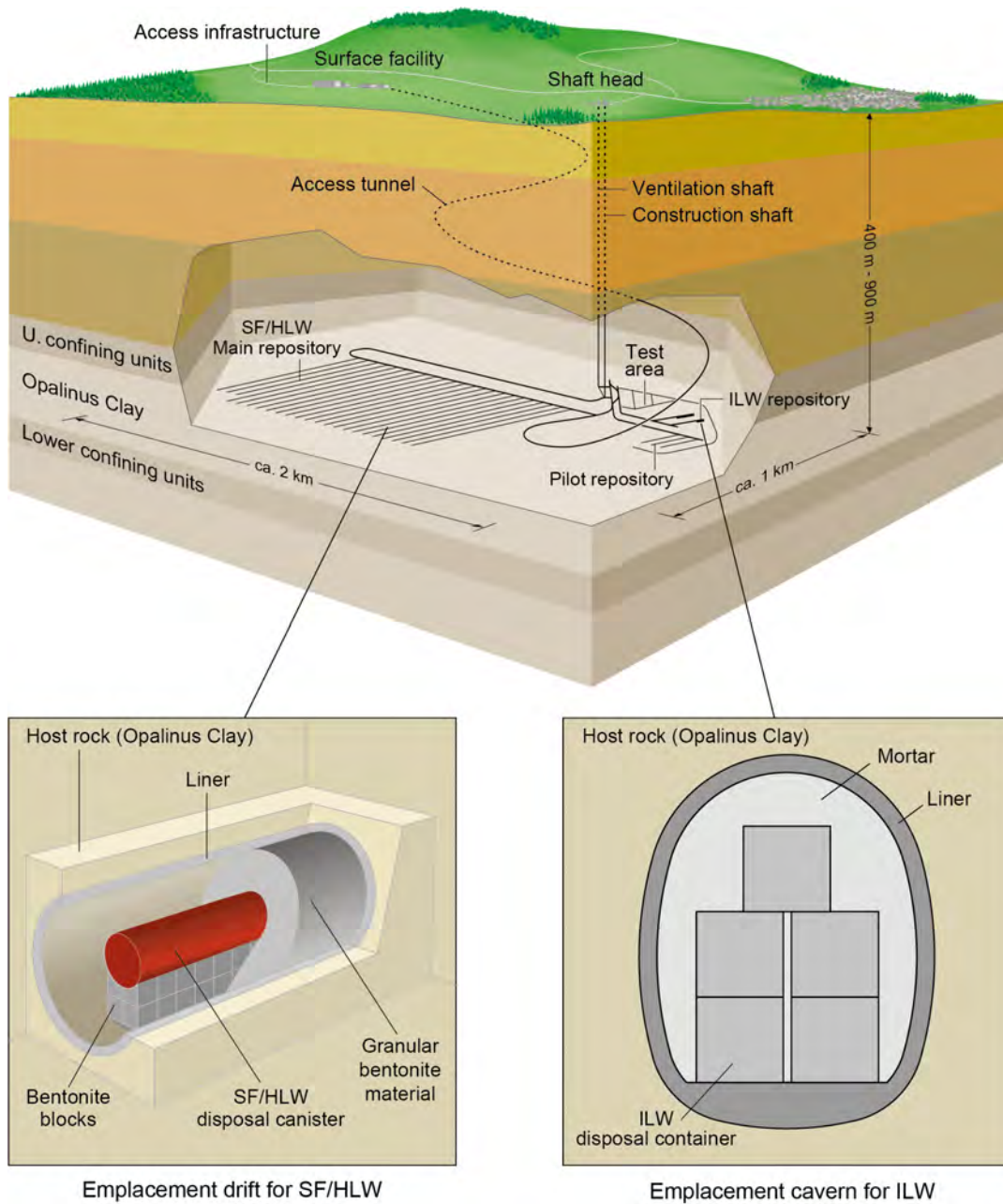


Fig. 2-1: Possible layout for a deep geological repository for SF / HLW and long-lived ILW in Opalinus Clay.

## 2.1 Full-Scale Emplacement (FE) experiment

Within the framework of the radioactive waste disposal program for HLW, the Full-Scale Emplacement (FE) experiment in the Mont Terri Underground Rock Laboratory is implemented on a 1:1 scale to a deep geological repository (Nagra, 2019). As such, the FE experiment represents the different phases of construction, waste emplacement, backfilling and early post-closure evolution of a spent fuel/vitrified HLW disposal tunnel as realistically as possible (Müller, et al., 2017).

### 2.1.1 Experiment aims

The main goal of the FE experiment is (1) to obtain a better understanding of the coupled effects of induced thermo-hydro-mechanical (THM) processes that may occur once the actual repository is in operation and (2) to validate existing coupled THM models (Müller et al., 2015). Furthermore, the FE experiment also aims to confirm the technical feasibility of constructing the disposal tunnels using standard equipment, to optimize the production of the bentonite buffer, and to investigate the procedures for the emplacement of canisters and the bentonite buffer under underground conditions (Weber et al., 2012; Bosgiraud et al., 2015, Müller et al., 2017).

### 2.1.2 Experiment layout

The FE experiment was implemented in the Mont Terri Underground Rock Laboratory to represent the construction and short-term behaviour of an actual geological repository. For this purpose, a 50 m long experimental tunnel, containing a 12 m long ISS at its deep end, was constructed (Fig. 2-2 and Fig. 2-3). The tunnel is supported by shotcrete, except at the ISS section where only steel sets were used (Müller et al., 2017). A 2 m long bentonite block wall was constructed within the ISS. On top of the bentonite block pedestals, three identical heaters with dimensions similar to those of the waste canisters (4.5 m long), were emplaced in the FE tunnel. The heater emplaced close to the ISS was named as heater 1 (H1, at the deep end of the tunnel), the one in the middle as heater 2 (H2) and the one close to the concrete plug as heater 3 (H3). Upon completion of the instrumentation and installation of the monitoring equipment, the remaining space was backfilled with highly compacted GBM with a prototype five-auger backfilling machine. The machine was designed to achieve a dense and homogeneous packing of the GBM (Köhler et al., 2015). Lastly, the experiment tunnel was sealed with a concrete plug (Müller et al., 2017).

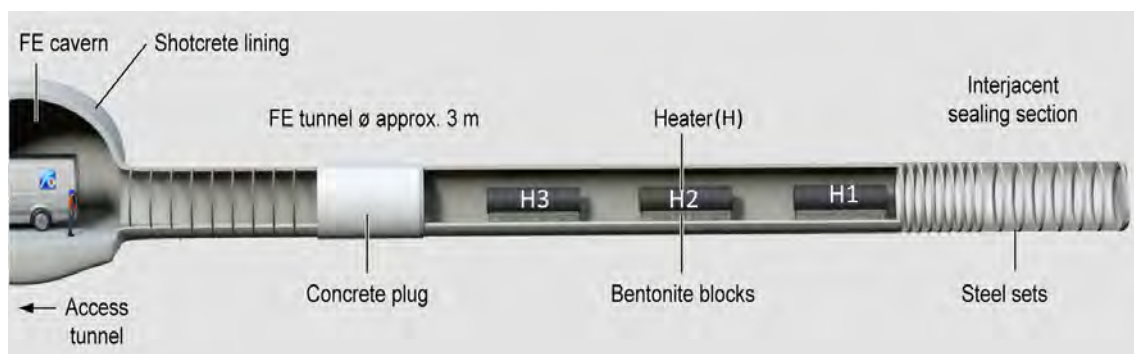


Fig. 2-2: Experimental layout with the FE cavern and FE tunnel main parts shown but without backfill.

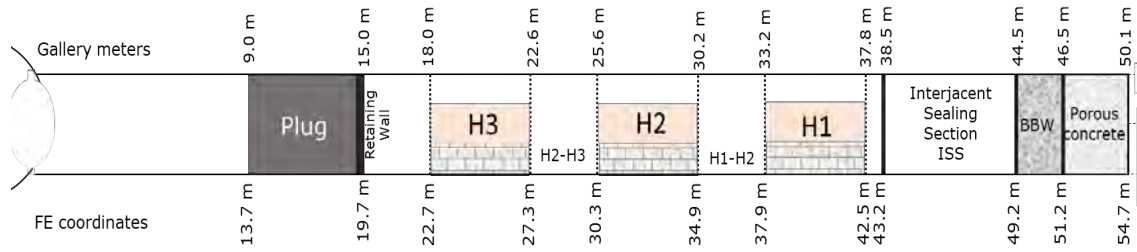


Fig. 2-3: Experimental layout with FE/GM coordinate systems - FE local coordinates of main sections and corresponding gallery meters.

## 2.2 Project history since LUCOEX

The project history of the FE experiment including the timeline of the predecessor project LUCOEX and post-MODERN2020 monitoring is shown in Fig. 2-4.

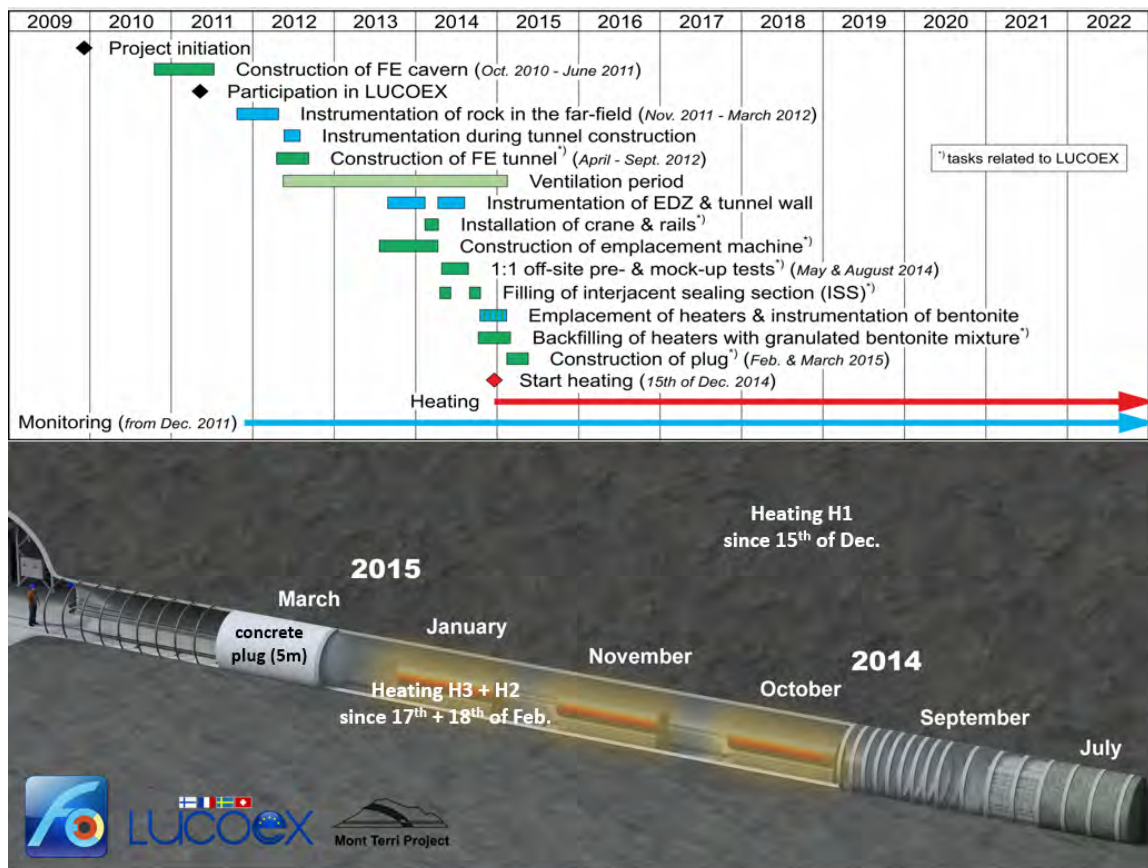


Fig. 2-4: Project history of the FE-part of WP4.4 and predecessor project.

### 2.2.1 Selection of the monitoring techniques and equipment

The test tunnel has been instrumented with hundreds of sensors that will detect the smallest changes in the tunnel environment and in the surrounding rock and on/around the three dummy containers (Müller et al., 2015). Therefore, the sensors are distributed in boreholes, in the tunnel lining in the bentonite buffer and on the heaters (Müller et al., 2017).

Tab. 2-1: Summary of measurements and sensors installed on the tunnel wall and in the bentonite buffer close to the tunnel wall.

	Variable	Installed instrument	Criteria for selection/purpose
Instrumentation on the tunnel wall and of the bentonite buffer close to the tunnel wall	Temperature	PT1000	Conventional, *
		Thermocouples	Conventional, *
		Integrated T sensors in RH and TP sensors	Integrated *
		FO for distributed temperature sensing (DTS)	To withstand corrosion, to obtain a T profile *
	Humidity/ water content	Relative humidity (RH) sensors (monolithic and capacitive)	Conventional
		Time-domain-reflectometers (TDR) and Frequency-domain-reflectometers (FDR)	Rock moisture monitoring in hotter sections to withstand long-term use under high T
	Total pressure	Total pressure (TP) sensors	Monitor the potential swelling of the bentonite buffer
	Deformation	Convergence measurements with total stations	Monitor any tunnel wall deformation after tunnel construction
		Displacement sensors	Monitor tunnel wall deformation after backfilling and during heating
		FO for distributed strain sensing (DSS)	
	Thermal conductivity	Thermal conductivity sensors (KD2 - TR 1 probes)	To monitor the change in thermal conductivity
	Geophysical monitoring	Gas-tight pipes	Provides long-term access thorough the concrete plug
		Acoustic sensor arrays	Permanent installations allow to capture subtle changes in acoustic waveforms
	Gas composition	Hydrogen concentration sensor	Conventional
		Oxygen concentration sensor	Conventional
		Gas sampling lines	Continuous gas monitoring by mass spectrometry as well as periodic gas sampling
Corrosion monitoring	Sample holders with different metal compositions (carbon, steel, wrought copper, electrodeposited copper and cold sprayed copper)	To investigate in-situ corrosion phenomena in the case of potential future dismantling	

\* *spatio-temporal temperature distribution and evolution of the tunnel wall and of the bentonite buffer*

Tab. 2-2: Summary of measurements and sensors installed in the host rock.

	Variable	Installed instrument for measurements	Criteria for selection/purpose
Instrumentation in the host rock	Temperature	PT1000	Conventional, *
		Thermocouples	Conventional, *
		Integrated T sensors in RH and Pressure sensors	Integrated *
		FO for DTS	To withstand corrosion, to obtain a T profile
	Humidity/water content	Dielectric profile probe	Development of the water content (WC) of the rock mass
		TDR	Rock moisture monitoring in hotter sections to withstand long-term use under high T
		Monolithic and capacitive RH sensors	Conventional
	Pressure	Multi packer systems	Conventional
		Single packer systems	Conventional
	Deformation	Horizontal inclinometers	Conventional
		Standard rod extensometers	Conventional
		Specially designed long-lasting rod extensometers	To withstand higher stress
Fibre optic (FO) extensometers		To withstand corrosion	

\* *spatio-temporal temperature distribution and evolution of the tunnel wall and of the bentonite buffer*

Tab. 2-3: Summary of measurements and sensors installed in/on the heaters and in the surrounding bentonite (GBM and pedestals).

	Variable	Installed instrument for measurements	Criteria for selection/purpose
Instrumentation in/on the heaters and in the surrounding bentonite (GBM and pedestals)	Temperature	TERMYA-Typ T	Can withstand high T *
		Thermocouples	Conventional *
		Integrated T sensors in RH and TP sensors	Integrated *
		FO for DTS	To withstand corrosion, to obtain a T profile
	Humidity/water content	High T and low T RH sensors	Conventional
	Total pressure	High T and low T TP sensors	Monitor the potential swelling of the bentonite buffer
	Deformation	Displacement sensors	Monitor any potential heater movement

\* *spatio-temporal temperature distribution and evolution of the tunnel wall and of the bentonite buffer*

### 3 Monitoring technologies

#### 3.1 Distributed temperature sensing (DTS) and conventional point temperature sensors

##### 3.1.1 DTS Working principle

DTS cables are optoelectronic devices measuring the temperature by using optical fibres. Functioning as a linear sensor, they can provide continuous temperature distribution profile along the cable. Initiated in 1980s, the technology and the application of the system have undergone significant improvements until now. Nowadays, with DTS systems it is possible to obtain high degree accuracy ( $\pm 1$  °C at resolution of  $0.01$  °C) temperature measurements at typically 1 m spatial resolution along tens of kilometres distances. However, the technique that uses a digital time-correlated single-photon count allows increasing the spatial resolution of the measurements to 0.1 m (Stierlin et al., 1987; Thorncraft et al., 1992; Feced et al., 1997; Ukil et al., 2011).

The measuring principle of the cables is based on the optical detection of the back-scattering of light, which may occur as Brillouin, Rayleigh and Raman scattering (Grattan and Sun, 1999; Ukil et al., 2011; Ciocca et al., 2012). Brillouin scattering takes place when the light wave is scattered by an acoustic wave due to the inelastic interaction with the acoustic photons of the medium. The Brillouin scattering based techniques are mainly used for obtaining the distributed strain and temperature measurements (Ukil et al., 2011). Rayleigh (elastic) scattering involves the largest energy portion and it is characterised by an incoming wavelength equal to the pulse wavelength (Ciocca et al., 2012). The Raman scattering, on the other hand, is less intense and inelastic compared to the Rayleigh and it produces incident wavelengths with different sizes.

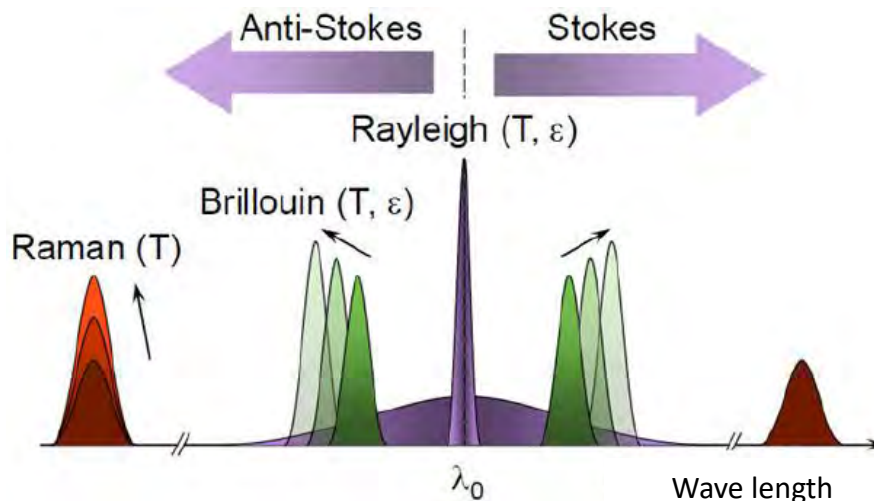


Fig. 3-1: Various types of backscatter

Temperatures are calculated based on the power of backscattering ( $P_{\text{Stokes}}$  and  $P_{\text{anti-Stokes}}$ ), instrument parameter and cable parameter as function of cable length. This is further explained for the Raman DTS in Chapter 5.1.5.

### 3.1.2 Fibre optic (FO) cables installed in the FE tunnel

Various FO cables serving for different purposes were installed along the tunnel walls of the FE tunnel (Fig. 3-2). Tab. 3-1 lists the cable types, cable names and technical specifications of the FO cables installed in FE and specifies the ones used in this report.

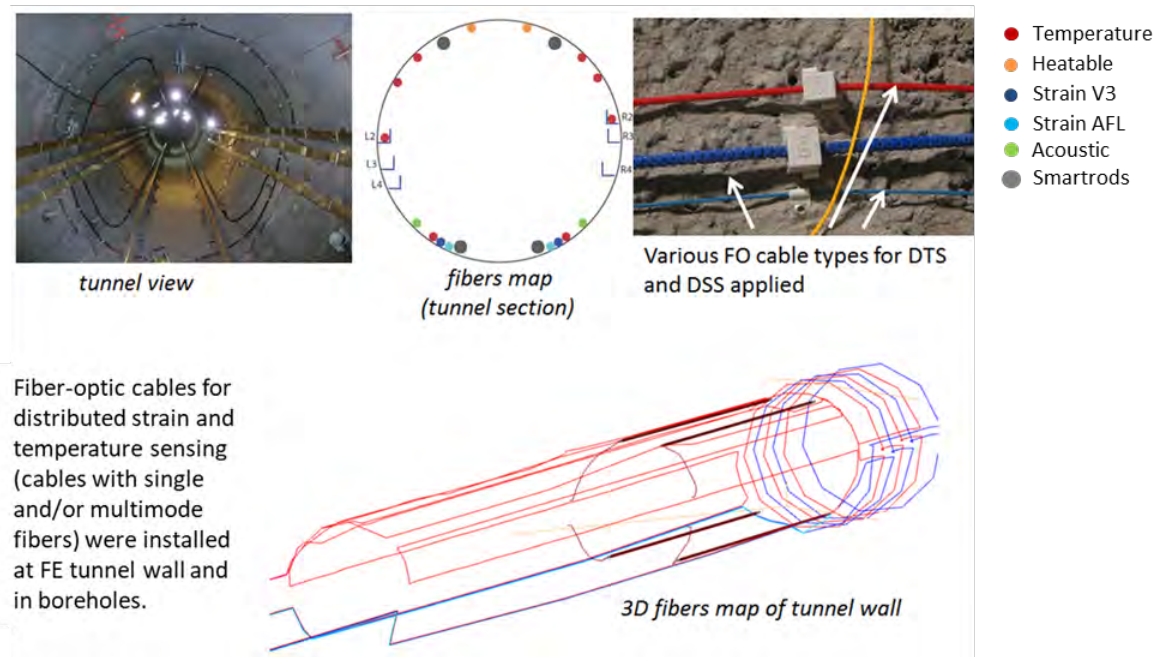


Fig. 3-2: Fibre optic cables that are installed in the FE-Tunnel

Note: Various FO cable types for different purposes were installed in the FE gallery. Cable positions are marked in the cross-section of the upper middle sketch of the figure. The red dots show the Brugg Standard cable, the orange dots show the Brugg Heatable cable, the light blue dots show the AFL cable. The other cables are used for FO strain measurements. The 2 inclinometer boreholes equipped with FO cable, BFEA010 and BFEA011, are not shown. Every cable does loops in the gallery parallel to the gallery axis.

Tab. 3-1: FO cables installed for FE experiment

Cable type	Cable name used in report / FEIS	Manufacturer	Fibres <sup>1)</sup>	Length, L in THM, Diameter	Measured parameter(s)
*BRUsens Temperature 85 °C	Brugg Standard / BK Temp	Brugg Kabel AG	2 mm 2 sm	350 m 189 m 3.8 mm	Temperature Strain
*BRUsens Temperature 85 °C heatable	Brugg Heatable / BK Heat	Brugg Kabel AG	2 mm 2 sm	250 m 84 m 4.0 mm	Temperature Strain
BRUsens strain V3	Brugg Strain	Brugg Kabel AG	1 sm	200 m 86 m 7.2 mm	Strain
*AFL	AFL	AFL Telecommunications	2 mm 2 sm	200 m 49 m 2.0 mm	Temperature Strain
BRUsens Acoustic AC2	-	Brugg Kabel AG	1 sm	180 m 73 m 6.6 mm	Seismicity
Futureneuro FN-SILL-1 (smart rods)	Smartrod	Neubrex Co. Ltd.	2 sm	4 x 135 m 120 m 3.8 x 2.0 mm	Strain

<sup>1)</sup> sm = single mode fibre, mm = multimode fibre

\* Cables studied through the report

The sensing cables (temperature, strain, acoustic) were installed along the tunnel wall. Between plug and interjacent sealing section (ISS), the cables run parallel to the tunnel axis at the heater positions. The cables were arranged in different runs at varying positions on the tunnel wall such that the cables span over the three heaters several times. Fig. 3-2 represents the locations of the heatable and standard temperature, strain and acoustic fibre optic cables. At both ends of each run the cables are fixed firmly preventing the cables to move. In between, the cables are attached on to the tunnel wall with 60 – 70 cm intervals without firm fixation. The cable is allowed moving slightly sideways. These loose fixations were conceived to prevent stress on the fibres during emplacement of the granular bentonite (backfilling).

In the ISS sections between GM 38.5 and 42.5, the Brugg Heatable and the Brugg Strain cables are routed multiple times around the tunnel profile and parallel to the steel arches. At all cable ends, single mode or multi-mode fibres, E2000 APC connectors were installed.

The FE measurements are focused on the THM tunnel section, GM 15 – GM 50 (see Fig. 2-2) between plug and end of the FE tunnel. 600 meters of the FO cables are installed within the THM section (Tab. 3-1).

The distributed temperature measurements in the tunnel are obtained from two cables of manufacturer Brugg Kabel AG, here referred to as the “Brugg Standard” and “Brugg Heatable” cable, and from the AFL cable (manufacturer: AFL Telecommunications, USA) using the Raman backscatter spectrum with the Smartec interrogator (See Fig. 5-1).

All DTS cables are measured using single ended configuration. This means that only on side of the cable (and of the fibre) is attached to the measuring unit (interrogator). The Brugg Standard,

Brugg Heating and AFL cables are additionally monitored for strain by measuring the Brillouin backscatter signal using Neubrex interrogator (See Fig. 5-1). Solely Brillouin backscatter is measured for Brugg V3 and the cable configured as Smartrods (see Fig. 3-3).

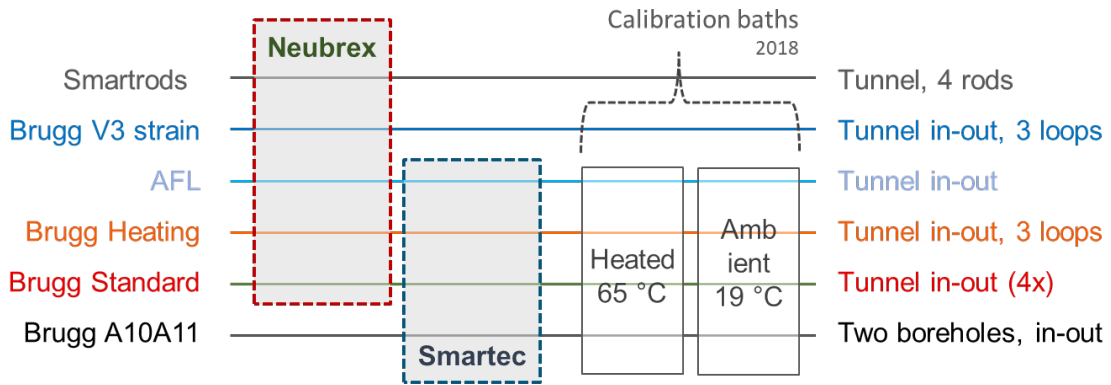


Fig. 3-3: Schematic sketch of FO cables measured by Smartec, Neubrex or by both units

### 3.1.3 FO cables installed in boreholes A10 and A11

The boreholes BFEA010 and BFEA011 start at the entrance of the FE gallery at 00:30 and 11:30 o’clock face positions, respectively, and run roughly parallel to the axis of the FE tunnel (Fig. 3-4) but with slightly uptrend direction. The elevation increases between the borehole mouth to the borehole end by 1.12 m for BFEA010 (Francois, 2012a) and by 1.02 m for BFEA011 (Francois, 2012b).

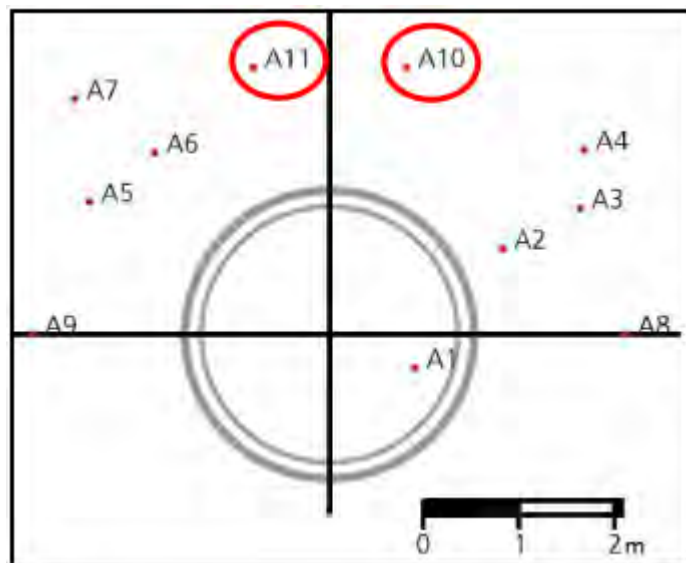


Fig. 3-4: Location of boreholes BFEA010 and BFEA011 (from Morel, 2013).

The borehole BFEA010 has a diameter of 131 mm with 48.08 m length. BFEA011 is 55.1 m long with diameter 131 mm from 0 to 46 m and 76 mm from 46 m to borehole end. DTS cables were routed in and out of the borehole along the outer part of the inclinometer casing such that they occupy four different clock positions (Fig. 3-5). Temperature in these boreholes are also measured using 2 x 40 thermistors distributed along the inclinometers.

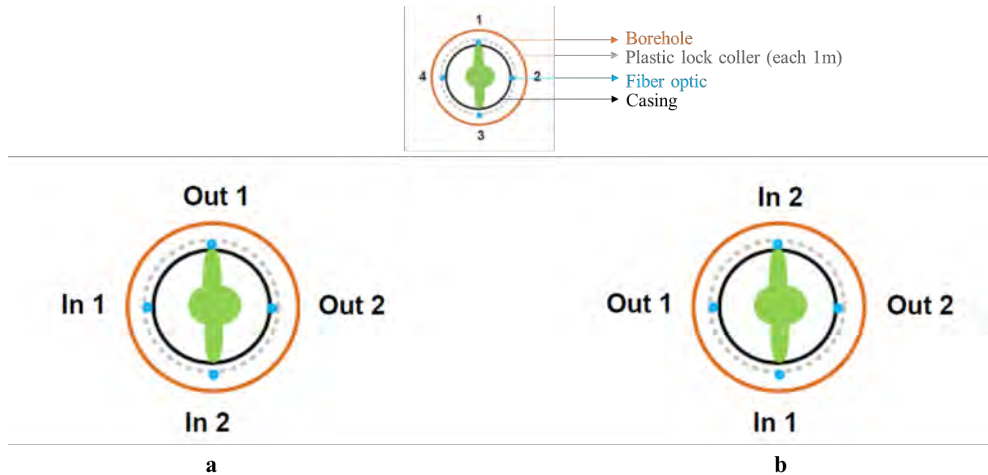


Fig. 3-5: Configuration of measurement position in boreholes a) BFEA010 and b) BFEA011

### 3.1.4 Conventional point temperature sensors in the FE tunnel wall

The conventional temperature measurements with point-temperature sensors (platinum resistance thermometers, Pt1000 installed on the tunnel wall and the Pt1000 sensors installed next to the relative humidity sensors on the tunnel wall) at or close to the tunnel wall were used to compare the results of DTS. The temperature sensors associated with pressure cells are not used for comparisons as they are usually not sufficiently close to the FO cables.

The temperature on the tunnel wall and in the GBM is monitored by Pt1000 sensors installed on the tunnel wall and on the holders. Fig. 3-6 and Fig. 3-7 shows the location of these sensors.

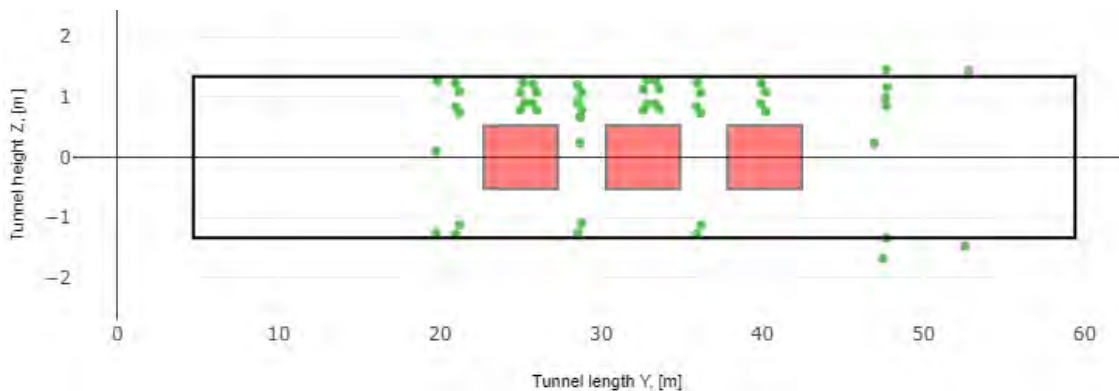


Fig. 3-6: Location of the 53 Pt1000 sensors installed on the tunnel wall and on holders attached to the tunnel wall - Side view of FE tunnel.

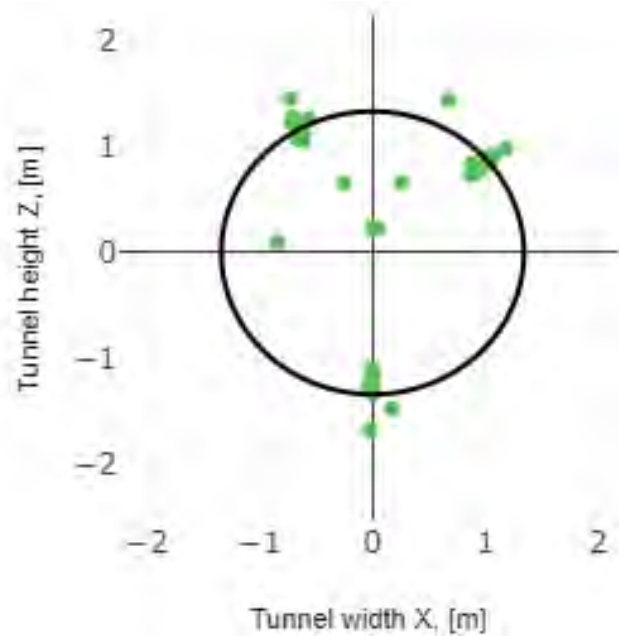


Fig. 3-7: Location of the 53 Pt1000 sensors installed on the tunnel wall and on holders attached to the tunnel wall - Cross-sectional view looking from the FE cavern to the deep end of the FE tunnel.

Tab. 3-2: List of Pt1000 sensors installed on the tunnel wall (plotted in this chapter and sorted according to the tunnel section in which they were installed).

Sensor code: FE_TEM_[XXX-XXX]*	Section
85-86	ISS, porous concrete
87-93	ISS
94-97	H1
98-103	H1-H2
104-111	H2
112-120	H2-H3
121-128	H3
129-134	Plug-H3
135-137	Behind the plug
140-147	In the geophysical pipe

\* XXX stands for the number of the sensor and [XXX-XXX] is a range for sensor numbers installed at the corresponding section

Two different types of relative humidity (RH) sensors (i.e., capacitive RH and monolithic RH) were installed on the tunnel wall and in the GBM (Fig. 3-8 and Fig. 3.9). Each sensor has an integrated temperature sensor inside. In this section (Firat Lüthi, 2018) the spatio-temporal evolution of the relative humidity around the tunnel wall and in the GBM is represented. The spatio-temporal distribution of temperature at the aforementioned sensors is also plotted.

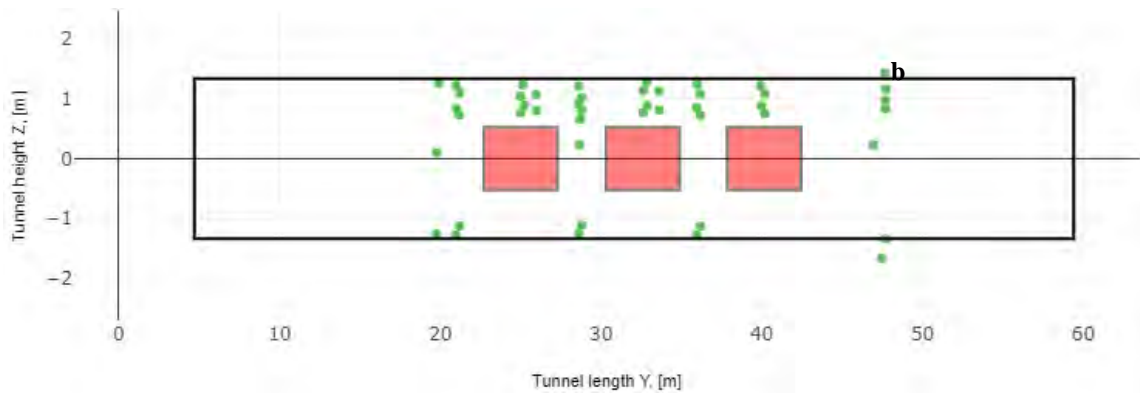


Fig. 3-8: Location of relative humidity and corresponding temperature sensors - Side view of FE tunnel.

Note: All sensors are installed on the tunnel wall or on the holders attached to the tunnel wall

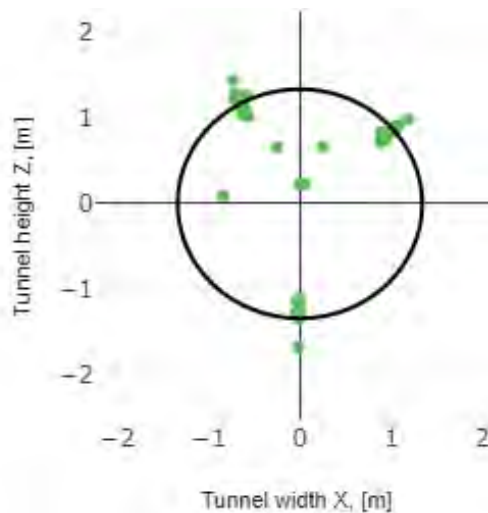


Fig. 3-9: Location of relative humidity and corresponding temperature sensors - Cross-sectional view - looking from the FE cavern to the deep end of the FE tunnel.

Note: All sensors are installed on the tunnel wall or on the holders attached to the tunnel wall

All Pt1000 sensors (except FE\_TEM [85,86,104,105,121 and 122] are installed next to a relative humidity sensor. Therefore, T-sensors of humidity measuring devices were usually not used for comparisons with DTS.

### 3.2 Time-Domain Reflectometry (TDR)

Water content is one of the essential parameters to monitor the (re-)saturation of host rock and backfill material. Hence, a set of water content sensors were installed at different sections in the FE-gallery. During the ventilation phase of the FE Experiment, a total of 30 TDR probes were placed to continuously monitor the evolution of water content in the Opalinus Clay, shotcrete and GBM at the "hot" sections where the effect of the heaters is expected to be significant as well as between the heaters (see Fig 3-10).

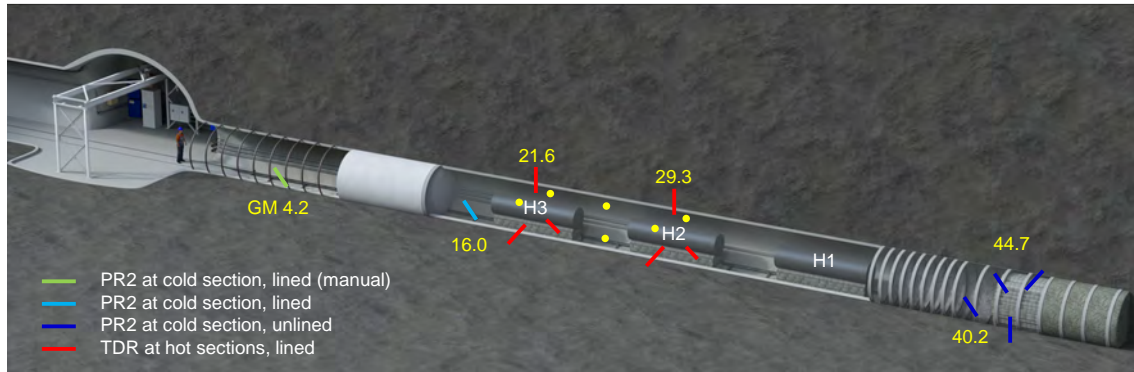


Fig. 3-10: Position of the water content TDR probes.

Red: Rock TDR probe at hot sections (each line has four sensors). Yellow dots: Bentonite TDR probes, Blue, light blue, light green: Commercial moisture probes at unlined cold sections (not discussed in this report).

#### 3.2.1 Working principle

Initially developed for the detection of the discontinuities in the electrical cables, the time domain reflectometry (TDR) became increasingly popular in determination of the water content of soils after its first application in soil water measurements by Topp et al. (1980).

The measurements are done by sending short electric pulses along an open-ended conductor and sampling the reflected signal (see Fig. 3-11). The pulse is reflected at conductor end and the travel time in the conductor can be determined by identifying the entry into the TDR probe and the reflection point in a time-signal voltage diagram.

The travel time of the TDR waveforms are directly related to the apparent dielectric permittivity of the soil material surrounding the TDR electrodes and thereby a function of the water content of this soil.

$$t_s = \frac{2L\sqrt{\epsilon_b}}{c} \quad \text{Equation 3-1}$$

where 2L is the length of the pulse that is travelling along the probe (down and back),  $\epsilon_b$  is the dielectric permittivity of the soil and c is the speed of light in vacuum ( $3 \times 10^8$  m/s).

Under the assumption that the real part of the complex electrical permittivity is close to the apparent dielectric permittivity, the water content  $\theta$  can be evaluated by means of empirical formulas (Evelt et al., 2005; Topp et al., 1980).

$$\theta = - 5.3 \times 10^{-2} + 2.92 \times 10^{-2} \epsilon_b - 5.5 \times 10^{-4} \epsilon_b^2 + 4.3 \times 10^{-6} \epsilon_b^3 \quad \text{Equation 3-2}$$

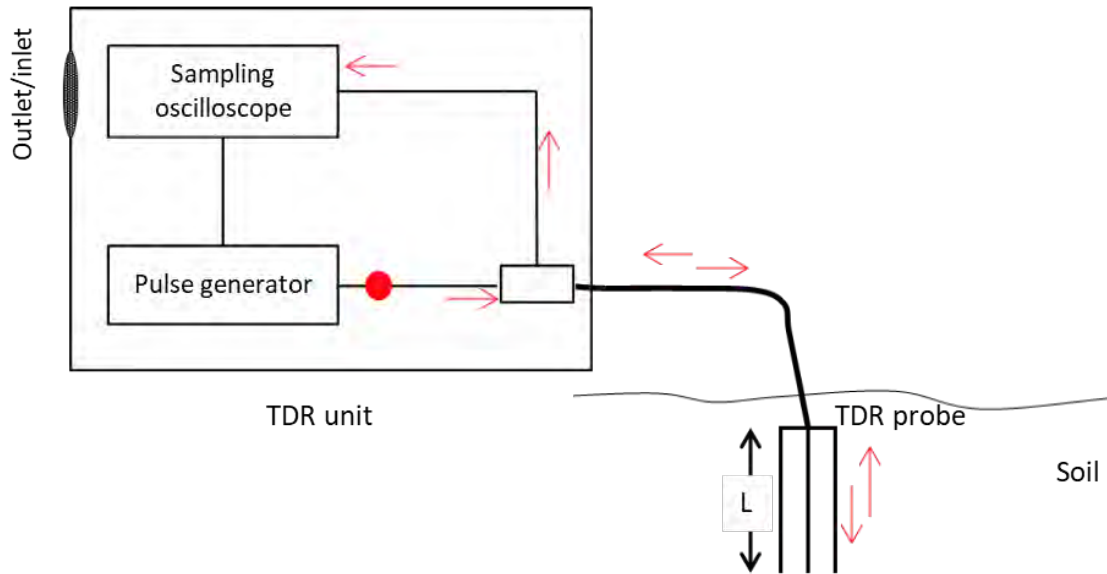


Fig. 3-11: Basic working mechanism of the TDR devices in soil moisture content determinations.

Higher water content will increase the charge storage capacity of the soil and therefore lead to slow reflection of the pulse. In general, the derivation of the soil moisture can be calculated by empirical equations like Eq. 3-2. However, due to the water binding ability of clay, the bulk dielectric constant is reduced, and the determination of the water content requires individual calibration (Jones et al., 2002).

### 3.2.2. TDR rock probes

#### 3.2.2.1 Rock probe design for Opalinus Clay

In order to describe the distribution of water content around the FE tunnel, pointwise measurements can be used. A cylindrical rock probe has been developed to combine four moisture and three temperature measurement points into one sensor unit that can be placed into a borehole.



Fig. 3-12: Customized TDR rock probe for “hot” sections using four TDRs and three temperature sensors for water content and temperature profile determination.

Fig. 3-12 shows the customized TDR probe that was used in the Opalinus Clay section. The total length of this sensor is 120 cm and its diameter is 9.9 cm. A single TDR sensor consists of a two-wire transmission line with open circuit at its end that runs along the circumference of the cylinder. The sampling volume of each TDR sensor is also shown in Fig. 3-10.

The distance between two adjacent TDR sensors is 30 cm and there is a temperature sensor between two adjacent TDR sensors. All feeding cables (four 50 Ohm low-loss H-155 coaxial cables for TDR and three electrical control cable for TEM) are placed inside the cylinder and are led through one side to reach the measurement equipment outside the “hot” section. Before the rock sensor were mounted in the FE tunnel, they have been calibrated using homogeneous and well-known materials.

### 3.2.2.2 Installation of rock probes

The rock probes were installed in boreholes with a 10.1 cm diameter. An inverted “Y” configuration was used to place probes perpendicular and parallel to bedding. Six boreholes were drilled in two cross-sections (around heater H2 and H3) with 24 TDR measurements points in Opalinus Clay. After placing the rock probe into the boreholes, the annulus of 1 mm was filled with grout material (see Fig. 3-13).



Fig. 3-13: Left: vertical inverted “Y” configuration (with probes perpendicular/parallel to bedding); Right: Rock probe after confirming the grout return

A fine grout was used to fill the annulus between rock probe and borehole. As grout components, cement, Opalinus clay powder and water were mixed (roughly 2:4:5 by weight) and injected through a tube from the backend of the sensor to avoid entrapped air. This was necessary to achieve good contact to the surrounded material.

### 3.2.3 TDR probes in granular bentonite

#### 3.2.3.1 Bentonite probe design

The design of the bentonite FE TDR sensors is very similar to that of the rock FE TDR sensors. The sensor material and dimensions are identical so the production process and calibration procedure can be performed in an efficient manner. A temperature sensor was placed in the vicinity of the TDR sensor to obtain individual temperature information at each bentonite TDR sensor position (see Fig. 3-12).

#### 3.2.3.2 Installation of bentonite probes

The bentonite sensors are placed at predefined positions of the tunnel cross-section to measure the water content of the granulated bentonite mixtures (GBM) that fills the space between the tunnel wall and the heaters. They were, thus, installed before the tunnel was backfilled and attached onto the tunnel surface using a retractable metal fixture as seen in Fig. 3-14.

Six bentonite probes were installed at various sections: Two at each tunnel ceiling near to heaters H2 and H3. And additional two at tunnel floor and ceiling between heaters H2 and H3 (compare Fig. 3-10).

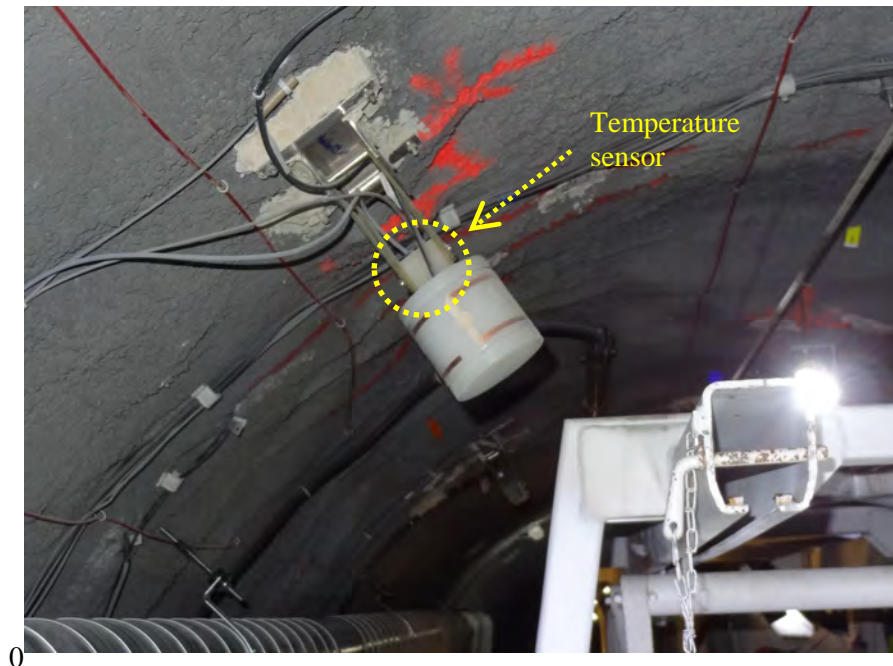


Fig. 3-14: Customized TDR bentonite probe for “hot” sections using a single TDR sensor module. The temperature sensor is located in the white block in the yellow circle.



## 4 FE Data collection and handling

### 4.1 Data acquisition systems (FE-DAS) and FE information system (FEIS)

More than one million data are acquired daily in the FE experiment. Different measurement devices are connected to different DASs (Fig. 4-1). The FE information system (FEIS) has been developed to collect all the acquired data under one roof, to control the quality of the recorded measurements and to easily compare data sets collected by different contractors. FEIS can be accessed through an internet browser installed on any computer or tablet with internet connection.

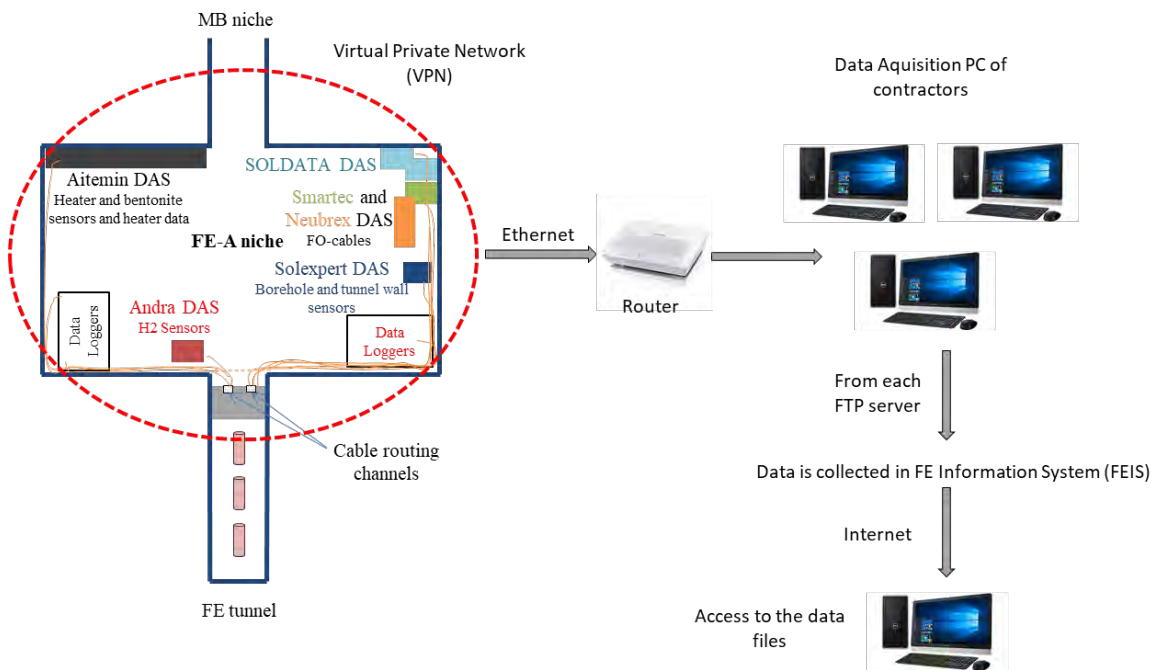


Fig. 4-1: Illustration of the DAS's installed in the FE-A niche (left) and workflow for data collection from all DASs (right).

In addition to the automatically received data and their representation in the database, manual measurements (e.g. geophysical logs and laboratory measurements) can also be entered into the system. The data can be queried and/or downloaded at any specified time intervals. Therefore, the FEIS provides efficient review, data analysis and reporting capabilities for the FE experiment.

The FEIS displays drawings and tables of the FE project construction and layout as well as plots and tables of the project's sensor measurements acquired from its numerous automatic monitoring systems, manually measured data, laboratory analyses and geophysical logs. The data in the database can be accessed and/or downloaded at any specified time intervals.

All FE relevant data presented in the next two chapters (5 & 6) are automatically stored and managed in the FEIS data base. This includes graphical representation of data as well as the processing of data, e.g. for automated calibrations (compare chapter 5.1.5.3). Further, FEIS can check validity / limits of measurements and failure of data pipelines and sends coded error messages via email and sms to selected users.

The FEIS database is continuously maintained to realise integration of new data formats or acquisition systems and to perform bug fixing or enhance usability. The FEIS technical manual and user manual are updated regularly.

### 4.2 Technical background and data pipeline structure

The FEIS is a data-intensive, cross-platform web application built using open-source programs and libraries: PostgreSQL database, Sencha Ext JS framework, the Plotly graphics library, the programming language object REXX and the PostgreSQL command line language psql.

Sencha Ext JS is a pure JavaScript application framework that leverages HTML5 features on modern browsers while maintaining compatibility and functionality for legacy browsers. Sencha has a nearly ten-year track record with more than 10,000 customers. For more information about Sencha Ext JS please see <https://www.sencha.com/>

Plotly is a free open source interactive JavaScript graphing library built on d3.js and WebGL. For more information about Plotly please see: <https://plot.ly/javascript/>.

Object REXX is an open source scripting and macro language which is able to call and control system commands and retrieve results from its execution. The Object REXX distribution includes a front end to the Regina library, enabling the execution of REXX programs directly from the command line. For more information about REXX please see: <http://www.rexxla.org/>

Psql is a PostgreSQL is a terminal-based front-end to PostgreSQL utility used to execute database processes. More information can be found at <https://www.postgresql.org>.

The flow of information through the data-pipeline is illustrated in Fig. 4-2. The term “FE data-pipeline” encompasses all the processes to acquire monitoring data from various FE contractors, evaluate measurement quality, check measurement limits and heater alarms, perform alarm actions, add measurements to the FE database, produce archives and log actions.

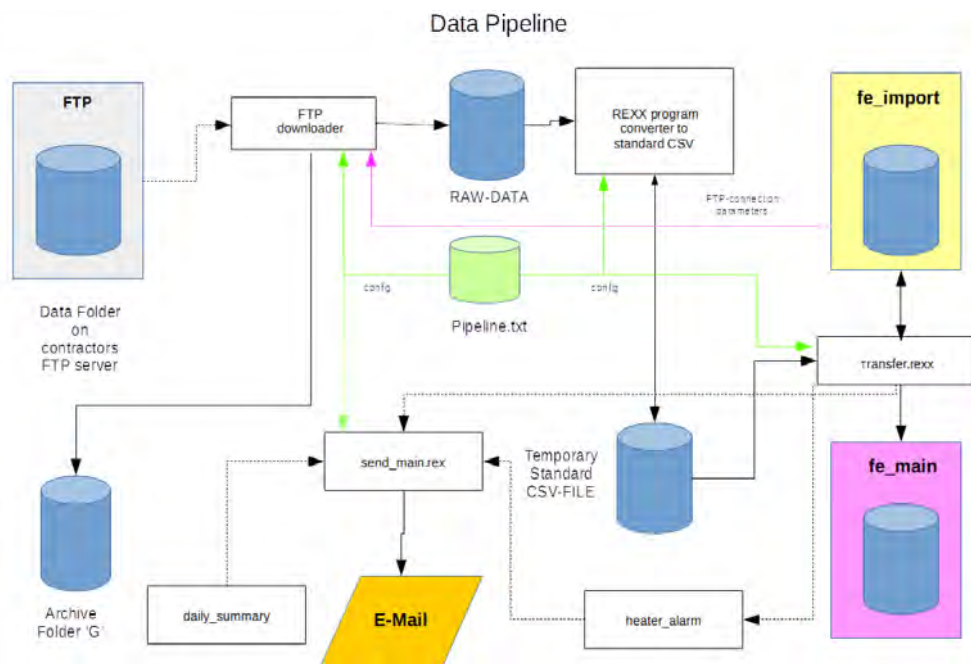


Fig. 4-2: Data Pipeline schematic of the FE information system (FEIS)

## 5 FE Data analysis

### 5.1 DTS data

The DTS method provides a continuous temperature profile along a FO cable, which serves as a distributed sensor, resulting in unique, detailed insights into the temporal and spatial variations of the temperature field in and around the heated FE tunnel. FO cables are routed along the tunnel wall (see Chapter 3.1.2) and in two boreholes parallel to the tunnel axis. After more than 4 years of monitoring (December 2014 – December 2018), all four FO cables are still providing valuable DTS data. A detailed assessment revealed that neither the default instrument settings nor a standard calibration using the DTS device's software provide the targeted measurement accuracy. The observed errors became significant ( $> 4\text{ }^{\circ}\text{C}$ ) over time as temperature differences along the cable rose to  $40\text{ }^{\circ}\text{C}$  as a result of heating. The accuracy was greatly improved in March 2018 after installation of a comprehensive calibration system covering the expected temperature range (described more in detail in Chapter 5.1.5).

Furthermore, with the aim to estimate the initial dry density at the time of the emplacement of the GBM and evaluate the changes in the moisture content through time (Sakaki et al., 2018), every second month active DTS (A-DTS) measurements are being conducted with the heatable FO cables, which are running at the 11:30 and 00:30 location of the tunnel (see Section 3.1.2).

#### 5.1.1 Setting parameters and specifications of the used DTS units

The FO cables in FE tunnel are being measured using two different permanently installed interrogators from the manufacturers Neubrex and Smartec with various settings. The measurement systems in the FE-project are named after them. Each cable is connected with E2000 APC connectors to a channel of the two units. Tab. 5-1 lists the measured FO cables with their corresponding measurement channels specific to the permanently installed interrogator units.

Tab. 5-1: FO cables, DTS devices and channel settings

Cable	Neubrex DTS channel	Smartec DTS channel	Length of cable [m]
<b>Brugg Std</b>	7	2	350
<b>Brugg Heatable</b>	8	3	250
<b>AFL</b>	6	4	205
<b>FO cables in BFEA010 and BFEA011</b>	Not connected	1	615

Furthermore, an additional DTS unit (referred as Silixa unit) has been temporarily used for fingerprinting and benchmarking during the installation of the calibration baths on 5th June 2018. General specifications of the permanently and temporarily used units are shown in Tab. 5-2. Neubrex and Smartec are permanently running during the entire monitoring period from 2014 - 2018.

Tab. 5-2: DTS devices - Technical specifications

Parameter	Neubrex NBX7020	Smartec DiTemp Sensornet: SEN2LR, 2013	Silixa Ultima S
Spatial resolution, $dX$ (m)	0.10	1.02	0.254
Sampling resolution, $dx$ (m)	0.05	1.02	0.127
Minimum sampling time, $dt$ (s)	5	10	1
Backscatter type	Brillouin	Raman	Raman
Data output	$\Delta$ Frequency (MHz) *	Temperature ( $^{\circ}$ C)	Temperature ( $^{\circ}$ C)

\* Strain ( $\mu\epsilon$ ) / Temperature ( $^{\circ}$ C) will be calculated.

The parameter mentioned in Tab. 5-2 are defined as following:

- **Spatial resolution ( $dX$ ):** The spatial resolution is defined as the minimum length over which 90 % of the local step temperature change can be measured.
- **Sampling resolution ( $dx$ ):** The FO cable is virtually divided into subsections having the length specified by the sampling resolution and the obtained data is reported at every specified sampling resolution. For Neubrex and Silixa units the sampling resolution is the half of the spatial resolution. However, for Smartec sampling resolution is equal to the spatial resolution.
- **Sampling time ( $dt$ ):** The sampling time,  $dt$ , is the interval over which the temperature data are to be collected and averaged.

The raw data output from Neubrex DTS provides frequency measurements, which is later processed with respect to the initial condition. The temperature at the start of the heating in 2014 is regarded as 0  $^{\circ}$ C. And therefore, the unit only provides temperature changes along the FO's with an accuracy of 7.5  $\mu\epsilon$  / 0.35  $^{\circ}$ C at 0.05 m sampling resolution (0.10 m spatial resolution).

However; the Smartec unit uses the ratio between the Stokes and anti-Stokes to calculate the absolute temperature with a temperature resolution less than 0.5  $^{\circ}$ C when the measurement interval is chosen 10 min or longer. The accuracy of the Smartec device is given as  $\pm 1$   $^{\circ}$ C depending on the initial calibration at installation.

Function		Property											
General Function	Separation of strain and temperature measured in single fiber, PPP-BOTDA / BOTDR / TW-COTDR / COTDR												
Function	PPP-BOTDA (BOTDR)						TW-COTDR						
Laser wavelength	1550±2 nm						1530 nm ~ 1560 nm						
Distance range	50 m, 100 m, 250 m, 500 m, 1 km, 2.5 km, 5 km, 10 km, 25 km												
Measurement frequency range	9~13 GHz						192300 ~196000 GHz						
Range of strain measurements	-30,000 to +40,000 $\mu\epsilon$ (-3% to +4%)						-15,000 to +20,000 $\mu\epsilon$ (-1.5 % to +2 %)						
Measurement frequency scan step	1, 2, 5, 10, 20, 50 MHz						100, 200, 250, 500 MHz						
Readout resolution	5 cm (default), 1cm (minimum)												
Spatial resolution, cm	2	5	10	20	100	200	2	5	10	20	100	200	
Dynamic range, dB *1	0.5	1	1.5	3 (1)	6 (5)	8 (8)	0.5	1	3	6	10	11	
Max. measurement Distance, km *2	0.5	1	2	5 (1)	18 (15)	25 (25)	0.5	1	10	20	25	25	
Optical budget, dB*1*3	1	2	5	7 (3)	10 (8)	12 (10)	1	2	5	7	13	15	
Measurement accuracy *3*4	15 $\mu\epsilon$ /0.75 °C		7.5 $\mu\epsilon$ /0.35 °C		5 $\mu\epsilon$ / 0.25 °C		0.5 $\mu\epsilon$ / 0.05 °C						

PERFORMANCE						
Parameter	Unit	Model				Comments
		LR	AX	XR	XRS	
Measurement time	s	≥10	≥10	≥10	≥10	>30 recommended
Temperature accuracy	°C	±1				dependent upon calibration at installation
Optical budget	dB	9	9	10	9	Includes 0.3dB for optical connector loss. (One way losses quoted)
Maximum Range	km	12	30	45	30	
Max fibre length	km	12	45	45	30	
Temperature resolution	°C	<0.5 @10km	<1 @30km	<1 @30km	<1 @30km	Acquisition time 10 min
Temperature range	°C	-200 to 600				Depending on cable
Sampling period	m	0.5 to 2				
Spatial Resolution	m	1				10-90% level of a temperature step of 20°C
Battery lifetime	Yr	15				
Fibre type		50/125 $\mu\text{m}$ graded index multimode			9/125 singlemode	62.5 $\mu\text{m}$ fibre may be used with reduced performance

Fig. 5-1: Specifications of two different interrogators installed in FE experiment - above: Neubrex; below: Smartec.

## 5.1.2 Identification of FO measurement positions in 3D space

### 5.1.2.1 Challenges specific to DTS

Depending on the investigation aims, DTS monitoring installation requires a detailed documentation of the FO cable routing. One of the major aims of WP4.4 is to compare the results of FO measurements with conventional sensors. This requires accurate coordinates to compare measuring results between sensors of different type/method. Precise geodetic information related to the Swiss and the FE coordinate system is available for all conventional temperature sensors of the FE experiment. The sensors positions were defined by means of geodetic survey (e.g. for sensors mounted on the tunnel wall) or determined indirectly based on equipment dimensions and borehole surveying data. Defining precise FO cable measuring positions in 3D space is more elaborate. This is mainly because of:

- Complex routing of cables
- Every point along the cable is a potential measuring point depending on the instruments sampling resolution.
- Measuring locations along the cable may vary with DTS set-up.
- Limited number of straight cable sections in tunnel.
- Along straight sections, and depending on the special fixation intervals, the cables distances are slightly longer than the straight point-to-point distances due to sagging of the cables between the fixation points.
- Marker positions along FO cable are often badly readable depending cable use (wear).
- Instrument-specific behaviour how the DTS unit assigns the measured temperature of the sampling interval to a measuring position (see text below and Fig. 5-3).

A DTS unit (interrogator) provides series of cable meter positions ( $z$ ) with related temperatures (calculated based on backscatter parameters) for each measurement. The number of measuring locations as a function of the spacing between the cable meter positions depends on the sampling resolution of the instrument (“The cable is the sensor”). A change of instruments settings or a replacement using a different brand or model results in a different number of measuring points along the cable at different location in the 3D-space of the experiment. Anticipating that more than one setting/instrument will be used over the duration of the project,  $x$ ,  $y$ , and  $z$  coordinates as function of cable distance need to be known for each FO cable position in the region of interest.

### 5.1.2.2 Methods applied

After installation of the FO cables in the FE tunnel and before installation of the buffer material, the cable routing was documented using the following methods:

- Geodetic survey of selected points along the FE cable and of the smart rods.
- Sketches with noted measured distances to already surveyed instruments or markings along tunnel wall.
- “Fingerprinting” (see below) using a point heat source (e.g. hair dryer, see Fig. 5-2) or cold spray.
- Georeferencing of clock positions for “profile sections” which are parallel to the tunnel axis.
- Finetuning of by comparison of DTS profiles against point-type T-sensor profiles.

Additional information is available from laser scanning of the tunnel surface (Eiholzer, 2014).



Fig. 5-2: Fingerprinting: punctual heating of FO cable at geodetically surveyed locations.

### 5.1.2.3 Further adjustments of cable meter positions

FO installation works in the FE tunnel including fixation of the Brugg Std and Brugg Heatable cables were conducted by the contractor Brugg Kabel AG in 2014 (Brugg Kabel AG, 2016). FO cable meter signal checks, referred to as fingerprinting, were conducted using the Neubrex DTS (which has a higher spatial resolution compared to Smartec) at cable locations with known geodetic coordinates.

The FO cables in the BFEA010 and BFEA011 boreholes were originally calibrated in 2012 subsequent to installation (Morel, 2013). At that time, the cables were directly connected to the interrogator. The cable metering changed in 2014 due to the added multiplexer installed between interrogator and the cable. The use of a multiplexer required the installation of additional FO cable meters.

In November 2015, instrument-independent calibration was carried out using three calibration baths (ambient temperature bath, ice bath and heated bath). The method outlined in Hausner et al. (2011) was applied for all cables measured by Smartec; Brugg Std, Brugg Heatable, AFL and A11A10. The results of this calibration are presented in Chapter 5.1.5. Further fingerprinting and correlating the old – new cable meters done by Nagra, it was calculated that the cable meter positions for all cables with corresponding shifts ranging between -4.1 m and -6.9 m for the data recorded between December 2014 and 22<sup>nd</sup> April 2015. Even larger corrections were proposed for the Smartec data recorded from April 22<sup>nd</sup> to November 2015. The reason for the general increase was the exchange of the Smartec unit: the serviced interrogator device was exchanged against the rented device of the same type (Smartec). The sampling resolution differed slightly (0.046 m) between the two instruments. The rented device had a resolution of 1.0154 m; the Nagra-owned instrument a resolution of 1.020 m. This example demonstrates the importance of a suitable data management and data processing system which is capable to calculate actual measuring positions based on the current instrument settings.

#### 5.1.2.4 Instrument-specific adjustments of measuring positions

When using interrogators with different sampling resolution (e.g. Smartec versus Neubrex or Silixa), one would expect to obtain very similar information for a common cable meter location. However, the difference between the resolutions causes a relative shift in the cable meter location which is significant for Smartec having a relatively large sampling resolution. Smartec assigns the result of a measurement representative of a cable section (with length according the specified sampling resolution) to the right side of measuring interval. This is illustrated in Fig. 5-3. Therefore, to compare the cables with different resolutions, additional offset values should be introduced. In that way the cables meter positions can be adjusted with respect to the known locations in the tunnel (i.e heater locations) to represent same information at the same location.

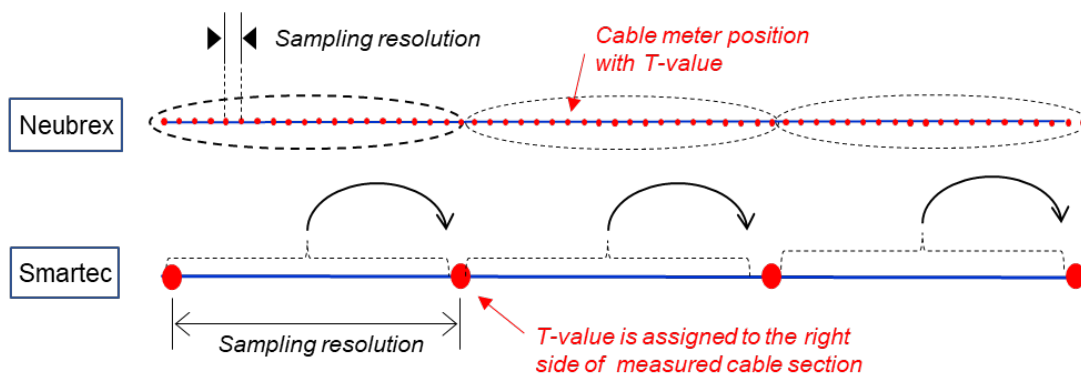


Fig. 5-3: Assignment of cable meter distance to measured temperature value.

The larger sampling resolution of Smartec leads to a shift in cable length of approximately +0.5 m per measurement compared to Neubrex (or Silixa).

#### 5.1.2.5 Cable position results based on fingerprinting and further shift optimization

Tab. 5-3 represents the final cable meter positions for each cable section running in and out of the tunnel with respect to two different DTS units, Smartec and Neubrex. The cable meter positions are given for the various cable sections. The positions shown are based on:

- Fingerprinting works
- Adjustment to compensate sagging of cable between surveyed fixation points (linear correction applied)
- Comparison of DTS profiles with point-type sensor data with exact known locations as well as the comparison to the fixed heater locations
- Instrument-specific adjustments for cable meter positions (Smartec, see above)

Note that the shown start / end cable meter positions differ between Smartec and Neubrex. The reason for the difference in cable meter information between the two DTSs is the addition of an extension cable that is connected to Neubrex DTS. Furthermore, Tab. 5-4 summarizes the corresponding cable meters in these DTS units at the ISS section for Brugg Heatable FO cable.

Note that in ISS section the FO cable is routed along loops at gap 2, 4 and 6. The cable enters the loop at around 04:00 direction and leaves the loop at 03:00 direction.

Tab. 5-3: Final cable fingerprinting for FO cables measured by two different DTS devices

Cable name	Cable section	Clock face position**	Smartec cable meter DTS		Neubrex cable meter DTS		Gallery meter		Comment
			Start	End	Start	End	Start	End	
<b>Brugg Standard</b>	A-B	07:00	85.73	109.19	95.84	118.48	15.61	37.98	
	C-D	09:00	109.19	132.65	120.17	143.01	43.1	15.6	In cable channel L2
	E-F	10:00	133.67	157.13	143.89	166.73	15.59	38.38	
	G-H	10:30	157.13	180.59	167.30	190.14	38.4	15.57	
	I-J	01:30	181.61	205.07	191.83	214.78	15.56	38.29	
	K-L	02:00	205.07	229.55	215.34	238.19	38.3	15.6	
	M-N	03:00	229.55	253.01	238.37	262.31	15.6	38.4	In cable channel R2
O-P	05:00	253.01	276.47	263.91	286.39	38.2	15.61		
<b>Brugg Heatable</b>	A-B	00:30	90.83	114.29	100.87	123.66	15.79	38.15	
	J-K	11:30	154.07	177.53	163.92	186.19	38.37	15.69	
<b>AFL</b>	-	05:00	79.61	103.072	80.95	103.49	20.26	42.72	
	-	07:00	106.132	129.591	107.39	129.87	37.98	15.61	
<b>A11A10*</b>	A10_1	00:00	385.606	431.505	-	-			Out
	A10_2	03:00	482.504	528.403	-	-			Out
	A10_3	06:00	437.625	483.524	-	-			In
	A10_4	09:00	339.707	385.606	-	-			In
	A11_1	00:00	183.65	229.549	-	-			In
	A11_2	03:00	228.529	274.428	-	-			Out
	A11_3	06:00	90.83	136.731	-	-			In
	A11_4	09:00	136.731	182.63	-	-			Out

\*Measured in boreholes BFEA010 (at 00:30) and BFEA011 (at 11:30)

\*\*Clock face positions of the Brugg Std, Brugg Heatable and AFL cables are relative to the FE tunnel (view from the FE-A Niche in direction to the tunnel end). Clock face positions given for the A11A10 cables are relative to the corresponding borehole; view from niche in the direction of the borehole axis.

Tab. 5-4: Final cable fingerprinting for Brugg Heatable FO cable in the ISS section.

Cable name	Cable section	Clock face position		Smartec cable meter DTS		Neubrex cable meter DTS		Gallery meter
		Start	End	Start	End	Start	End	
Brugg Heatable	Gap 2	04:00	03:00	117.75	126.14	127.24	135.93	39.25
	Gap 4	04:00	03:00	127.80	136.84	137.42	146.46	40.24
	Gap 6	04:00	03:00	137.40	146.18	148.55	157.33	41.23

### 5.1.3 Signal analysis

The cables in FE are measured with two different DTS devices, Smartec and Neubrex. The Smartec DTS uses Raman backscattering to calculate the absolute temperature from the returning signals. The back-scattered light in this method contains two spectral components; the Stokes component with the higher wavelength in which the photons are generated, and the anti-Stokes components with a lower wavelength (Tyler et al., 2009). As the temperature increases, the number of the molecules that are in high energy state will also increase, which will intensify the fraction of anti-Stokes scattering relative to the Stokes signal. As a result, the local temperature measurements can be obtained from the ratio between the anti-Stokes and Stokes (Ciocca et al., 2012).

The Neubrex interrogator uses Brillouin frequency shift to calculate the changes in temperature with respect to start of the experiment. Therefore, the calculated data provide the change in the temperature (with respect to the reference data at installation) rather than the absolute values. The temperature is calculated by using Equation 5-1.

$$T = \frac{\Delta\nu_R}{\tilde{c}_{22}} \quad \text{Equation 5-1}$$

where  $T$ ,  $\Delta\nu_R$ , and  $\tilde{c}_{22}$  stand for temperature, Rayleigh frequency shift, and modified Rayleigh frequency-temperature conversion coefficient, respectively.

### 5.1.4 Effects of changes in fibre quality over time

A constant good quality of the fibre properties is a prerequisite for accurate DTS measurements, at least in the absence of an independent dynamic calibration system (Chapter 5.1.5). Attenuation is defined as the loss of signal per unit length of fibre (in dB/m) and is a function not only of fibre construction but of wavelength of signal. Simple attenuation typically results in a noisier temperature signal as less light is returning to the detector per unit time (Tyler et al., 2009).

After installation at the FE experiment, all cables were checked with respect to attenuation using an optical power meter. The multi-mode fibres were checked at 1300 nm wavelength and the single-mode fibres at 1550 nm. All cables types were proved to be in good condition after installation (Brugg Kabel AG, 2016).

The DTS without independent dynamic calibration does not compensate for signal damping along the length of the cable. The attenuation of the FO cable can be affected by the following factors:

- Strain on the cable, e.g. at locations with sharp bends or kinks
- Cable damage
- Dust in splices
- Cable aging (by hydrogen gas penetration)

The presence of these factors can change the intensity of the Stokes and anti-Stokes (Tyler et al., 2009). DTS temperature is calculated from the ratio of Stokes and anti-Stokes returning signal. If attenuation affects these two signals differently, DTS calculation become erroneous. Therefore, it is important to detect any step-losses along the cable (Chapter 5.1.4.3) and apply the signal loss correction to the data (Chapter 5.1.5).

#### 5.1.4.1 Example showing the effect of varying signal-loss

The effect of changing light-loss at specific cable position  $z=115$  m is illustrated for the AFL cable in Fig. 5-4 and Fig. 5-5. No dynamic calibration system was available during the examined timeframe. In Fig. 5-4, power of Stokes, anti-Stokes and  $R(z)$  (equals the natural logarithm of the ratio  $P_s/P_{as}$  at cable distance  $z$ ) are plotted together with DTS device (Smartec DiTemp) temperatures against time. Until 1<sup>st</sup> of September 2016, the change of these parameters essentially reflects the increase of temperature due to heating. On 1<sup>st</sup> September,  $R(z)$ , power of Stokes and anti-Stokes dropped abruptly and continued at a lower level. At the same time, temperature increased. After 14 ½ months, the backscattered light changed again abruptly and established at comparable levels as before the initial change. Note that the scatter of the Smartec temperature is increased during the period with increased step-loss, as one would expect for a cable with decreased light transmission.

Fig. 5-5 shows the lateral change of the same parameters along the AFL cable for three instances: before the abrupt signal loss, before the signal increase after 14 ½ months and a day later after the signal increase. Without verifying in detail, the temperature curve seems reasonable between cable meter 65 and 113 which covers the entire cable section at clock face position 05:00 and one third of the cable section at clock face position 07:00. Plausible temperature bumps are visible at heater positions H3, H2, at 07:00 direction. At distances greater 135 m, the temperature bumps seem plausible for the temperature curves recorded on 2016-08-31 and 2017-11-14 but not for the temperature curve of 2017-11-13. These data show an extra distinct peak at H2 position which relates to the cable range with distinct temporary light-loss and the period of increased signal loss.

The temporary character of the described changes suggests that the signal loss was due to increased strain on the cable between cable meter 113 and 116 during a limited time period from 1<sup>st</sup> of September 2016 to 13<sup>th</sup> of November 2017. As far as the strain is below the damage threshold, the strain-induced effect is reversable. The Neubrex strain data (not shown here) show increased data scatter in this period which coincide with the abnormal Smartec temperatures. The strain on the cable was relieved on 13<sup>th</sup> of November 2017 due to unknown reason.

The Brugg Standard cable runs parallel and very closely to the AFL cable at the 05:00 and 07:00 clock face positions. However, the Brugg Standard data do not show abnormal temperatures for the examined time period. This can be explained by the different design of the Brugg cable with a concept of loose fibre buffering in the tube which reduces the tensile stress on the fibres.

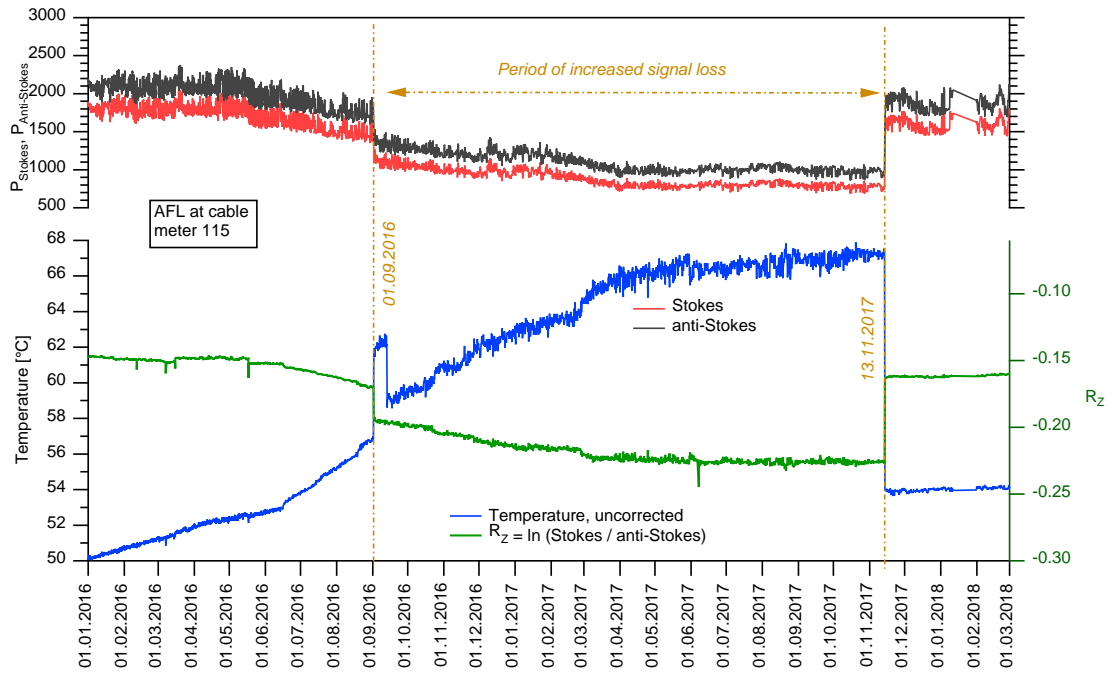


Fig. 5-4: Effect of abruptly changing Stokes/anti-Stokes ratios on DTS instrument temperatures shown in time-series graph.

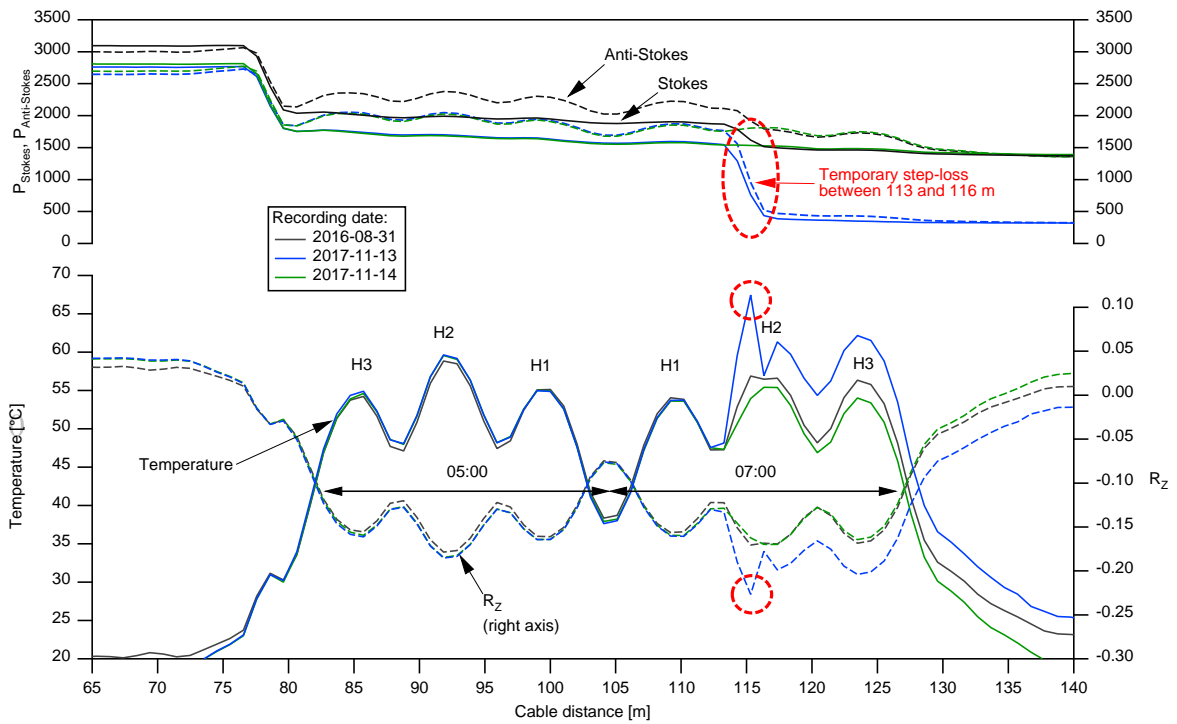


Fig. 5-5: Effect of abruptly changing Stokes/anti-Stokes ratios on DTS instrument temperatures shown in DTS profile graph.

### 5.1.4.2 Detection of signal quality

The signal quality can be checked by using a coloured temperature plot, where the temperature along the cable is plotted versus time. Such an overview plots is illustrating, that the temperature evolution of a cable section are useful to detect changes in signal quality and events impacting the measurements. Irregular patterns in the graph of Fig. 5-6 reveal missing data (white vertical lines/bars) and changes in signal quality.

Alternatively, the below mentioned signal issues could be retrieved from a simple time series graph for one or a couple of measuring locations along the cable. However, the plot-type of Fig. 5-6 provides an additional dimension by using the colour as temperature information which is provided for all measurement points of the distributed sensor along the Y-coordinate.

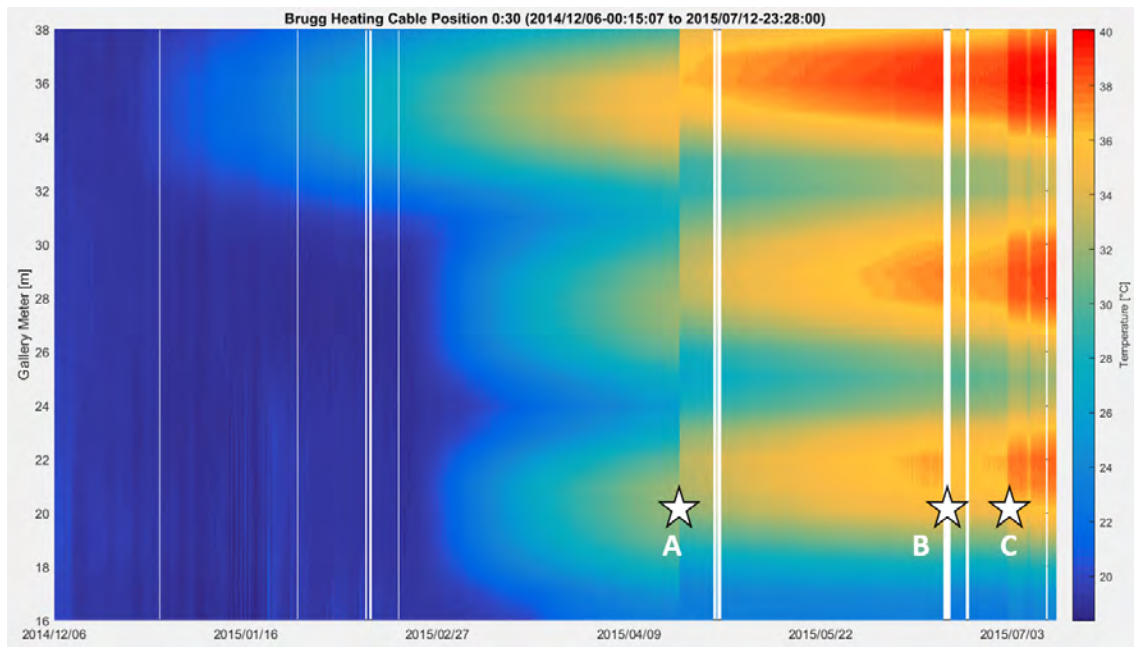


Fig. 5-6: Irregular patterns in a coloured heat plume plot

Note: The plot shows the temperature evolution of a cable section and provides useful information with respect to signal quality issues. The white vertical lines or bars indicate missing data. Other events are marked with the star symbol: A) Exchange of interrogator creates an artefact in form of a lateral temperature shift because the new unit has a slightly different spatial resolution; B) After rerouting of the FO cable, dust is trapped in the connector; C) The connector is cleaned.

### 5.1.4.3 OTDR measurements for the localisation of signal losses

The most recent OTDR measurements are conducted on 28 March 2018 with two different wavelengths (850 nm and 1300 nm) on the FO cables measured by Smartec DTS (i.e. Brugg Std, Brugg Heating, AFL and A11A10).

According to the results, there is one point with signal loss in A11A10 where the cable has spliced in A11A10 where the cable has spliced between the boreholes, and the other signal loss occurs in AFL cable around the cable meter 74. This part of the cable corresponds to the plug region where the cable is routed towards the tunnel. The values of the signal losses from two different wavelength measurements are summarized in Tab. 5-5.

Tab. 5-5: Step-loss at 850 nm and 1350 nm

Cable Name	850 nm		1350 nm		Remarks
	Distance (m)	Loos (dB)	Distance (m)	Loos (dB)	
<b>Brugg Std</b>	-	-	-	-	-
<b>Brugg Heating</b>	-	-	-	-	-
<b>AFL</b>	74.4	0.674	74.34	0.417	at the entrance of plug
<b>A11A10</b>	315.5	0.321	322.69	0.238	at the splice

### 5.1.5 DTS Calibration

Subsequent to the installation and start operation of the FE DTS system in September 2014, the default calibration of the DTS units was used. The default calibration of the DTS provides good measurement accuracy under stable operating conditions. However, the obtained temperature measurements from a Raman spectrum based DTS can be affected by multiple factors. The operating temperature and conditions of the machine, quality of the incident laser pulse, physical conditions and the cleanliness of the connections, presence of strain or sharp bends at any location along the fibre and the consistency of the power supply are amongst the most important conditions to have an impact on the temperature accuracy. For example, a DTS calibrated to have  $\pm 0.2$  °C accuracy under stable conditions might provide measurements with  $\pm 1-2$  °C accuracies while rapid heating and cooling (Hausner et al., 2011).

Therefore, although the DTS units can provide high accuracies at the time of installation, dynamic calibration which is applied to each measurement and includes the use of baths of exactly known temperature is important to obtain improved and consistent accuracy. The dynamic calibration system of the FE FO temperature monitoring system was put in operation by end of March 2018.

#### 5.1.5.1 Design specifications

Two tanks (~220 l) are used for calibration purpose, an ambient temperature bath (CB1) and heated bath (CB2). The calibration baths were designed such that the inside temperature is kept constant spatially and over time. Pictures of the hardware installations are given in Fig. 5-8 and Fig. 5-9.

The ambient bath is not heated, and it equilibrates continuously with at the ambient FE-A niche temperature. Because the niche is deep within the tunnel system, the temperature is relatively steady, and the minor changes are very slow. An air bubbler line is used to mix the ambient water to help keep temperature even throughout the bath. An electric heating element and control unit in the heated bath keep the water temperature relatively constant (within about  $\pm 0.1^{\circ}\text{C}$ ). An electric motor turns an impeller to mix the heated water to keep temperature even throughout the bath.

The baths were designed such that “external factors”, such as temporary temperature changes in the niche or a temporary power interruption (affecting heat supply) would have only minimal effect on the bath temperatures.

The main design specification can be summarized as follows:

- Large water volume (~220 l) of the baths contribute to the thermal inertia of the system. Outside dimensions without top cover: 1.2 m x 0.7 m x 0.63 m; inside dimensions: 1.0 m x 0.5 m x 0.5 m.
- Uniform temperature distribution in the baths. The internal heat stratification is prevented by circulation of the water (mixing).
- The water temperature of the heated bath is controlled within a narrow range ( $0.1^{\circ}\text{C}$ ).
- The walls, the bottom and the cover of the baths are thermally isolated using 10 cm thick Styrofoam.
- The heat input is uniformly distributed by using a 14 m long heating coil routed along parallel lines on the bottom of the bath.
- The temperature span between ambient bath ( $19^{\circ}\text{C}$ ) and heated bath ( $65^{\circ}\text{C}$ ) covers the temperature range present at the tunnel wall in the FE tunnel.

The thermal isolation is somewhat compromised by a recess at the top of the front wall which is required to run the FO cables in and out of the baths. Currently an improved sealing of the voids between the cables at the entry/exit of the cables is evaluated. The heated bath is currently losing about 5 litres of de-ionized water per month due to increased vapor pressure inside the bath leakage (through the cable channel) to the outside. The increased inside vapor pressure also led to water migration of water along the wires through the heating cable. An appropriate inside sealing procedure had to be applied to interrupt this leakage path.

High precision thermometers, connected to a separate data acquisition system, are used to measure the inside bath water temperatures. The thermostat controls the temperature of the heated bath using a separate sensor. The bath temperatures are recorded every 5 minutes. For calibration calculations, average bath temperatures over a time span corresponding to the interrogation time of the FO measurement are used.

No heat control is applied to the ambient temperature bath. Its temperature is equilibrating with the average niche temperature. An air aquarium bubbler is used to avoid any heat stratification in the ambient temperature bath.

The water circulation in the heated bath is maintained by an industrial mixer at about 20 turns per minute.

### 5.1.5.2 Set-up of the calibration system

Single-ended FO measurement configuration is used as shown in Fig. 5-7. Each cable runs through the ambient temperature bath (CB1) and then through the heated bath (CB2) before entering the tunnel. In the return section, cables enter first the warm bath (CB2) then the ambient bath (CB1). Two calibrated high precision sensors (CTP5000) are connected to the precision thermometer ASL CTR2000 and record the bath temperatures with an accuracy of  $\pm 0.03$  °C.

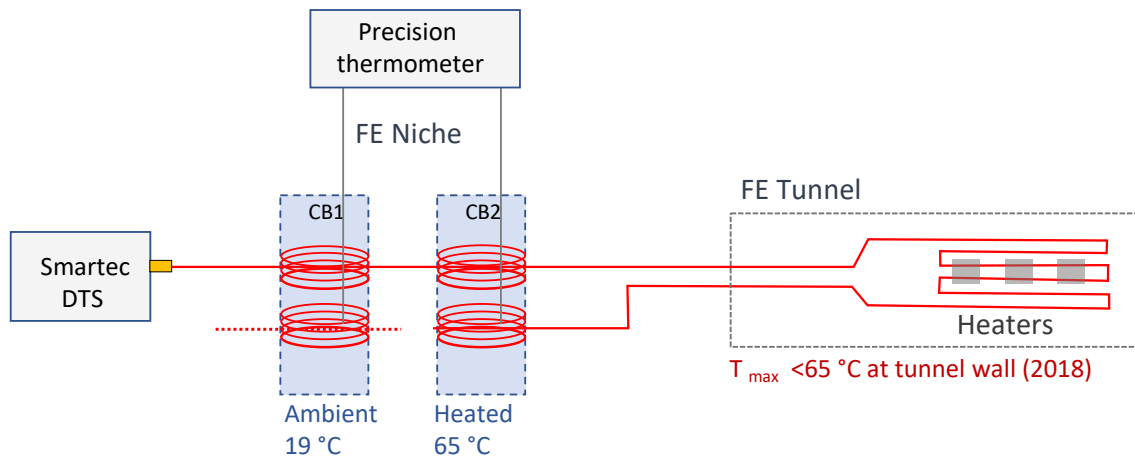


Fig. 5-7: Single-ended configuration of permanent calibration system.

For DTS calibration and validation, reference temperatures of CB1 and CB2 are used as follows:

- Outbound / CB1: independent reference temperature T1 used for calibration
- Outbound / CB2: independent reference temperature T2 used for calibration
- Return / CB2: independent reference temperature T3 used for calibration
- Return / CB1: independent reference temperature used for validation

The calibration procedure is described in Chapter 5.1.5.3. Calibrated temperatures at four measuring points within the cable section passing through CB1 (on cable return) are then compared to the reference temperature of CB1. The differences are expressed as root mean square errors (RMSE, see Chapter 5.1.5.4).

The locations of the cables in baths are also represented in Fig. 5-8. With exception of the AFL cable, all cables are fixed at two different sections in the baths. Approximately 2-4 m of cable were kept as a buffer between the two baths at each transition and for each cable to minimize heat exchange between baths.

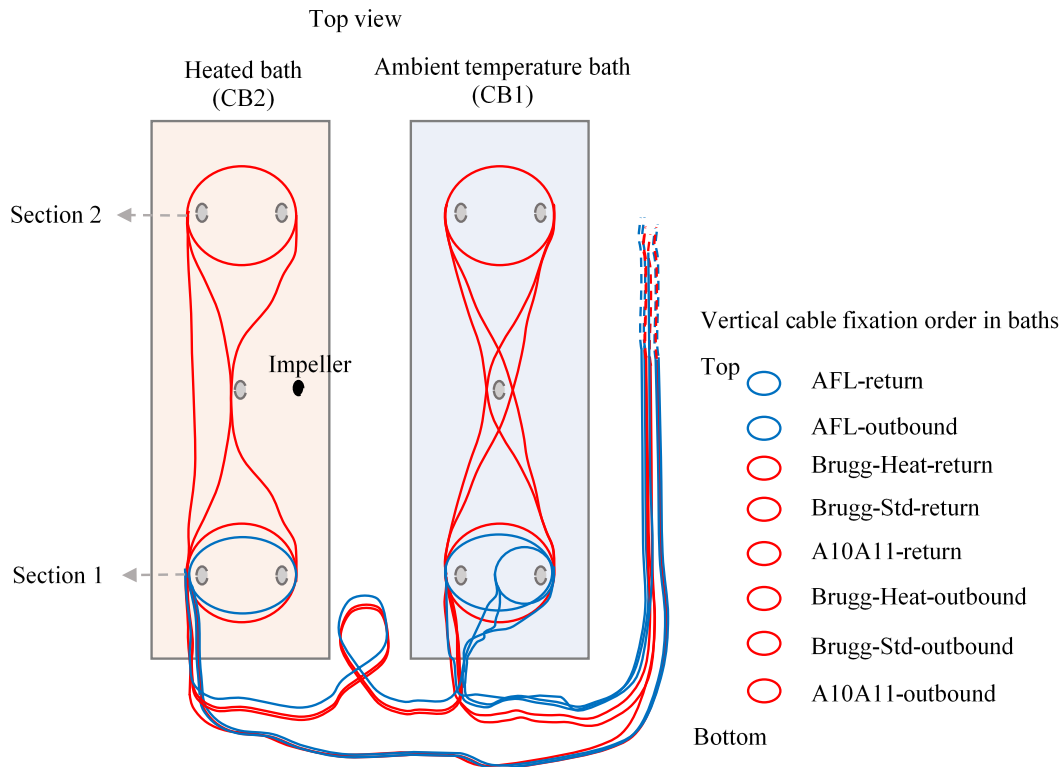


Fig. 5-8: Arrangement of cables in the calibration baths.

Two DTS devices, Smartec and Neubrex are in permanent operation at the FE experiment measuring partly the same FO cables. To obtain the best results for independently calibrated data, the length of the cable submerged in the bath should have a length which equals about ten times the spatial resolution of the DTS (Tyler et al., 2009). Based on Smartec's spatial interval of 1.02 m, 10 m long cable sections for the outbound and return runs were targeted for each bath, depending on availability. The cable lengths as installed are given in Tab. 5-6. The lengths were read from the printed cable meter labels during installation. Calculating the amount of FO cable being fully equilibrated with the bath temperature and excluding sampling intervals with start/end point outside or near bath entry/exit gives shorter theoretically usable cable lengths (for calibration purpose). Start/end points near bath entry/exit were looked up in the DTS data files. The theoretically usable cable meter lengths for calibration are listed in Tab. 5-7

The calibration procedure includes averaging of Stokes and anti-Stokes values from representative measuring points in the bath sections (Chapter 5.1.5.3). The amount of cable meter submerged in baths seems well dimensioned for calibration purpose at first sight. However, during calibration works it became evident that only a fraction of the theoretically available measuring points could effectively be considered for calibration purpose. The limitation arises from a signal smearing effect which is probably caused by secondary pulses of the DiTemp's (Smartec) laser. The effect is normally not visible for moderate lateral temperature gradients but becomes important at the abrupt temperature changes at the transition from/to the heated bath (Chapter 5.1.6). The number of DTS (Smartec) measurement points used for dynamic calibration as implemented in FEIS (since 28.03.2018) is given in Tab. 5-8.

Tab. 5-6: Cable meter lengths in baths as-built (field assessment / as given by FEIS).

Cable name	CB1: ambient temperature bath		CB2: heated bath	
	Outbound (m)	Return (m)	Outbound (m)	Return (m)
<b>Brugg Standard</b>	15 / 16.7	11 / 14.2	17 / 11.2	14 / 10.2
<b>Brugg Heatable</b>	19 / 20.2	19 / 19.3	15 / 13.3	14 / 12.2
<b>AFL</b>	10 / 9.8	14 / 13.2	11 / 6.1	18 / 14.3
<b>A11A10</b>	22 / 24.5	19 / 20.6	23 / 19.3	19 / 15.3

Tab. 5-7: Cable meter lengths in baths theoretically usable for calibration (Smarterc).

Cable name	CB1: ambient temperature bath		CB2: heated bath	
	Outbound	Return	Outbound	Return
<b>Brugg Standard</b>	12.2	10.20	11.2	11.2
<b>Brugg Heatable</b>	16.3	17.3	13.2	12.2
<b>AFL</b>	7.1	11.2	7.1	14.3
<b>A11A10</b>	19.4	16.3	19.4	16.3

Tab. 5-8: Number of measuring points in baths used for dynamic calibration (Smarterc)

Cable name	CB1: ambient temperature bath		CB2: heated bath	
	Outbound (calibration)	Return (validation)	Outbound (calibration)	Return (calibration)
<b>Brugg Standard</b>	8	4	3	4
<b>Brugg Heatable</b>	5	9	5	4
<b>AFL</b>	3	3	3	3
<b>A11A10</b>	5	4	5	3

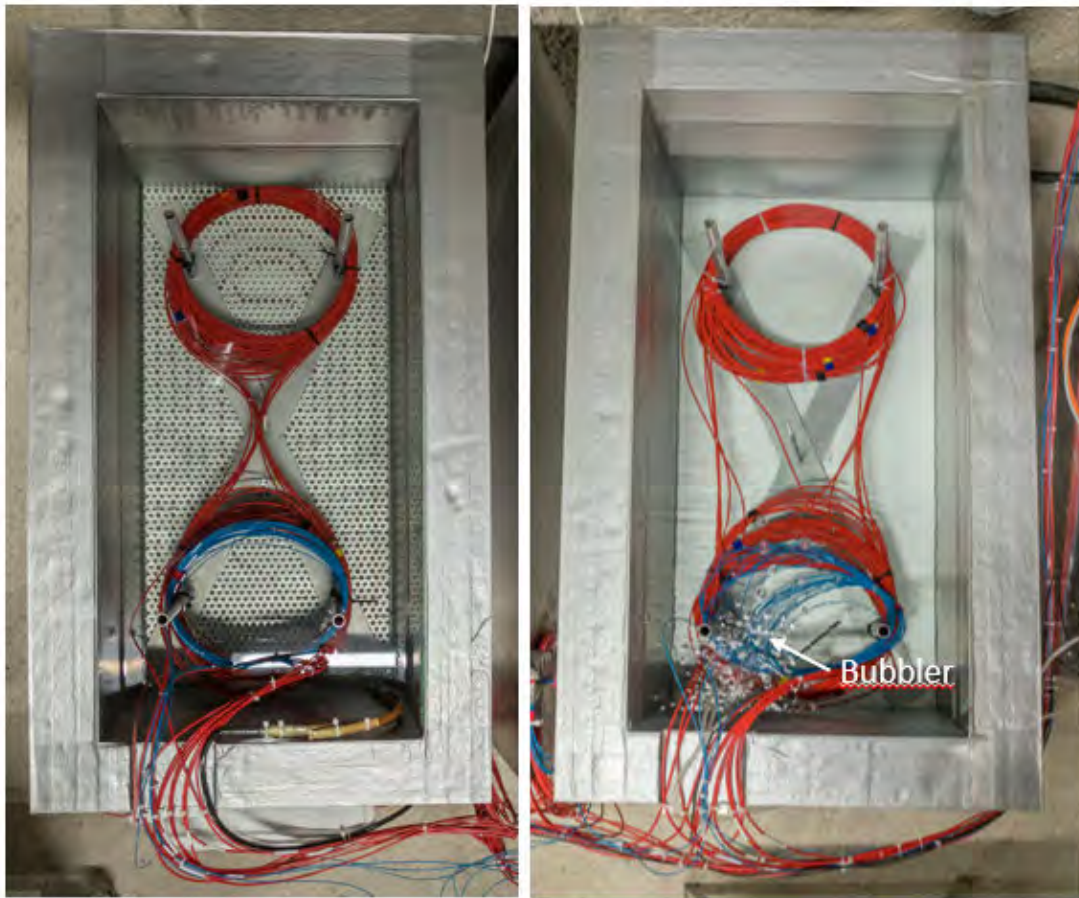


Fig. 5-9: Heated bath (left) and ambient temperature bath (right) without cover

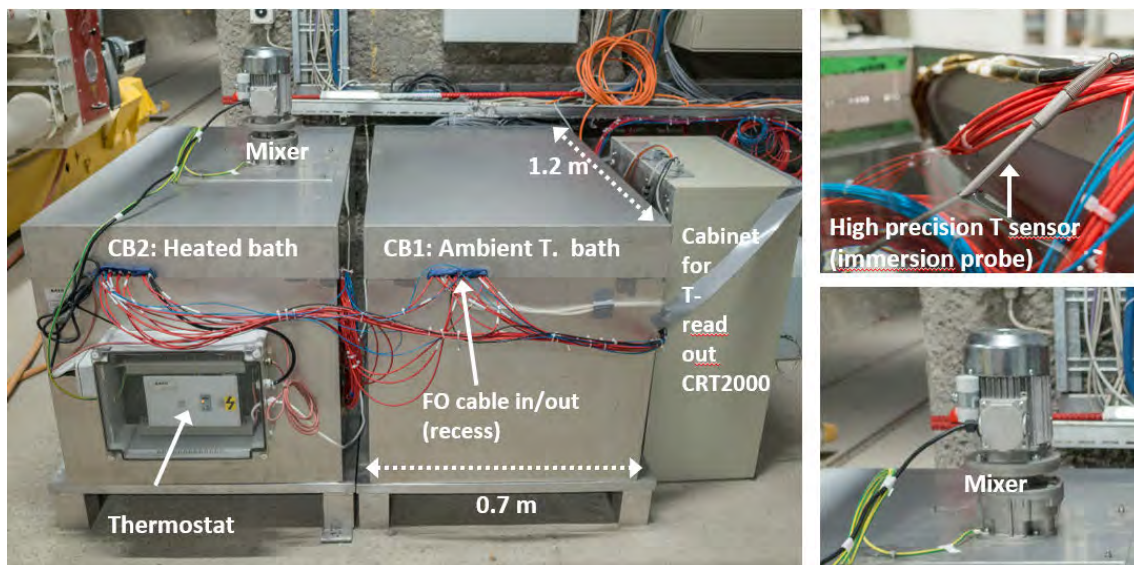


Fig. 5-10: Calibration baths and components

### 5.1.5.3 Dynamic calibration formula

The FE information system (FEIS) calculates “dynamic” coefficients for each Smartec FO cable measurement based on:

- Raman spectra backscatter measurements.
- Equations described by Hausner et al. (2011).
- Calibration bath temperatures.
- Signal step losses.

The Raman backscatter is measured by the Smartec interrogator and recorded as paired values, power of Stokes and power of anti-Stokes. The Stokes signal has a slightly longer wavelength than incident laser light. The anti-Stokes signal has a slightly shorter wavelength than incident laser light. The power of the Stokes signal is relatively temperature independent while the power of the anti-Stokes is strongly dependent on the temperature of the fibre. The difference in the signal temperature responses makes it possible to calculate temperatures along the fibre based on the Raman spectra backscatter measurements.

The two Raman signals have distinct attenuation (damping) rates in an optical fibre because of their different wavelengths. The differential attenuation rate  $\Delta\alpha$  (the difference between the attenuation rates of the Raman Stokes and anti-Stokes signals along the glass fibre) is required in the calibration equation described below. The formulas presented by Hausner et al. (2011) are used to calculate the temperatures as a function of cable length ( $z$ ) and measured power of Stokes and anti-Stokes ( $P_S, P_{aS}$ ):

$$T(z) = \frac{\gamma}{\ln \frac{P_S(z)}{P_{aS}(z)} + C - \Delta\alpha z} \quad \text{Equation 5-2}$$

Where:

- $\gamma$  = coefficient related to material of the fibre and dependent on the DTS instrument; the change in energy between a photon at the incident wavelength and a scattered photon in the Raman spectra
- $C$  = dimensionless coefficient related to the incident laser and photon detectors of the DTS instrument and the glass fibre; the fraction of the scattered light that is directed back into the fibre towards the initial light source
- $\Delta\alpha$  = differential attenuation rates of the Raman Stokes and anti-Stokes signals; the coefficient related to damping (continuous signal loss over the cable)
- $P_S$  = Stokes
- $P_{aS}$  = anti-Stokes
- $z$  = distance from the instrument along the fibre

The glass fibre differential attenuation rate  $\Delta\alpha$  of the Raman Stokes and anti-Stokes signals along the fibre is affected by strains, impingements, sharp bends, as well as damage to the fibre itself (including splices). A sudden change of  $\Delta\alpha$  at a point or over a short section on the fibre is referred

to as a “step loss”. Step loss correction options are included in the dynamic calibration routines of FEIS.

The large temperature gradients in the FE tunnel make detection of step losses by evaluating the Raman Stokes and anti-Stokes signals and  $R_z$  difficult. Step losses were identified using optical time-domain reflectometry (OTDR) that measures the Stokes and anti-Stokes signals at frequencies where ratios are less influenced.

A procedure in FEIS solves for the system of linear equations given by Equation 5-2 for  $\gamma$ ,  $c$ ,  $\Delta\alpha$  using the reference temperatures  $T_1$ ,  $T_2$  and the Stokes and anti-Stokes  $P_s$ ,  $P_{as}$  at the calibration bath mid-points. The procedure solves the system given in Equations 5-3, 5-4, 5-5 and 5-6.

$$\bar{A}\vec{x} = \vec{b} \quad \text{Equation 5-3}$$

$$\bar{A} = \begin{bmatrix} 1 & -T_1 & T_1 z_1 \\ 1 & -T_2 & T_2 z_2 \\ 1 & -T_3 & T_3 z_3 \end{bmatrix} \quad \text{Equation 5-4}$$

$$\vec{x} = \begin{bmatrix} \gamma \\ c \\ \Delta\alpha \end{bmatrix} \quad \text{Equation 5-5}$$

$$\vec{b} = \begin{bmatrix} T_1 \ln \frac{P_s(z_1)}{P_{AS}(z_1)} \\ T_2 \ln \frac{P_s(z_2)}{P_{AS}(z_2)} \\ T_3 \ln \frac{P_s(z_3)}{P_{AS}(z_3)} \end{bmatrix} \quad \text{Equation 5-6}$$

#### 5.1.5.4 Verification of calculated temperatures (RMSE)

The root-mean square error (RMSE) (Equation 5-7) is determined using the difference between the calculated temperature and the measured bath temperature at cable positions within the verification bath (at cable return) using the equation shown below. The RMSE value is stored with every cable measurement. The RMSE gives an idea about the quality of the calibration by representing how far the calculated temperature deviates from the measured bath temperature. An increase in the RMSE indicates that the quality of the calibration has decreased and suggests that something in the system has changed (a new step loss has developed, the cable properties have changed, the hardware is not working properly, etc).

$$RMSE = \sqrt{\frac{1}{n} \sum_1^n (T_{DTS} - T_{obs})^2} \quad \text{Equation 5-7}$$

### 5.1.6 Comparison of calibration results between Smartec and Silixa

During an FE site visit on 5th of June 2018, a Silixa Ultima-S unit was used to temporarily measure the four FO cables usually connected to Smartec:

- Brugg Standard
- Brugg Heatable
- AFL
- A11A10

The FO cables were disconnected from the permanently installed Smartec DiTemp unit and connected to the Silixa unit using an approximately 10 m long patch cord. During a period of 15 minutes, 30 measurements were taken of each cable. The integration time for each measurement was 30 seconds. The sampling resolution was set to 0.127 meters.

The integration time for the Smartec is 1 hour. The Silixa temperature for each data point is shown as average of the 30 measurements which is equivalent to an integration time of 15 minutes.

The Smartec and Silixa data files provide for each measurement the cable distance (measurement location), temperature, power of Stokes and power of anti-Stokes.

The permanent calibration system was in operation (Chapter 5.1.5) with automated real-time calibration routines in FEIS for Smartec but not for Silixa.

#### 5.1.6.1 General comments on the graphs of this sub-chapter.

The below graphs aim to visualize the quality of data produced by two interrogators of different manufacturers. Note that recording time of Smartec and Silixa differ by a few hours. This is of little significance since the bath temperatures are well controlled and the temperature trend in the FE tunnel is less than  $1\text{E-}03$  °C per hour (Chapter 5.1.9).

In each graph, several parameters are plotted against the entire cable length. From bottom to top:

- Temperature vs cable distance for Smartec and Silixa
- Power of Stokes and anti-Stokes
- $R(z) = \ln(P_s(z)/P_{as}(z))$
- $\Delta T$  of calibrated temperature values compared against instrument values of Silixa and the difference of the corrected (calibrated) values between Silixa and Smartec.

The reference temperatures of ambient temperature bath (CB1) and heated bath (CB2) are shown as horizontal red dashed lines on the lower part of the graph. The bath positions are shown as brown vertical dashed lines. The lines mark approximate start / end cable positions and correspond to the cable section where FO cable temperature are expected to be representative of the bath temperature (i.e. effect of transition zone at cable entry and exit is avoided). At the same time, these vertical lines mark the Silixa Stokes/anti-Stokes data range used as average value for the calculation of the calibration parameters  $\gamma$ ,  $C$ ,  $\Delta\alpha$  (Chapter 5.1.5.3).

Data processing and calibration calculations for Smartec are processed on-the-fly in FEIS. Corresponding procedures were applied for Silixa using a programmable graphing software Igor Pro (Wavemetrics, Inc., 2018).

Note that large  $\Delta T$  values exist for Smartec across the heated bath entry & exit zones which are not representative to the true temperatures (due to secondary pulse effects discussed in Chapters 5.1.6.2 and 5.1.6.6). The axis range is set to visualize the errors across the heaters and the calibration baths and does not cover the extremes values. Prior to calculation of the  $\Delta T$  values, the Smartec T values were interpolated using the Silixa data spacing as reference on the X-axis.

### 5.1.6.2 Calibration results for Brugg Standard cable

DTS temperatures for the Brugg Standard cable are shown as instrument output and as calibrated data for Smartec and Silixa in Fig. 5-11.

The Brugg Standard cable runs along the tunnel wall in four loops parallel to the alignment of the heaters. The temperature peaks are shown in Fig. 5-12 versus cable meter distance and relative to the heaters and cable sections (clock face positions).

Fig. 5-13 provides a detailed view of the Smartec and Silixa temperature curves across the baths CB1 and CB2 (ambient and heated, outbound direction). Note that low and high temperature data appear on separate Y-axes to show maximum detail. The temperature range between 25 °C and 60 °C is not shown. Vertical lines mark cable meter positions for end of CB1, start of CB2 and end of CB2. Subranges are shown for Silixa where Stokes and anti-Stokes average values were taken for calibration. The Smartec temperatures however are inaccurate at CB2 bath entry and CB2 bath exit. The increase of temperature starts 1-2 meters before the bath entry which is not plausible.

Both calibrated Smartec and calibrated Silixa temperatures are aligning along the red dashed horizontal lines marking the bath temperatures measured by the independent high-precision thermometers. The temperature value at about 1 m after bath CB2 entry at cable meter 36.8 m is at 63.7 °C, about 1.6 °C below the true bath temperatures. The Smartec temperature is then increasing and reaches true bath temperature not before 9 meters after bath entry. The difference to the reference temperature is illustrated in Fig. 5-13 as yellow-shaded inverted “shoe” (see also  $\Delta T$  in upper part of graph). A similar behaviour is observed after the exit of the heated bath CB2. To indicate the sudden 45 °C temperature drop, Smartec requires again about 9 cable meters to reach the true temperature (indicated by the Silixa temperature). The difference to the true temperature forms a symmetrical pattern (shoe shape). This behaviour of Smartec shown in Fig. 5-13 is visible for all cables measured (see Fig. 5-14, Fig. 5-16 and Fig. 5-17).

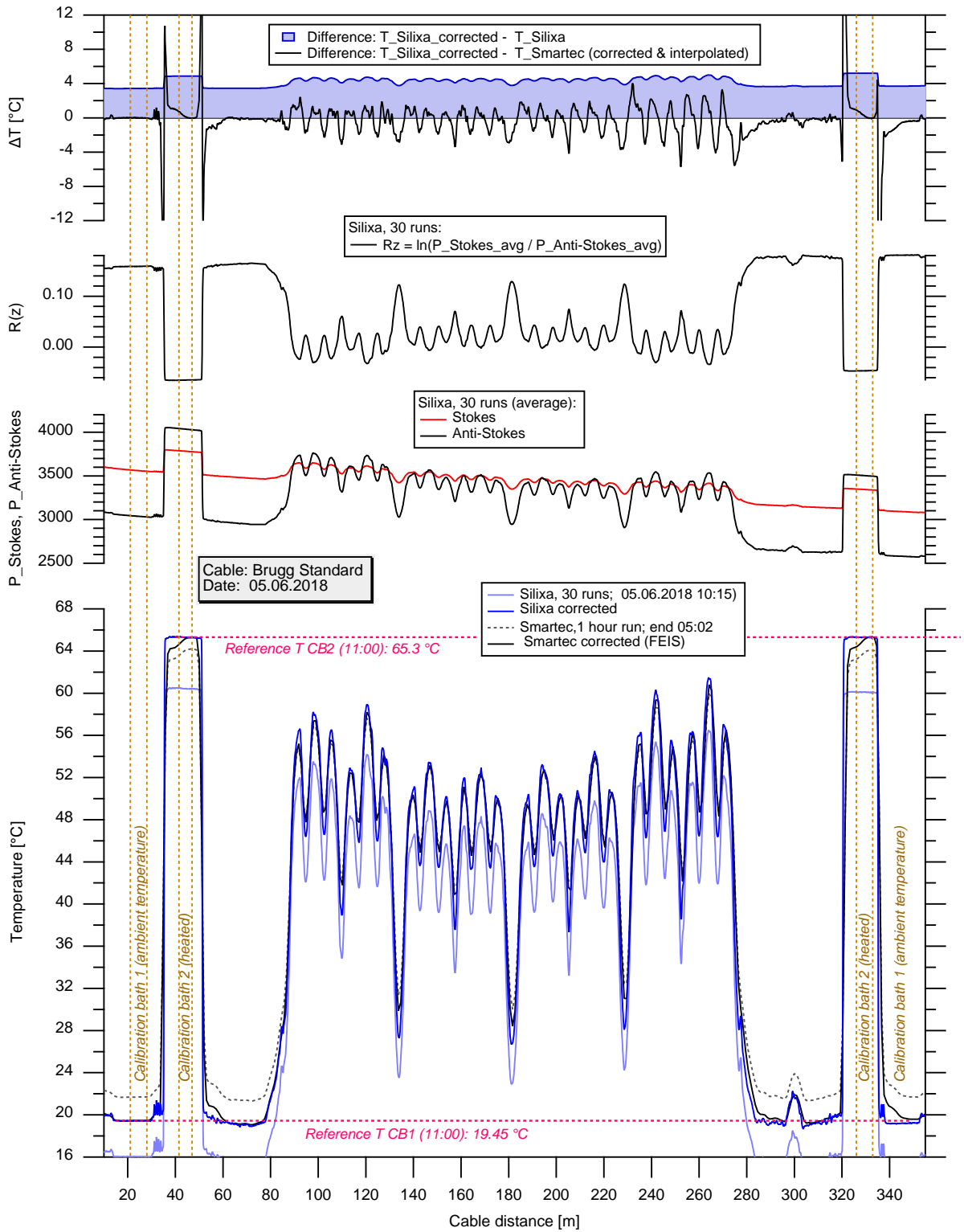


Fig. 5-11: Brugg Standard cable - Results of calibration using Smartec and Silixa shown for entire cable.

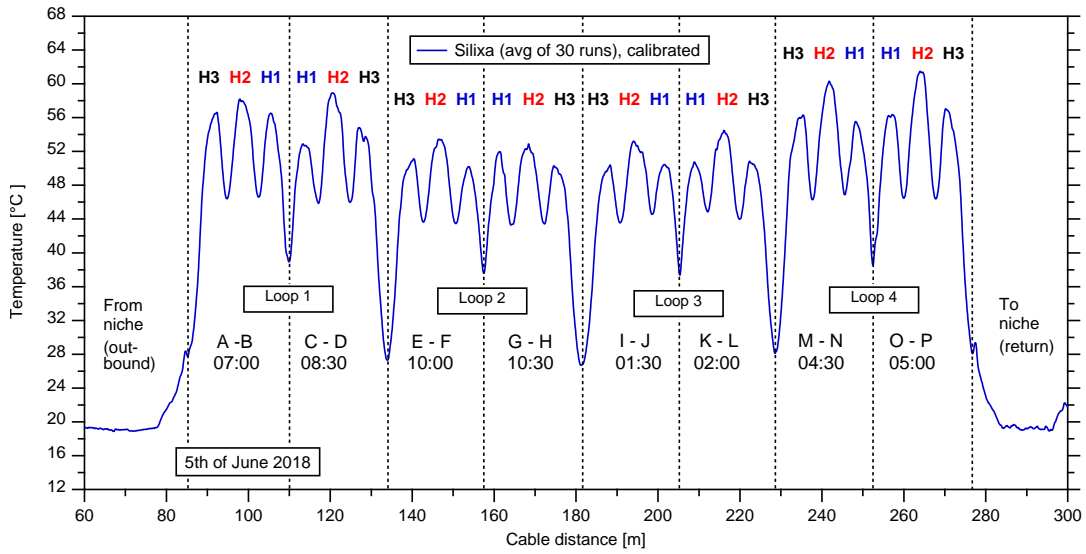


Fig. 5-12: Brugg Standard cable - Temperature peaks related to cable sections parallel and across heaters.

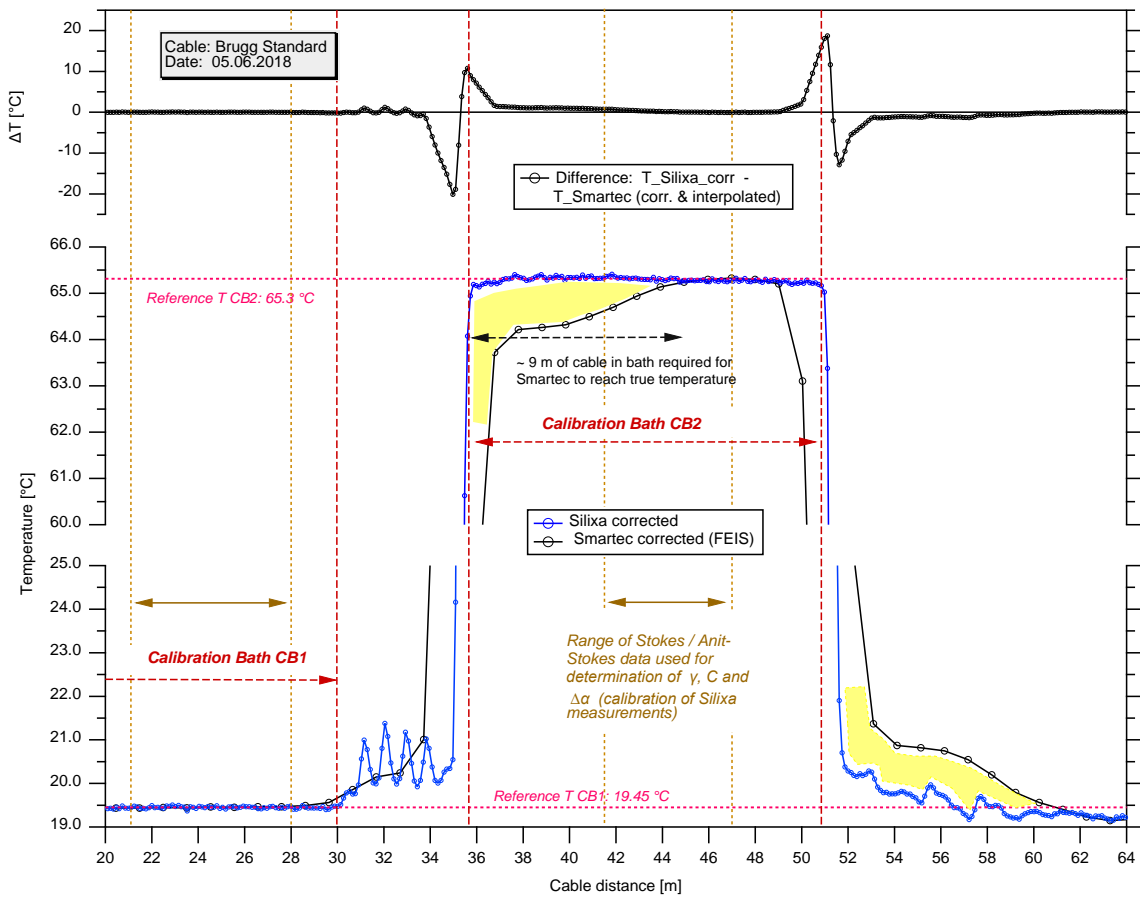


Fig. 5-13: Brugg Standard cable - Smartec and Silixa calibrated temperatures across CB1 and CB2

### 5.1.6.3 Calibration results for Brugg Heatable cable

DTS measurements for the Brugg Heatable cable are shown as instrument output and as calibrated data for Smartec and Silixa in Fig. 5-14.

The temperature maxima between cable distance 90 – 180 m correspond to the crossing of the heater positions on the runs into the FE tunnel (section A-B: H3-H2-H1 at 00:30 clock face position) and out of the tunnel (section J-K: H1-H2-H3 at 11:30 clock face position, see Chapter 5.1.2.5).

The differences between the Silixa and the interpolated Smartec temperatures across the heater vary between -3 and +3 °C.

Fig. 5-15 shows a detailed view of calibrated Silixa and Smartec temperatures for the temperature peaks above the three heaters of cable section A–B at 00:30 clock face position. The Silixa temperature profile is characterized by an additional shoulder at H2, a sharper peak at H3 and an extra pointy peak at H1 which are not visible in the Smartec temperature profile.

The pointy peaks in the Silixa temperature profile may reflect zones in the buffer material where convective heat transport prevails over conductive heat transport. The heterogeneity of the buffer material is likely to be greatest at the roof of the tunnel due the greater technical difficulty to fill the voids in the upper part of the tunnel profile during the buffer emplacement. The FO cable at locations where voids extend to the tunnel wall may see increased temperatures assuming that the heat is evenly distributed in the voids due to convection. Due to the increased spatial resolution, the Smartec device is not capable to reveal the presumed buffer heterogeneity.

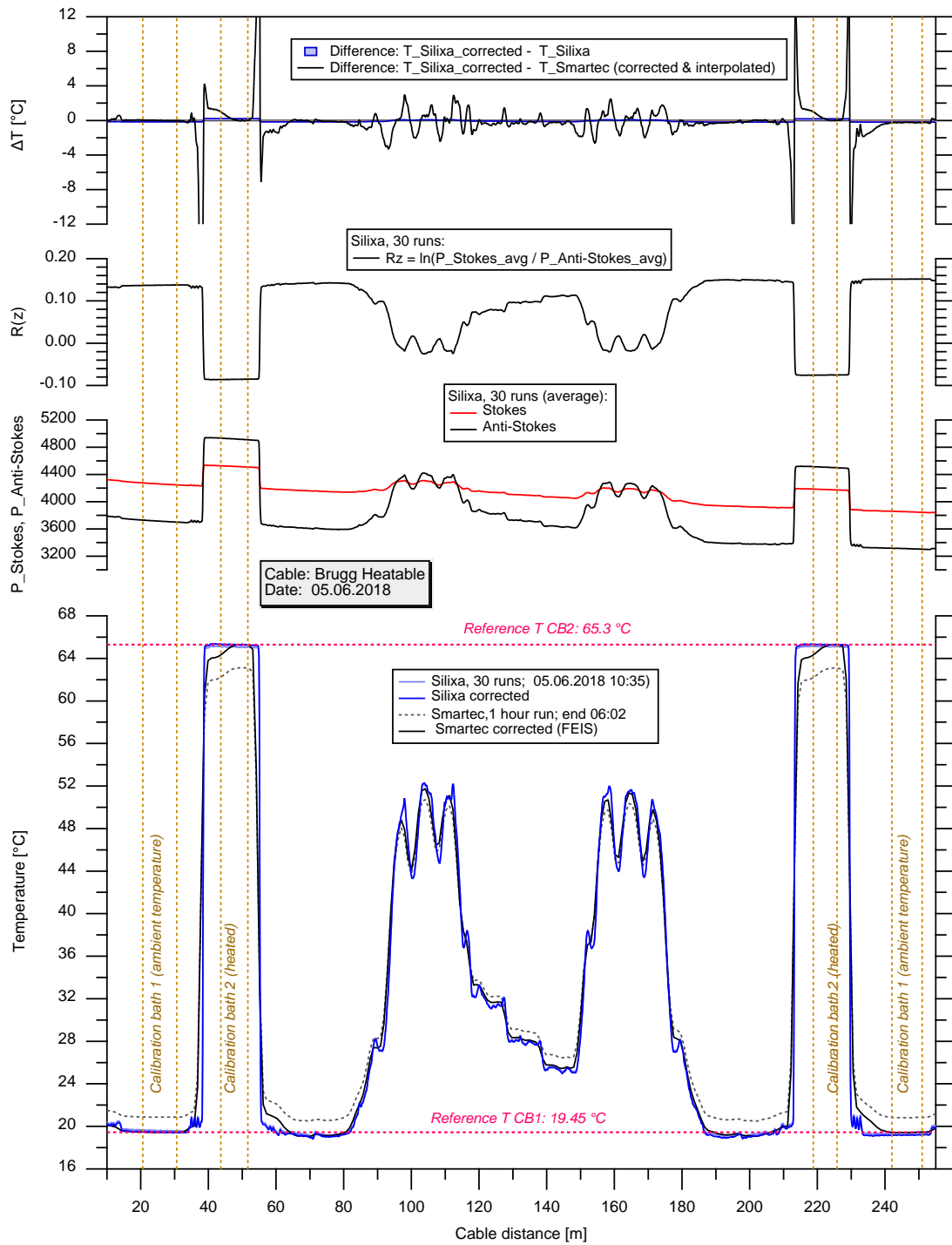


Fig. 5-14: Brugg Heatable - Results of calibration using Smartec and Silixa shown for entire cable.

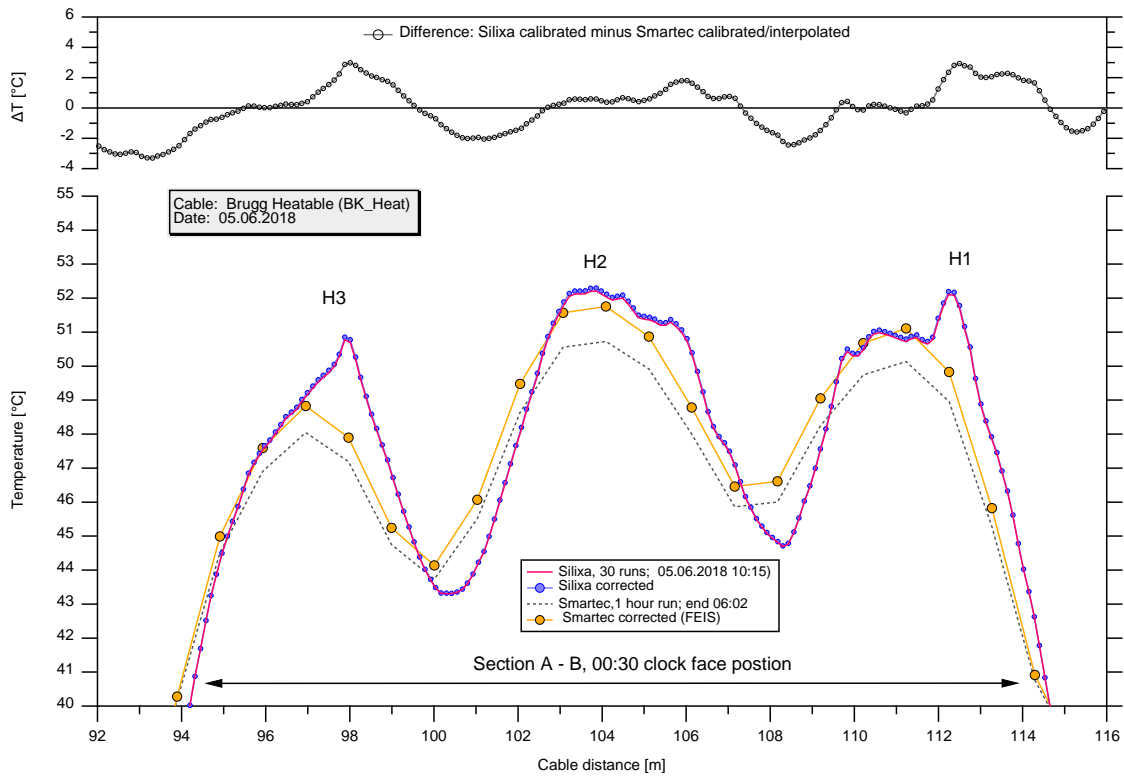


Fig. 5-15: Detailed view of temperature differences between Silixa and Smartec.

**5.1.6.4 Calibration results for AFL cable using Smartec and Silixa units**

DTS temperatures for the AFL cable are shown as instrument output and as calibrated data for Smartec and Silixa in Fig. 5-16. The temperatures between cable distance 75 – 140 m correspond to the crossing of the heater positions on the runs in (H3 -> H2 -> H1 at 05:00 position) and out (H1 -> H2 -> H3 at 07:00) of the tunnel.

The  $P_S$  and  $P_{aS}$  data shown in the middle of the graph are affected by signal step-loss, indicated by a sharp fall-off at around 79 m cable length. The step-loss is also visible in the  $R(z)$  data. The step-loss occurs where the cable runs from tunnel entry towards H3 (along tunnel wall, 05:00 position) and where the temperature is increasing significantly with every additional cable meter (~7.7 °C per meter). The application of a step-loss correction on the Stokes and anti-Stokes data is therefore questionable. Step-loss corrections should generally be applied only on cable sections where no spatial temperature gradient is present (Hausner et al., 2011).

The difference between the calibrated Smartec data and calibrated Silixa data are visible across the heated bath CB2 (on the outbound cable section and on return) and across the heaters. Not considering the gap at the first H1-position (step-loss), the  $\Delta T$  values range between -3 °C and +7 °C. Assuming the Silixa calibrated temperatures are most representative of the true temperatures, the latter value indicates that the Smartec calibrated value underestimates the temperature at H2 position by 7 °C.

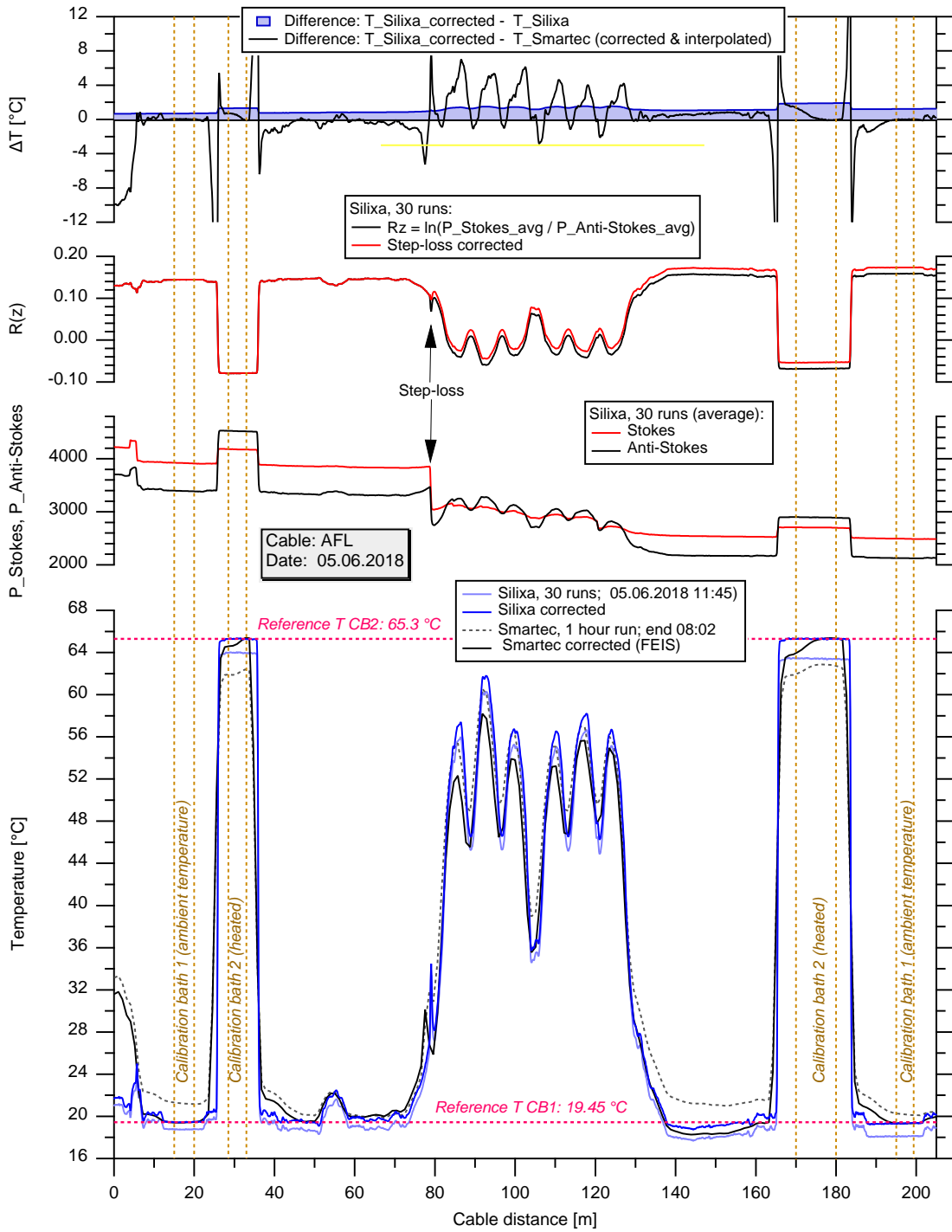


Fig. 5-16: AFL cable: results of calibration using Smartec and Silixa shown for entire cable.

### 5.1.6.5 Calibration results for A11A10 cable using Smartec and Silixa units

DTS temperatures for the A11A10 cable are shown as instrument output and as calibrated data for Smartec and Silixa in Fig. 5-17.

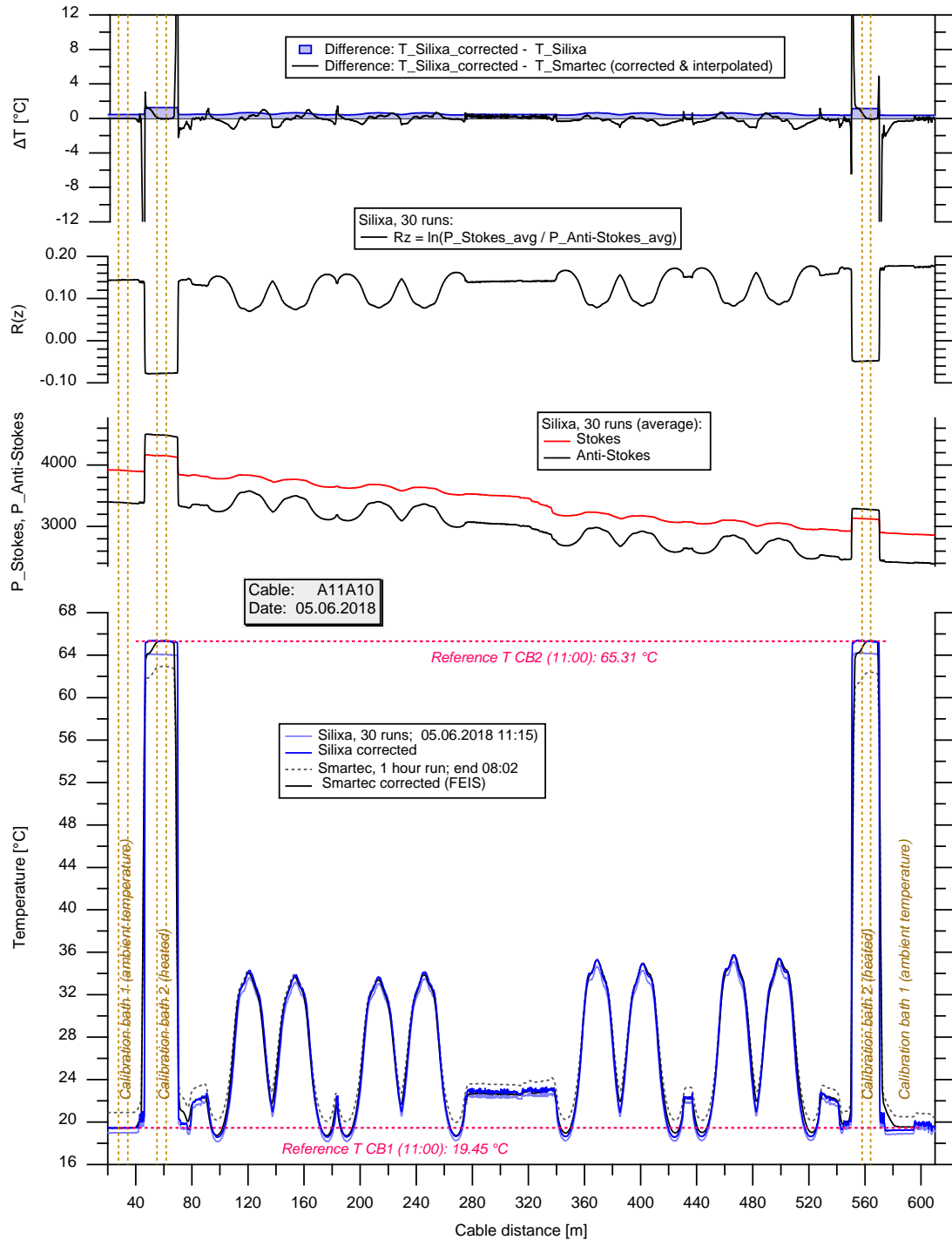


Fig. 5-17: A11A10 cable: results of calibration using Smartec and Silixa shown for entire cable.

### 5.1.6.6 Discussion of results

The Smartec DiTemp shows impure temperature signals at abrupt  $\Delta T$  changes as it occurs at entry and exit of the heated calibration bath CB2 and across the heaters in the FE tunnel. Differences compared to the true temperature are visible for a few data points before the abrupt temperature change and on about 9 data points (corresponding approximately to 9 meters) after the temperature change.

According to the manufacturer Sensornet Ltd., the Smartec DiTemp unit produces light pulses by switching the laser rapidly on and off (pulse driven laser). Modulating the pulse gives a flatter pulse shape. The pulse driven laser gives a rounded pulse with a tail (2<sup>nd</sup> order effect). Normally, with relatively small temperature changes, the 2<sup>nd</sup> order effect of the tail is not visible. Where sudden large temperature changes do occur (such as in this case) the 2<sup>nd</sup> order effect of the tail is visible in the data.

For most industrial and scientific applications, the effect is negligible in comparison to the overall change in temperature and the DiTemp's ability to detect small changes in temperature is not compromised. However, at the FE experiment with significant spatial temperature gradients across the heater, the errors are significant.

Note that for calibration, the FEIS only uses the average of a few Stokes / anti-Stokes values (2 – 5, depending on cable length in bath). The selection is based on the condition that a series of related uncorrected temperatures form a plateau in the bath.

### 5.1.7 Temperature analysis DTS versus point-type sensors in FE tunnel

Comprehensive analyses were conducted at multiple stages of the project to investigate how well the DTS temperatures match the respective values of conventional point-type temperature sensors (thermocouples and Pt1000 probes) at comparable locations. The comparisons were repeated several times in the course of the heating of the FE tunnel between 2015 and 2018 (Fig. 5-18). The quality of these comparisons improved over time with the improvement of calibrations and the development of database related tools. Previously performed analyses were repeated, revised or extended because:

- the accuracy of the 3D-coordinates of the FO cable positions was improved in the course of the project;
- the installation of permanent calibration system led to improved accuracy of the DTS measurements;
- temporarily installed DTS units with improved spatial resolution (Silixa) provided DTS profiles with greatly increased detail. Significant temperatures variations were found to be present over short lateral distances which were not visible before;
- the introduction of the FO extension of the FEIS allowed for systematic and fast selection of point-type sensors at a specified radial distance of a selected FO cable sections.

Using the high-resolution Silixa Ultima-S unit as a benchmark revealed a data quality issue of Smartec which was considered significant at cable sections with important spatial temperature gradients (Chapter 5.1.6). Along the boreholes and within the heated tunnel where temperature gradients of up to 6 °C/m exist, a direct comparison to standard electrical point temperature sensors is difficult due to the DTS spatial resolution, which ranges from 0.254 – 1.02 m depending on the Raman based DTS device used the FE experiment. We could show that, in general, a good agreement exists between DTS data with 1.02 m spatial resolution and data of standard “point”

temperature sensors, especially where small to moderate temperature gradients ( $< 1\text{ }^{\circ}\text{C/m}$ ) prevail along the FO cable. DTS instruments with a high spatial resolution (Silixa: 0.254 m) can even provide reliable data for sections with large temperature gradients along the FO cable.

Tab. 5-9: Comparisons of DTS versus point-type sensors at various times & configurations.

<b>Date of DTS measurements</b>	<b>FO Cables</b>	<b>Interrogators used</b>	<b>Calibrated data used Yes/No</b>
<b>05.12.2014</b>	Brugg Std, Brugg Heat, A11A10 <sup>1)</sup>	Smartec, Neubrex	No
<b>10.02.2015</b>	Brugg Std, Brugg Heat, A11A10 <sup>1)</sup>	Smartec, Neubrex	
<b>01.07.2015</b>	Brugg Std, Brugg Heat, A11A10 <sup>1)</sup>	Smartec, Neubrex	
<b>01.07.2016</b>	Brugg Std, Brugg Heat, A11A10 <sup>1)</sup>	Smartec, Neubrex	
<b>01.07.2017</b>	Brugg Std, Brugg Heat	Smartec, Neubrex	
<b>14.07.2017</b>	A11A10 <sup>1)</sup>	Smartec	
<b>05.06.2018</b>	Brugg Std, Brugg Heat, AFL	Smartec, Silixa	Yes
<b>05.06.2018</b>	A11A10 <sup>1)</sup>	Smartec, Silixa	Yes

<sup>1)</sup> The A11A10 cable is not measured by Neubrex

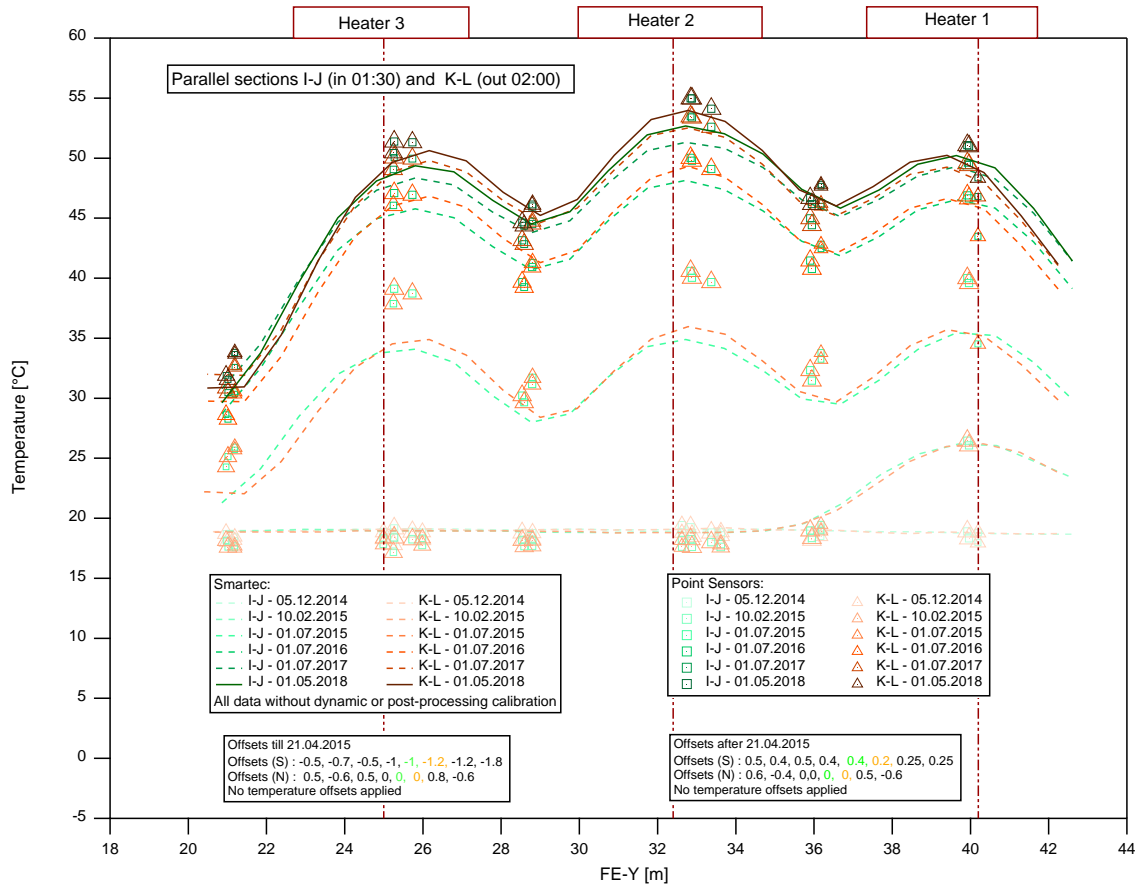


Fig. 5-18: DTS compared to point-type temperatures at various stages of the project (2014 - 2018).

Note: H1 was started on 15.10.2014, between the profiles labelled “05.12.2014” and “10.02.2015”. H2+H3 were started on 17/18.02.2015, between the profiles “10.02.2015” and “01.07.2015”. The latest DTS profile from 01.05.2018 shows dynamically calibrated data.

### 5.1.7.1 Temperature profiles of the FE tunnel and point-type sensors

The graphs in the subsequent sections show temperature profiles of parallel FO cable sections together with T-values of conventional “point-type” sensors (e.g. Pt1000 sensors) at a certain distance to the FO cables. The point-type sensors were selected using the “query” option in FEIS by specifying the desired maximal radial distance from the FO cable. Usually, a radial distance between 0.6 m and 0.8 m was specified, depending on the number of available point-type T-sensors. Note that for two shown parallel FO cable sections, a point-type sensor may fulfil the selection criteria for either zero, one or both cable sections. To visualize the distance of a point-type sensor with respect to a selected FO cable, the size of the respective plot symbol (of the point-type sensor) is scaled according a specified distance range: The symbol is large if the point sensor is located close to the FO cable, e.g. 0.1 m, or it is small if it the distance is comparably large to the FO cable, e.g. 0.6 m.

Additional plots are provided that include the radial distance information of the point-type sensors. Two examples are shown in Fig. 5-19. The cropped graphs show data of two parallel FO

cable sections and T-values of conventional sensors. For each section, two parallel DTS profiles are shown as they were measured using two interrogators.

A triangle and a square symbol at identical location represent the same T-value (of the same point-type sensor) but mark different distances to separate FO cables. The symbol size is a function of the sensor's distance to the respective FO cable section, e.g. A-B or C-D. In the left (cropped) graph of Fig. 5-19, the orange tags (labels) are attached to the red triangle symbols indicating the distance to the FO cable section marked in similar colour (orange dashed line for Smartec and orange circles for Silixa). The triangle/square symbols indicate the temperature whereas the symbol size and the attached tags indicate the distance to the FO cable. Labels are plotted only for one cable section for better legibility.

In the example shown on the right of Fig. 5-19, the red triangle symbol with orange label indicates the sensor name and the sensor distance with respect to the FO cable section represented by orange circles (Silixa) and orange line (Smartec), respectively. The distance to this cable section is only 0.31 m (relatively large symbol). The distance of the same point-type sensor to the other cable section (represented blue circles for Silixa and blue line for Smartec) is large (1.0 m) which is also reflected by the small size of the square marker.

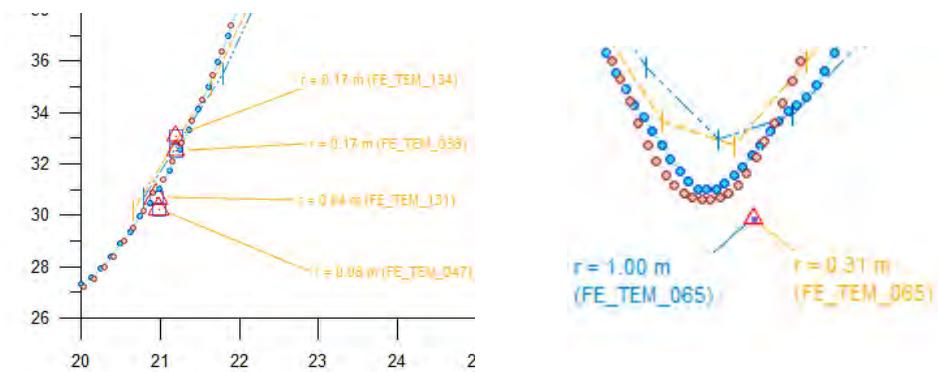


Fig. 5-19: Examples of labelled plot markers indicating sensor name and its distance to the FO cable

Note: Silixa data are shown using orange or blue circle symbols; Smartec data are shown using orange or blue lines; Point-type T data are displayed as triangle or square symbols.

### 5.1.7.2 Comparison of Brugg Standard Temperature FO measurements versus point-type T-sensors

Four FO cable loops each with two parallel sections are available for comparison with conventional T sensors (see Fig. 5-12). Here only the profile of Loop 3 with sections I-J at 01:30 clock face position and K-L at 02:00 clock face position is presented. The DTS temperatures are shown together with near point-type T sensors in Fig. 5-20 and Fig. 5-21.

Note that these two figures show the same temperature data but differ by the labels indicating the radial distance between FO cable and point-type T-sensor. Fig. 5-20 shows distance labels relating to the I-J profile whereas Fig. 5-21 shows distance labels relating to the K-L profile.

The following observations are made:

- Silixa peak temperatures are slightly higher compared to Smartec, especially at H1 position.
- Minima between heaters are more pronounced for Silixa (compared to Smartec)
- Excellent match of Silixa temperatures with point sensor data for small distances. The differences in temperature are generally smaller than 1.5 °C. Many comparisons with near point-type sensors ( $r < 0.1$  m) show very small differences (distances to cable section KL).
- The differences are generally smaller than 1 °C.

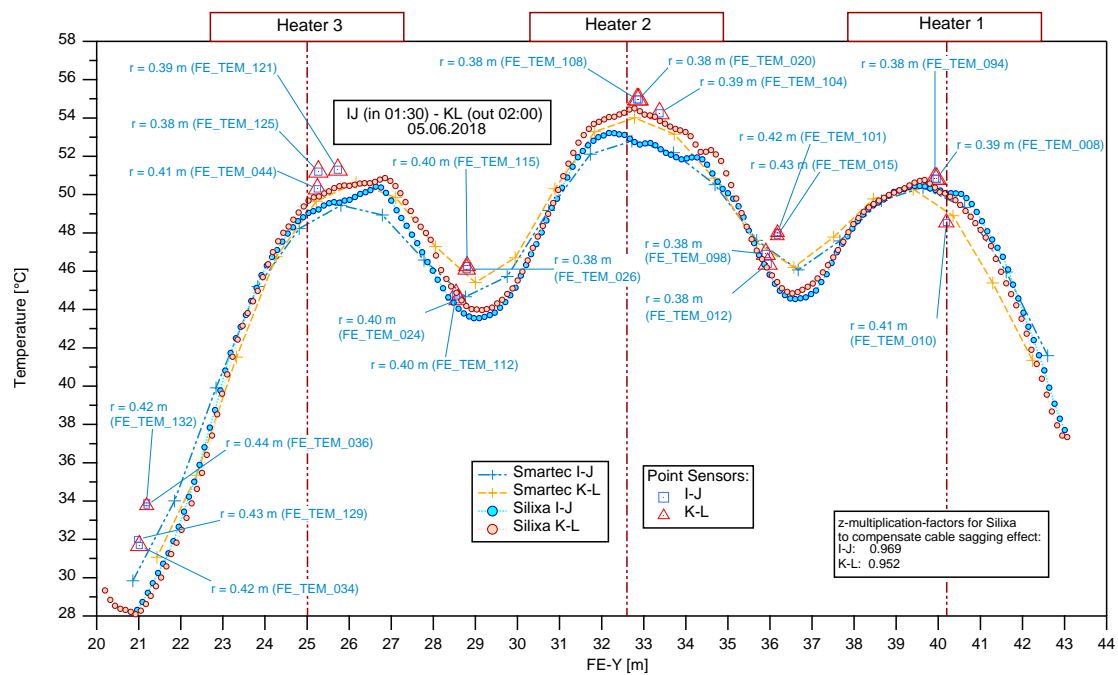


Fig. 5-20: Brugg Std cable, Sections I-J & K-L: point T-data vs DTS measurements

Note: Blue tags: distances to I-J cable section.

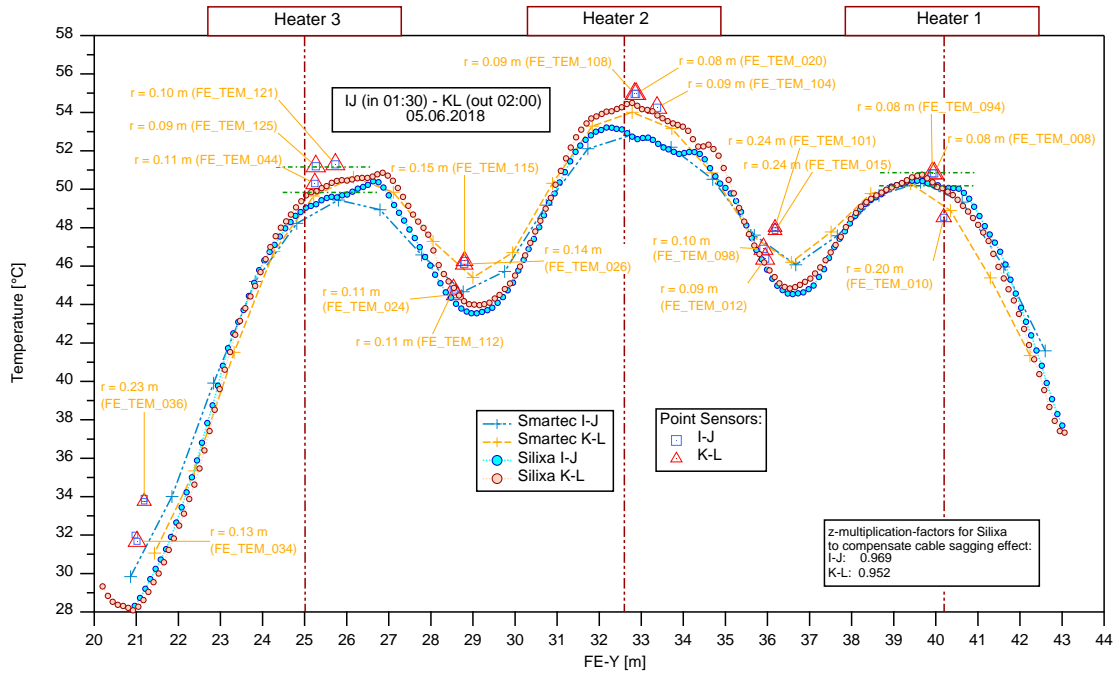


Fig. 5-21: Brugg Std cable, Sections I-J & K-L: point T-data vs DTS measurements (2).

Note: Orange tags representing the distances to K-L cable section.

### 5.1.7.3 Comparison of Brugg Heatable FO measurements versus point-type T sensors

The temperature distribution along the entire Brugg Heatable cable measured by the Silixa unit is shown for the 5th of June in Fig. 5-22. Start and end positions of the two parallel sections along the heater axis are shown as vertical lines: Section A-B at 00:30 clock face position and Section J-K at 11:30 clock face position. The horizontal dashed lines mark the temperatures of the ambient temperature bath (CB1) and heated calibration bath (CB2). The Silixa DTS temperatures match the reference temperatures of the calibration baths nicely but there is a small difference with respect to the validation bath at cable meter 235 - 250 (see also Chapter 5.1.5).

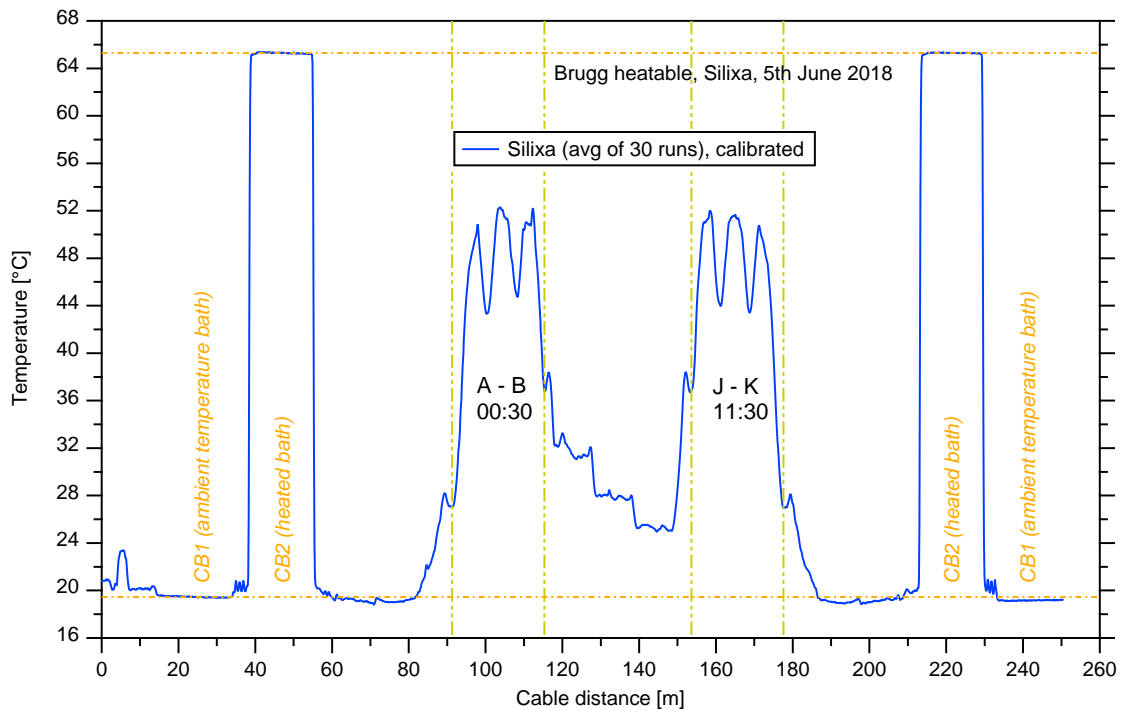


Fig. 5-22: Entire Brugg Heatable cable measured using the Silixa device (average of 30 runs shown).

One FO cable loop with two parallel sections is available for comparison with conventional T sensors: A-B at 00:30 clock face position and J-K at 11:30 clock face position. The DTS temperatures are shown together with near point-type T sensors in Fig. 5-23 and Fig. 5-24.

Note that these two figures show the same temperature data but differ by the labels indicating the radial distance between FO cable and point-type T sensors. Fig. 5-23 shows distance labels relating to the A-B section whereas Fig. 5-24 shows distance labels relating to the J-K section.

The following observations are made:

- Silixa peak temperatures are slightly higher compared to Smartec, especially at H1 position.
- Minima between heaters are more pronounced for Silixa (compared to Smartec)
- Excellent match of Silixa temperatures with point sensor data for distances smaller than 0.1 m. The differences are smaller than 1.5 °C. At the region of H2 and H3, the difference is smaller than 1 °C.

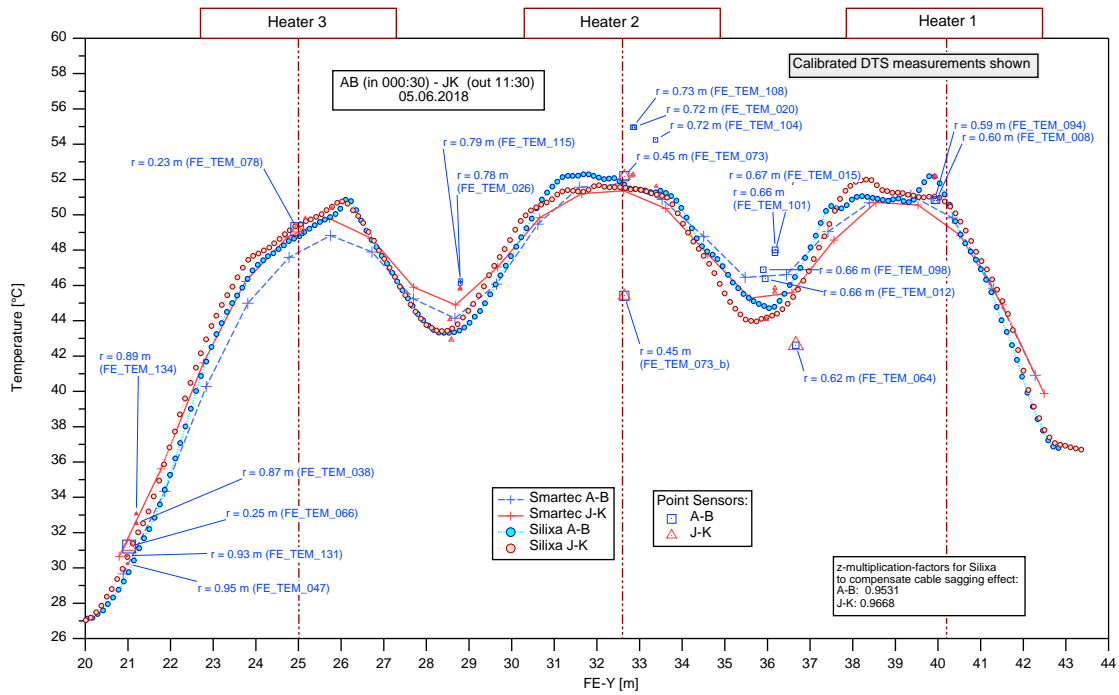


Fig. 5-23: Brugg Heatable cable, Sections A-B & J-K: point T-data vs DTS data (1).

Note: Blue tags representing the distances to A-B cable section.

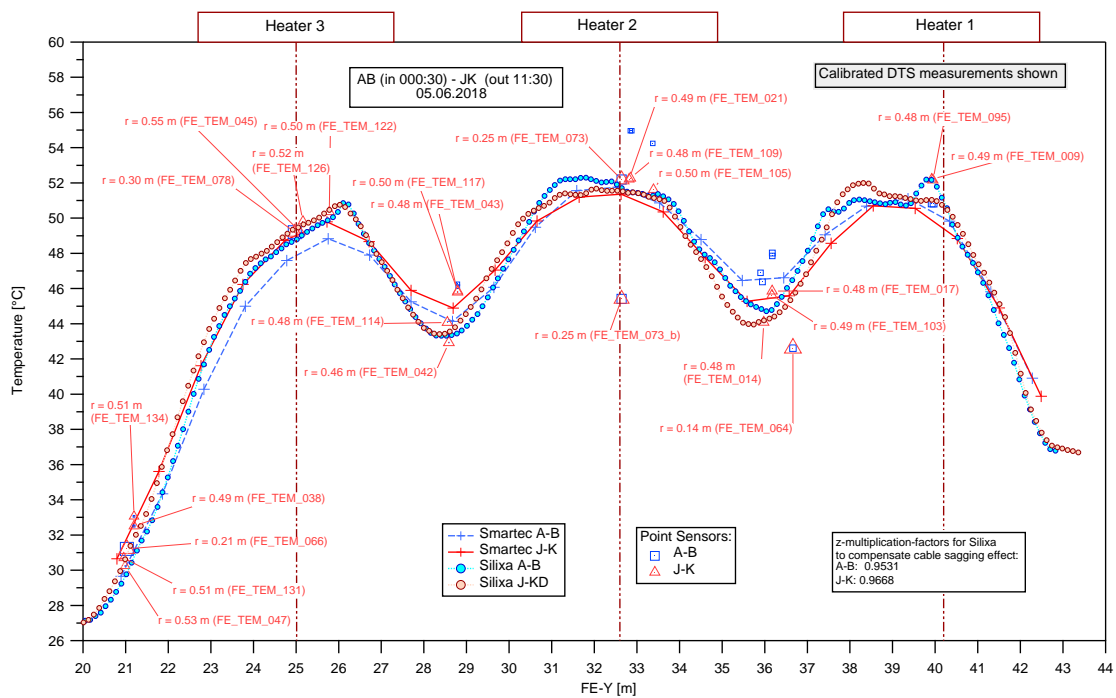


Fig. 5-24: Brugg Heatable cable, Sections A-B & J-K: point T-data vs DTS data (2).

Note: Red tags representing the distances to J-K cable section shown.

#### 5.1.7.4 Comparison of DTS on AFL cable versus point-type T-sensors

The temperature distribution along the entire AFL cable measured by the Silixa unit is shown for the 5th of June in Fig. 5-25. Start and end positions of the two parallel sections along the heater axis are shown as vertical lines: Section A-B at 05:00 clock face position and Section C-D at 07:00 clock face position. The horizontal dashed lines mark the temperatures of the ambient temperature bath (CB1) and heated calibration bath (CB2). The Silixa DTS temperatures match the reference temperatures of the calibration baths perfectly (see also Chapter 5.1.5).

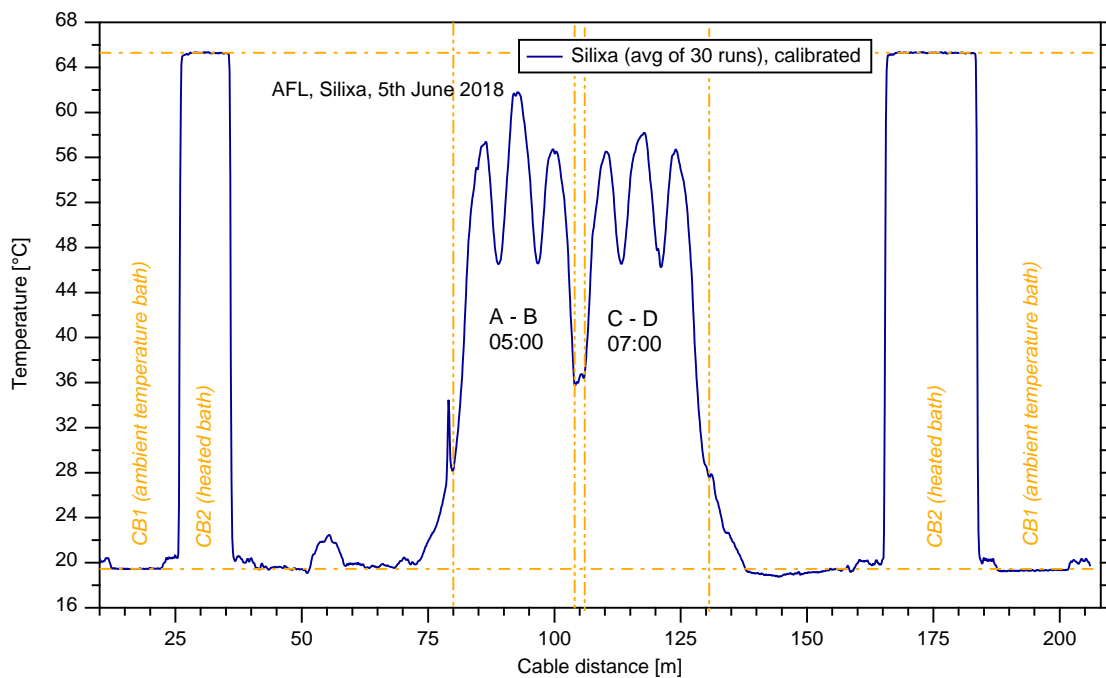


Fig. 5-25: AFL - Entire cable measured using the Silixa device (average of 30 runs shown).

DTS data along the AFL cable are shown together with T-values of near point-type sensors in Fig. 5-26. Only one point-type sensor is near to an AFL cable: FE\_TEM\_079 in 0.13 m distance to the A-B section. The temperature of the sensor FE\_TEM\_079 is in very good agreement with the Silixa DTS data at H3 position. The difference at FE-Y = 25.3 m is only 0.6 °C.

Other point-type sensors located at low temperature regions between H2 and H3 (FE\_TEM-076 and -077) and between H1 and H2 (FE\_TEM\_065) are also in good agreement with the Silixa DTS data both of section A-B and of section C-D ( $\Delta T \sim 1.0$  C).

The distances of these sensors to the DTS cable sections vary between 0.33 m and 0.39 m. These sensors are attached to the tunnel wall (FE\_TEM\_077 at 08:00 position and FE\_TEM\_065 & FE\_TEM\_076 at 04:00 position) and are at very similar distances to the heat source as compared to the FO AFL cable.

Near to the heaters, the Smartec DTS temperatures are significantly lower compared to the Silixa values.

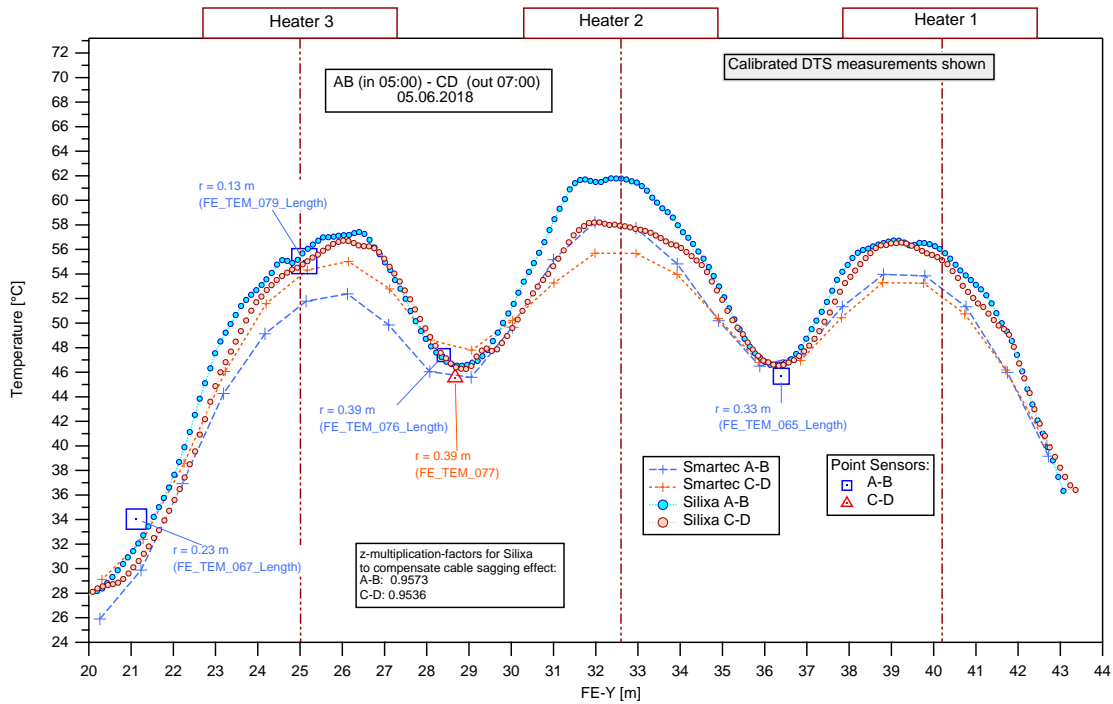


Fig. 5-26: AFL cable, Sections A-B & C-D: point T-data vs DTS measurements.

### 5.1.7.5 Comparison of AFL versus Brugg Standard cable

At 05:00 clock face position the cable sections AFL A-B and Brugg Standard O-P run in parallel (Fig. 5-27), both cables being attached to the tunnel wall at varying distance of 1 to 7 cm to each other. The same is true for the cable sections AFL C-D and Brugg Standard A-B at 07:00 clock face position (Fig. 5-27 and Fig. 5-28).

Temperature profiles of different cables (AFL and Brugg Standard) measured using Silixa are shown in Fig. 5-29 for the 05:00 clock face position and in Fig. 5-30 for the 07:00 position.

The differences in  $\Delta T$  (based on calibrated temperatures) between the two cables at the same clock face position are very small.

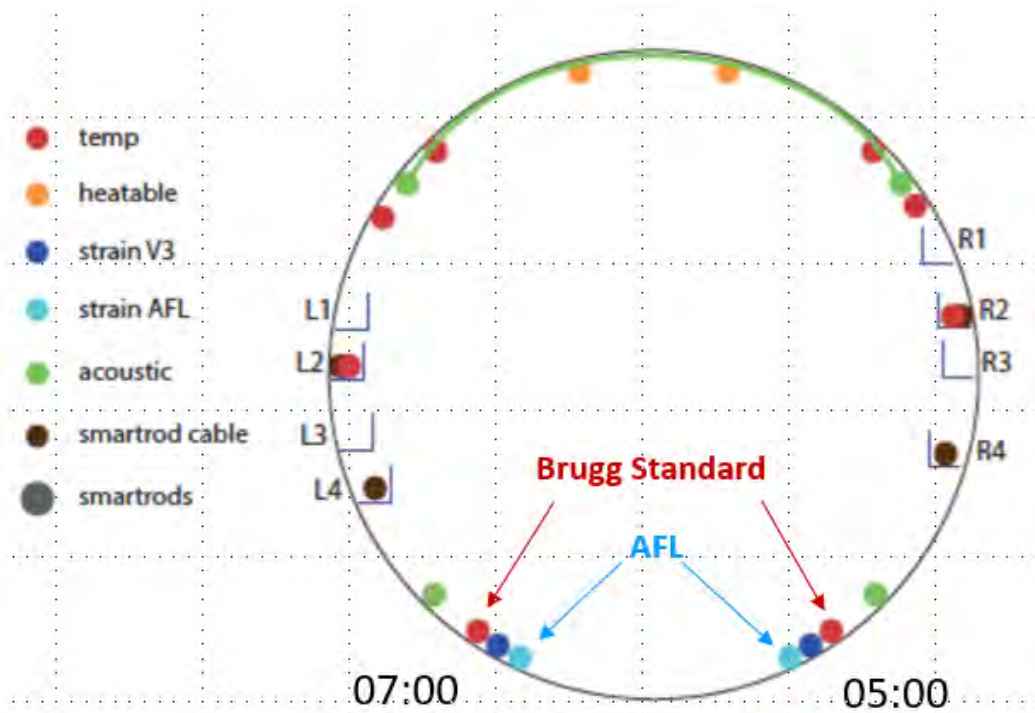


Fig. 5-27: Clock face position of selected cables sections shown at gallery cross-section GM25.

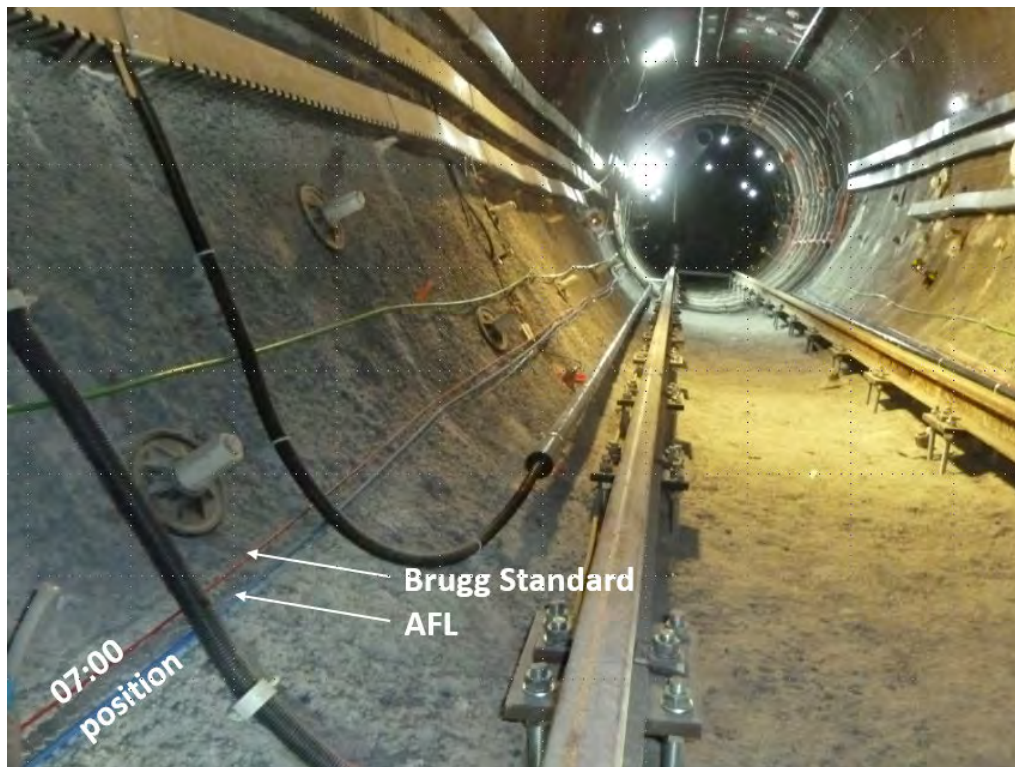


Fig. 5-28: Routing of Brugg Standard cable (Section A-B) and AFL cable (Section C-D) in FE tunnel at 07:00 position.

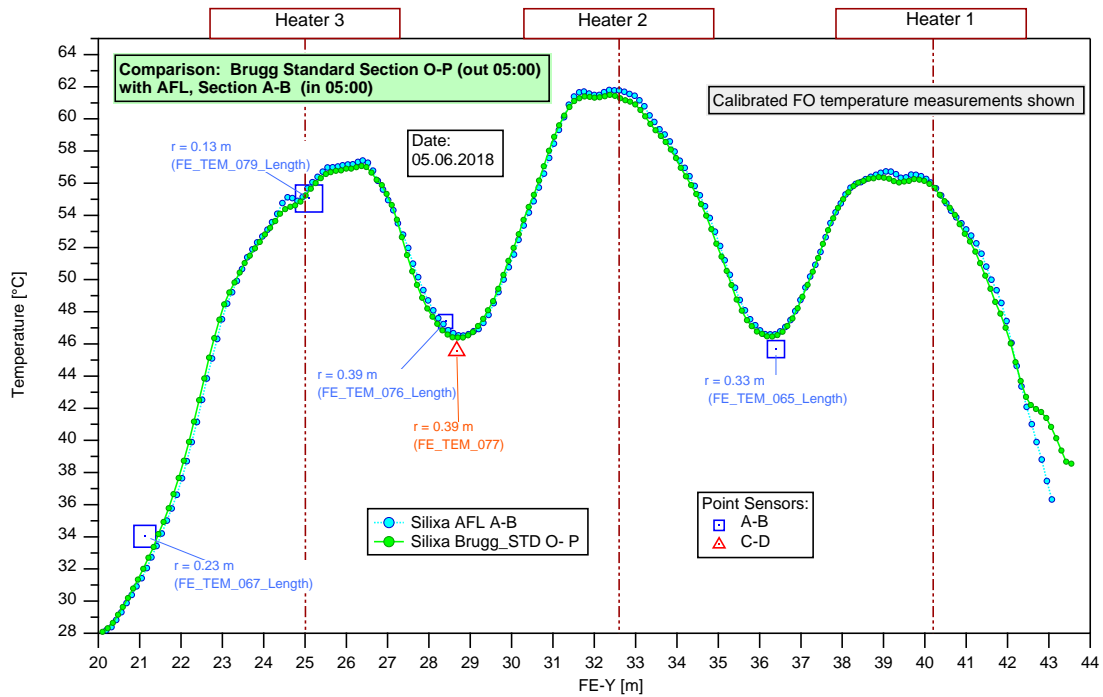


Fig. 5-29: Brugg Standard Section O-P and AFL Section A-B - Silixa DTS vs Point T-data.

Note: Point-type sensor labels indicate distances to AFL cable ( $\approx$  distance to Brugg Standard).

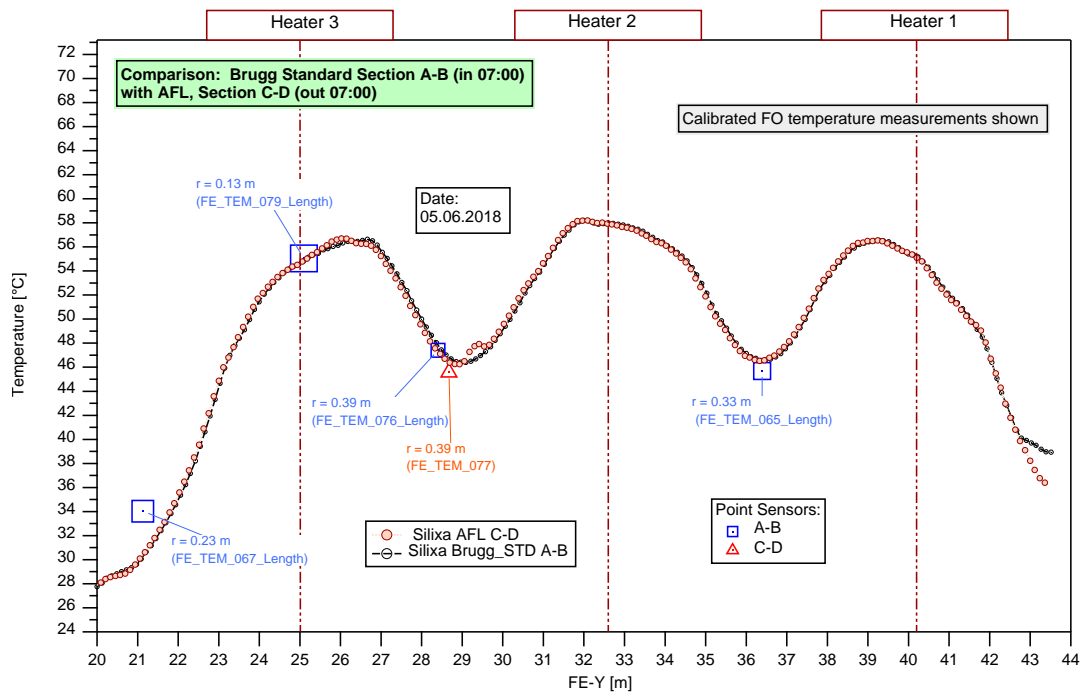


Fig. 5-30: Brugg Standard Section A-B and AFL Section C-D - Silixa DTS vs Point T-data.

Note: Point-type sensor labels indicate distances to AFL cable ( $\approx$  distance to Brugg Standard).

### 5.1.8 Comparison of DTS versus point-type T-sensors

During a FE site visit on 5th of June 2018, a Silixa Ultima-S unit was used to measure the A11A10 FO cable which is routed at four different clock positions in and out of boreholes BFEA011 and then in and out of BFEA010 (Morel, 2013). The boreholes run parallel to the FE Y-coordinate and run slightly upwards, 1.0 - 1.1 m upward on a length of 45 metres.

The FO cable was disconnected from the permanently installed Smartec DiTemp unit and connected to the Silixa unit using a 10 m long patch cord. During a period of 15 minutes, 30 measurements were taken. The integration time for each measurement was 30 seconds. The sampling resolution was set to 0.127 metres. The Silixa data file provides for each measurements the cable distance (measurement location), temperature, power of Stokes and power of anti-Stokes.

The borehole completion on BFEA010 (A10) and BFEA011 (A11) with 45 m long inclinometer chains and 40 thermistors per borehole provide a suitable experimental setup to compare measurements of DTS cable sections with data or thermistors in the same borehole (TN2012-29rev). The thermistors are integrated components of the inclinometer chain and are aligned along the central axis of the inclinometer casing in the borehole. The cable routing of the DTS cable in the A10 and A11 borehole is shown in square boxes of Fig. 5-31 and Fig. 5-32 (see also Chapter 3.1.3). The DTS cable positions were verified during calibration bath installation and additional fingerprinting on 28/29.03.2018 (Chapter 5.1.5). Given that the FO cables are attached outside of the inclinometer plastic (ABS) pipe and routed parallel to the pipe axis at four clock face positions, 12:00, 03:00, 06:00 and 09:00, the distance between FO cable and the thermistor array is constant for each cable section (about 1/2 of the inclinometer ABS casing diameter:  $0.085 \text{ m} / 2 = 0.043 \text{ m}$ ). The space between ABS pipe and wellbore was grouted using a bentonite-cement mixture (Morel, 2013).

For the comparison Smartec versus Silixa, corrected data were used. The on-the-fly calibrated Smartec data were obtained from the FEIS FO database.

The coordinate positions were shifted slightly by -0.3 to +0.5 m compared to the actual FE database settings in order to obtain best matches with the thermistor temperature curve.

The Silixa data were calibrated using the same procedure as described by Hausner et al. (2011). The Smartec data were recorded 3 - 4 hours before the Silixa measurement using 1-hour interrogation time. Given that the spatial temperature distributions in the boreholes had reached stationarity, the time delay between the Smartec and Silixa measurements is not significant. Silixa data were noisier due the short signal integration time of only 30 seconds. Therefore, average temperature values of the 30 measurements were calculated and used for the comparison with Smartec.

#### 5.1.8.1 Comparison of temperatures in Borehole BFEA010

Thermistor temperatures and Smartec and Silixa measurements for the four cable sections (12:00, 03:00, 06:00 and 09:00 clock face positions) are shown in the box drawing of Fig. 5-31 for the borehole A10. Data from A10 are plotted against the FE Y-coordinate. The temperatures in the monitored borehole section range roughly between 18 and 35 °C. The maximum temperature at  $Y = 32 \text{ m}$  (FE Y-coordinate, parallel to the gallery elongation) corresponds to H2. The shoulder-shaped high-T regions left and right of the peak at around 26 m and 38 m correspond to the heater positions of H3 and H1, respectively.

The highest temperatures for Smartec and Silixa are measured in cable section 3, the cable along the bottom line of the inclinometer casing (6:00 position). This is expected due to nearer distance to the heater array. The temperatures along cable section 1 (top of casing at 12:00 position) are showing generally lowest T value compared to the temperatures in other sections at same Y coordinate value and measured with the same interrogator. Most of the DTS profiles show temperatures 0.5 to 1 °C higher (in average) than the thermistor temperatures along the borehole profile.

The middle graph in Fig. 5-31 shows the difference in temperature between the 03:00 and 09:00 positions along the borehole BFEA010. Given the expected comparable distance to the heaters (left and right of the inclinometer pipe), the difference in T should be close to zero. The maximum absolute  $\Delta T$  measured by Silixa is 0.34 °C at FE Y = 41 m. The maximum absolute  $\Delta T$  measured by Smartec is 0.54°C at FE Y-coordinate = 23 m. Note that the distance and T-values were interpolated to enable comparison between different cable sections and interrogators.

The top graph of Fig. 5-31 shows that most of the DTS values are higher compared to those of the thermistors. The differences are mainly positive but less than 1.0 °C for most of the measurement locations. The asymmetric shape of the Smartec, Section 1 curve suggests that the  $\Delta T$  values could be further minimized by adjusting the start/end cable distance values for this section (i.e. correct fingerprint parameters).

For both Smartec and Silixa, the  $\Delta T$  values (difference to thermistors) of Section 3 (bottom of pipe) are significantly higher than the  $\Delta T$  values of Section 1 (top of the pipe) in the middle range of the borehole section. This is expected given that Section 3 measuring points are closer to the heat source compared to Section 1.

The  $\Delta T$  values for section 3 are higher in the middle range of the profile compared to the values of the lateral ends of the profile which could be explained by the heat-conducting properties of the inclinometer chain affecting the thermistor measurements. The metallic inclinometer chain is likely to act as heat conductor and could abating the differences in temperature along the borehole.

### 5.1.8.2 Comparison of temperatures in Borehole BFEA011

Thermistor temperatures and Smartec and Silixa measurements for the four cable sections (12:00, 03:00, 06:00 and 09:00 clock face positions) are shown in the box drawing of Fig. 5-32 for the borehole A11. A11 data are plotted against the FE Y-coordinate. The temperatures are ranging roughly between 18 and 35 °C. The maximum temperature at FE Y = 33 m corresponds to H2. The shoulder-shaped high-T regions left and right of the peak at around 27 m and 39 m correspond to the heater positions H3 and H1, respectively.

The highest temperatures for Smartec and Silixa are measured in cable section 3, the cable along the bottom line of the inclinometer casing (06:00 position). This is expected due to nearer distance to the heater array. The temperatures along cable section 1 (top of casing at 12:00 position) are showing generally lowest T value compared to the temperatures in other sections at same FE Y-coordinate (measured with same interrogator). Most of the DTS profiles show temperatures 0.2 to 0.7 °C higher (in average) than the thermistor temperatures along the borehole profile.

The middle graph in Fig. 5-32 shows the difference in T between the 03:00 and 09:00 position along the borehole A11. Given the expected comparable distance to the heaters (left and right of the inclinometer pipe), the difference in T should be close to zero. The maximum absolute  $\Delta T$  measured by Silixa is 0.5 °C. The maximum absolute  $\Delta T$  measured by Smartec is 0.37 °C. Note

that the distance and T-values were interpolated to enable comparison between different cable sections and interrogators.

The top graph of Fig. 5-32 shows that most of the DTS values are higher compared to those of the thermistors. The differences are mainly positive and less than 1.0 °C for most of the measurement locations.

The slightly asymmetric shape of the Smartec Section 2 curve suggests that the  $\Delta T$  values could be further minimized by adjusting the start/end cable distance values for this section (i.e. by adjusting the fingerprint parameters).

For both Smartec and Silixa, the  $\Delta T$  values (difference to thermistors) of Section 3 (bottom of pipe) are significantly higher than the  $\Delta T$  values of Section 1 (top of the pipe) in the middle range of the borehole section. This is expected given that Section 3 measuring points are closer to the heat source compared to those of Section 1.

### 5.1.8.3 Discussion of results

Temperature measurements using DTS and conventional thermistors installed in the same borehole provide comparable temperature profiles with differences smaller than 1 °C.

In borehole BFEA010, the differences between Smartec DTS and thermistor temperatures are largest in a borehole section from about 12 to 34 m. Corresponding Smartec  $\Delta T$  values at left and especially at the right side of the profile are higher. This could be due Smartec's delayed response in regions with high spatial temperature gradient (Chapter 5.1.6).

The generally slightly lower temperatures of the thermistors could be the result of heat dissipation within the borehole inclinometer casing, partly supported by the heat-conductive properties of the inclinometer chain. These effects are likely to affect the built-in thermistors to a greater degree than the FO cable outside of the inclinometer casing.

The shown characteristics of the DTS temperature distributions in comparison to the thermistor profile are very similar for both boreholes BFEA010 and BFEA011. Therefore, it can be concluded that the DTS measurement agree with the thermistor values within 1 °C. The differences would likely be smaller if other influencing factors as the slightly different distances to heat source and the potential inclinometer heat sink effect could be subtracted.

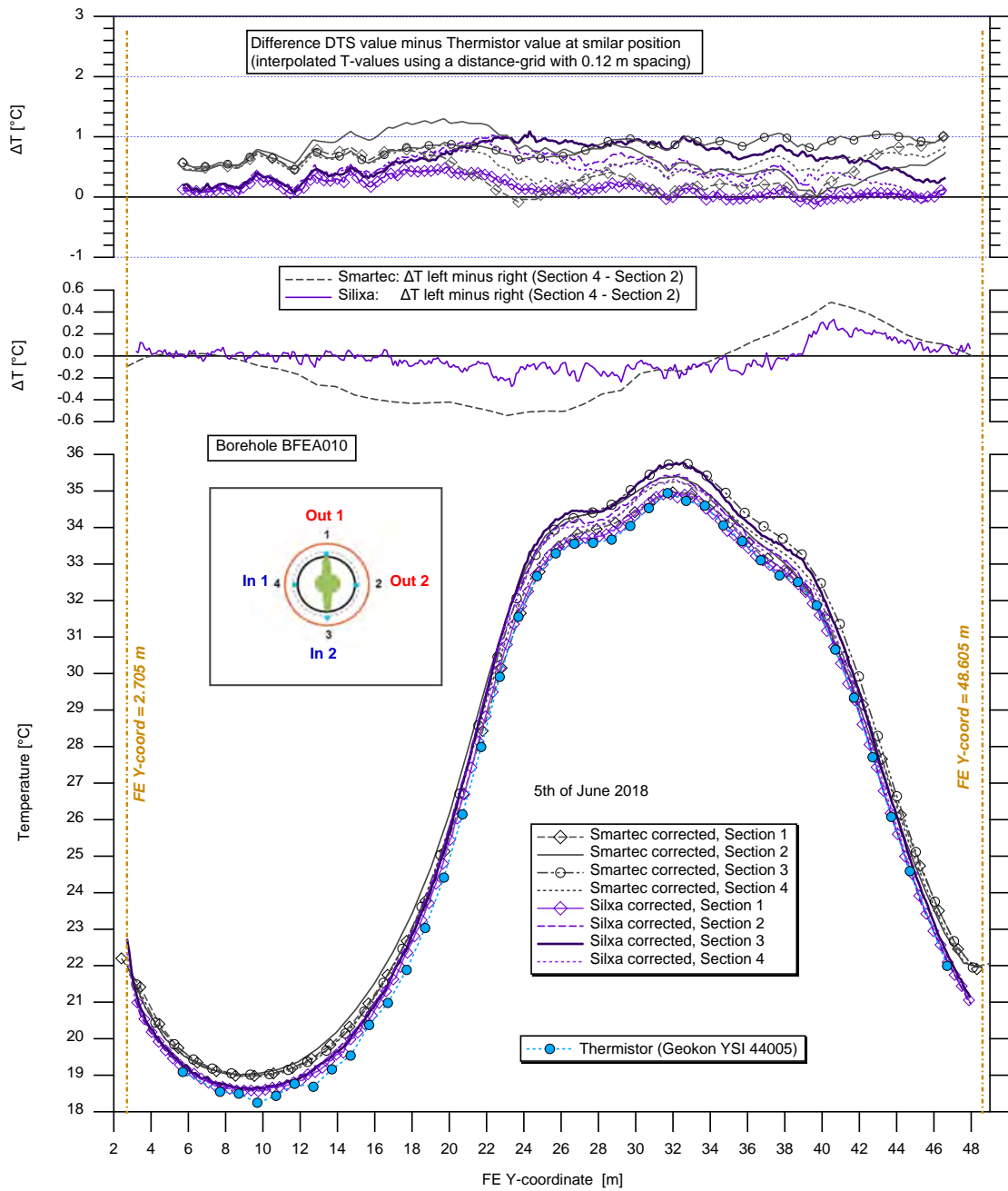


Fig. 5-31: BFEA010 - Comparison of 40 thermistor values with DTS data using Smartec and Silixa.

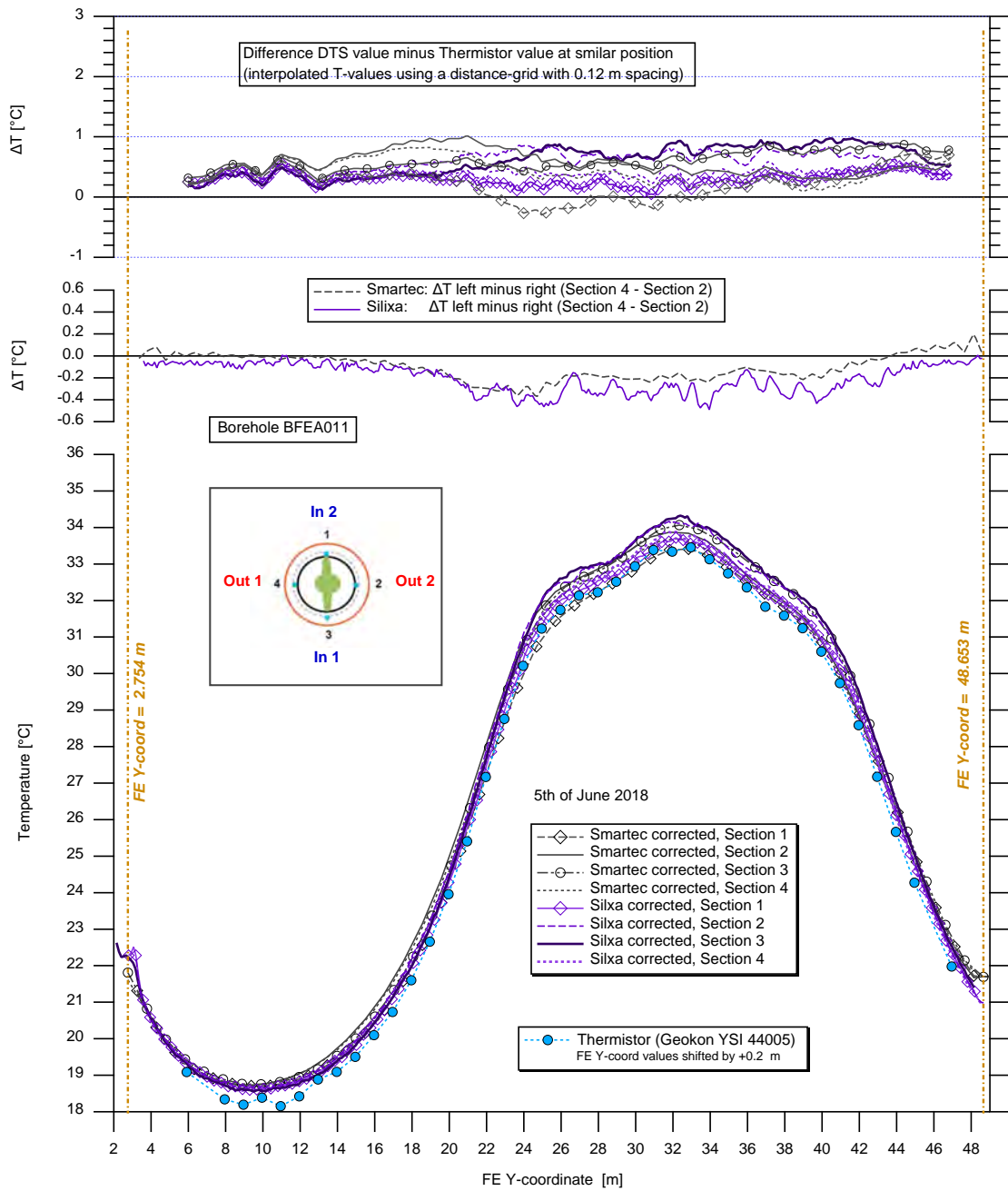


Fig. 5-32: BFEA011 - Comparison of 40 thermistor values with DTS data using Smartec and Silixa.

### 5.1.9 Temperature evolution in the FE tunnel from 2014 until 2018

#### 5.1.9.1 Time series of point-type temperature sensors

The evolution of the temperatures in the FE tunnel is shown in Fig. 5-33 and Fig. 5-34. The monitoring period shown extends over 4 years, from October 2014 to November 2018.

Fig. 5-33 shows the evolution of the heater surface temperatures at top and bottom of the simulated canisters for each heater. The sensor positions are illustrated in the three cross sections on the right to the graph. In the cross-sections at positions H1, H2 and H3 (from top to bottom), the tunnel shotcrete profile, the heater circumference in the centre and the locations of the temperature sensor are shown.

The highest temperatures around the heaters were recorded at the top side of the heaters (00:00 position). This can be explained by the lower heat conductivities at the top section which is covered with GBM. On the bottom part of the heaters, on the other hand, the temperature is 4-5 °C lower due to higher heat conductive properties of the bentonite block pedestals resulting in an increased heat dissipation in downward direction from the heaters. Most of the temperature increase was recorded in the first six months after start of heating. During the last 12 months, the incremental increase for all sensors shown is less than 1 °C.

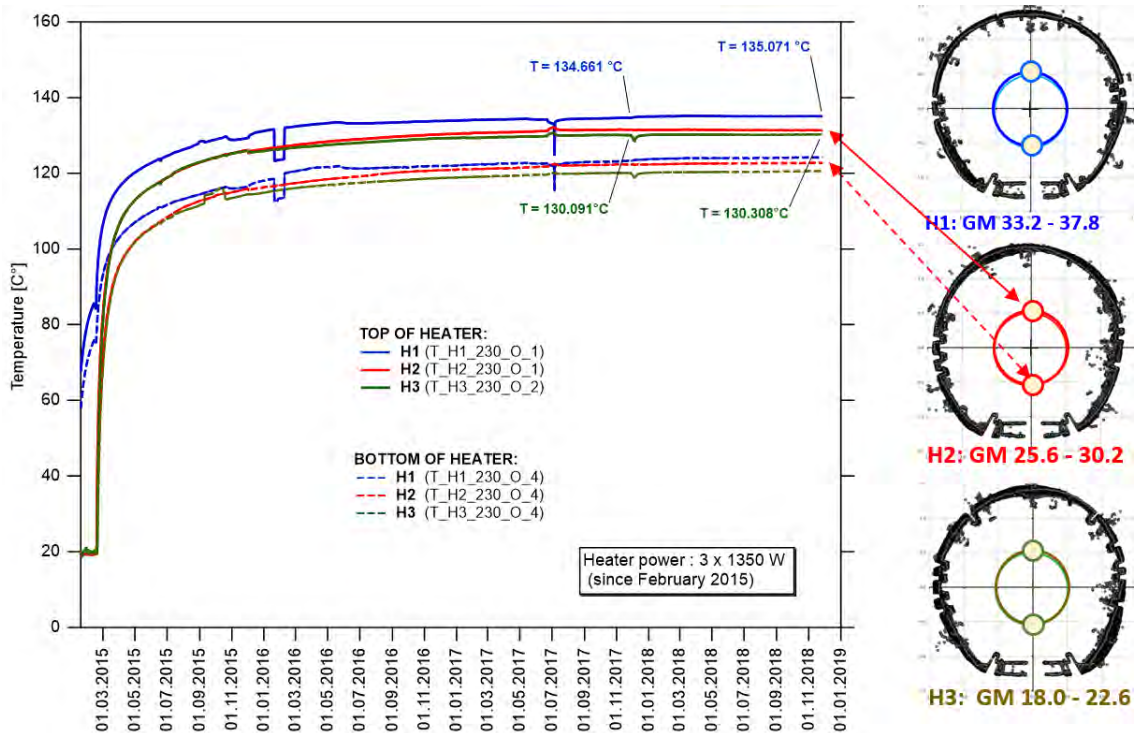


Fig. 5-33: Evolution of the temperatures at bottom and top side of each heater (2014 - 2018).

Fig. 5-34 shows in addition to surface temperatures of H2, the temperatures at the tunnel wall at various positions. The positions are shown in the tunnel cross section right to the graph window. The sensors at the wall are separated from the sensors at the heater surface by about 0.6 m – 0.8 m of bentonite buffer material. The temperature increase at the tunnel wall during the last 12 months varies between 0.9 and 1.5 °C.

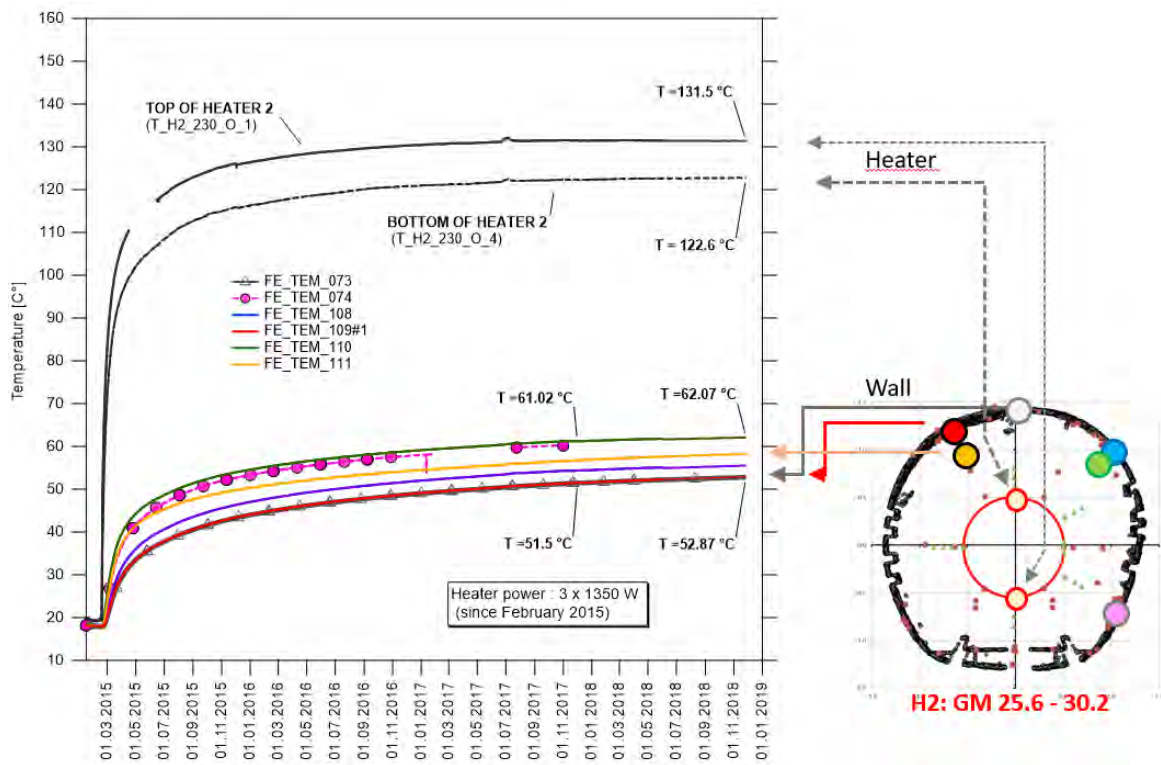


Fig. 5-34: Evolution of the temperatures at the heaters and at the tunnel wall (2014 – 2018).

### 5.1.9.2 Thermal maps of FE tunnel heater section based on DTS data

The temperature evolution in the FE tunnel section from Y-coordinate 21.0 m to 43.0 m is shown with a series of thermal maps based on interpolated DTS data. The four thermal maps in Fig. 5-35 show the temperature increase from February 2015 (top graph, before start of heaters H2 and H3) to December 2015 (bottom graph). The four graphs of Fig. 5-36 cover the time period from 2016 to 2018. The temperature is indicated by a colour scale ranging from 18 to 60 °C. The maps represent developed surfaces of the tunnel cylinder where the circumference value 0 corresponds to the top line (roof) of the tunnel. The top and bottom border of the graphs correspond to the bottom line of the shown tunnel section.

The temperature distributions are calculated based on the 8 Brugg Standard and 2 Brugg Heatable cable sections using the Kriging interpolation method with a spherical variogram model. Note that significant gaps exist between the cable section sections (Tab. 5-10), there are only two cable sections clearly in the bottom part of tunnel.

The top graph of Fig. 5-35 shows the temperature distribution on 10th of February 2015, seven weeks after start of H1. The temperature increase at H1 position (FE coordinates 37.9 – 42.5 m) is lower in the roof compared to the bottom.

The 2<sup>nd</sup> graph from top of Fig. 5-35 shows the temperature distribution on 1<sup>st</sup> of April 2015, 6 weeks after start of heaters H3 and H2 (17th and 18th of February).

By end of year 2015, the temperature in the tunnel section is above 30 °C. The region with highest tunnel wall temperature is below H2 at about 04:30 clock face position.

Tab. 5-10: Clock face positions and corresponding circumference values used for thermal map interpolation.

FO cable	Cable run section	Field clock face position	Thermal map model clock face position	Cicumference m (roof = 0.00)
<b>Brugg Std</b>	A – B projected *	07:00	07:26	+ 5.24
<b>Brugg Std</b>	A-B	07:00	07:26	+ 3.22
<b>Brugg Std</b>	C – D	08:30	09:08	+ 2.02
<b>Brugg Std</b>	E – F	10:00	10:26	+ 1.10
<b>Brugg Std</b>	G – H	10:30	11:02	+ 0.68
<b>Brugg Heatable</b>	J - K	11:30	11:40	+ 0.23
<b>Brugg Heatable</b>	A - B	12:30	12:17	- 0.20
<b>Brugg Std</b>	I – J	01:30	01:06	- 0.78
<b>Brugg Std</b>	K – L	02:00	01:34	- 1.10
<b>Brugg Std</b>	M – N	04:30	02:36	- 1.83
<b>Brugg Std</b>	O – P	05:00	04:34	- 3.22
<b>Brugg Std</b>	O – P projected *	05:00	04:34	- 5.24

\*) used for interpolation across the top / bottom borders of the developed surface

Only the two lower thermal maps of Fig. 5-36 (7th July 2018 and 1<sup>st</sup> of December 2018) are based on dynamically calibrated DTS data. All maps include imprecisions due to Smartec's spatial resolution (and sampling resolution) of 1.02 m, technical measurement issues in regions with large spatial temperature gradient (see Chapter 5.1.6.6), limited measurement coverage corresponding to the amount of FO cable meters installed and shortcomings of the interpolation algorithm applied. Although the thermal maps do not provide precise temperature information for every location of the developed tunnel surface, the maps are useful to describe and visualize the transient temperature trends during the process of heating.

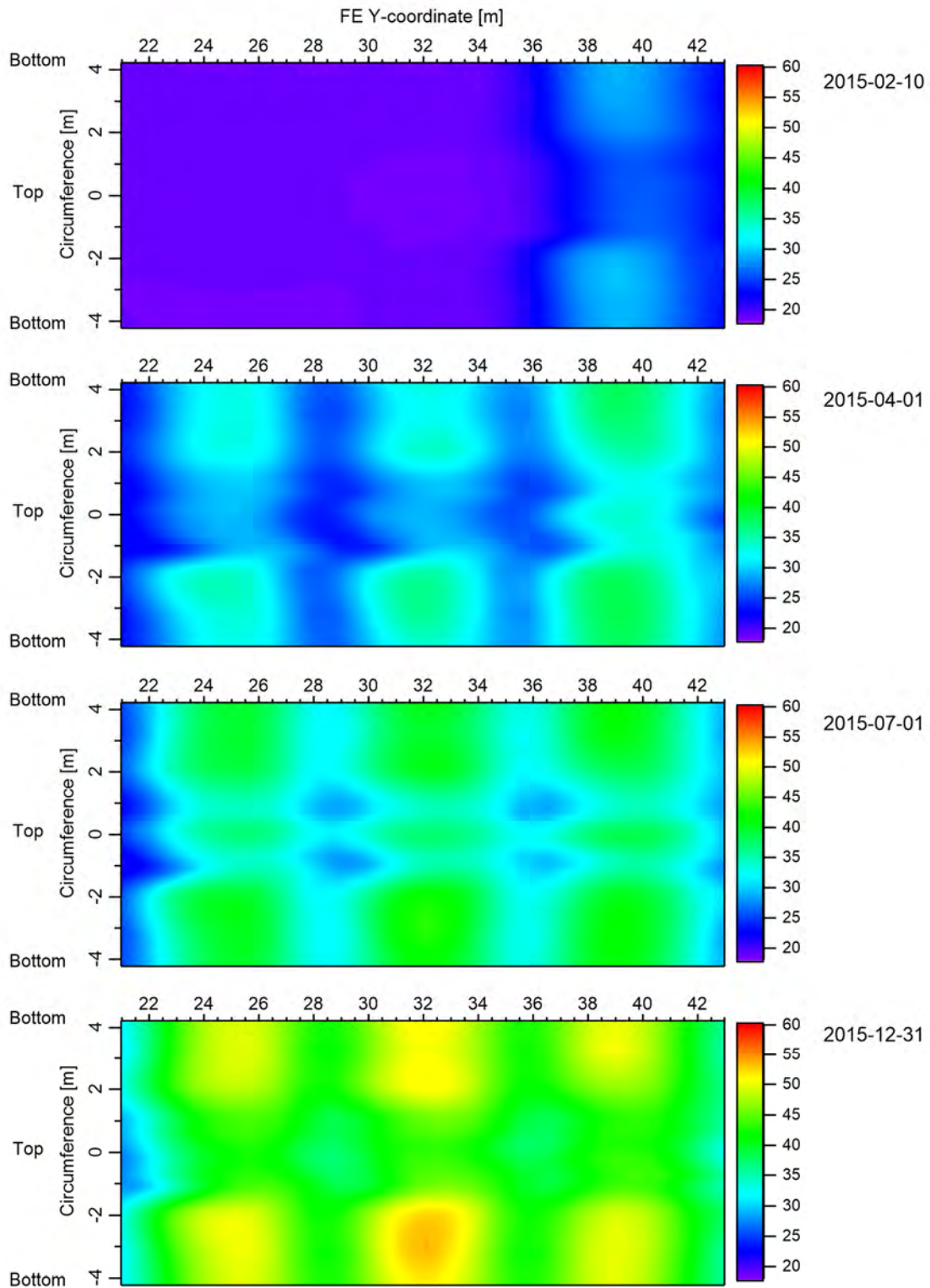


Fig. 5-35: Temperature evolution along the tunnel recorded by DTS-FO cables in 2015.

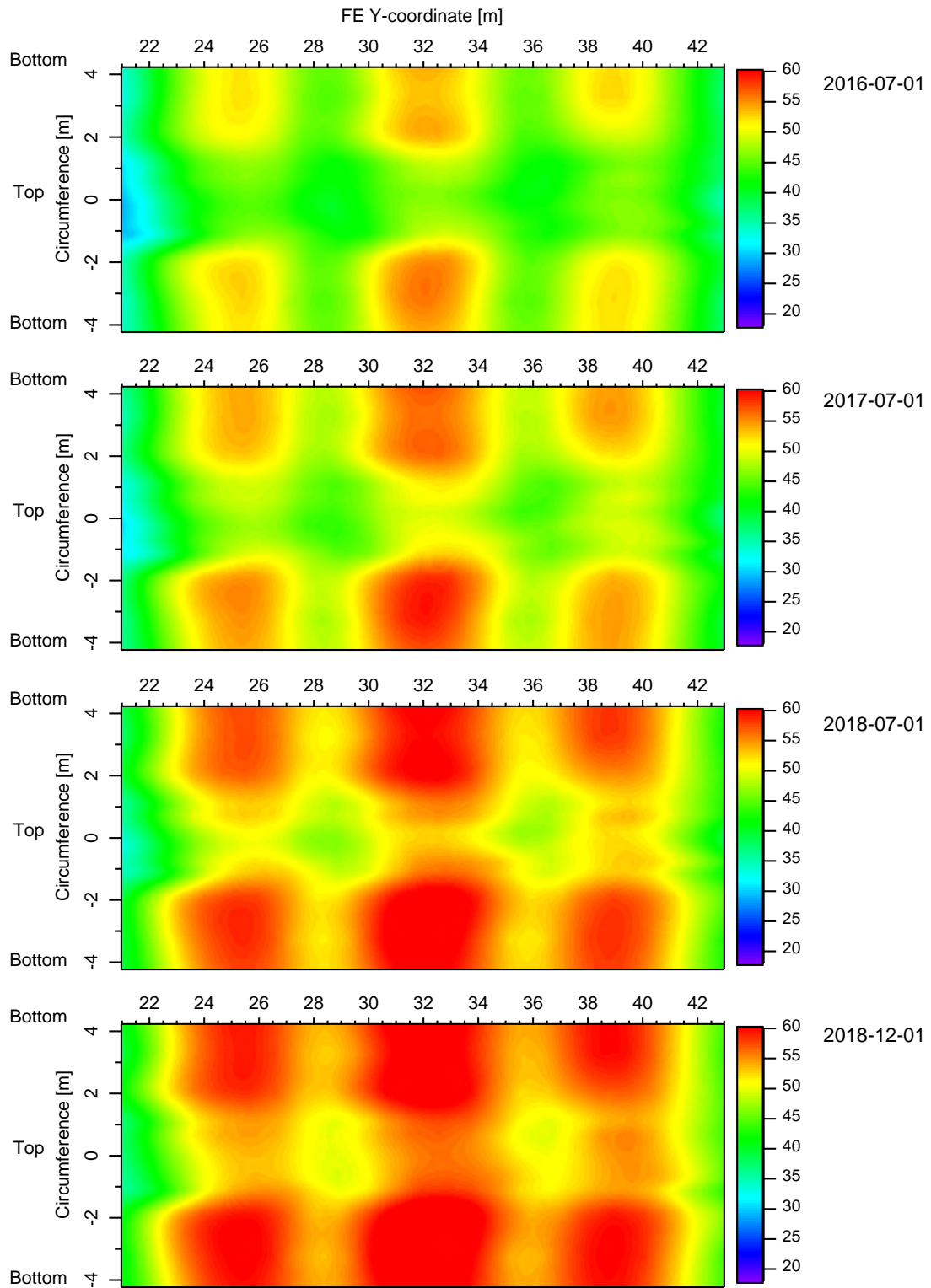


Fig. 5-36: Temperature evolution along the tunnel recorded by DTS-FO cables between 2016 - 2018.

### 5.1.9.3 Discussion of results

The temperature changes measured with the FO cables along the tunnel wall reflect the heat flow from the heaters across the bentonite buffer (GBM and bentonite block pedestals) towards the rock. Series of heat maps are useful to visualize the evolution of the temperature in the tunnel as the buffer material is heated up. The thermal maps show that bottom part of the tunnel heats up faster than the upper part. This is due to the higher heat conducting properties of the pedestals below the heaters compared to the granulated bentonite buffer material. Since end of 2015, the FO cables measure the highest tunnel wall temperatures around H2. This can be explained by the heat production of H1 and H3 which limit the horizontal heat flow gradient (along tunnel axis) between H1 - H2 and between H2 - H3.

### 5.1.10 Temperature evolution in ISS section from 2014 to 2018

Between the A-B and J-K cable sections, the Brugg Heatable cable is directed in the Interjacent Sealing Section (ISS, see Fig. 2-2) and loops there three times normal to the tunnel axis (in between the steel arches), each time from 04:00 and 03:00 clock face position around the tunnel profile. Ahead of each loop start, the cable is routed from the roof with an additional positive increment along the FE Y coordinate down to the 03:00 clock position. The cable meter positions for each loop are given in Tab. 5-11. The loop positions are also illustrated in the temperature profile of Fig. 5-37.

The evolution of the temperatures in the ISS section between December 2014 and December 2018 is shown in Fig. 5-38. For each loop, two reference locations were chosen which approximately relate to tunnel roof and tunnel bottom, respectively.

Tab. 5-11: Start and end positions of G2, G4 and G6 loops and corresponding cable meters after fingerprinting.

<b>ISS loop</b>	<b>Clock position at start</b>	<b>Clock position at end</b>	<b>Cable meter at start</b>	<b>Cable meter at end</b>
<b>Loop G2</b>	04:00	03:00	117.5	126.2
<b>Loop G4</b>	04:00	03:00	127.1	136.1
<b>Loop G6</b>	04:00	03:00	136.7	145.5

Static temperature corrections were applied for the data until 21.04.2015 (-1.0 °C) and for the subsequent period until 28.03.2018 (-1.5 °C). After 28.03.2018, the displayed temperatures represent dynamically calibrated DTS data. As expected, the temperatures are generally lower at increased distance to the heaters. It appears that within a loop turn the bottom temperatures are slightly higher than the roof temperatures.

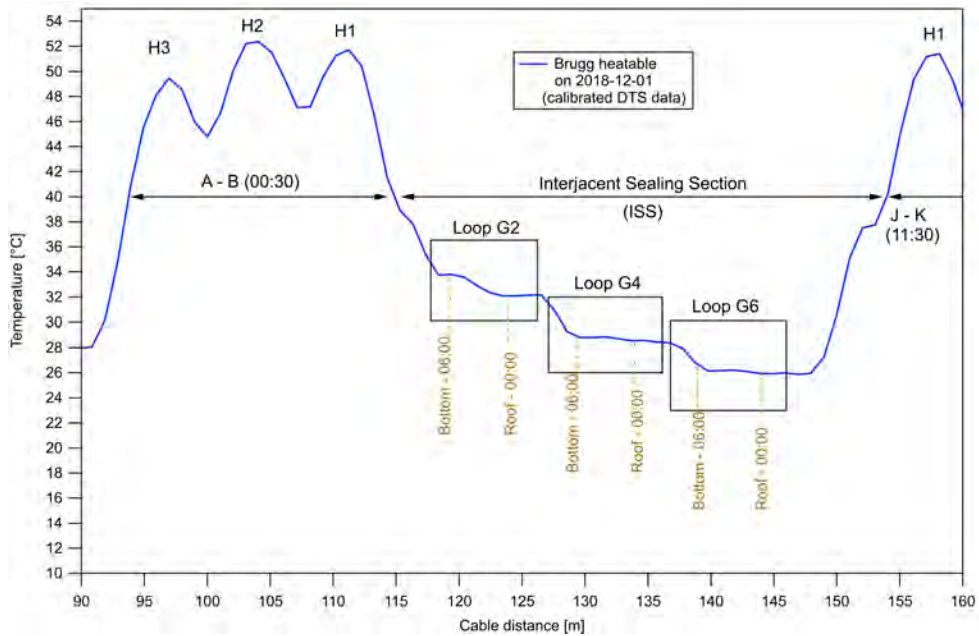


Fig. 5-37: ISS Loop positions G2, G4 and G6 along the Brugg Heatable cable.

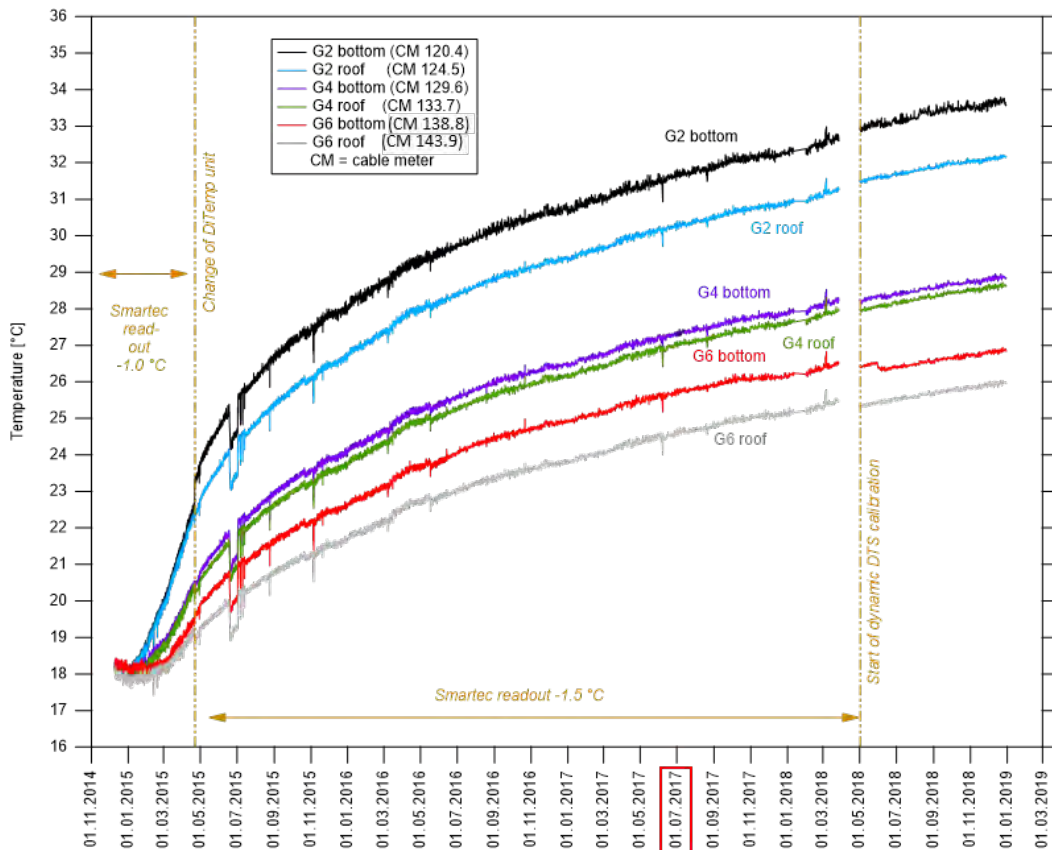


Fig. 5-38: Evolution of temperatures in the Interjacent Sealing Section (ISS) (December 2014 – December 2018).

Note: For the date 01.07.2017 the illustration of the loop plots is shown at G2, G4 and G6 in Fig. 5-39.

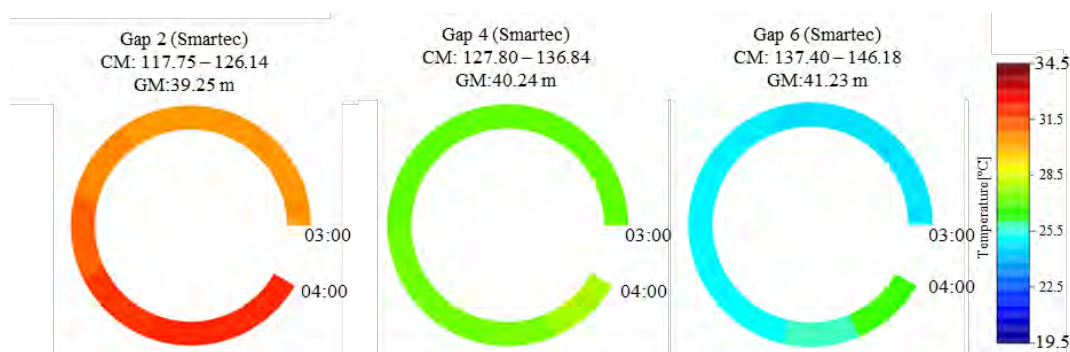


Fig. 5-39: Temperatures (Smartec) on 01.07.2017 as loop plots at G2, G4 and G6 of ISS.

Note: A (- 1.5) °C temperature correction has been applied to raw data on 01.07.2017 as also shown in Fig. 5-38.

### 5.1.11 Temperature evolution in the BFEA011 borehole from 2014 to 2018

The temperature evolution of Smartec DTS measurements at FE Y - coordinate 25.8 m and of near point-type sensors are shown for the Borehole A11 in Fig. 5-40 to Fig. 5-42. The range of the time axis spans over 4 years, from November 2014 to November 2018. Fig. 5-41 shows a sub-range with focus on calibrated data since March 2018.

The location of 25.8 m on the FE Y - coordinate with respect to the FO sections can be viewed in the temperature profile of Fig. 5-32 (Chapter 5.1.8). The FO cable installations in the BFEA011 are described in Chapter 3.1.3. Note that the directions of the BFEA010 and BFEA011 boreholes are quasi-parallel to the FE tunnel axis.

The DTS data shown represent 1 measurement per 6 hours or 4 hours (4 hours after 28.03.2018; 60 minutes integration time per measurement). The temperatures of the point-type sensors are averaged per 24 hours.

Until the installation of the permanent calibration baths on 28th of March 2018, the Smartec temperatures (instrument output) are 1.5 to 2.7 °C higher than the shown point-type sensor temperatures. The time of the implementation of real-time calibration is marked by a vertical dashed line in Fig. 5-40 to Fig. 5-42. After implementation of the real-time calibration, the DTS temperatures are in good agreement with the point-type T-sensors.

The clock positions of the FO cable sections are shown in Fig. 5-40 and Fig. 5-42 together with the respective line symbols. In the Fig. 5-42, static temperature corrections are applied for the DTS data recorded before implementation of the permanent calibration baths.

Considering that the FE tunnel and the heat source (heaters) are located to the lower-right relative to the A11 borehole (view in tunnel direction), we would expect the highest temperatures at cable sections A11-3 (06:00) and A11-2 (03:00) which are closest to the heaters. This is confirmed by the data. The data also suggest that the DTS temperatures of sections A11-3 and A11-2 match better with the temperatures of point-type T-sensor at positions 26.75 and 27.75 m (see detailed view in Fig. 5-41). However, the differences in temperatures are small (< 0.5 °C). There might be a systematic temperature difference between the inside and outside space of the inclinometer casing, as observed in T-profile (along A11 borehole) comparing DTS with point-type sensor data (Fig. 5-32 in Chapter 5.1.8).

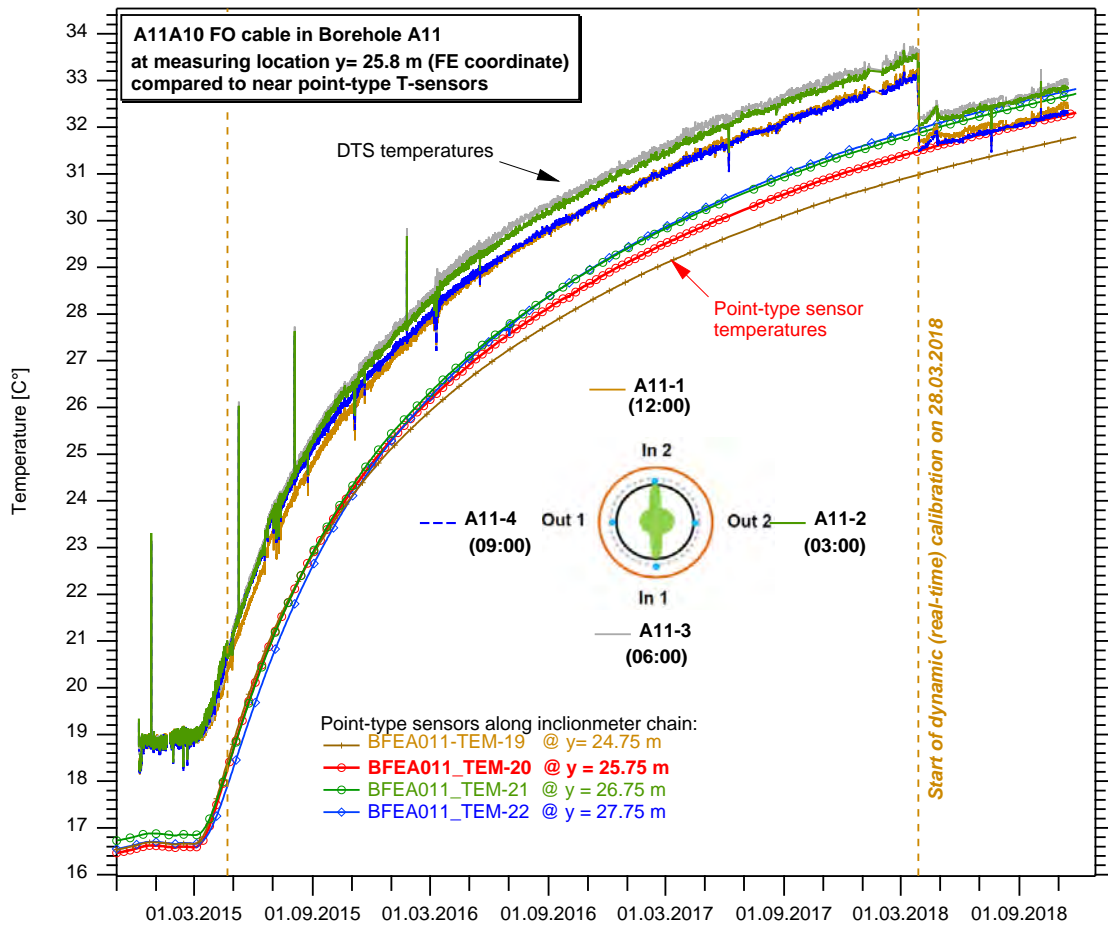


Fig. 5-40: Borehole A11 - DTS and point-type T sensor temperatures 2014 - 2018.

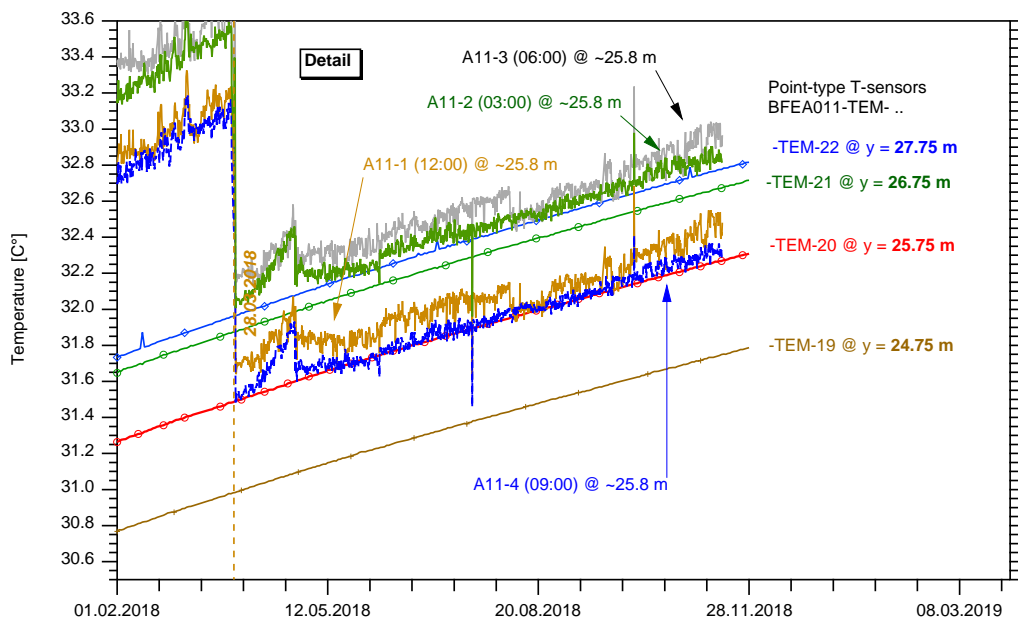


Fig. 5-41: Detail from previous graph Fig. 5-40.

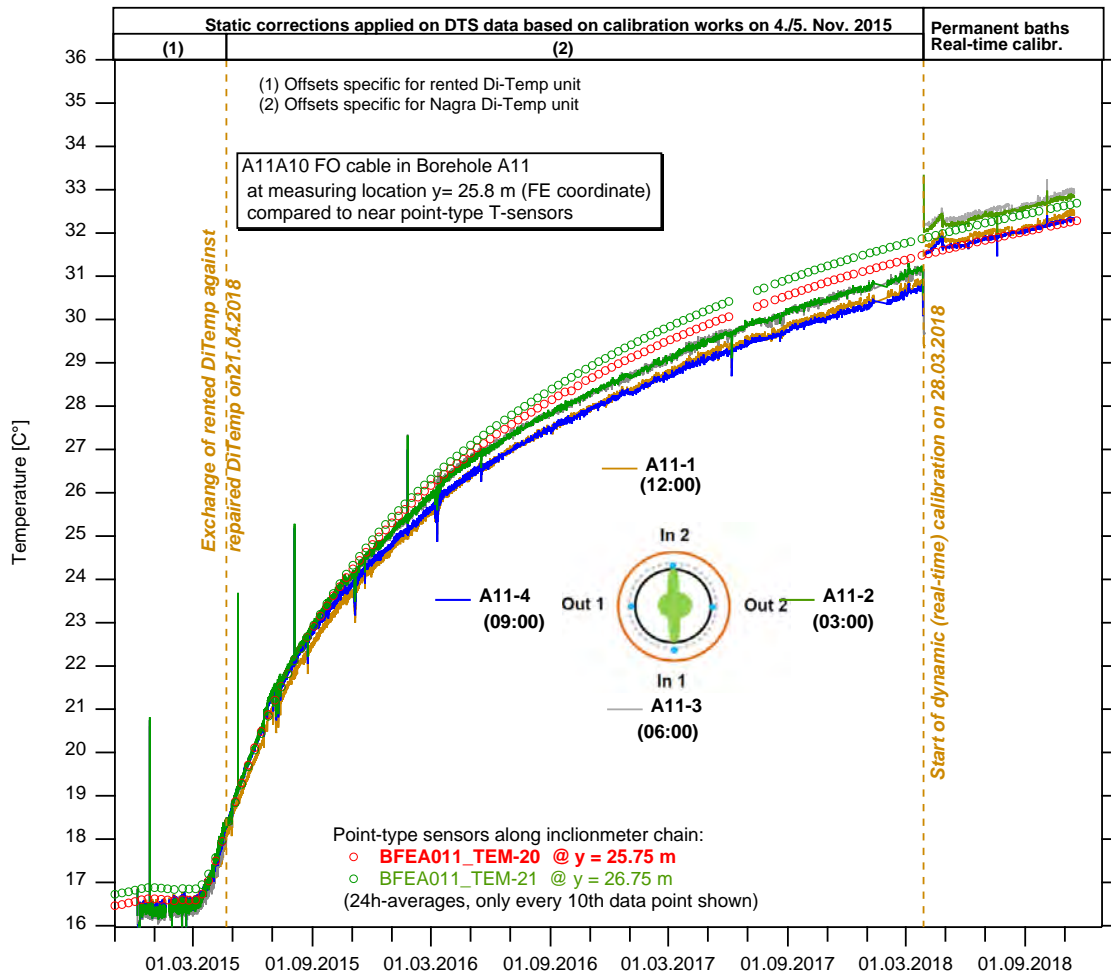


Fig. 5-42: Static T-corrections applied to DTS data Dec. 2014 to March 2018

### 5.1.12 Change of FO calibration parameters

At the FE experiment, new calibration baths were installed on 28th March 2018 (Chapter 5.1.5). Since then, calibrated temperatures are calculated dynamically in the FE Information System (FEIS) based on Stokes and anti-Stokes values recorded along cable sections located inside the calibration baths and based on precisely known bath temperatures. The calibration and related procedures are described in Chapter 5.1.5. Since 28.03.2018, the calibration parameters  $C$  [-],  $\gamma$  [K] and  $\Delta\alpha$  [m<sup>-1</sup>] are derived for each Smartec measurement of the following cables:

- Brugg Standard
- Brugg Heatable
- AFL
- A11A10

Calibrated temperatures are then calculated in function of the calibration parameters and cable length using the equation:

$$T(z) = \frac{\gamma}{\ln \frac{P_S(z)}{P_{AS}(z)} + C - \Delta\alpha z} \quad \text{Equation 5-8}$$

All calibration parameters and root mean square errors (RMSE) are stored in the FEIS data base.

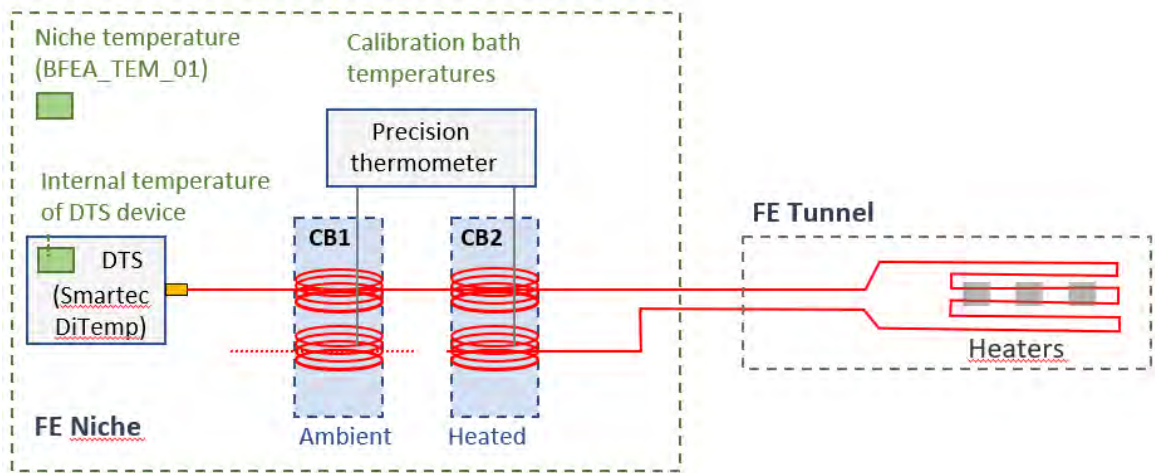


Fig. 5-43: Schematic sketch of the calibration system and potential factors influencing the quality of measurement

This chapter aims to document and to visualize the trends of the calibration parameters since May 2018 and to reveal possible dependences of calibration parameters on other (external) factors such as niche temperature, interrogator temperatures, and effects of any on-site activities, e.g. incidents related with the calibration baths. The observation period currently available (with calibration baths in operation) is 6 ½ month only. Further monitoring will be required in the following years to answer the questions below with more certainty:

- To what extent do changes of the interrogator's internal temperature affect the data and the calibration quality?
- How do calibration parameters change over time?
- How do calibrated temperatures compare to the Smartec T-values?
- How do irregularities related to the calibration baths affect the corrected temperatures?

### 5.1.12.1 Overview of additional parameters checked for possible correlation

In Fig. 5-44 four additional temperatures are shown on the two uppermost Y-axes:

- Temperatures of calibration baths CB1 and CB2
- Niche temperature sensor BFEA\_TEM\_01 mounted on the wall at the left side of the niche, see Francois (2012c)
- Temperature inside the Smartec interrogator unit.

Note that the Smartec internal temperature is very close to the upper limit of the allowed range.

In Fig. 5-45, the evolution of DTS temperature data are given for all four cables for a selected cable positions on the uppermost section of the graph:

- Brugg Standard: temperature at cable distance 145 m

- Brugg Heatable: temperature at cable distance 96 m
- AFL: temperature at cable distance 91 m
- A11A10: temperature at cable distance 120 m

Calibrated data are shown using full lines, uncorrected data (i.e. Smartec T-output) is shown using dashed lines.

### 5.1.12.2 Short-term irregularities (spikes) of C- and $\gamma$ -parameters

Fig. 5-44 and Fig. 5-45 show that the calibration parameter C is fairly steady for the Brugg Heatable and the A11A10 cable but it is varying significantly for the AFL and Brugg Standard cable. Short term (temporary) C-changes which manifest as spikes in the graph are related to the re-filling of the calibration bath on 19th of July and on 4th of October 2018. The spikes of the C-parameter coincide with negative spikes on the heated bath temperature (T-decrease because of temporary removal of bath cover and refill using cold de-ionized water) and with spikes of the  $\gamma$ -parameter. The latter are negative or positive, depending on cable type and date of the event. C- and  $\gamma$  spikes concur also at system re-start after a power failure. No respective irregularities are visible for the AFL and Brugg Heatable cable.

The C-spikes (indicating the re-filling of the calibration baths) seem not to affect the temperature measurements along the cables as suggested by +/- constant RSME values and constant temperatures in the gallery (Fig. 5-45).

### 5.1.12.3 Abrupt trend-change of the C-parameter

On the 5th of June 2018, the Smartec measurements were suspended temporarily to enable tests using the Silixa interrogator. After re-start of the Smartec DiTemp unit, Smartec SA adjusted the instruments settings to better match the temperatures span between ambient temperature bath and heated bath. This resulted in abrupt changes of the C-parameter followed by slower gradual changes over the following days/weeks for the Brugg Standard cable whereas the slightly downward trends of AFL, Brugg Heatable and A11A10 remained mostly unaffected. Note that the abrupt change of the C parameter did not affect the RMSE values and apparently there is no visual effect on the gallery temperatures (Fig. 5-45, see curves shown on top section of the graph).

The  $\Delta\alpha$ -parameter is constant for all but the AFL cable.

Fig. 5-44 and Fig. 5-45 show that the signal attenuation is constant for A11A10, Brugg Standard and Brugg Heatable over the entire observation period with similar values between  $5.4\text{E-}5$  and  $6.6\text{E-}5 \text{ m}^{-1}$ . The signal attenuation is significantly higher for the AFL cable and it is varying in a broad range between the initial  $1.52\text{E-}04 \text{ m}^{-1}$  and the low of  $8.7\text{E-}05 \text{ m}^{-1}$  near to the end of the observation period. The AFL cable shows also significantly higher RMSE values. The AFL RMSE values are generally higher after 6th of August with maxima at around  $0.6 \text{ }^\circ\text{C}$ . The rise on 6th of August cannot be linked to any other event or a specific irregularity of the data shown in the graphs.

#### **5.1.12.4 Discussion of results**

Despite of the irregularities and events mentioned above, the calculated temperatures based on the derived calibration parameters are very smooth (see top section of Fig. 5-45) and accurate (see RMSE values). The non-calibrated temperatures given by the interrogator (Smartec instrument output) deviate from the calibrated values by several degrees Celsius.

The presented 6 ½-month monitoring period suggests that the implemented calibration system is robust. It is unaffected by the so far observed external impacts (e.g. bath refill using cold water, system re-start after power failure) and it provides good calibration results also for cables of inferior quality and varying attenuation (see AFL cable). The effects of external effects are mitigated by using a relatively long integration time of one hour per measurement.

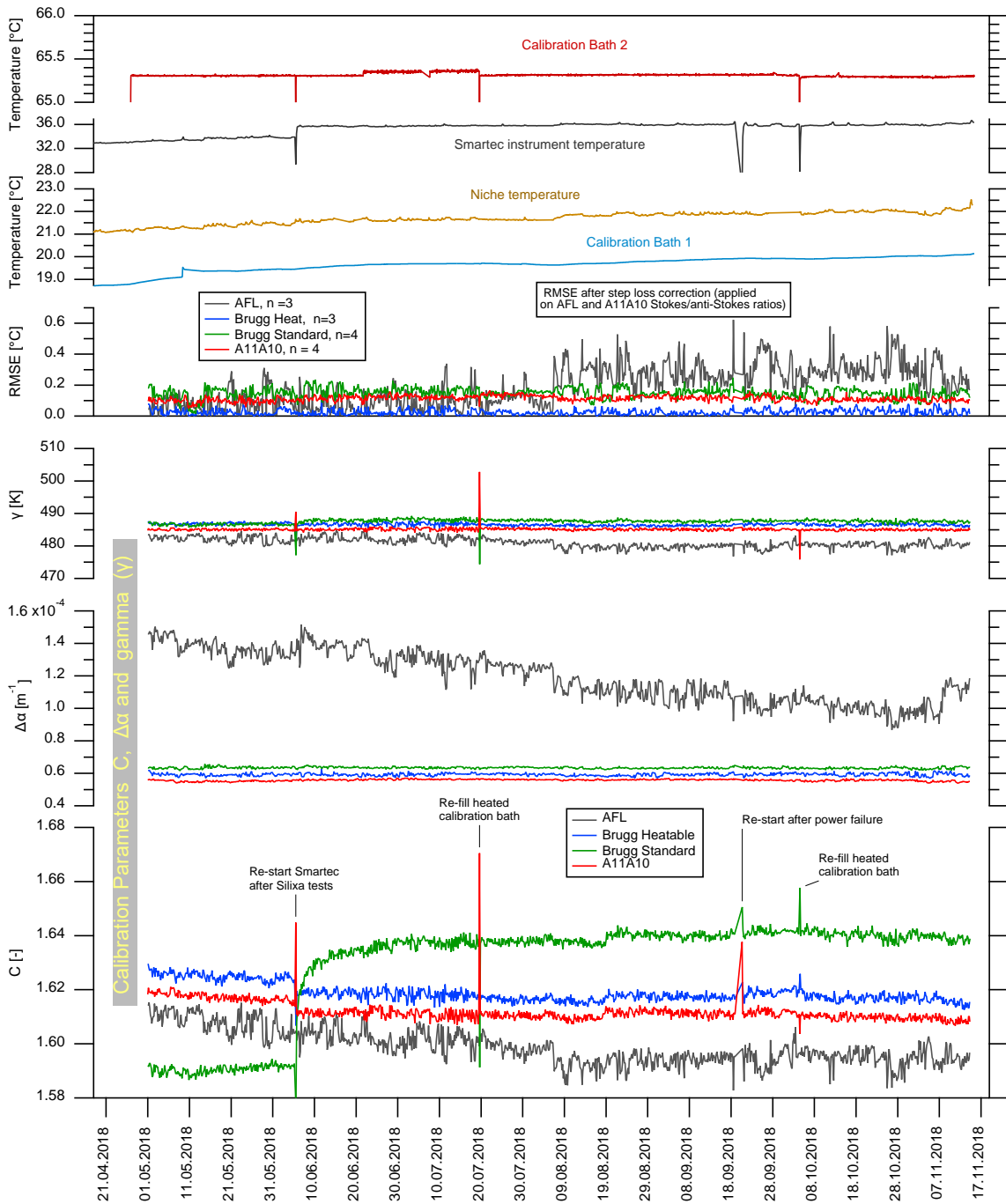


Fig. 5-44: Calibration parameters - RMSE, T-values of niche, interrogator and calibration baths (May - Nov. 2018).

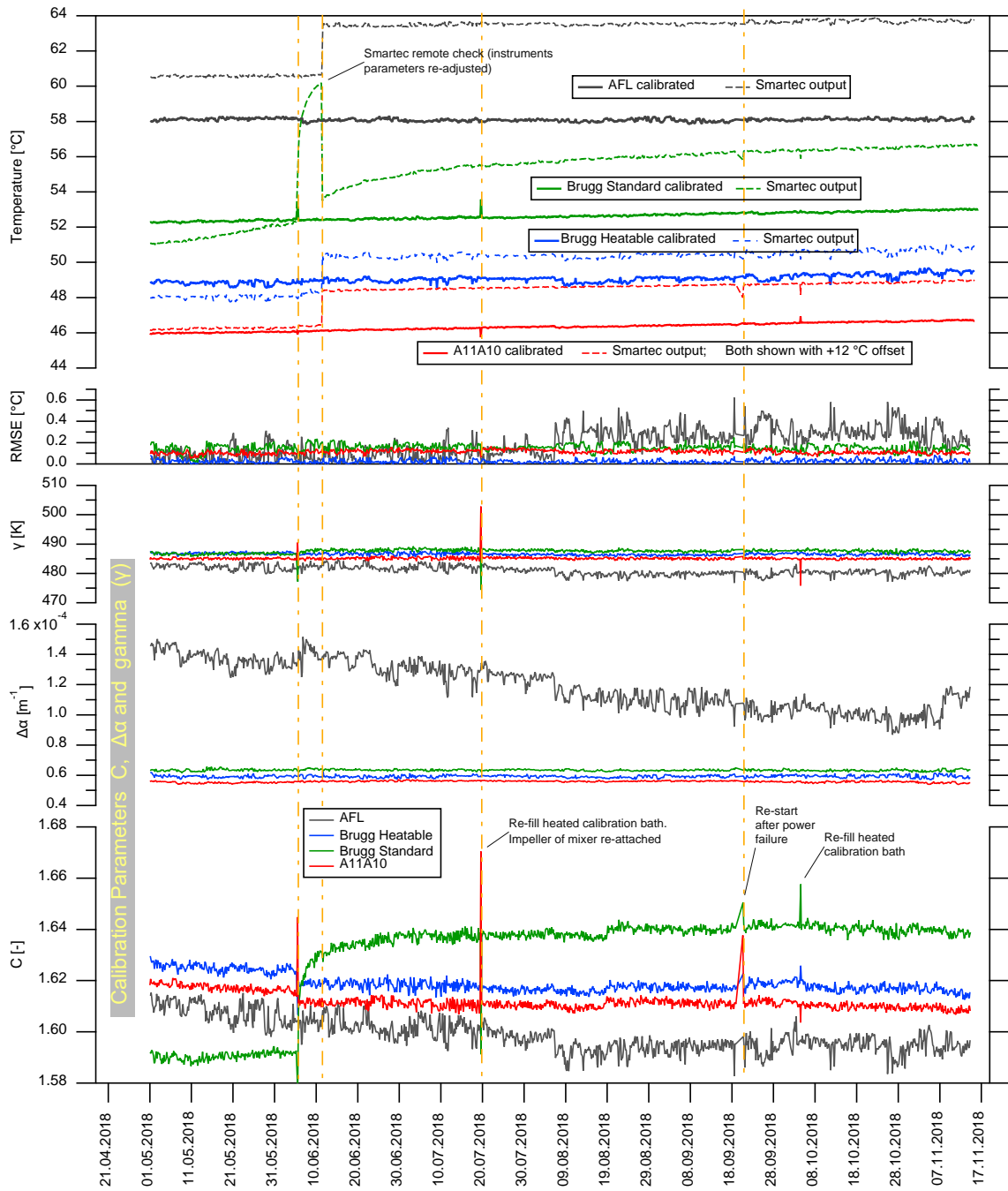


Fig. 5-45: Calibration parameters - RMSE and cable temperatures (May - Nov. 2018)

## 6 TDR data

This chapter provides a brief overview of the calibration procedure, field data acquisition and data interpretation of the TDR probes installed in the Opalinus Clay and granular bentonite backfill in the FE gallery (see Fig. 3-8 for locations).

### 6.1. TDR probe verification

#### 6.1.1. Verification of rock probes

The rock probes were custom-made by Solexperts AG. Before the rock sensors were mounted in the FE tunnel, they have been verified for consistency using standard homogeneous materials with known dielectric properties (Sakaki et al., 2013). Measurements in air, water, dry and saturated glass beads were executed. Different lengths of feeding cable (5, 19, 25 and 31 m) were tested to estimate the influence of cable length and individual sensor production. The dielectric permittivity of the test materials is shown in Tab. 6-1. All laboratory measurements were executed by Okayama University, Japan.

Tab. 6-1: Relative permittivity of verification material for FE TDR sensors

Name	Relative Permittivity	Comment
Air	1.0	
Dry glass beads	2.1	
Saturated glass beads	28.5	T = 20 °C
Tap water	80.0	T = 20 °C

Fig. 6-1 illustrates the variability of the TDR sensors response when plotting individual travel time of each sensor against permittivity for TDR rock probe BFEB017. Where the variations between the sensor responses are obvious, the characteristic behavior of the sensors remains comparable to each other.

The relationship between the permittivity and travel time can be described by a fitting function of type

$$\varepsilon_r(T) = a_i + b_i * e^{c_i * T} \quad \text{Equation 6-1}$$

with fitting parameters  $a_i$ ,  $b_i$  and  $c_i$ , for  $i$  = Sensor ID.

Fig. 6-1 shows the fitting curve for sensor BFEB017\_SEA\_01 and its associated parameters. This fitting procedure was executed for all TDR rock probe sensors.

The above function is insufficient to transform the permittivity to water content as a relationship between the water content and permittivity is needed or a direct relationship between travel time and water content. The second method was selected and is described in chapter 6.3.

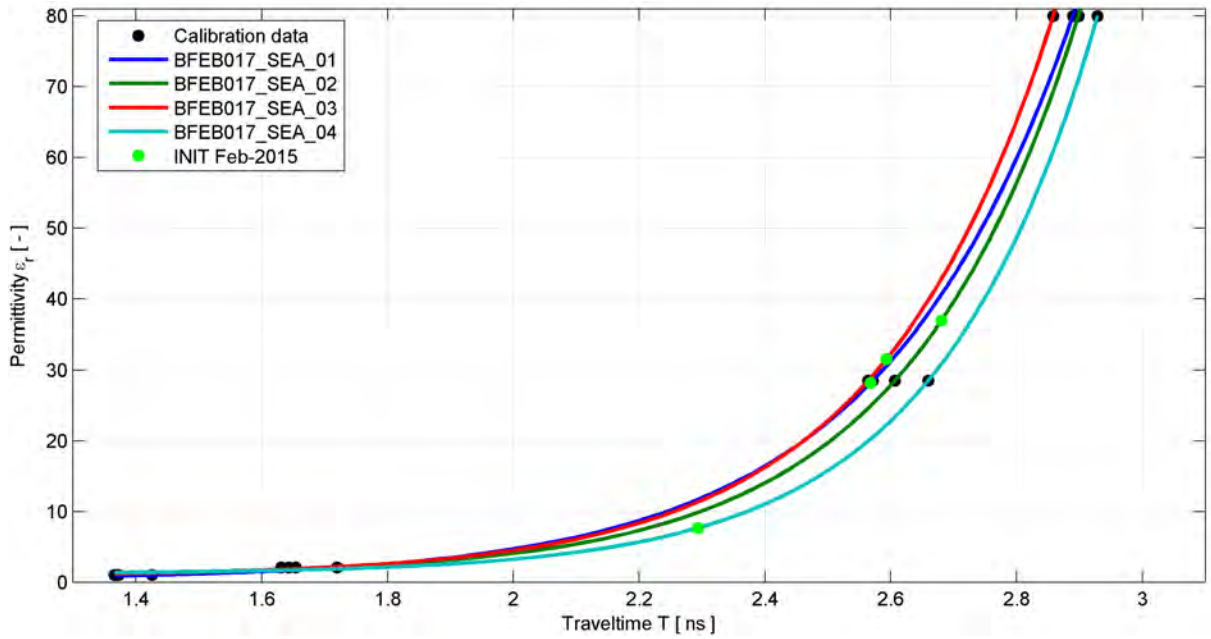


Fig. 6-1: Transformation between travel time and rel. permittivity for FE TDR sensors of rock probe BFEB017.

Note: The initial field data (just before heaters were started) are also plotted to the function.

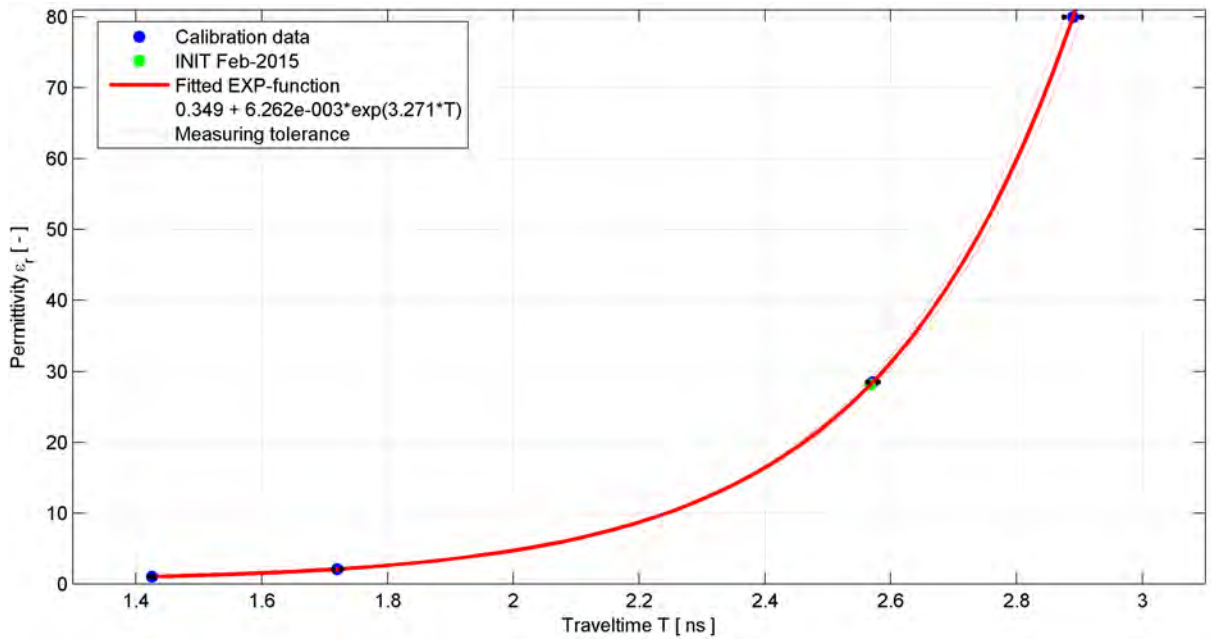


Fig. 6-2: Transformation function between travel time and relative permittivity for FE TDR sensor BFEB017\_SEA\_01 including measurement tolerance as a result of multiple measurements.

### 6.1.2 Verification of bentonite probes

The verification of the bentonite TDR sensors was done similar to the rock TDR sensor verification (see previous chapter). Fig. 6-3 shows the transformation functions to convert travel time into relative permittivity. All laboratory measurements were executed by Okayama University, Japan.

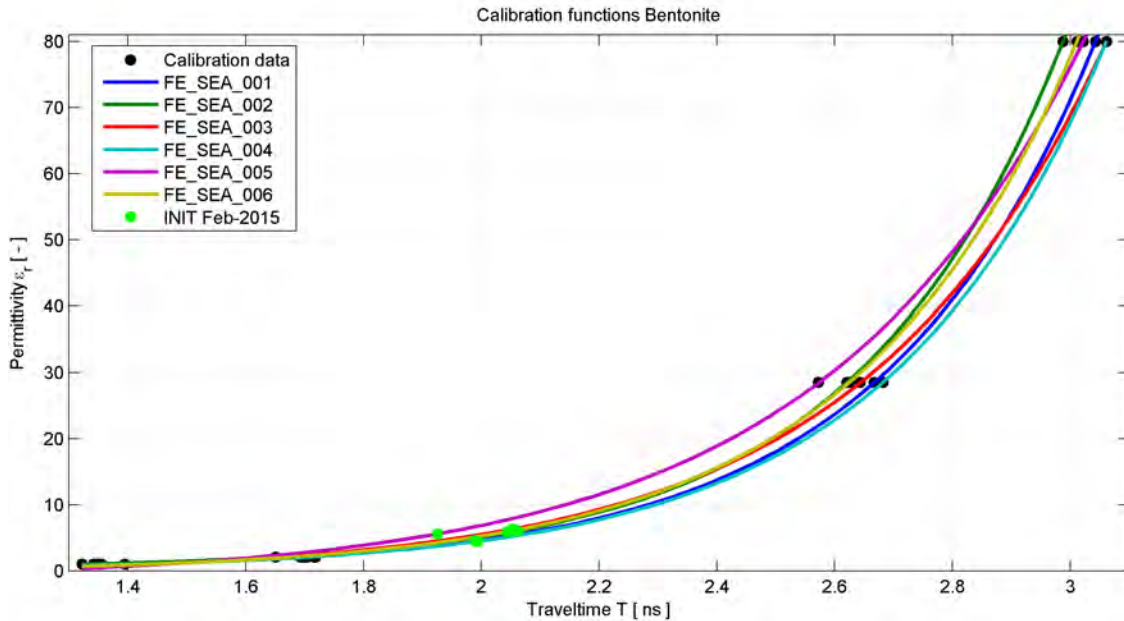


Fig. 6-3: Transformation between travel time and rel. permittivity for FE TDR bentonite probes. The initial field data (just before heaters were started) are also plotted to the function.

### 6.2. Travel time analysis of TDR measurements

An electromagnetic pulse which propagates along a waveguide is affected by the dielectric properties of the surrounding material. Parameters, like the dielectric permittivity  $\epsilon$ , change the wave propagation velocity of a signal whereas parameters, like the electric conductivity  $\sigma$ , change the magnitude (dissipation) and shape (dispersion) of the signal amplitude.

The travel time of an electromagnetic pulse is related to the dielectric permittivity of the surrounding material. To get the travel time of a TDR pulse along a sensor, two characteristic points within the TDR trace that represent the beginning and the end of the probe need to be identified. One way is to use the inflection points (maxima in first derivative of the TDR signal) the other way is to identify the base points of the signal using characteristic tangent and regression lines. Both methods have their advantages and disadvantages.

The inflection point method is much faster but also more affected by signal variation during main reflections. This leads to a large variability in travel time determination although the signal shape does not change significantly. A more stable method is the tangent method which is used in this analysis to determine signal travel time.

To identify the beginning of the sensor, the first main inflection is used (maximum of first derivative). The intersection between tangent through first inflection point and regression line

through base level identifies the beginning of the sensor (see Fig. 6-4, left intersection). The end of the sensor is determined in a similar way. For this graphical method, a stable algorithm has been developed to determine signal travel time without any user interaction.

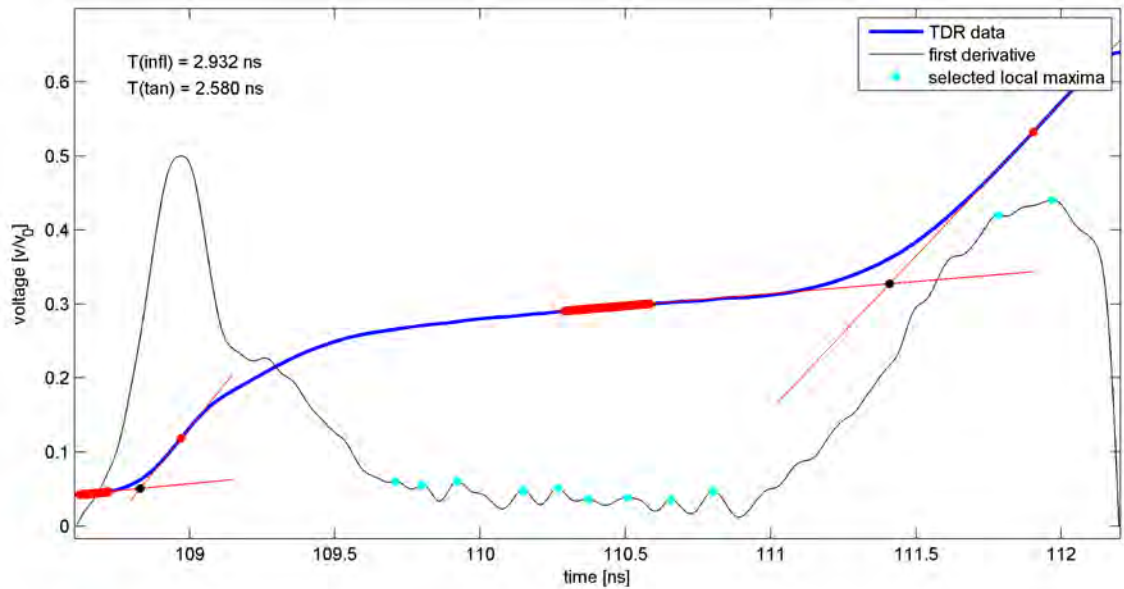


Fig. 6-4: Example of the travel time analysis of the TDR signal (Schlaeger & Sakaki, 2017).  
 Note: The first derivative indicates the positions to steepest slope (red dots) which is used to generate the vertical tangents.

For illustration, the travel time data of BFEB017 TDR rock probe and all TDR bentonite probes have been plotted in Fig. 6-5 and Fig. 6-6. The evolution of travel time during the observation period until mid of 2018 is shown. The visual inspection allows identifying periods of change and periods of stability.

### 6.3 Analysis of TDR measurements

#### 6.3.1 Water content calibration

The TDR measurement is based on the travel time of an electromagnetic pulse needs to propagate along the sensor. This travel time is influenced by the surrounding material including the water content of the material and the temperature. To calculate the volumetric water content from a travel time measurement the following steps are required:

- (1) A sensor calibration to eliminate all effects of the individual sensor design.
- (2) A material calibration to include temperature and water content correlations of the surrounding material.

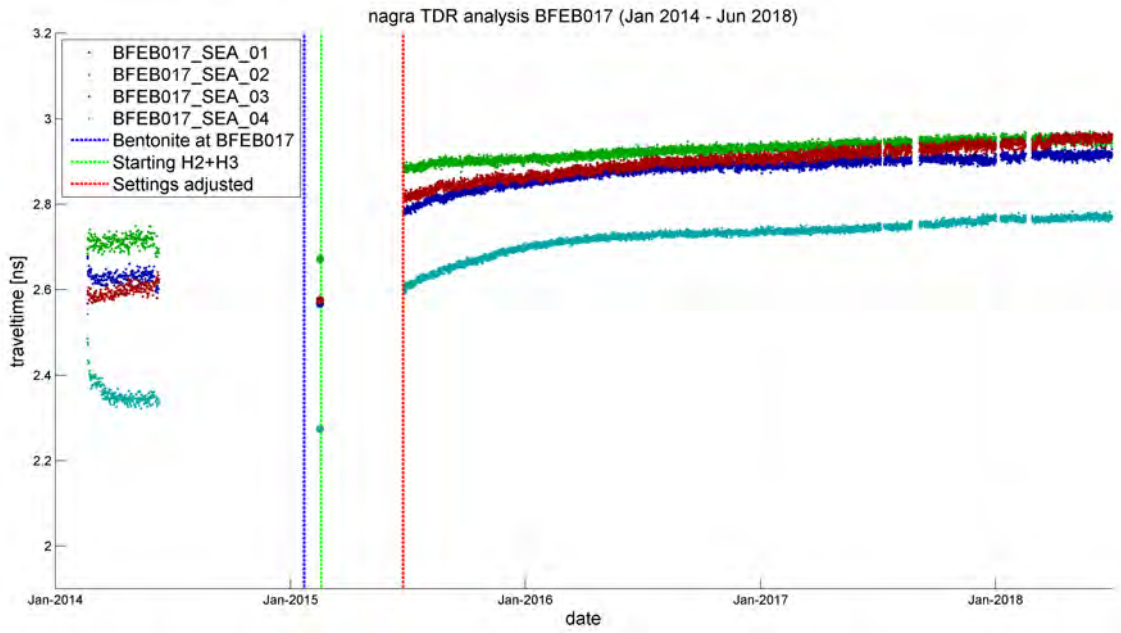


Fig. 6-5: Travel time of TDR probes at rock sensor BFEB017 - TDRs 01-04 are located in Opalinus Clay.

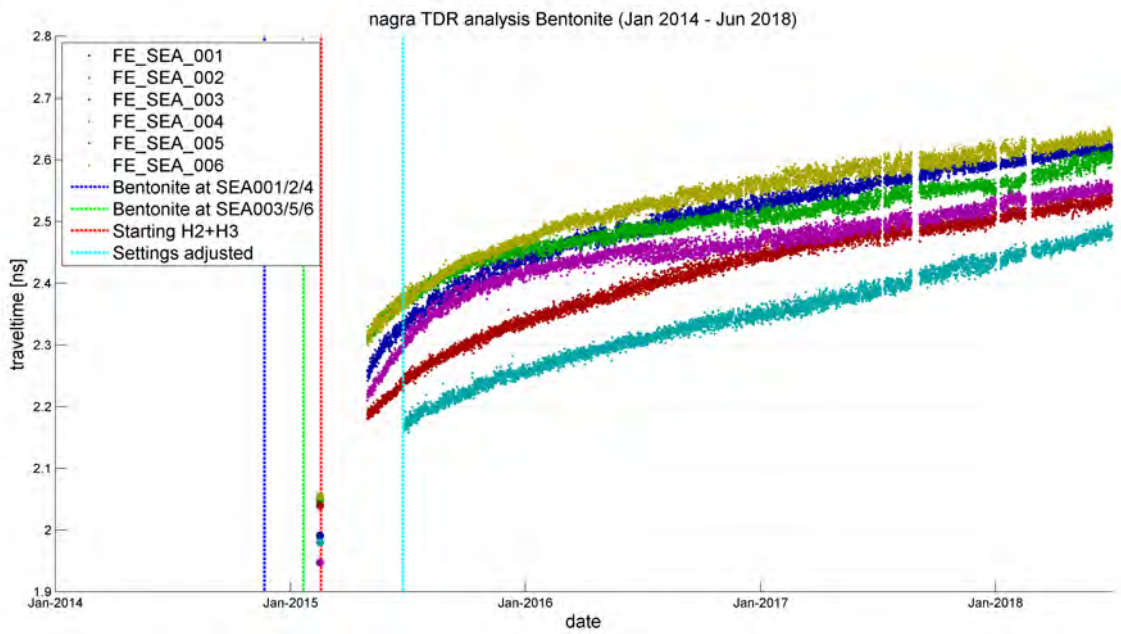


Fig. 6-6: Travel time of TDR probes in bentonite.

This approach is appropriate when the same sensor is used in different materials or when many sensors are used in the same material. In case each sensor is placed permanently in one location surrounded by a material with varying properties, the effect of individual sensor production needs to be addressed in addition. Therefore, two main calibration campaigns have been executed.

In the first campaign, all individual sensors have been measured using the standard homogeneous materials: air, water, dry and saturated glass beads and referenced to the reference probe. The second campaign focused the calibration of the reference probe for variations of water content at different temperature levels. This approach allows for a cost-effective calibration of all installed sensors.

### 6.3.2 Cable length calibration

Due to various positions of the TDR probes in rock and bentonite in the FE experiment, the length of the feeding coaxial cable varies (Tab. 6-2). The length of the feeding coaxial cables changes the shape of the travelling pulse because of its attenuation. The reflection of the pulse becomes smoother when the length of the coaxial cable increases (Fig. 6-7). This influences the determination of travel time because the graphical method uses tangents through the slope of the reflections to identify the beginning and end of the sensor. The calibration measurements were, therefore, executed using different lengths of coaxial feeding cable (5m, 25m, and 31m).

Tab. 6-2: Feeding coaxial cable length (including multiplexer path)

<b>Probe name</b>	<b>Cable length (m) mean value</b>	<b>Variability of cable length (m)</b>
BFEB017_SEA_01~04	25.8	25.77 – 25.81
BFEB018_SEA_01~04	24.9	24.82 – 25.05
BFEB019_SEA_01~04	27.7	27.63 – 27.70
BFEB020_SEA_01~04	33.3	33.20 – 33.40
BFEB021_SEA_01~04	32.8	32.77 – 32.91
BFEB022_SEA_01~04	35.3	35.29 – 35.37
FE_SEA_01	31.1	
FE_SEA_02	35.6	
FE_SEA_03	26.1	
FE_SEA_04	26.7	
FE_SEA_05	22.0	
FE_SEA_06	26.4	
Average of all	29.5	Used as reference cable length

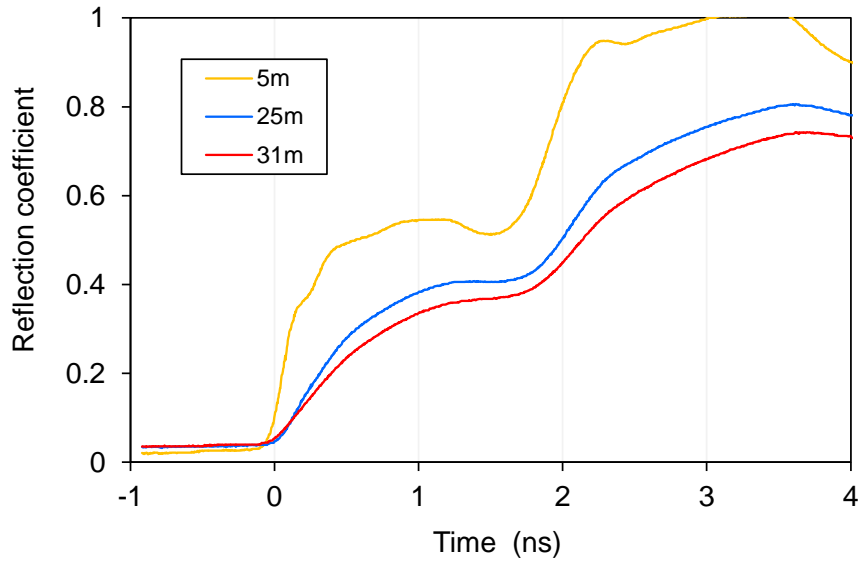


Fig. 6-7: Effect of the feeding coaxial cable length on the TDR traces (dry Opalinus Clay).

To simplify the calibration development, the cable length dependency was eliminated by correcting to reference length of 29.5 m (mean value of all cable length according to Tab. 6-2). Therefore, the travel time value measured for each probe ( $T_{meas}$ ) was normalized ( $T_{norm}$ ) to 29.5 m. A linear relation between cable length and individual travel time was used for the correction:

$$T_{norm} = T_{meas} + 0.01 * (29.5 - L_{meas}) \quad \text{Equation 6-2}$$

$$T_{norm} = T_{meas} + 0.01 * (29.5 - 0.8 * c_0 * T_{coax}) \quad \text{Equation 6-3}$$

where:  $L_{meas}$  represents the actual length of the coaxial cable.

This value represents the total length of feeding line (including all connected coaxial cables + all multiplexers). In travel time determination, the coaxial travel time,  $T_{coax}$  is used instead of constant cable length from a table. The coaxial cable H-155 has a nominal velocity of propagation of 80 % of speed of light  $c_0$ . This coaxial travel time is calculated for every individual TDR trace.

### 6.3.3 Correction to the reference probe

In order to compare the individual sensor that is used in the field to the *reference sensor* (Fig. 6-8) that has been used for laboratory measurements, a linear transformation is applied using air and water calibration measurements:

$$T_{ref} = a_i * T_{norm} + b_i \quad \text{Equation 6-4}$$

where,  $T_{ref}$  is the normalized travel time of the reference sensor,  $T_{norm}$  is the normalized travel time of the individual field sensor,  $a$  and  $b$  are fitting coefficients, and  $i$  is the sensor ID.

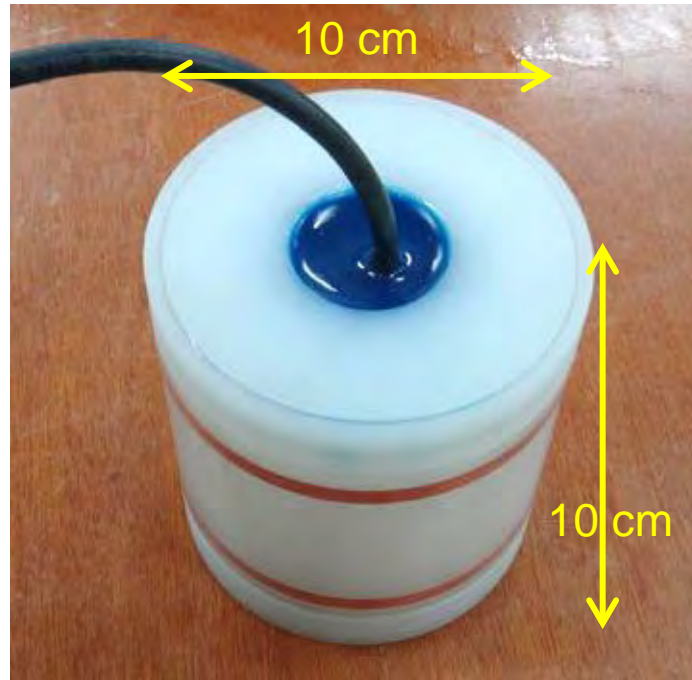


Fig. 6-8: Reference sensor used for material calibration.

The reference sensor was tested in a specific material using different porosity, water content and temperature conditions. These investigations are very time consuming and were executed at Okayama University, Japan for two materials; Opalinus Clay (see chapter 6.3.4) and granulated bentonite (see chapter 6.3.5).

Tab. 6-3: Schematic sketch of the transformations from individual measured travel time to material specific volumetric water content.

Campaign 1: sensor calibration		Campaign 2: Opalinus Clay calibration		Campaign 3: bentonite calibration	
	coaxial calibration (cable length correction)		sensor calibration (sensor-to-sensor-variability correction)		Material + temperature calibration
$T_{meas}$ <i>individual travel time</i>	→ (29.5 m)	$T_{norm}$ <i>normalized travel time</i>	→ to sensor used in laboratory	$T_{ref}$ <i>reference travel time</i>	→ $\Theta_v$ <i>water content</i>

### 6.3.4 Calibration for Opalinus Clay

19 out of 30 sensors are located in Opalinus Clay. Tab. 6-4 summarizes the laboratory test results for the samples taken from the FE TDR boreholes. The results indicate that Opalinus Clay in the measurement sections has a porosity of ~18% and is nearly or fully saturated.

### 6.3.4.1 TDR trace acquisition under varied water content

The first material calibration was done for Opalinus Clay under various water content and temperature conditions. The reference sensor was installed in a block of Opalinus Clay with a borehole of the same size that was used in the field installation (Fig. 6-9). The size of the block was determined to fully contain the sampling volume of the sensor within the block. The annulus has been filled with grout to create the same conditions as in the field. After the grout has hardened, several TDR measurements were executed during drying process (air dried) to observe the different states of water content. Tab. 6-5 shows the selected water content states.

Tab. 6-4: Material characterization from FE TDR borehole samples (located in Opalinus Clay and shotcrete) to identify parameter range for calibration campaign

Borehole ID	sample no.	TDR center position (cm)	grain density (Mg/m <sup>3</sup> )	bulk density (Mg/m <sup>3</sup> )	dry density (Mg/m <sup>3</sup> )	mass water content (%)	void ratio	porosity	saturation (%)	vol. water content (%)	remark
BFEB017	1	105	2.76	2.45	2.31	6.30	0.19	0.16	89.50	14.50	
	2	75	2.76	2.43	2.26	7.70	0.22	0.18	96.10	17.30	
	3	45	2.75	2.42	2.25	7.70	0.22	0.18	95.60	17.40	
	4	15	2.77	2.43	2.26	7.40	0.22	0.18	91.90	16.70	
BFEB018	1	104	2.74	2.43	2.26	7.60	0.21	0.18	97.30	17.20	
	2	74	2.78	2.43	2.26	7.80	0.23	0.19	92.50	17.50	
	3	44	2.80	2.43	2.25	7.80	0.24	0.19	90.10	17.50	
	4	14	2.74	2.17	1.97	9.90	0.39	0.28	69.70	19.40	shotcrete
BFEB019	1	105	2.73	2.46	2.31	6.60	0.18	0.15	99.60	15.30	
	2	75	2.74	2.50	2.37	5.50	0.16	0.14	96.20	13.10	
	3	45	2.73	2.44	2.27	7.40	0.20	0.17	100.00	16.90	
	4	15	2.72	2.12	1.91	11.50	0.43	0.30	73.20	21.80	shotcrete
BFEB020	1	110	2.75	2.45	2.28	7.50	0.21	0.17	98.70	17.00	
	2	80	2.78	2.45	2.28	7.40	0.22	0.18	93.90	16.80	
	3	50	2.79	2.43	2.25	7.80	0.24	0.19	90.20	17.40	
	4	20	2.76	2.17	1.97	10.00	0.40	0.29	68.80	19.70	shotcrete
BFEB021	1	109	2.74	2.39	2.21	8.30	0.24	0.20	94.20	18.40	
	2	79	2.73	2.41	2.23	8.20	0.23	0.18	100.00	18.40	
	3	49	2.73	2.41	2.23	7.90	0.22	0.18	96.80	17.60	
	4	19	2.77	2.18	1.94	11.90	0.43	0.30	77.80	23.20	shotcrete
BFEB022	1	108	2.77	2.44	2.26	7.70	0.22	0.18	96.20	17.50	
	2	78	2.78	2.43	2.26	7.70	0.23	0.19	93.40	17.40	
	3	48	2.78	2.44	2.26	7.60	0.23	0.18	93.60	17.20	
	4	18	2.71	2.20	1.99	10.80	0.36	0.27	80.60	21.50	shotcrete
<b>mean</b>			<b>2.76</b>	<b>2.44</b>	<b>2.27</b>	<b>7.47</b>	<b>0.216</b>	<b>0.177</b>	<b>95.04</b>	<b>16.90</b>	<b>rock</b>
<b>mean</b>			<b>2.74</b>	<b>2.17</b>	<b>1.96</b>	<b>10.82</b>	<b>0.402</b>	<b>0.288</b>	<b>74.02</b>	<b>21.12</b>	<b>shotcrete</b>

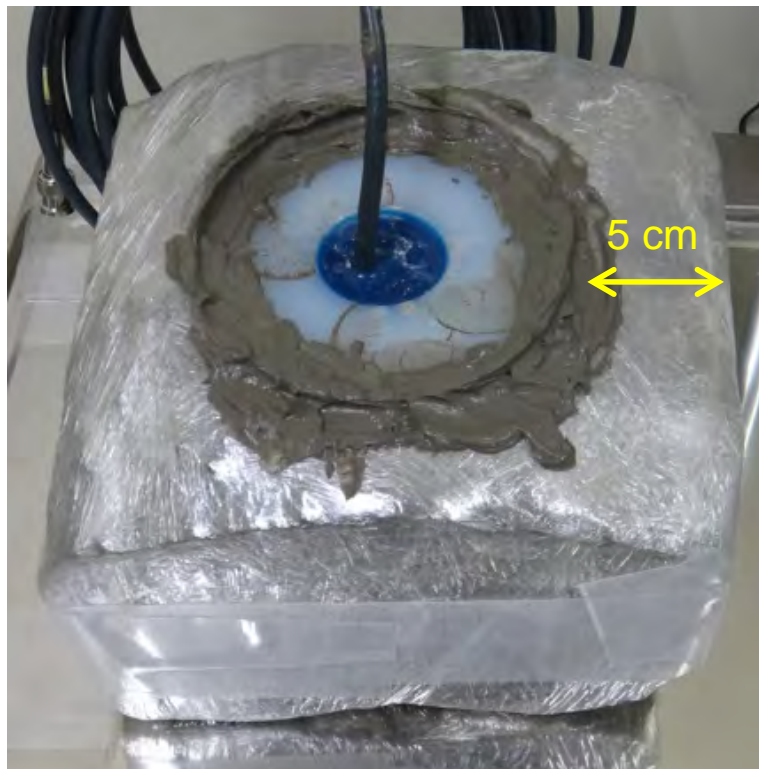


Fig. 6-9: Reference calibration sensor installed in the calibration block.

Tab. 6-5: Variations in water content and temperature during Opalinus Clay calibration campaign

days after grout	Saturation (%)	vol. water content (%)	Temperature (°C)
9	93.2	15.2	17.9
17	78.7	12.8	18.7
28	60.1	9.8	15.8
39	47.7	7.8	13.1
56	23.4	3.8	12.3
65	0.0	0.0	60.0
66	0.0	0.0	40.0
67	0.0	0.0	20.0
69	0.0	0.0	11.5

### 6.3.4.2 TDR trace acquisition under varied temperature

The temperature was varied in the dry state of Opalinus Clay block. For the saturated state, the data from the field was used as described below. The dielectric parameters of water are known to depend highly on temperature. Therefore, two-dimensional relation between travel time and water content at various temperatures need to be established.

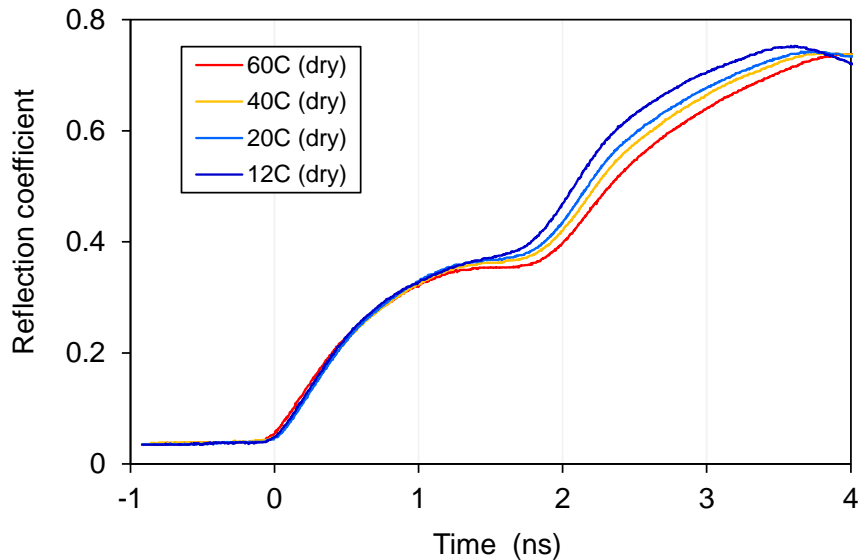


Fig. 6-10: TDR traces obtained for dry Opalinus Clay block under varied temperatures.

Under the assumption that the Opalinus Clay in the FE experiment is saturated before the heaters have been started (17.02.2015) and will stay saturated for some time during heating up procedure, these measurements can be used to complete the calibration data base. Due to the heavy construction works, the DAS was temporarily removed and the first evaluable measurements in Opalinus Clay were started in July 2015. Thus, the initial period where the temperature significantly increased was left out. Important to note that the temperature range for this additional calibration data set varies depending on sensor position, i.e., higher temperature was expected around the heaters whereas lower in between the heaters.

In the following, the calibration procedure is described using rock sensor BFEB017.

When the temperature increases, the relative dielectric permittivity of free water decreases (see Fig. 6-11) which makes a travelling pulse faster. Therefore, the resulting travel time should decrease. Our measurements, however, showed that the travel time increased indicating that an additional effect overlaid the dielectric property change. This behaviour was also observed in dry condition when temperature changed from 60°C to 11.5 °C. The cause for this effect has not been investigated further to date. Still, the temperature-to-travel time relation can be incorporated to optimize the water content determination procedure.

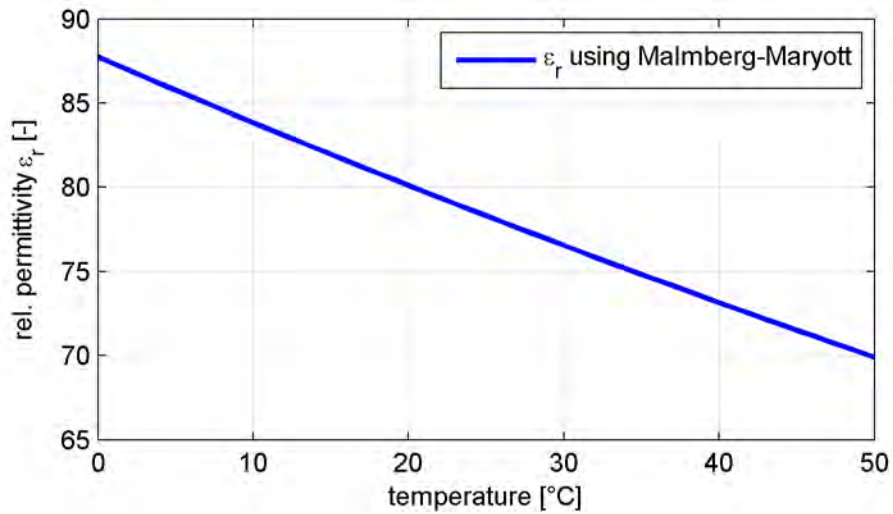


Fig. 6-11: Relative dielectric permittivity of water depending on temperature

Fig. 6-12 shows the relationship between temperature and reference travel time  $T_{ref}$  for sensor BFEB017\_SEA\_01. An empirical regression function was fitted to correlate the temperature to travel time. Under the assumption that the water content did not change during this period, the increase in travel time results only from the increase in temperature.

**Two-point α-mixing model**

To describe the volumetric water content (VWC), two-point α-mixing model was used. The travel time of a partially saturated material lies between the travel time for dry and saturated states. The model delivers values between 0 (dry condition) and 1 (saturated condition) that is to be multiplied with the porosity to yield VWC. The fitting parameter α has been determined via fitting to the laboratory measurements with different volumetric water conditions as described below:

$$\theta_v = n * \frac{T_{ref}^\alpha - T_{dry}^\alpha}{\underbrace{T_{sat}^\alpha - T_{dry}^\alpha}_{saturation}} \tag{Equation 6-5}$$

Where:

- $n = 17.7\%$  - Mean field porosity of Opalinus Clay
- $T_{ref}$  = Measured travel time, normalized and transferred to reference sensor
- $T_{dry}$  = Temperature *dependent* travel time in dry Opalinus Clay (from laboratory, see Fig. 6-10 and 6-13)
- $T_{sat}$  = Temperature dependent travel time in saturated Opalinus Clay (from field, see Fig. 6-12)
- $\alpha = 5.033$  - Fitting parameter from water content varying laboratory measurements (5.033 is an overall fitting parameter for all sensors)

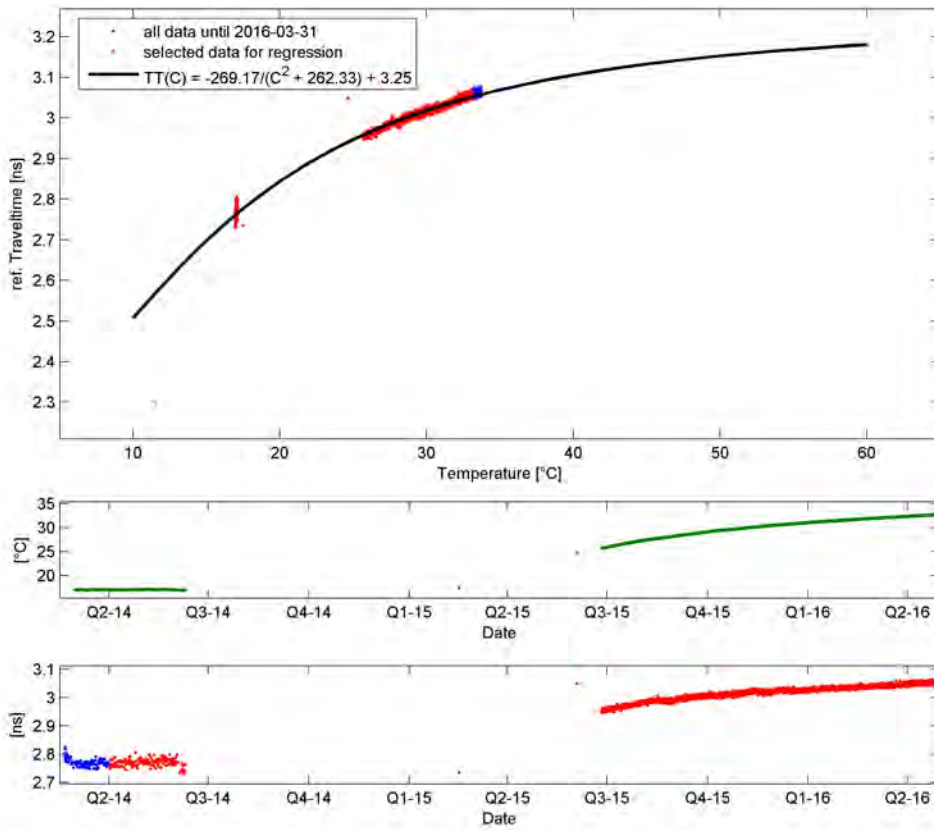


Fig. 6-12: Empirical determination of a temperature to travel time relation for Sensor BFEB017\_SEA\_01 - Rock was assumed to have remained saturated.

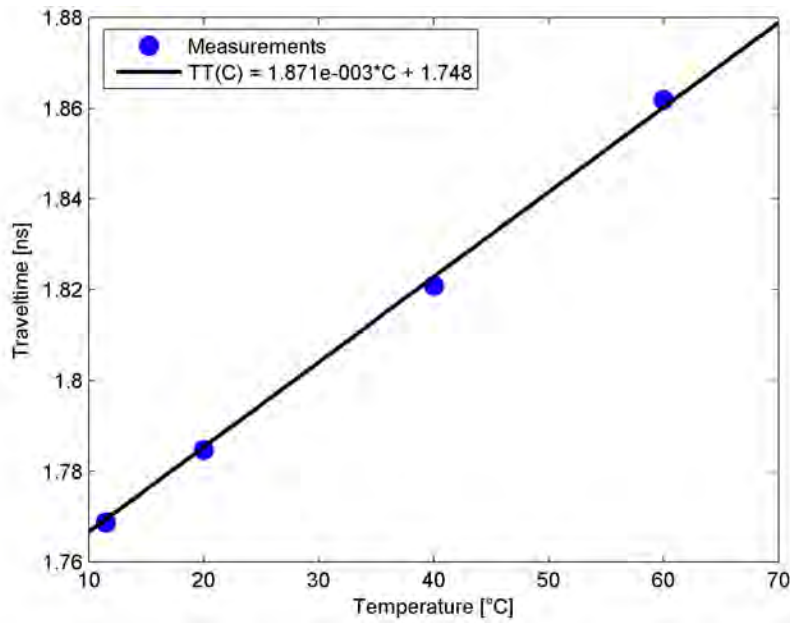


Fig. 6-13: Linear relation between temperature and travel time for dry Opalinus Clay

Based on the data available from the laboratory experiments and field measurements, the two-point  $\alpha$ -mixing model for estimating water content in Opalinus Clay under different temperature was developed as below:

- Travel time under varied water content in Tab. 6-5 were indeed obtained at temperatures between 11.5 and 18.7 °C. These values were corrected to 11.5 °C.
- The corrected travel time (green solid circles in Fig. 6-14) as well as the field saturated travel time (green \* in Fig. 6-14, also corrected to 11.5 °C) were used to compute the  $\alpha$  value that best describes the travel time – water content relationship. The best fit  $\alpha$  value was found to be 5.033.
- It was assumed that  $\alpha = 5.033$  would also apply for higher temperatures up to 60 °C.
- $T_{dry}$  and  $T_{sat}$  values, e.g., at 20, 40 and 60 °C available from the laboratory experiments and field measurements were used to develop two-point  $\alpha$ -mixing model at these temperatures as shown in Fig. 6-14.
- For other intermediate temperatures,  $T_{dry}$  and  $T_{sat}$  values were estimated using the temperature correction equation provided in Fig. 6-13 (dry) and Fig. 6-12 (saturated, BFEB017\_SEA\_01, other sensors not shown here), with which two-point  $\alpha$ -mixing model at arbitrary temperatures were established with  $\alpha = 5.033$ .

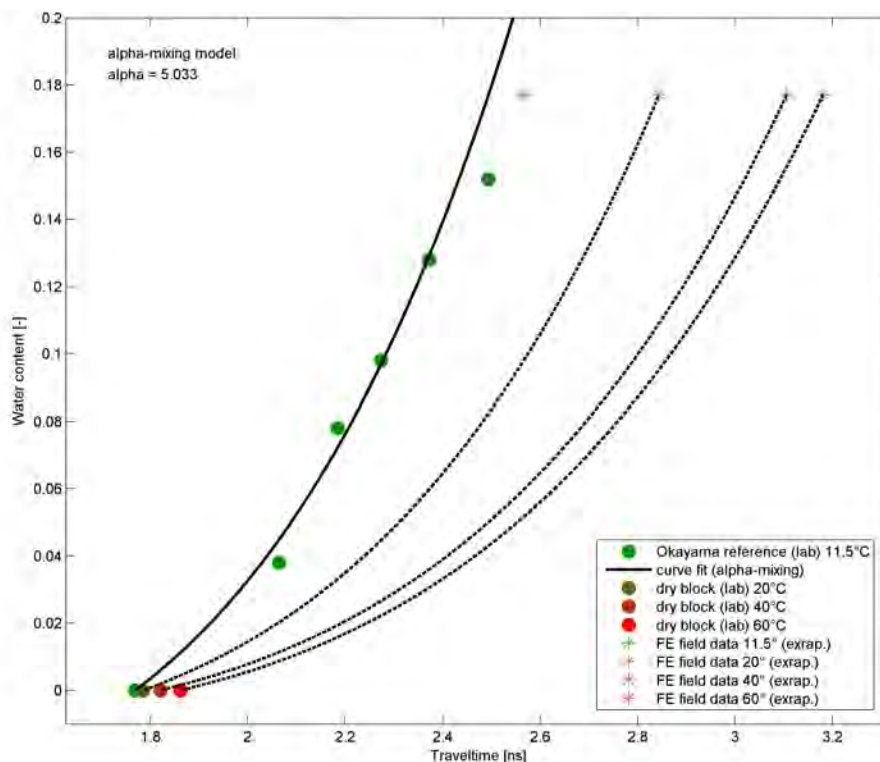


Fig. 6-14: Alpha-mixing model for sensor BFEB017\_SEA\_01 to describe relation between reference travel time and volumetric water content using additional temperature information (Sensor BFEB017\_SEA\_01).

Note: Each line (solid or dotted) represents a mixing model for a given temperature (11.5, 20, 40, 60 °C). To transform travel time into water content an individual mixing model parameter set must be derived for each temperature.

Using this model, the travel time measurements can be transformed into volumetric water content. Fig. 6-15 shows the water content for the initial measurements in Opalinus Clay (full saturation; water content equals mean global porosity).

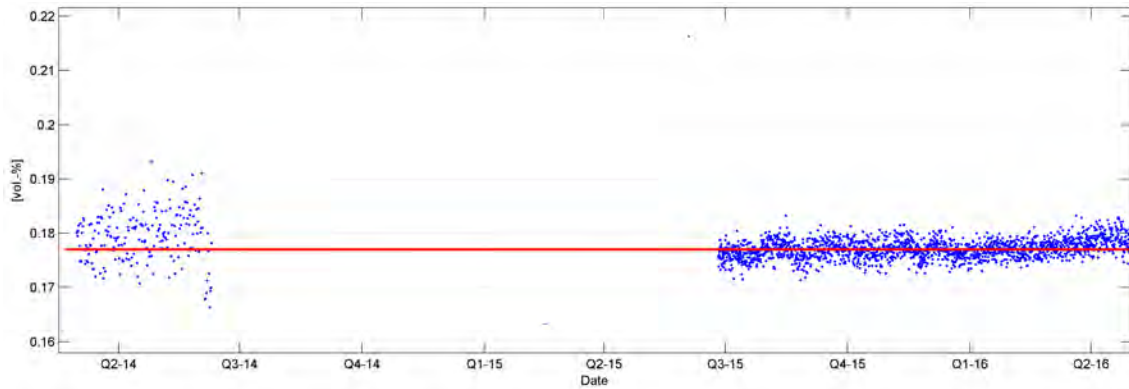


Fig. 6-15: Volumetric water content calculation using the initial data used for calibration (showing full saturation; Sensor BFEB017\_SEA\_01)

### 6.3.5 Calibration for bentonite

Six sensors are located in the bentonite sealing (FE\_SEA\_001 to FE\_SEA\_006). To calibrate these sensors to volumetric water content additional measurements were executed using the same reference sensor as used in the previous chapter. Traces were obtained under different water content conditions and different temperatures, with cable length of 5, 19, 25 and 31 m. Tab. 6-6 shows 6 cases. Case 0 to case 5 with different water content that deliver reliable results for sensor calibration. An additional case with saturated condition (case 6) performed separately. This one was excluded from further analysis because the travel time data show unexpected behaviour.

Tab. 6-6: FE bentonite TDR calibration data generation

Case no.	Water content (g/g)	Dry density (g/cm <sup>3</sup> )	Porosity	Vol. water content (%)	Saturation (%)	Remark
case 0	0.000	1.52	0.45	0.00	0.000	Oven dried after case 5 min DD achieved was 1.52
case 1	0.057	1.40	0.49	0.08	0.164	
case 2	0.109	1.40	0.49	0.15	0.311	
case 3	0.170	1.35	0.51	0.23	0.453	Not able to achieve DD 1.4
case 4	0.247	1.31	0.52	0.32	0.620	Not able to achieve DD 1.4
case 5	0.305	1.33	0.52	0.41	0.785	Not able to achieve DD 1.4
case 6	0.352	1.40	0.49	0.49	0.998	separately performed Extremely difficult Travel time seemed faster (Discard this case)

The tests from Tab. 6-6 were executed in the following order:

- Case 1 → 2 → 3 → 4 → 5 by adding water stepwise
- Case 0 after oven drying,
- Case 6 was done separately.

Within each case the temperature was changed as: 18 - 25 - 30 - 35 - 40 - 45 - 50 - 55 - 60 - 20. The last 20 °C measurements typically showed effect of material shrinkage (fast travel time, thus, discarded the data). The target dry density was set to 1.4 g/cm<sup>3</sup> (value expected around the bentonite TDR sensors). In the case 0 (oven-dried), it was not possible to pack the bentonite as loose as 1.4. In other cases, dry density ended up somewhat lower (to avoid damage to the probe/container during compaction).

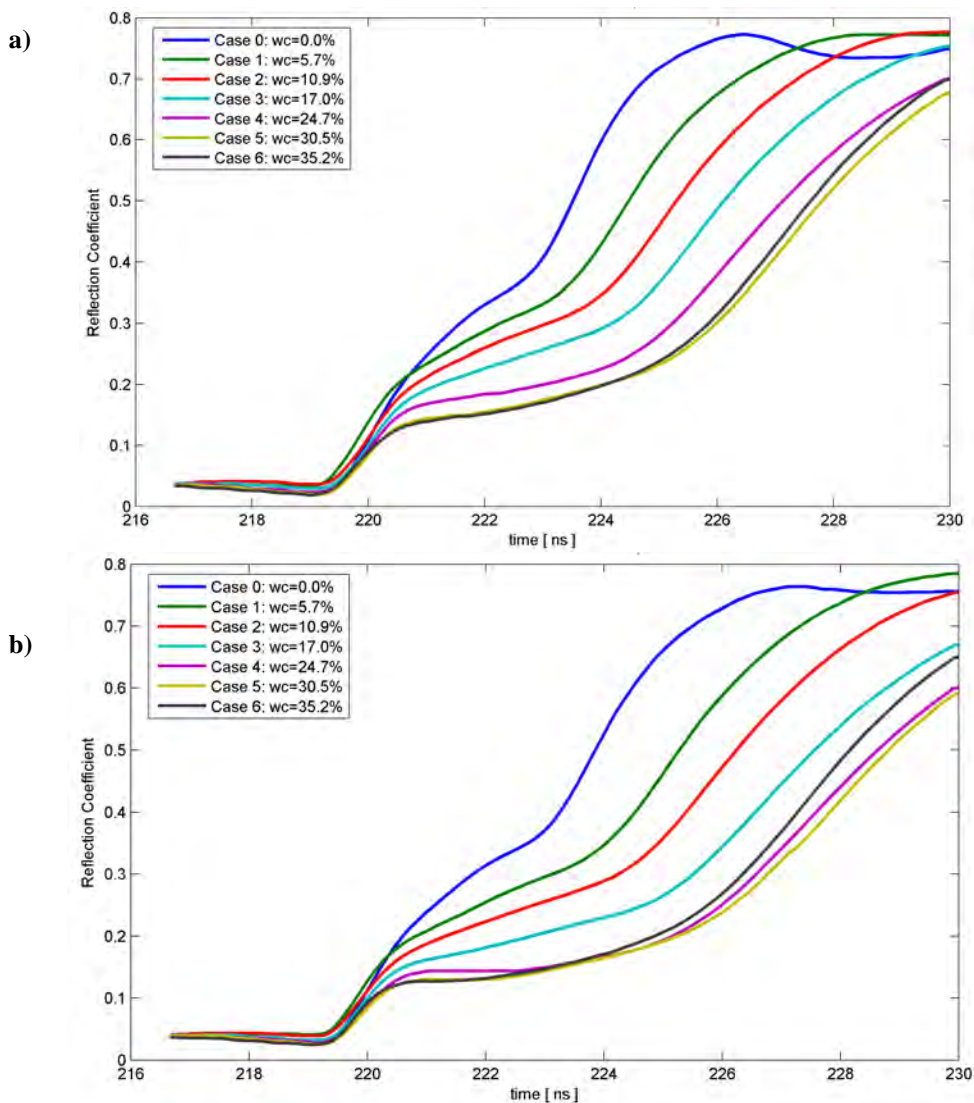


Fig. 6-16: Comparison of TDR traces in bentonite with different water content (Cable length = 25 m - Temperatures 18°C (a) and 60°C (b).

Note: Case 6 (full saturation) shows unusual behaviour (shorter travel time than non-saturated state) and was therefore excluded from further analysis.

Direct application of the  $\alpha$ -mixing model to the bentonite calibration data resulted in an insufficient match of laboratory measurement and interpolated data. Instead of  $\alpha$  mixing model, an empirical approach was used to describe the relation between travel time and volumetric water content at a given temperature  $T$ . The best results were achieved using an exponential function with temperature dependent parameters  $a$ ,  $b$  and  $c$ .

$$\theta_v(T) = \frac{e^{(T_{ref}-a(T))-b(T)}}{c(T)} \quad \text{Equation 6-6}$$

where:

$$a(T) = 0.00817 \cdot T + 2.83$$

$$b(T) = -0.00156 \cdot T + 0.33$$

$$c(T) = 0.00417 \cdot T + 1.62$$

The linear dependency of  $a$ ,  $b$  and  $c$  was verified by determination of all fitting parameters for temperatures between 18°C and 60°C. Fig. 6-17 shows the individual fitting parameters and the temperature dependency of  $a(T)$ ,  $b(T)$ , and  $c(T)$ .

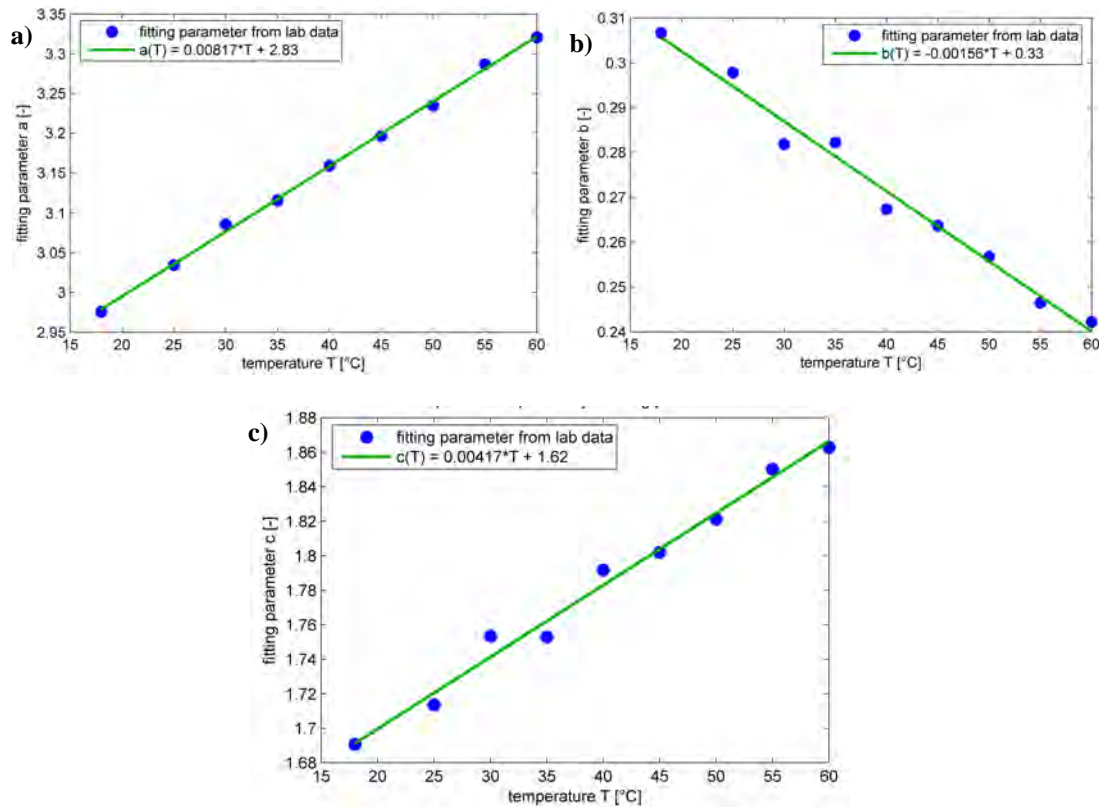


Fig. 6-17: Linear regression of transformation parameters  $a$  (a),  $b$  (b) and  $c$  (c) within the exponential travel time to water content transformation.

Fig. 6-18 shows the transformation from travel time to volumetric water content for sensor FE\_SEA\_001. This transformation will be used in further water content analysis. The transformations for the other bentonite sensors are done in a similar way. Each sensor has an individual set of transformation parameters. Note that volumetric water content can be estimated from travel time for any temperature between 15 and 60 C.

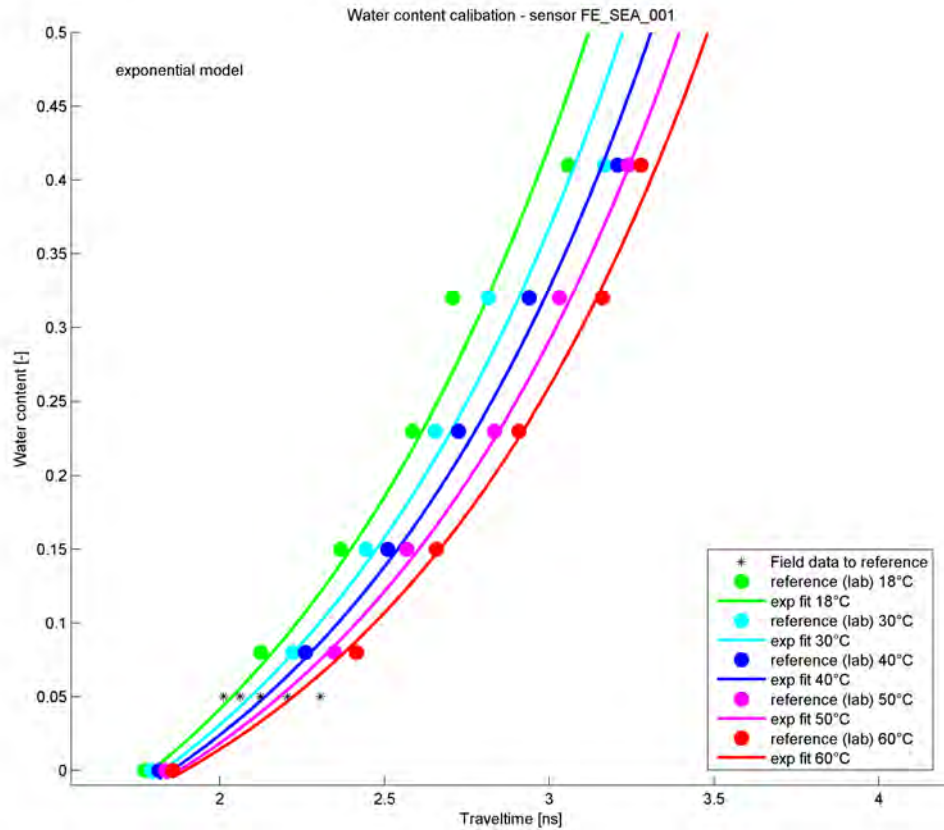


Fig. 6-18: Exponential model for sensor FE\_SEA\_001 to describe relation between reference travel time and volumetric water content using additional temperature information.

Note: The field data (\*) are those during the early phase where the temperature increased, whereas the moisture was assumed to have remained constant.

### 6.4 Water content

In this section, the travel time data obtained with the rock and bentonite TDR sensors in FE experiment were converted into volumetric water content using the  $\alpha$ -mixing model for the rock sensors, and the temperature-dependent exponential calibration function for the bentonite sensors.

Water content values for the Opalinus Clay rock probes BFBE017 – BFBE021 and granular bentonite sensors FE\_SEA01-06 are plotted in Fig. 6-19 until Fig. 6-25 for the time period from April 2014 until May 2018. The data from sensors located in shotcrete are not shown in the plots as these sensors have not been calibrated for water content variations as a function of temperature.

The periodic data losses after June 2017 are an artefact from the communication between the data recorder and the data acquisition system and will be solved in future.

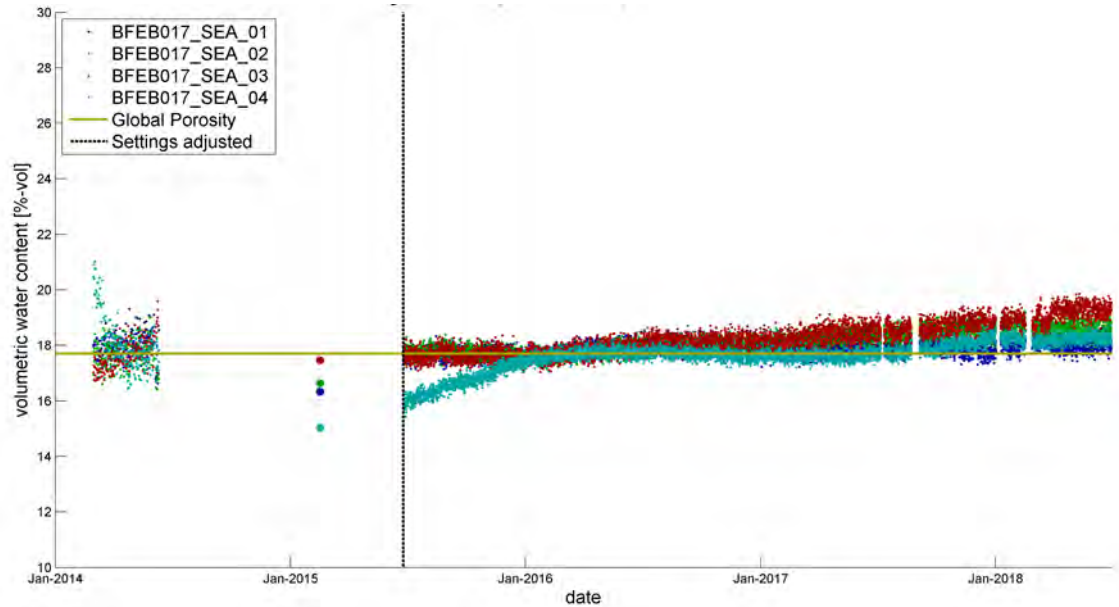


Fig. 6-19: Water content at TDR probes at rock sensor BFEB017 - TDRs 01-04 are in Opalinus Clay (Jan. 2014 – Jun. 2018).

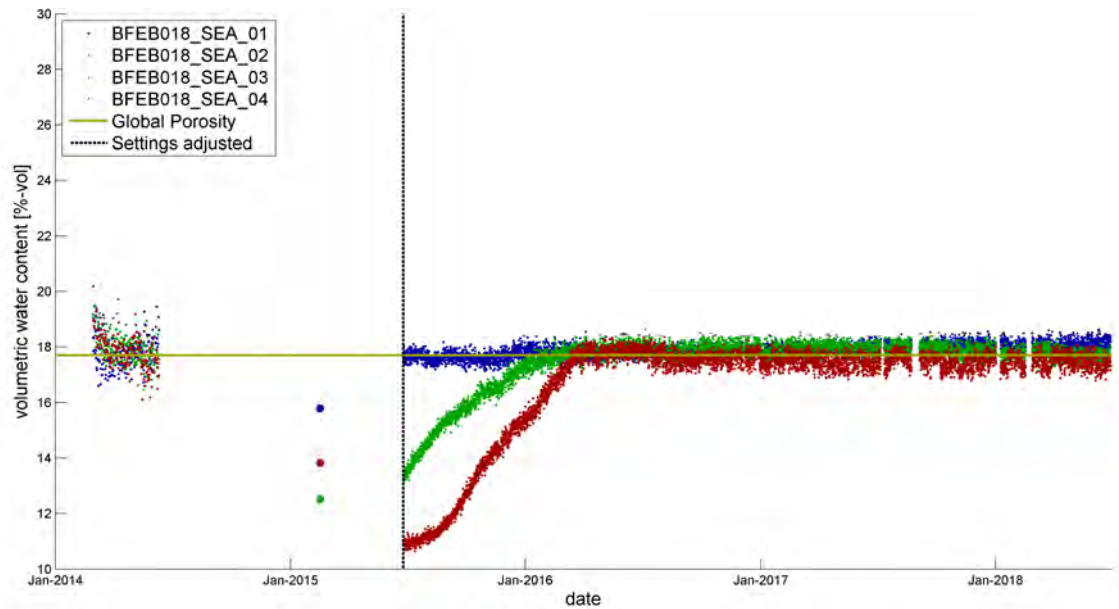


Fig. 6-20: Water content at TDR probes at rock sensor BFEB018 (Jan. 2014 – Jun. 2018).

Note The TDR's 01-03 are located in the Opalinus Clay, whereas the TDR 04 is located in the shotcrete. Due to the lack of data in the severe non-linearity in the travel time – temperature relationship, the data after the DAS unit installation could not be properly converted to full saturation.

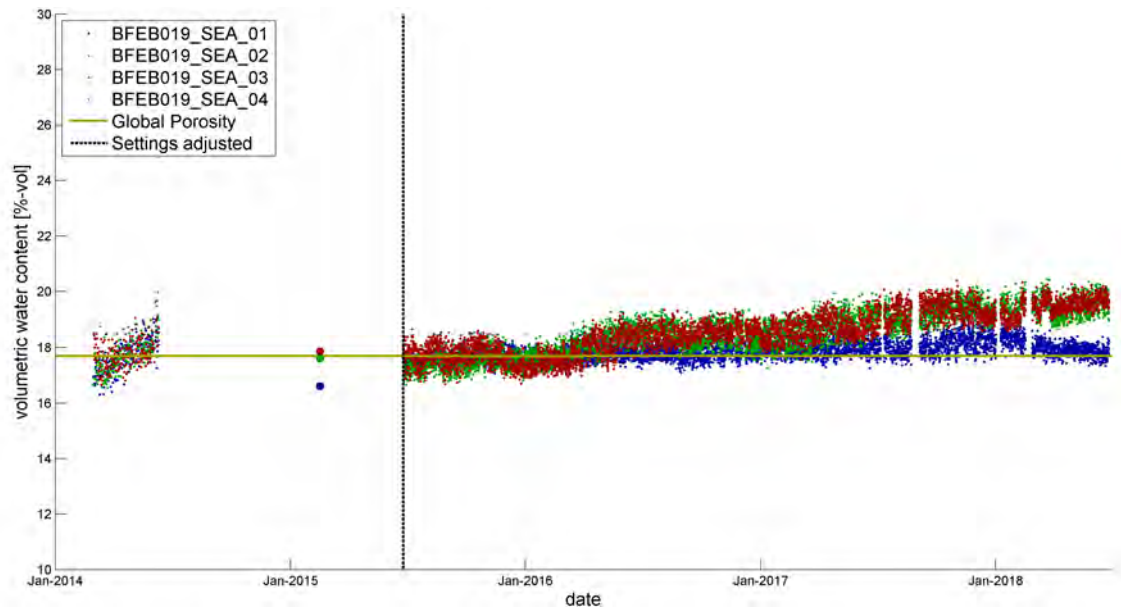


Fig. 6-21: Water content at TDR probes at rock sensor BFEB019 (Jan. 2014 – Jun. 2018).

Note: The TDR's 01-03 are located in the Opalinus Clay, whereas the TDR 04 is located in the shotcrete and is not converted to a water content.

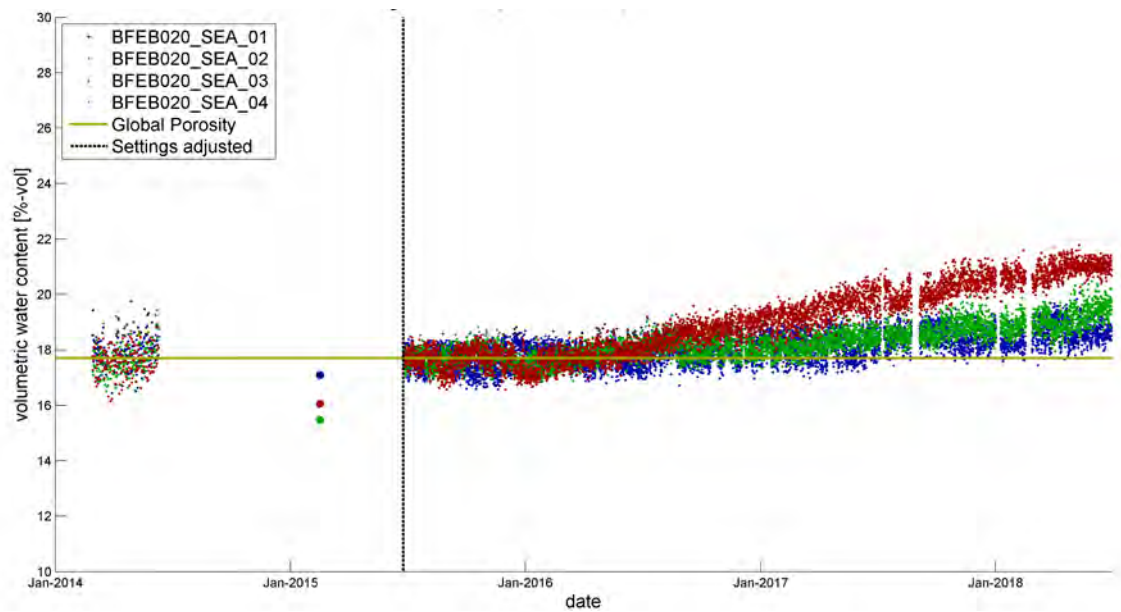


Fig. 6-22: Water content at TDR probes at rock sensor BFEB020 (Jan. 2014 – Jun. 2018).

Note: The TDR's 01-03 are located in the Opalinus Clay, whereas the TDR 04 is located in the shotcrete and is not converted to a water content.

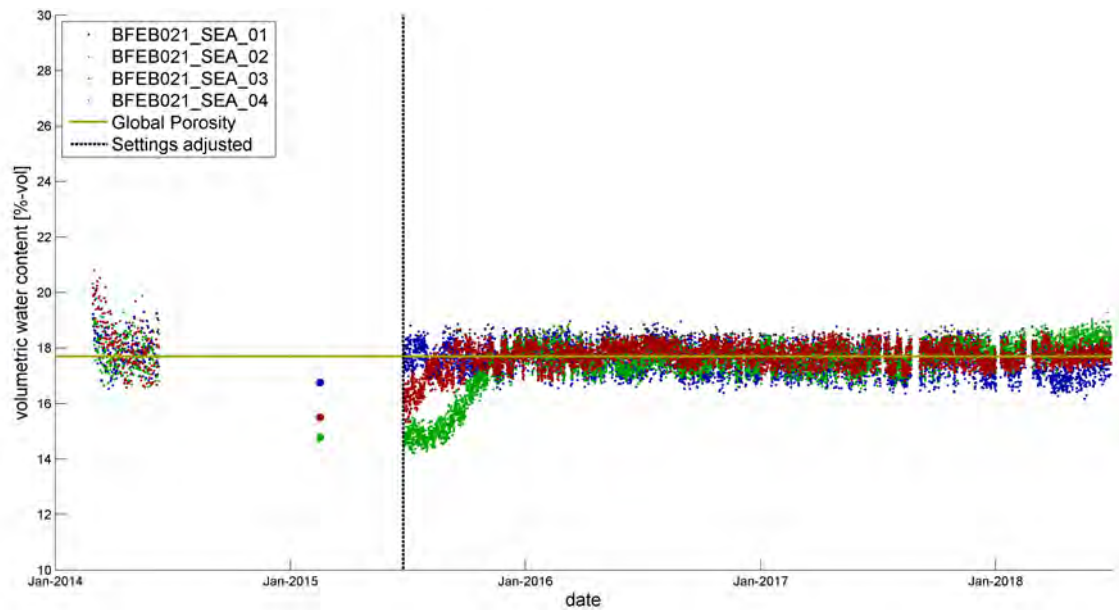


Fig. 6-23: Water content at TDR probes at rock sensor BFEB021 (Jan. 2014 – Jun. 2018).

Note: TDR's 01-03 are located in the Opalinus Clay, whereas the TDR 04 is located in the shotcrete and is not converted to a water content. Due to the lack of data in the severe non-linearity in the travel time – temperature relationship, the data after the DAS unit installation could not be properly converted to full saturation.

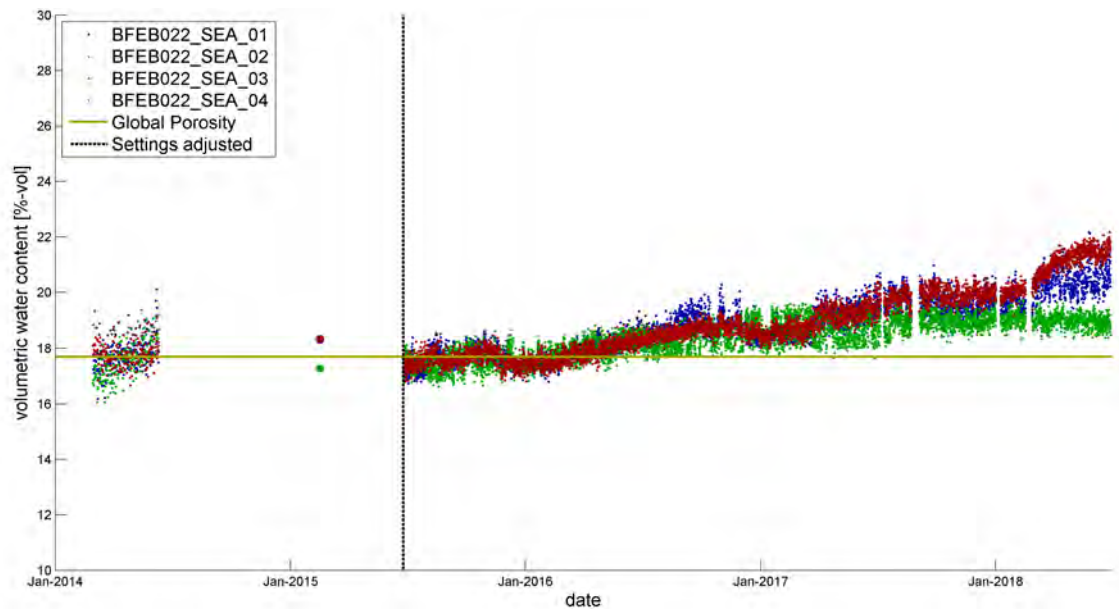


Fig. 6-24: Water content at TDR probes at rock sensor BFEB022 (Jan. 2014 – Jun. 2018).

Note: TDR's 01-03 are located in the Opalinus Clay, whereas the TDR 04 is located in the shotcrete and is not converted to water content.

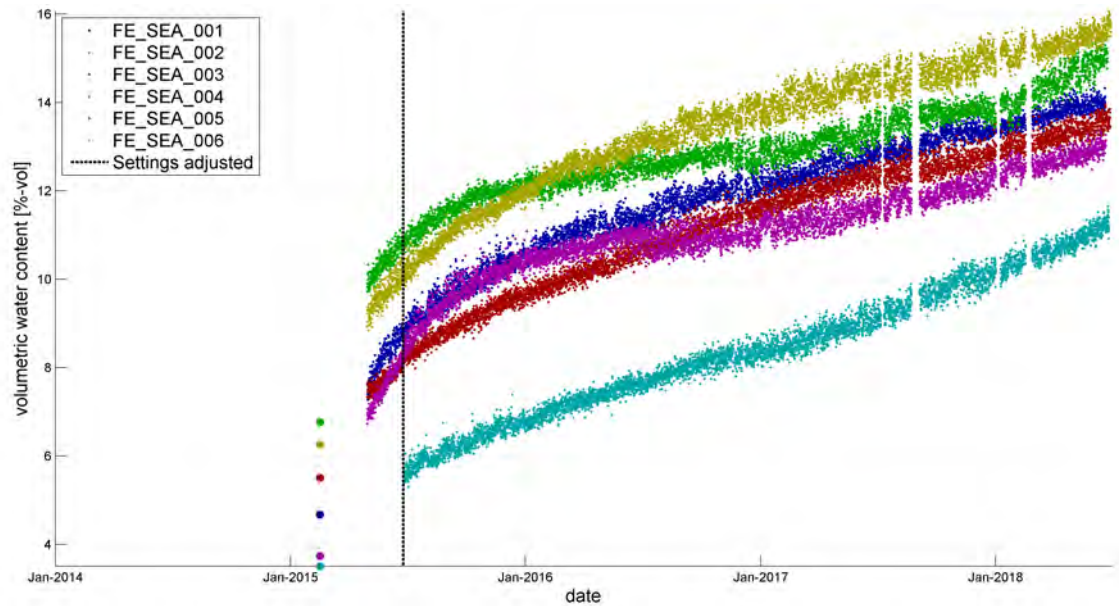


Fig. 6-25: Water content at TDR probes at bentonite sensor FE\_SEA (Jan. 2014 – Jun. 2018).

## 6.5 Summary and results

The observation made during the TDR-measurement period are summarized and lead to the following results so far:

- At all measurement locations of the six rock probes, the water content equals the global porosity of the Opalinus Clay (~18 %). Hence, full saturation at all locations is reached in April 2016 latest, about four years after FE tunnel construction and about one year after backfilling.
- The TDR sensors close to the tunnel wall show the longest re-saturation time. The main part of re-saturation phase could not be monitored due to the lack of monitoring in the backfilling phase.
- At certain locations, the saturation reaches values above the global porosity with increasing trend. This might be an effect of locally high porosity, potentially in combination with the vicinity of a wet spot.
- In contrast to Opalinus Clay, the saturation process in bentonite is steadily ongoing. All bentonite probes show an approximately linear trend preceded from an initially steeper trend of saturation increase.
- Saturations between 9 and 15 % have been reached, where the lowest value is measured in the cold section between the heaters at the bottom of the tunnel. A possible explanation for this difference is the higher quality of shotcrete at the tunnel bottom accompanied by a lower transmissibility of this shotcrete layer.
- In general, saturation above heater locations (hot sections) are higher than saturation determined from the two bentonite sensors in the cold section.

## **7 Conclusions**

### **7.1 Fibre optic monitoring**

#### **7.1.1 Installation and documentation**

At design stage of the project it can be beneficial to plan sufficient cable meter reserves, especially for use in calibration baths but also for other testing purposes. Alternatively, FO cables can be extended using splices, but this option includes a loss of light across the connection. Cable reserves should be foreseen between interrogator and measuring object, both for the outbound routing and the cable return.

The interrogators mainly in operation (Neubrex and Smartec) proved to be reliable over the four years monitoring period, even at elevated internal device temperature (Smartec). One of the major factors to assure smooth operation of them is to isolate the DTS devices from dust. The air-tight sealing of the cabinets containing the devices hampers the cooling of the devices. Therefore, additional cooling devices should be foreseen to keep the instruments temperature on an acceptable level.

The FO cable routing should be documented meticulously. Ideally, the x,y,z coordinates of each cable are measured at short spatial intervals and corresponding cable meter positions are determined. The density of georeferencing points along the cable should be adjusted in dependency of the curviness. Cable length positions are to be confirmed by fingerprinting at a sufficient number of heating/cooling spots along the cable. The use of an interrogator with a good (small) spatial resolution improves the precision of fingerprinting work significantly.

#### **7.1.2 FO cable selection**

Proper FO cable selection is crucial and must be adapted to expected environment. Under repository like conditions durable and robust FO cables are necessary, although sensitivity for strain measurements is reduced if a very stiff cable is used.

Lose tube buffering proved to be a reliable FO cable concept for DTS measurement at the FE experiment. The measurements of the only FO cable without this feature (e.g. AFL cable) were partially compromised by strain on the fibre.

#### **7.1.3 Dynamic (real-time) calibration**

The implementation of permanent calibration baths in combination with independent dynamic calibration of each DTS measurement increased greatly the precision of the DTS measurements. The difference between corrected and uncorrected measurements was important (several degrees °C) especially for the upper part of the temperature range experienced during the project.

The dynamic calibration also proved to be robust, i.e. unaffected by external impacts such as bath refill using cold water and system re-start after power failure. In addition, it provides good calibration results also for a cable of inferior quality and varying attenuation (e.g. AFL cable).

#### **7.1.4 Selection of interrogator**

The scientific nature of the FE experiment, the relatively large measuring range (~ 18 to 65 °C) and the long monitoring period of > 10 years pose high demands on the DTS device: robustness, stability, measurement accuracy and spatial resolution. When comparing the Smartec DiTemp data (1.02 m sampling and spatial resolution) with those of a Silixa Ultima S (0.127 m sampling resolution and 0.254 spatial resolution) across the calibration baths it became evident that the Smartec DiTemp unit fails to reproduce abrupt temperature changes. Also, the heat bumps with spatial temperature gradients of 3 - 8 °C per meter across the heaters are reproduced inaccurately and with much less detail compared to the Silixa temperature curves. The calibrated Smartec temperatures differed with respect to the calibrated Silixa temperature by up to 5.5 °C (Brugg Standard cable). For the AFL cable, the maximum observed difference was 8.5 °C.

In the boreholes BFEA010 and BFEA011, the spatial temperature gradients generally do not exceed 1.5 °C per meter. For this application, the Smartec DiTemp did accurately trace the temperature curve with an accuracy of +/- 1.2 °C.

The inaccuracy of the Smartec DiTemp at spatial temperature gradients above 3-4 °C per meter is presumably caused by secondary pulse effects of the incident laser. According the manufacturer, it is due to the technology used to control the light impulses and does not indicate a defect or a set-up issue of the instrument.

Comparing Smartec with Silixa temperature profiles across the heaters makes apparent that the 1.02 m spatial (and sampling-for Smartec) resolution is too large to resolve the present variability of temperature at small scale.

In view of the large temperature gradients of the FE experiment, an exchange of the Smartec Unit against a device with improved spatial resolution and better accuracy is recommended.

#### **7.1.5 Monitoring of cable quality by means of OTDR measurements**

The FE project optical fibres pass through regions with high temperature gradients making detection of step losses by evaluating the Raman Stokes and anti-Stokes signals and R(z) difficult. Step losses were identified using optical time-domain reflectometry (OTDR) that measures the Stokes and anti-Stokes signals at frequencies where ratios are less influenced temperature. Repeated OTDR measurements at regular time intervals aid in the investigation of fibre degrading (darkening of the glass fibre with age) and enable detecting new or quantitatively changed step-losses. For long term DTS monitoring, repeated OTDR measurements are considered as indispensable measure to maintain high quality (step-loss corrected) DTS data.

#### **7.1.6 Data processing and visualization**

Adequate & customisable database & data visualisation system is an important tool facilitating data transfer, system checking/maintenance, data analysis, data export and reporting. The existing FEIS system was extended in the framework of Modern2020 to support these tasks with respect to the FO data. Data base table structures were built for about 1 billion of FO measurements. Measuring positions are calculated automatically based on the specified instruments sampling resolution. The FO FEIS supports the real-time dynamic calibration of the FO data, stores the calibration parameters and calculates the RMSE for the cable sections running through the validation bath. FO data can be viewed together with temperature data of point-type sensors in profiles or as time series. For the straight cable sections across the heaters, the point-type temperature sensors can be selected by specifying the maximum radial distance to the FO cable.

The implemented data management software became an indispensable tool to efficiently check the performance of the system.

Thermal maps showing the evolution of the temperature along the full cable over the time (currently not implemented in FEIS) is also considered as a useful graphical representation to quickly spot any irregularities in recorded DTS data.

## **7.2 TDR monitoring**

As part of the FE Experiment, custom-made Time Domain Reflectometry (TDR) sensors have been installed to monitor the evolution of the water content in bentonite back fill as well as in the Opalinus Clay surrounding the FE excavation tunnel. In total 30 TDR probes have been placed, where 6 are located in bentonite in hot and cold sections and the other 24 are placed at heaters H2 and H3 in a Y-configuration normal, parallel and at a defined angle to the bedding planes.

To reach an optimized accuracy of TDR probes, a calibration hierarchy was developed that relates the individual response of each sensor, influenced by the manufacturing process, to a reference sensor. Subsequently, this reference sensor was used to perform the calibration of travel time vs. water content as a function of temperature. This calibration procedure was successfully applied to the probes in bentonite and Opalinus Clay. The probes located in shotcrete lining could not be evaluated for water content as the calibration was not executed for shotcrete material.

Automated procedures for TDR measurements and data evaluation including travel time picking are implemented successfully and all 12h a measurement is recorded. During the backfilling process of the tunnel, no automated data recording was feasible and hence, the main periods of measurements are before backfilling (until Feb. 2014) and after backfilling (from May 2015 onwards).

With the custom-made sensors and the specific calibration procedure, a high-quality water content data set has been produced with low measurement noise level and high reliability. The data scatter is in the range of 1 – 2 % water content. All sensors are still active, and monitoring is continued.



## 8 References

- Bosgiraud, J.-M., Nachmilner, L., Hooper, A., Pettersson, S., Fries, T., Verstricht, J., Bollingerfehr, W. & Pihlainen, H. (2015). - Expert group report. EU project LUCOEX, Deliverable D1.14. [www.lucoex.eu](http://www.lucoex.eu).
- Brugg Kabel AG (2016): FE-B Experiment Phase 19 - Installation of fibre optic cables at the tunnel wall of the FE tunnel – installation report. - Mt. Terri Technical Note, TN2014-53; Mont Terri Project.
- Ciocca, F., Lunati, I., van de Giesen, N. & Parlange, M.B. (2012): Heated Optical Fiber for Distributed Soil-Moisture Measurements: A Lysimeter Experiment - Vadose Zone J. - doi:10.2136/vzj2011.0199.
- Eiholzer, L. (2014): Update of 3D model with boreholes and sensors and laser scanning of the FE Gallery. -tn2012 Mt. Terri Technical Note, TN2012-89, Flotron AG (Switzerland); Mont Terri Project.
- Evett, S., Tolk, J. & Howell, T. (2005): Time domain reflectometry laboratory calibration in travel time, bulk electrical conductivity, and effective frequency. - Vadose Zone J.4: 1020–1029.
- Feced, R., Farhadiroushan, M., Handerek, V. A. & Rogers, A. J. (1997): A high spatial resolution distributed optical fiber sensor for high-temperature measurements. - Rev. Sci. Instrum., 68, 3772–3776.
- Firat Lüthi, B. (2018): Full-Scale Emplacement (FE) experiment – Data Trend Report, Data covering: excavation and 3 first years of heating 01.01.2012 - 31.08.2018. - Nagra Working Report, NAB 18-39; Nagra (Wettingen, Switzerland).
- François, L. (2012a): FE A Experiment: Logging report - Borehole Logging in the Mont Terri Test Site, in the hole BFE-A10, 15th and 29th February 2012. – Mt. Terri Technical Note, TN2012-24, SolData (France); Mont Terri Project.
- François, L. (2012b): FE A Experiment: Logging report - Borehole Logging in the Mont Terri Test Site, in the hole BFE-A11, 08th and 29th February 2012. – Mt. Terri Technical Note, TN2012-25, SolData (France); Mont Terri Project.
- François, L. (2012c): FE A Experiment: Installation report WP2. - Mt. Terri Technical Note, TN2012-26, SolData (France); Mont Terri Project.
- Grattan, K. T. V. & Sun, T. (1999): Fiber optic sensor technology: an overview. - Sensors and Actuators 82 (2000) 40-61.
- Hausner, M. B., Suárez, F., Glander, K. E., Van de Giesen, N., Selker, J. S. & Tyler, S. W. (2011): Calibrating single-ended fibreoptic raman spectra distributed temperature sensing data. - Sensors, 11, 10859–10879, doi:10.3390/s111110859.
- Jones, S. B., Wraith, J. M. & Or, D. (2002): Time domain reflectometry measurement principles and applications. - Hydrol. Process. 16, 141-153. DOI: 10.1002/hyp.513.

- Köhler, S., Garitte, B., Weber, H. P. & Müller, H. R. (2015). FE/LUCOEX: Emplacement report. - Nagra Working Report, NAB 15-27, Nagra, Wettingen, Switzerland and EU Project LUCOEX, Deliverable D2.5. [www.lucoex.eu](http://www.lucoex.eu).
- Modern2020 (2016), WP2 Repository Monitoring Strategies and Screening Methodologies. - Modern2020 Work Package 2, Deliverable D2.1.
- Modern2020 (2018a): Activities. - Retrieved from <http://www.modern2020.eu/activities.html>.
- Modern2020 (2018b): Activities WP4 – Demonstration of monitoring. - Retrieved from <http://www.modern2020.eu/activities/wp4-demonstration-of-monitoring.html>.
- Morel, J. (2013): FE-A experiment: Installation report of inclinometer and fibre optic temperature system in BFEA10 and BFE-A11 boreholes. - Mt. Terri Technical Note, TN2012-29rev., Soldata (France); Mont Terri Project.
- Müller, H. R., Garitte, B., Köhler, S., Vogt, T., Sakaki, T., Weber, H.P. & Vietor, T. (2015). FE/LUCOEX: Final report. - Nagra Working Report, NAB 15-28, Nagra, Wettingen, Switzerland and EU Project LUCOEX, Deliverable D2.6. [www.lucoex.eu](http://www.lucoex.eu).
- Müller, H., Garitte, B., Vogt, T., Köhler, S., Sakaki, T., Weber, H., Spillmann, T., Hertrich, M., Becker, J., Giroud, N., Cloet, V., Diomidis, N. & Vietor, T. (2017): Implementation of the Full-scale Emplacement (FE) Experiment at the Mont Terri Rock Laboratory. - Swiss Journal of Geosciences, Volume 110, Issue 1, Pages 287-306.
- Nagra (2002): Konzept für die Anlage und den Betrieb eines geologischen Tiefenlagers. Entsorgungsnachweis für abgebrannte Brennelemente, verglaste hochaktive sowie langlebige mittelaktive Abfälle. - Nagra Technical Report, NTB 02-02; Nagra (Wettingen, Switzerland). [Report in German].
- Nagra (2008a): Entsorgungsprogramm 2008 der Entsorgungspflichtigen [Waste Management Programme 2008 of the Waste Producers]. - Nagra Technical Report, NTB 08-01; Nagra (Wettingen, Switzerland). [Report in German].
- Nagra (2008b): Vorschlag geologischer Standortgebiete für das SMA- und das HAA-Lager: Darlegung der Anforderungen, des Vorgehens und der Ergebnisse. - Nagra Technical Report, NTB 08-03; Nagra (Wettingen, Switzerland). [Report in German].
- Nagra (2016): The Nagra Research, Development and Demonstration (RD&D) - Plan for the Disposal of Radioactive Waste in Switzerland. - Nagra Technical Report, NTB 16-02; Nagra (Wettingen, Switzerland).
- Nagra (2019): Implementation of the Full-scale Emplacement Experiment in Mont Terri: Design, Construction and Preliminary Results. - Nagra Technical Report, NTB 15-02, May 2019; Nagra (Wettingen, Switzerland).
- Sakaki, T., Vogt, T., Komatsu, M. & Müller, H.R. (2013): Monitoring water content in Opalinus Clay in the FE-experiment: Test application of a dielectric water content sensor. - The 46<sup>th</sup> AGU annual Fall Meeting, H31G-1275, December 9 – 13, San Francisco, California.

- Sakaki, T., Firat Lüthi, B. & Vogt, T. (2018): Feasibility Experiments for Monitoring the State of Granulated Bentonite Mixtures using Heated Fiber-optic Cables; Contribution to the Modern2020 Final Report: WP 3 Task 4. - Nagra Working Report, NAB 18-37; Nagra (Wettingen, Switzerland).
- Schlaeger, N.S. & Sakaki, T. (2017): FE experiment: Water content monitoring with TDR in Opalinus Clay and bentonite Annual Report Raw data trend and rock probe calibration Phase 21: July 2015 – June 2016. - Nagra Working Report NAB 17-21; Nagra (Wettingen, Switzerland).
- Silixa Ultima User Manual (2015): © Copyright Silixa Ltd 2015; [www.silixa.com](http://www.silixa.com).
- Stierlin, R., Ricka, J., Zysset, B., Bättig, R., Weber, P. H., Binkert, T. & Borer, J. W. (1987): Distributed fiber-optic temperature sensor using single photon counting detection. - Applied optics. 26. 1368-70. 10.1364/AO.26.001368.
- Thorncraft, D. A., Sceats, M. G. & Poole, S. B., (1992): An ultra high resolution distributed temperature sensor. – in: Proc. 8th Int. Conf. On Optical Fiber Sensors OFS-8., Monterey, USA, p. 258-259.
- Topp, G. C., Davis, J. L. & Annan., A. P. (1980): Electromagnetic determination of soil water content: measurements in coaxial transmission lines. - Water Resources Research 16: 574–582.
- Tuñon Valladares, S., García-Siñeriz, J. L., Spillmann, T. & Frieg, B. (2019): Evolution of TEM experiment at the Grimsel Test Site (GTS) during the timeframe of Modern2020 project. – Nagra Working Report, NAB 19-33, July 2019; Nagra (Wettingen, Switzerland).
- Tyler, S. W., Selker, J. S., Hausner, M. B., Hatch, C. E., Torgersen, T., Thodal, C. E. & Schladow, S. G. (2009): Environmental temperature sensing using Raman spectra DTS fibreoptic methods. - Water Resour. Res. 45, W00D23, doi:10.1029/2008WR007052.
- Ukil, A., Braendle, H. & Krippner, P. (2011): Distributed Temperature Sensing: Review of Technology and Applications. - IEEE Sensors Journal, Vol. 12-5, 885–892, doi: 10.1109/JSEN.2011.2162060.
- Wavemetrics, Inc. (2018): Igor Pro ©. - <https://www.wavemetrics.com/>
- Weber, H. P., Köhler, S., Teodori, S., Müller, H. R. & Vietor, T. (2012): Work plan, work package 2: Full scale emplacement experiment (FE) at Mont Terri. - Nagra Working Report, NAB 12-10. Nagra, Wettingen, Switzerland and EU Project LUCOEX, Deliverable D2.1. [www.lucoex.eu](http://www.lucoex.eu).
- White, M. J. (ed.) (2014): Monitoring During the Staged Implementation of Geological Disposal: The MoDeRn Project Synthesis. - Modern-Project under Euratom Research and Training Programme on Nuclear Energy within the 7th Framework Programme (2007 - 2013), Contract Number: 232598, Modern Deliverable (D-6.1); 20 January 2014.

## 2. PARTIE II : Test and Evaluation of Monitoring Systems (TEM)

---



# Arbeitsbericht NAB 19-33

## Evolution of TEM experiment at the Grimsel Test Site (GTS) during the timeframe of Modern2020 project

July 2019

S. Tuñon Valladares<sup>1)</sup>, J. L. García-Siñeriz<sup>1)</sup>  
T. Spillmann<sup>2)</sup> & B. Frieg<sup>2)</sup>

<sup>1)</sup> Amberg Infraestructuras, Alcobendas, Spain

<sup>2)</sup> Nagra, Wettingen, Switzerland

### KEYWORDS

Modern2020, Work package 4, TEM, GTS, radioactive waste disposal, crystalline rock, non-keyed plugs, low-pH concrete, wireless monitoring, geophysical monitoring, bentonite buffer, research, testing

**National Cooperative  
for the Disposal of  
Radioactive Waste**

Hardstrasse 73  
P.O. Box 280  
5430 Wettingen  
Switzerland  
Tel. +41 56 437 11 11  
[www.nagra.ch](http://www.nagra.ch)

Nagra Arbeitsberichte ("Working Reports") present the results of work in progress that have not necessarily been subject to a comprehensive review. They are intended to provide rapid dissemination of current information.

"Copyright © 2019 by Nagra, Wetztingen (Switzerland) / All rights reserved.

All parts of this work are protected by copyright. Any utilisation outwith the remit of the copyright law is unlawful and liable to prosecution. This applies in particular to translations, storage and processing in electronic systems and programs, microfilms, reproductions, etc."

## Table of Contents

Table of Contents .....	I
List of Tables.....	II
List of Figures .....	II
<b>1 Introduction and background .....</b>	<b>1</b>
<b>2 Experiment aims .....</b>	<b>3</b>
<b>3 Experiment layout .....</b>	<b>5</b>
<b>4 Monitoring technologies.....</b>	<b>7</b>
4.1 Conventional wired technique .....	7
4.2 Non-intrusive technique.....	7
4.3 Low-frequency wireless transmission system .....	8
4.3.1 Working principle and implementation .....	9
4.3.2 Sensors measured with MI wireless transmission system .....	10
4.3.2.1 Total pressure .....	10
4.3.2.2 Pore pressure.....	10
4.3.2.3 Water content.....	11
4.4 High-frequency wireless transmission system.....	11
<b>5 Hydration System .....</b>	<b>15</b>
<b>6 Results from non-intrusive technique .....</b>	<b>17</b>
6.1 Low-frequency wireless transmission system .....	17
6.1.1 Battery voltage analysis.....	17
6.1.2 Data transmission analysis.....	18
6.1.3 Test data analysis.....	21
6.1.4 Error analysis .....	23
6.2 High-frequency wireless transmission system.....	26
6.3 Cross-hole seismic tomography.....	28
<b>7 Attempts for buffer pressure increase .....</b>	<b>29</b>
7.1 Objective.....	29
7.2 System review.....	29
7.3 Actions carried out to resume the hydration.....	31

<b>8</b>	<b>Results from conventional wired technique sensors</b> .....	41
8.1	Pressure injection and inflow graphs.....	41
8.2	Total pressure graphs.....	43
8.3	Pore pressure graphs.....	45
8.4	Displacement graphs.....	47
<b>9</b>	<b>Summary, discussion and recommendations</b> .....	49
<b>10</b>	<b>References</b> .....	53

## List of Tables

Tab. 6-1:	Transmission status of the MI wireless technique between Dec. 2006 – Dec. 2017 .....	19
Tab. 6-2:	Percent of the ‘empty data’ for all sensors from 2007 to 2017.....	21
Tab. 7-1:	Table of events.....	35

## List of Figures

Fig. 1-1:	Location of the full-scale test in VE tunnel .....	1
Fig. 3-1:	Sequence of the buffer construction with the mats.....	5
Fig. 3-2:	General layout of the TEM Project with hard-wired and wireless instrumentation .....	6
Fig. 3-3:	Illustration of the sensor locations: pore pressure sensors (Pp) and water content probes (Wc) in section B4 (left); total pressure sensors (Tp) and boreholes for Solexperts data logger and MISL transmitter (right).....	6
Fig. 4-1:	Experimental configuration for the non-intrusive seismic tomography technique .....	8
Fig. 4-2:	Concept of the magneto-inductive (MI) wireless transmission monitoring .....	9
Fig. 4-3:	MI transmitter (a) and MI receiver (b).....	10
Fig. 4-4:	HFW wireless nodes with receiver unit (left) and controller unit (right) .....	11
Fig. 4-5:	Sketch of a HFW node.....	12
Fig. 4-6:	Position of the five different boreholes.....	13
Fig. 4-7:	Layout of installed instrumentation (including HFW) .....	13
Fig. 5-1:	Overall view of TEM hydration system .....	15
Fig. 5-2:	Scheme of TEM hydration system .....	16
Fig. 5-3:	Hydration panels.....	16

Fig. 6-1	Battery voltage before the relocation shows significant decrease in MISL voltage (from Spillman, 2008) .....	17
Fig. 6-2:	Battery voltage for Solexperts datalogger and MISL transmitter from August 2007 to December 2017 .....	18
Fig. 6-3:	Missing measurements between January 2007 and December 2017.....	20
Fig. 6-4:	Percentage of P (Perfect), G (Good), and E (Erroneous) messages and empty fields (E) between December 2006 and December 2017.....	21
Fig. 6-5:	Overview of data between December 2006 to December 2017 .....	22
Fig. 6-6:	Total pressure cell and water content measurements between 2009 and 2017.....	23
Fig. 6-7:	Pore pressure and total pressure cell measurements between 2009 and 2017 .....	23
Fig. 6-8:	Error type messages and the part of transmitter parameters for reception status E (and partly G) between December 2006 and December 2017 .....	24
Fig. 6-9:	Transmitter parameters for reception status E (and partly G) between December 2006 and December 2017.....	25
Fig. 6-10	Data of the total pressures (bar) in the buffer gathered from HFW nodes after being installed.....	26
Fig. 6-11:	Data of the pore pressures (bar) in the buffer gathered from HFW nodes after being installed.....	27
Fig. 6-12:	Data of the relative humidity (%; HSB1-5) and temperature (°C; HSB1-5_T) in the buffer gathered from HFW nodes after being installed .....	27
Fig. 6-13:	Data of the pore pressure in plug (PPC; bar) and rock (PZC; bar) gathered from HFW nodes after being installed.....	28
Fig. 7-1:	General view of the hydration system control panel .....	29
Fig. 7-2:	New computer sensor table view .....	30
Fig. 7-3:	View of the back-pressure regulation key .....	31
Fig. 7-4:	Mats injection pressure status on 26 September 2017 .....	31
Fig. 7-5:	Mats injection pressure status on 28 September 2017 .....	32
Fig. 7-6:	Pressure injection and mass flow values graph on 29 September 2017 .....	32
Fig. 7-7:	By-pass of the regulation valve .....	33
Fig. 7-8:	Mat 5 injection pressure status on 3 October 2017.....	33
Fig. 7-9:	Pressure injection and mass flow values graph on 5 October 2017.....	34
Fig. 7-10:	Pressure injection and mass flow values graph on 9 October 2017.....	34
Fig. 7-11:	Pressure injection and mass flow values graph on 11 October 2017.....	36
Fig. 7-12:	Total Pressure and Pore Pressure graph with values on 11 October 2017.....	36
Fig. 7-13:	Pressure injection and mass flow values graph on 11 October 2017.....	37
Fig. 7-14:	Pump leakage and injection manometer pressure.....	37
Fig. 7-15:	Mats pressure on 20 October 2017 .....	38
Fig. 7-16:	Mats pressure on 24 October 2017 .....	39

Fig. 7-17:	Mats pressure on 24 November 2017 .....	39
Fig. 7-18:	Mats pressure on 19 December 2017.....	40
Fig. 8-1:	Pressure injection and inflow from 1 October 2017 to 8 January 2018.....	41
Fig. 8-2:	Pressure injection and inflow from 4 January 2018 to 13 April 2018.....	42
Fig. 8-3:	Pressure injection and inflow from 13 April 2018 to 21 July 2018.....	42
Fig. 8-4:	Total pressure trend from 1 October 2017 to 8 January 2018 .....	43
Fig. 8-5:	Total pressure trend from 4 January 2018 to 13 April 2018.....	44
Fig. 8-6:	Total pressure trend from 14 April 2018 to 22 July 2018 .....	44
Fig. 8-7:	Pore pressure sensors trend from 1 October 2017 to 8 January 2018.....	45
Fig. 8-8:	Pore pressure sensors trend from 4 January 2018 to 13 April 2018 .....	46
Fig. 8-9:	Plug displacement sensors - extensometers trend from March 2017 to February 2019.....	47
Fig. 9-1:	Comparison of wireless and wired monitoring.....	49
Fig. 9-2:	Comparison of seismic data (after Marelli et al., 2010 & Marelli, 2011).....	50



Demonstration of Monitoring Strategies and Technologies for Geological Disposal" (Rösli, 2012 & 2013; NDA et al. 2013).

And was continued in the follow up project Modern2020 (2016 - 2019) supported by EURATOM titled: "Development and Demonstration of Monitoring Strategies and Technologies for Geological Disposal".

## 2 Experiment aims

The aim of the TEM project in the framework of the Modern2020 Project was to further examine and evaluate the three monitoring techniques at GTS as already discussed in Spillmann (2008):

- Conventional "hard" wired techniques based on conventional wired signal transmission from the EBS; part of the ESDRED Module 4 experiment conducted by ENRESA/Aitemin.
- Geophysical tomographic technique based on repeated seismic measurements as a non-intrusive technique to observe the EBS development from the geosphere, performed by ETH Zurich under the leadership of NDA (Nuclear Decommissioning Authority of UK).
- Wireless techniques as a combination of the wireless data transmission method developed by Magneto-Inductive Systems Limited (MISL) and the data acquisition systems of Solexperts AG; tested and evaluated for the first time in an environment relevant to radioactive waste disposal.

Another relevant objective of the project was to demonstrate the load bearing capacity of this concrete plugs in order to refine the design basis for future use. Therefore, a requirement was to increase of the total pressure to values as high as 5 MPa in addition to saturation of the buffer and measurement of the THM evolution.

The plug was designed to withstand up to 5MPa of total stress and the goal is to check if it is capable or not (breaks or moves). If it no breaks or moves occur up to 5 MPa then the aim was to ascertain what is the maximum stress the plug could hold (if feasible).

Usually the plugs are designed with recesses in the rock and they are so called keyed plugs. This one has no recesses and thus called parallel type concrete plug.



### 3 Experiment layout

The basic setup at the site consists of a 4 m long low-pH shotcrete plug constructed at the back end of a 3.5 m diameter horizontal tunnel excavated in granite with a tunnel boring machine (TBM). The plug is sealed off from the rockface at the end of the tunnel by a 1 m thick buffer constructed with blocks of highly compacted bentonite (dry density of bentonite buffer is 1550 kg/m<sup>3</sup>) (Fig. 3-1).

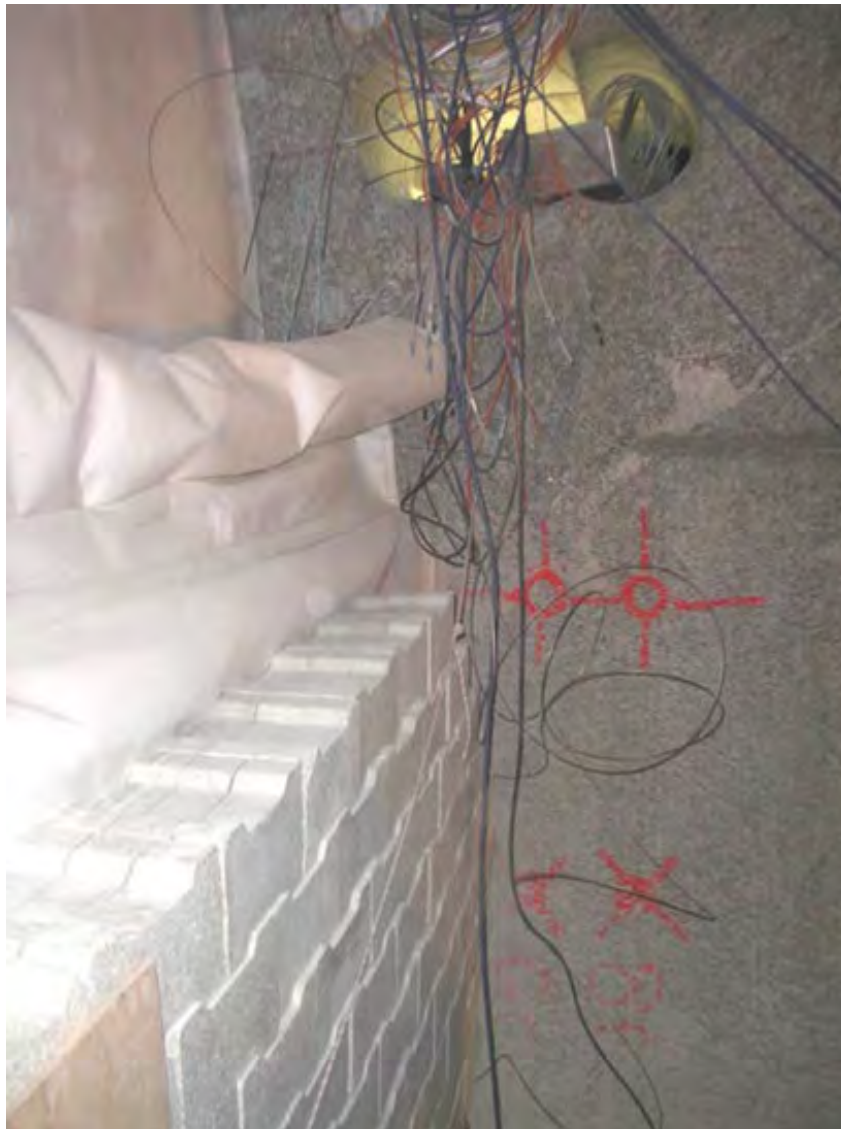


Fig. 3-1: Sequence of the buffer construction with the mats

The blocks were installed to build 7 vertical bentonite slices, B1 to B7 (in yellow, Fig. 3-2), and six geotextile mats were installed in between to accelerate the saturation process (see Fig. 3-1). The shotcrete plug thus confines a bentonite buffer in a granite host rock that should be saturated. All details about the test construction are given in Bércena & García-Siñeriz (2008 & 2009). The general layout is given in Fig. 3-2 & Fig. 3-3.

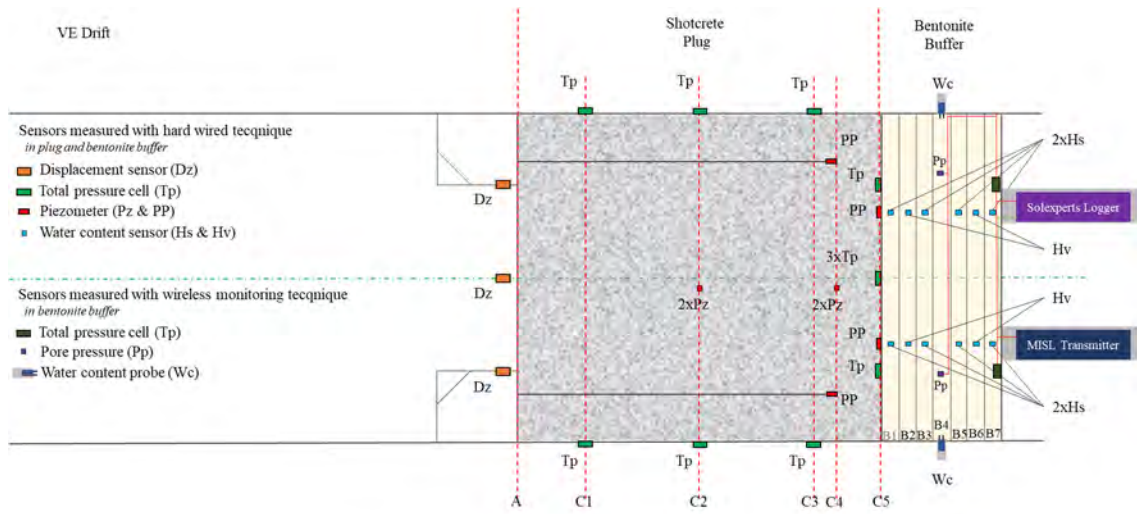


Fig. 3-2: General layout of the TEM Project with hard-wired and wireless instrumentation (Note: Not to scale)

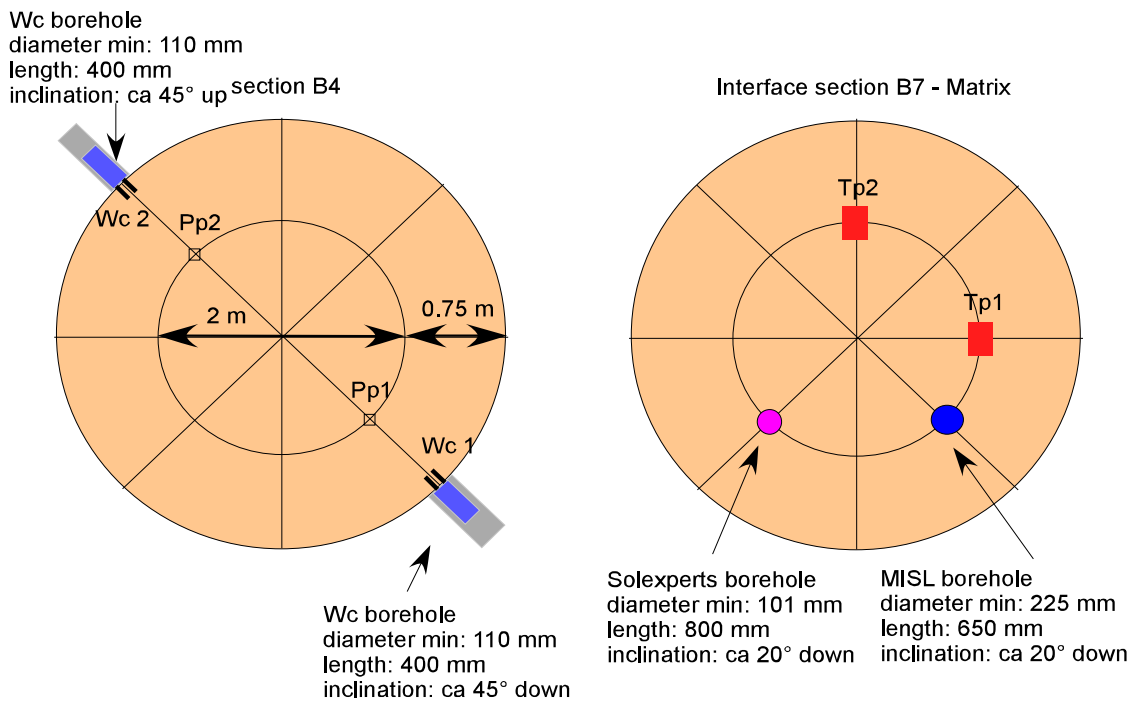


Fig. 3-3: Illustration of the sensor locations: pore pressure sensors (Pp) and water content probes (Wc) in section B4 (left); total pressure sensors (Tp) and boreholes for Solexperts data logger and MISL transmitter (right)

## 4 Monitoring technologies

### 4.1 Conventional wired technique

Various hard-wired sensors were installed to allow the evolution of the test to be surveyed continuously. The sensors measure different parameters at different locations in the rock, the bentonite and the shotcrete mass (Fig. 3-2). These conventional hard-wired sensors were connected to a Data Acquisition, Display and Control System.

As illustrated in Fig. 3-2, the sensors in the rock consisted of piezometers (Pz) installed in four short radial boreholes and total pressure cells (Tp) installed in the rock surface. All these sensors measure the radial pressure at the interface shotcrete/rock. The sensors in the bentonite comprised two different capacitive type humidity sensors (Hs and Hv) installed half-way through the width of each of the bentonite buffer layers except for the central layer. Their purpose is to follow the hydration process. These two sensor types incorporate also a temperature measurement. Because this is an isothermal test, additional accurate temperature measurements are not necessary.

Along the interface plug/buffer, piezometers (PP) and total pressure cells (Tp) measure the swelling pressure of the buffer. The sensors in the shotcrete mass consist of piezometers (PP) inserted in two horizontal boreholes of 0.035 m diameter, drilled from the plug face up to 0.5 m from the rear end, and four extensometers (Dz) placed at the plug face, for tracking potential displacements.

The test plan and the implementation of the technique are summarized in Spillmann (2008). The complete test plan of the test is given by García-Siñeriz et al. (2008).

### 4.2 Non-intrusive technique

The component of interest in the experiment setup with the long low-pH shotcrete plug is the bentonite buffer at the end of the tunnel. During saturation, the bentonite swells, creating pressure within the confined zone behind the plug. In principle, the swelling process changes the elastic properties of bentonite sufficiently high to enable detection by using cross-hole seismic techniques.

During the planning phase of the non-intrusive measurement technique, numerical simulations were prepared to decide the most advantageous positions for the seismic measurements (Spillmann, 2008). The results from these numerical simulations were used to design the setup for the cross-hole seismic tomography experiment which was performed with a fan of six boreholes that surround the bentonite buffer and the shotcrete plug. The experimental setup in its final version is illustrated in Fig. 4-1.

The six boreholes were equally spaced around the perimeter of the main tunnel to ensure sufficient redundancy for the transmitted wavefields and good angular coverage for the reflected wavefields. Since changes in the synthetic seismic sections extended well beyond the end of the tunnel, borehole lengths were chosen to be 25 m (Fig. 4-1).

A high-frequency sparker served as the seismic source. It was fired sequentially every 0.25 m along boreholes 3, 4 and 5. Three 24-channel hydrophone streamers with 1 m spacing were simultaneously deployed in boreholes 1, 2 and 6 (Fig. 4-1, front view). By shifting the streamer three times at intervals of 0.25 m and repeating each source, a 96-channel hydrophone streamer with 0.25 m element spacing was synthesized (Spillmann, 2008).

From January 2007 to April 2008, six measurement campaigns (also referred to as seismic experiments) were carried out, each with different conditions at the end of the tunnel (Spillmann, 2008). The first two experiments were performed before and after emplacement of the dry bentonite buffer and concrete plug. Subsequently, water was injected into the bentonite buffer and the seismic experiments were repeated 1, 4, 10 and 13 months after the initial injection.

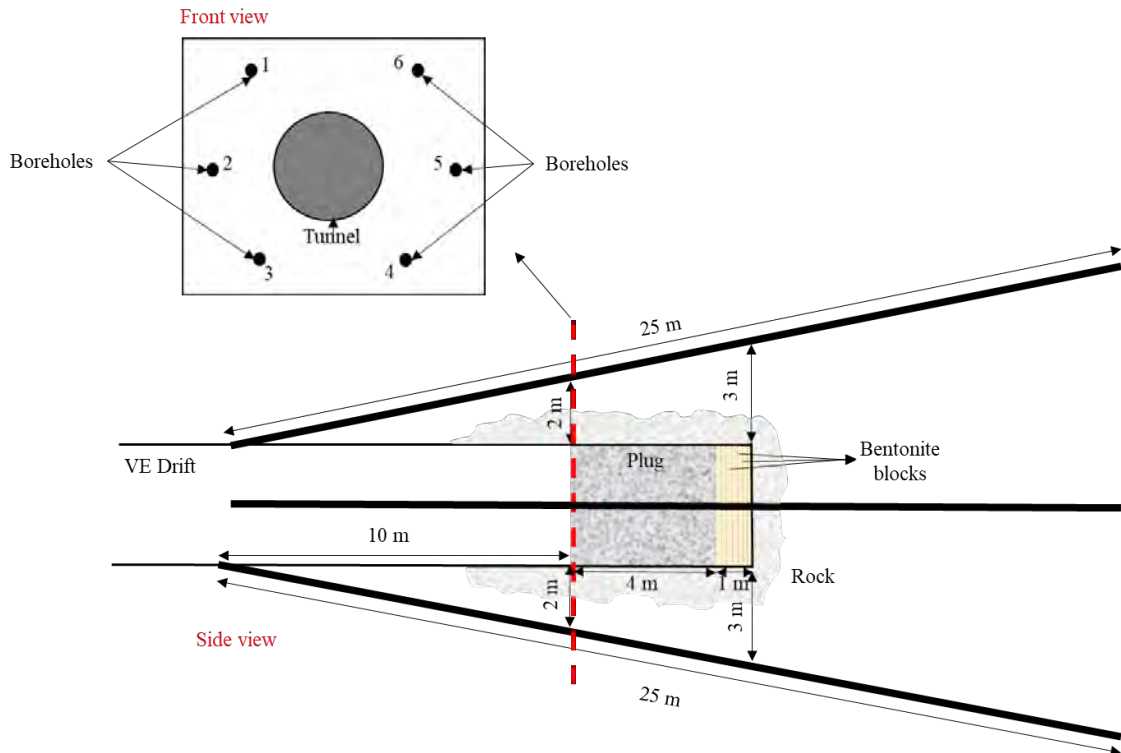


Fig. 4-1: Experimental configuration for the non-intrusive seismic tomography technique (Note: Not to scale.)

During MoDeRn project 25 single-component geophones with a natural frequency of 100 Hz were installed at the front face of the concrete plug.

### 4.3 Low-frequency wireless transmission system

The unique physical properties of low-frequency magnetic fields enable secure and reliable system performance in the most challenging operating environments. The channel is immune to scattering, reflection or multi-pathing and can penetrate any medium including water, ice, earth and rock (including subterranean tunnels, caves or bunkers), as well as dense urban structures. Consequently, the magneto inductive (MI) monitoring technology is appropriate in areas where traditional wireless systems (very high frequency) are unreliable and where direct cabling is problematic.

At the back of the test site, two boreholes were drilled; one housing the Solexperts data logger and one the MI transmitter (see Fig. 3-2 and Fig. 4-1). The specifications of the boreholes are given in Fig. 3-3. Total pressure sensors were installed at the interface bentonite/host rock as

shown in Fig. 4-1. At the edge of layer B4, two boreholes were drilled in the host rock housing the water content probes (Theta Probe soil moisture sensors). Two pore pressure filters were emplaced inside layer B4 (Fig. 4-1), all these sensors were connected to the Solexperts data logger borehole and the gathered values transmitted by the MI unit.

#### 4.3.1 Working principle and implementation

The magneto-inductive (MI) transmission is a monitoring technique based on the concept shown in Fig. 4-2. The system utilizes an AC magnetic field as communication channel and a communication frequency of 575 Hz. The system is comprised of an MI transmitter and an MI receiver, possessing modulation and demodulation capabilities for wireless data communications through any intervening media. The frequency shift keying (FSK) technique is used for modulation. Extensive explanation of the working principle, performance and the equipment of the MI wireless transmission system can be found in Spillmann (2008).

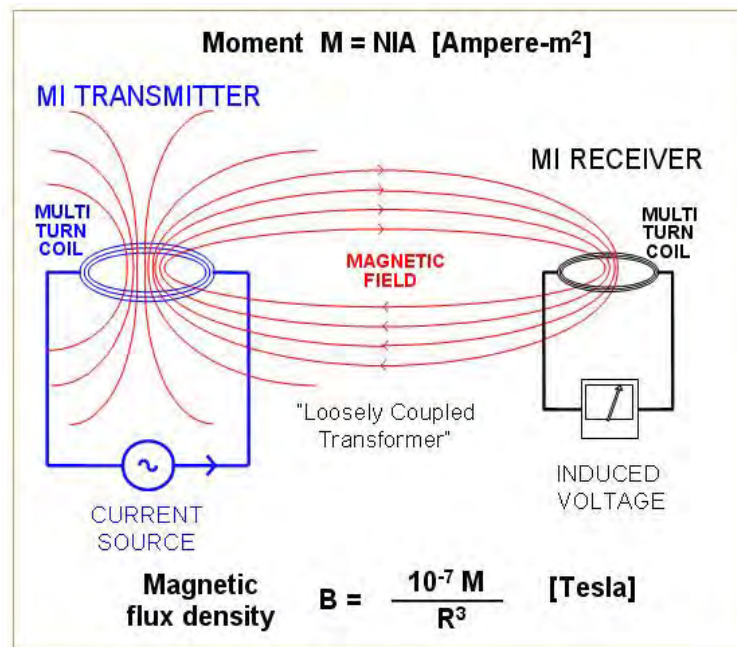


Fig. 4-2: Concept of the magneto-inductive (MI) wireless transmission monitoring

The MI wireless transmission system was emplaced in TEM at the end of 2006 and has been operated since then by Solexperts. The system is comprised of an MI transmitter (at the back of the bentonite buffer) and an MI receiver (located in the VE gallery beyond the concrete plug), possessing modulation and demodulation capabilities for wireless data communications through any intervening media.

Solexperts installed a PC connected to the MI receiver. The WaveMetrics program IGOR was programmed to record the data transmitted from the MI receiver in an ASCII file.

The MI Receiver and the Solexperts DAS are located outside of the VE-Drift. To test the range for successful data transmission, the MISL receiver was firstly placed in the MI drift of the GTS at a distance of about 100 m of the transmitter location. In May 2007, the transmission started to

work badly, erroneous data were transmitted, or the transmission failed. Therefore, the receiver was relocated on June 16th, 2007, to Location 2 near the GMT (Gas Migration Test in the EBS and Geosphere) experiment at about 30 m from the transmitter (compare Fig. 1-1).

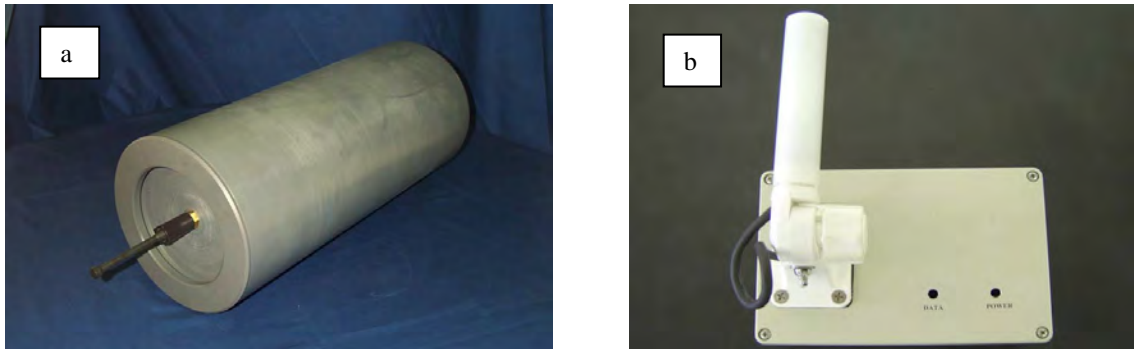


Fig. 4-3: MI transmitter (a) and MI receiver (b)

The MI transmitter in Fig. 4-3 (a) is a self-contained, autonomous unit housed in a PVC pressure vessel measuring 510 mm long by 220 mm in diameter. The pressure vessel was originally designed for underwater use and has a depth rating of 100 feet (45 psi). The transmitter in Fig. 4-3 (b) weighs approximately 30 kg when fully assembled. The receiver receives the sensor data transmitted by the transmitter. It is housed in an aluminum environmental enclosure measuring 240 mm by 160 mm by 100 mm, with an articulating antenna 140 mm in length. The receiver weighs approximately 3 kg when fully assembled. The receiver is programmed to interface with Solexperts' data acquisition system and has a serial data link for connecting to a PC. The receiver has a power cable for connecting to an AC source (50 Hz). The receiver also contains a 4 V rechargeable lithium battery for indigenous power.

The data acquired by the Solexperts data logger is sent by the MISL transmitter to the MISL receiver, located at about 30 m from the transmitter in the GMT niche (Fig. 1-1). The transmitter is programmed to transmit the data of all sensors twice a day every 12 hour.

### 4.3.2 Sensors measured with MI wireless transmission system

#### 4.3.2.1 Total pressure

Two total pressure (Tp) cells are installed in contact with the interface between the bentonite section B7 and the end of the VE-Drift to measure the swelling pressure of the bentonite. Glötzl EEKE 17 K50 A Z4 probes are used. The characteristics of the total pressure probes can be found in NAB08-52.

#### 4.3.2.2 Pore pressure

Pore pressures (Pp) in the bentonite buffer are measured with Keller PA-22S sensors at two locations within the section B4 (Fig. 3-3). The sensors are placed within the Solexperts data logger housing. A 6/4 mm stainless steel tube filled with water links the sensors and the measuring points within section B4. The length of the tube, which follows the back wall and enters horizontally into the bentonite section, is 1.93 m for both sensors. In order to avoid clogging of the tube, the

measuring points are equipped with sintered stainless-steel screens. The sensor specifications and dimensions can be found in Spillmann (2008).

#### 4.3.2.3 Water content

Water content (Wc) is measured within the bentonite section B4 using Theta Probe soil moisture sensors. The probes are equipped with additional protection housings to withstand total pressures up to 5 MPa and 15 bar pore water pressure. The Theta Probe measures volumetric soil moisture content by the well-established method of responding to changes in the apparent dielectric constant. These changes are converted into a DC voltage, virtually proportional to the soil moisture content over a wide working range. The sensor specifications and dimensions can be found in Spillmann (2008).

Volumetric soil moisture content is the ratio between the volume of water present and volume of the sample. This is a dimensionless parameter, expressed either as a percentage (% vol), or a ratio ( $\text{m}^3/\text{m}^3$ ).

#### 4.4 High-frequency wireless transmission system

A High Frequency Wireless (HFW) system was installed during MoDeRn project. A total of six HFW sensing units, a receiver and a controller were produced (see Fig 4-4). The main specifications of the nodes are as following:

- VHF band MHz radio transceiver;
- Inputs for up to 6 general purpose sensors [0 – 2 V, 0 – 10 V, 4 – 20 mA, digital];
- Robust, compact and high pressure resistant reinforced polyester enclosure;
- Built-in lithium battery. Expected life time: 1 – 25 years (depending of the specific application requirements);
- Dimensions: 190 x 75 (Ø) mm



Fig. 4-4: HFW wireless nodes with receiver unit (left) and controller unit (right)

Main specifications of the controller unit are:

- VHF band MHz radio transceiver;
- Up to 16 wireless nodes management;
- 5.4" TFT graphic display and friendly user interface for real time data visualization;
- Configuration parameters and data accessible both locally and remotely via Ethernet, Internet (built-in web server), MODBUS-TCP, etc.;
- IP54 plastic-metallic enclosure;
- Wide input voltage [9 – 24 V] and low power consumption.

Fig. 4-5 shows a sketch of a node, which can measure pore pressure, total pressure, relative humidity and temperature. Finally, in October 2011 only five nodes were installed into four boreholes of 86 mm drilled at the plug and one in the rock (Fig. 4-6). Two of them reached the bentonite buffer to measure pore pressure, total pressure and relative humidity, whereas the other three served to install nodes in the rock and in the shotcrete plug, measuring pore pressure only.

The HFW nodes were manually installed in the boreholes and then grouted. The scheme of the overall layout including the precedent instrumentation is shown in Fig. 4-7.

The signals from the five HFW nodes are gathered at the open gallery in the reception unit and integrated, via the controller, into the existing AITEMIN data monitoring and control system (SCADA based).

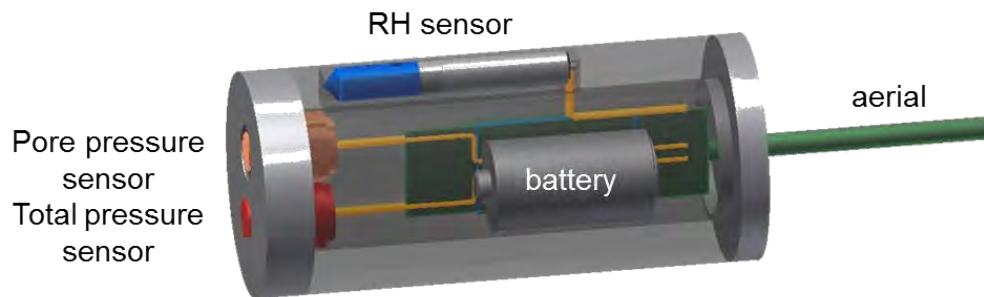


Fig. 4-5: Sketch of a HFW node

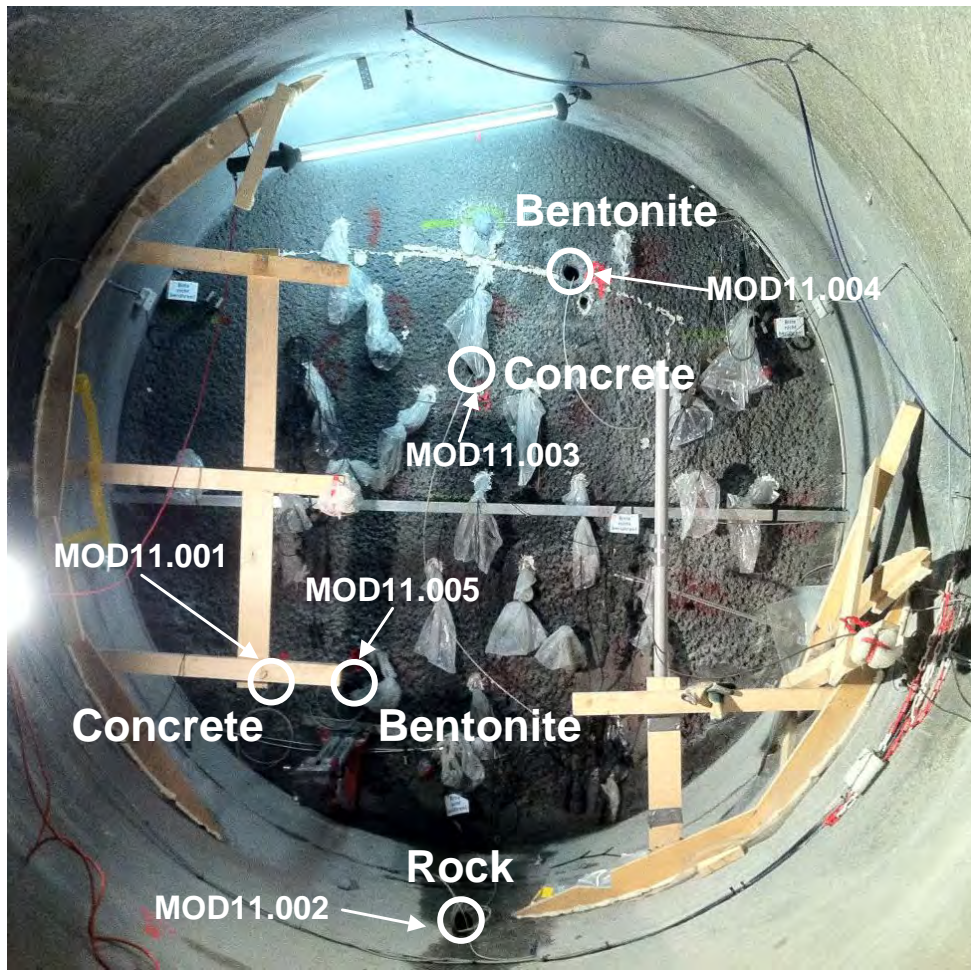


Fig. 4-6: Position of the five different boreholes

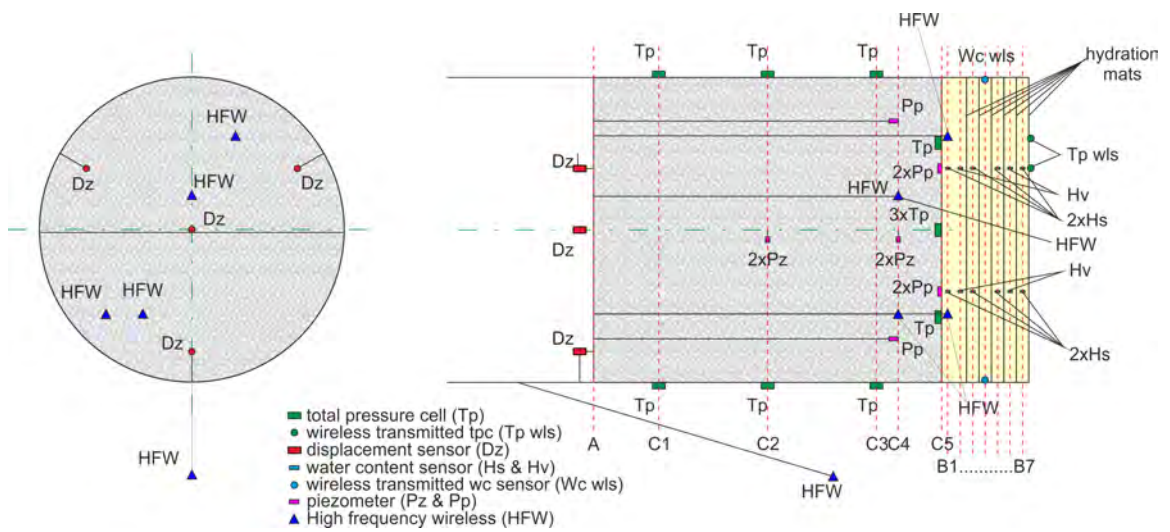


Fig. 4-7: Layout of installed instrumentation (including HFW)



## 5 Hydration System

The hydration cabinet is housed in a metallic box that includes different elements:

- High-pressure pulse pump
- Air compressor
- Back-pressure.
- Diaphragm Pulsation Damper
- Flow meter
- Regulation valve
- Mass flow meter/controller
- Pressure sensor to read the injection pressure
- Control pressure (Bronkhorst Hi-tec)
- Electronic unit: Mass Flow/Pressure meter and controller
- 11 different control valves

The hydration cabinet pumps the water to the mats located inside the buffer (Fig. 5-1) by feeding them with water from an open water tank. Each mat has an inlet and outlet pipe that are controlled by two hydration panels located behind the hydration cabinet at the rock wall. The inflow line from the hydration cabinet feeds the inlet hydration panel that distributes the water and enables, using manual valves, to select which mats are on use. The inflow pressure is measured thanks to local manometers and electrical transducers. The outflow lines of the mats are driven to the outflow panel where the pressures can be monitored and the lines drained to eliminate the trapped air. All lines to the mats are driven by a borehole that reaches the middle of the buffer.



Fig. 5-1: Overall view of TEM hydration system

The water injected by the water pump is controlled by the mass flow meter/controller, fed by the values of the flow meter and the injection pressure. The scheme of the hydration system is shown in Fig. 5-2.

The water output of the hydration system goes to the mats panels, located in a panel installed close the injection borehole. Through these panels is possible to select where the water is going to be injected, Fig. 5-3, and it is also possible to drain the air of the different mats' lines.

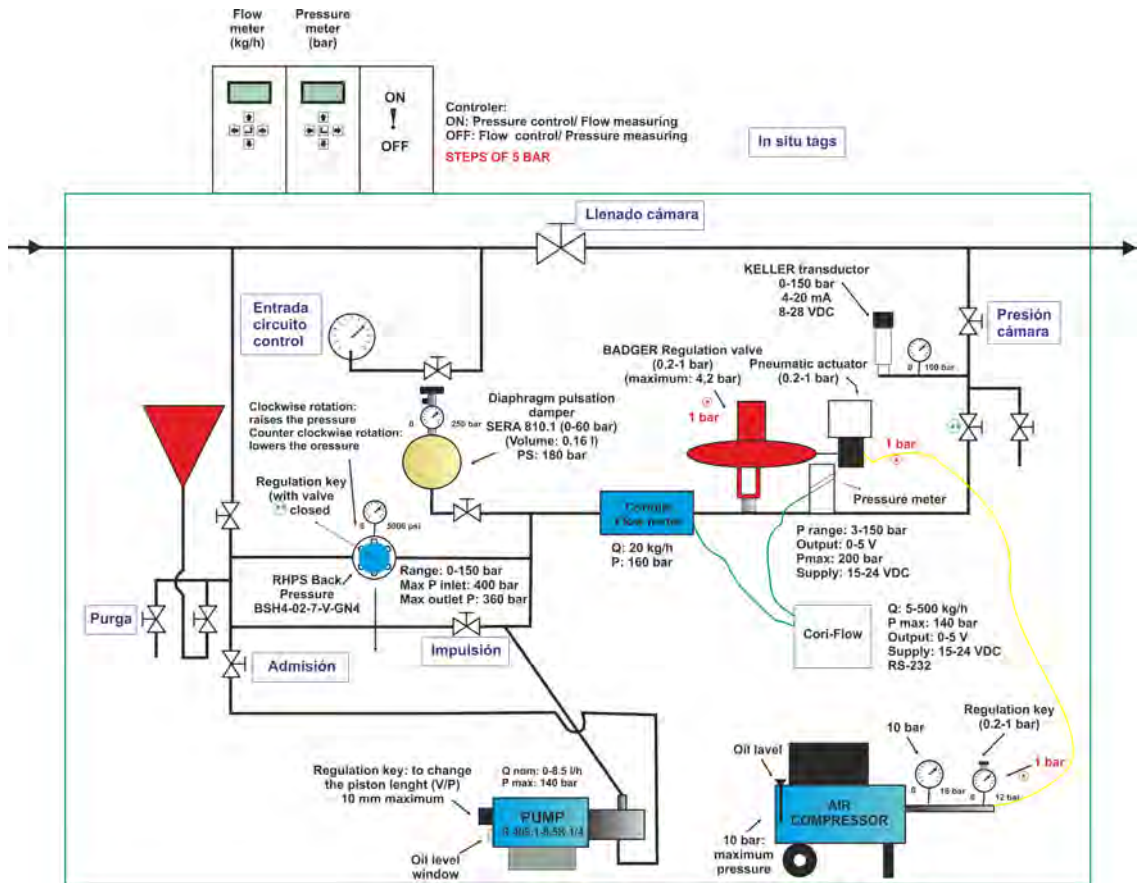


Fig. 5-2: Scheme of TEM hydration system

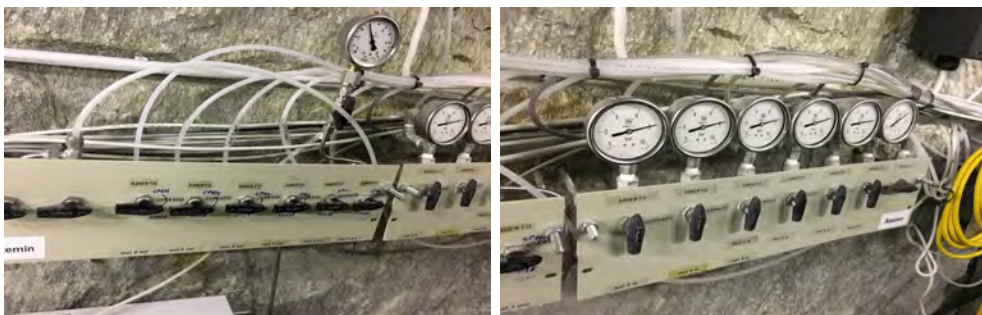


Fig. 5-3: Hydration panels

## 6 Results from non-intrusive technique

### 6.1 Low-frequency wireless transmission system

#### 6.1.1 Battery voltage analysis

The power necessary for the wireless data transmission is supplied by two independent and non-rechargeable batteries: one for the Solexperts data logger and one for the MISL transmitter. The data of the battery voltage from 2007 until summer 2008 were already presented in Spillmann (2008; Fig. 6-1).

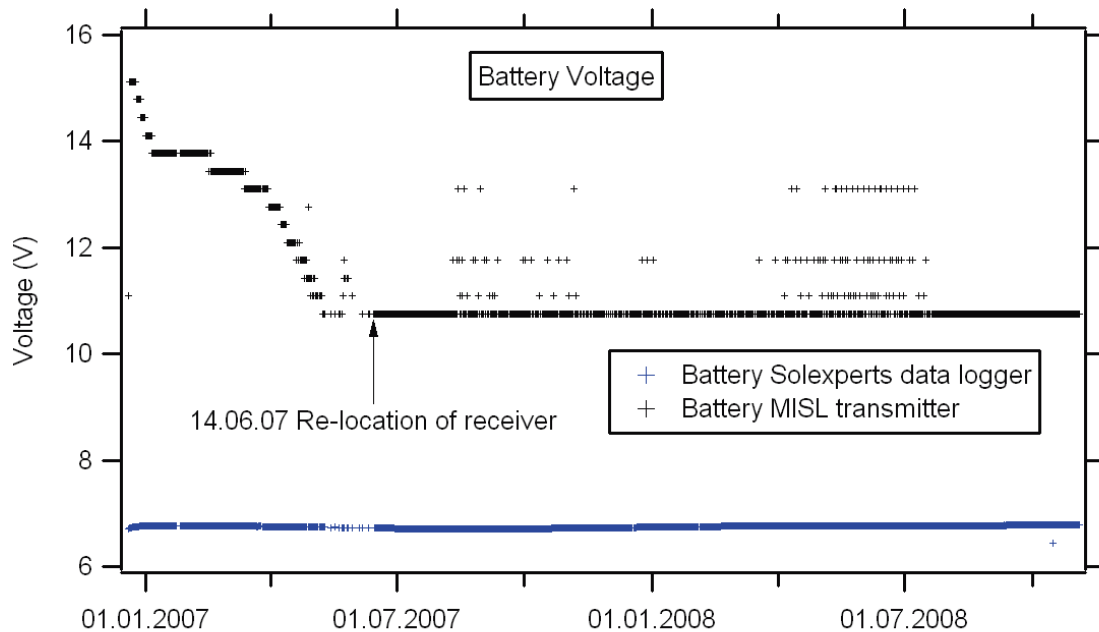


Fig. 6-1 Battery voltage before the relocation shows significant decrease in MISL voltage (from Spillman, 2008)

Fig. 6-2 displays the battery voltages between August 2007 after the relocation of the receiver and December 2017. The voltage of the Solexperts data logger battery was slightly increasing until January 2010 and stabilised at about 6.8 V. Since April 2014, the battery voltage measurements of the Solexperts data logger are mostly missing because of the disturbed data transmission. The voltage of the MISL transmitter was mostly constant at 10.75 V until the 12<sup>th</sup> of May 2013 when it started to be noisy and vary between 10.75 and 21.17 V.

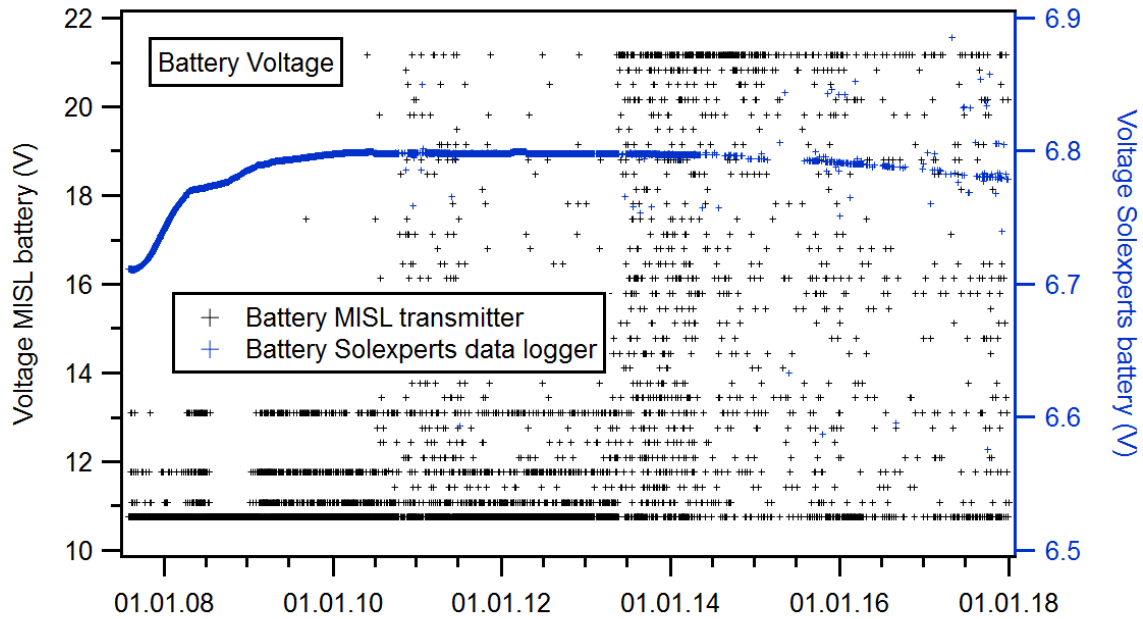


Fig. 6-2: Battery voltage for Solexperts datalogger and MISL transmitter from August 2007 to December 2017

**6.1.2 Data transmission analysis**

The MISL data packet output contains a character representing the MI channel transmission/reception status:

- P = Perfect -> no errors
- G = Good -> all errors corrected
- E = Uncorrectable error -> uncorrectable errors occurred

In the case of a status E, an additional error data packet is appended to the standard data set. Some of the corrupted data packages with the status E could be manually corrected and the values assigned to the corresponding sensor. These data were retrieved, whereas the corrupted data of the other sensors was discharged. Unreadable data packages were classified as ‘empty data’. Table 6-1 summarizes the details of changes in the status of the transmission between the December 2006 and December 2017.

Since 15th of May 2013, the MISL transmission was disturbed and most data transferred by the MISL transmitter were not valid and are referred as empty. Between January and the 21st of April 2014, the transmitted data mostly have the long error packet format with status E and the full data string including checksum together with some status P with the short error packet (but no checksum) or status G with both the long and the short error packet.

Tab. 6-1: Transmission status of the MI wireless technique between Dec. 2006 – Dec. 2017

<b>Date</b>	<b>Transmission Status</b>	<b>Comments / Details</b>
19.12.2006 – 10.05.2007	P/G	19.12.06: Installation and connection to the DAS
10.05.2007 – 14.06.2007	Often E or no data	Bad transmission, receiver re-located on 14.06.2007
14.06.2007 – 10.07.2007	P with error data packet	
10.07.2007 – 15.08.2007	E	
15.08.2007 – 01.05.2008	P/E	
01.05.2008 – 12.04.2009	E	
13.04.2009 – 14.05.2009	E with some P	If status E, column with checksum (CS) together with Wc2 data→ some erroneous data
14.05.2009 – 11.10.2010	Alternatively, E or P (mostly every second measurement)	If status E, column with checksum (CS) together with Wc2 data→ often erroneous data
12.10.2010 – 18.11.2010	E	Often no data transmission, the transmitted data are mostly erroneous
19.11.2010 – 23.12.2010	Alternatively, E or G/P (alternatively)	If status E, column with checksum (CS) together with Wc2 data→ often erroneous data
23.12.2010 – 04.02.2011	E	
05.02.2011 – 23.05.2011	Alternatively, E or G/P (alternatively)	If status E, column with checksum (CS) together with Wc2 data→ often erroneous data
24.05.2011 – 25.07.2011	Alternatively, E or G very few P	If status E, column with checksum (CS) together with Wc2 data→ often erroneous data
26.07-2011 – 27.03.2013	Alternatively, E or P very few G	If status E, column with checksum (CS) together with Wc2 data→ often erroneous data
28.03.2013 – 14.05.2013	Mostly E, few P	If status E, full data package with separate checksum after Wc2
15.05.2013 – 31.12.2013	Mostly E, few G	Mostly status E and partially G, full data package with separate checksum after Wc2
01.01.2014 – 21.04.2014	Mostly E few P and G	Mostly status E, long error packet with separate checksum after Wc2 G and P with short error packet
22.04.2014 – 14.08.2015	Mostly E, very few G	Mostly status E with long error packet, checksum not recognisable, often failure of data transmission
14.08.2015 – 31.12.2017	Mostly E, very few G	Mostly status E with or without long error packet, checksum not recognisable, often failure of data transmission

Since the 22nd of April 2014, the transmission of the entire data packages often failed. The recorded data mostly show the status E and few G with the long error packet. Between May 2016 and April 2017 only 17 % of the standard data packages were transmitted with a minimum of four packages in June 2016. Fig. 6-3 shows the percentage of transmitted measurements compared to a transmission of two measurements per day which gives 100 % of measurements. Missing measurements were already observed in May and June 2007, between October 2010 and January 2011 and partly during 2013. Since May 2014 between 37 % and 93 % of the data packages are missing.

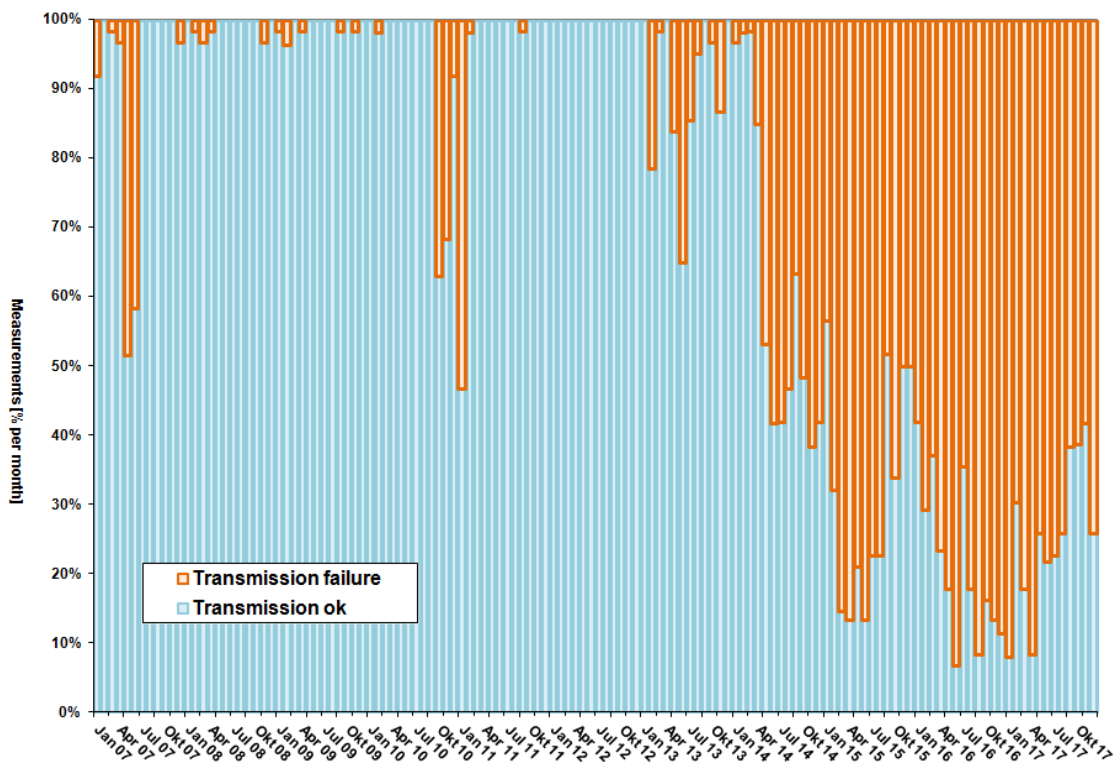


Fig. 6-3: Missing measurements between January 2007 and December 2017

Fig. 6-4 displays the percentage of P, G, E of MI channel transmission/reception status messages per month from December 2006 until December 2017. Between April 2008 and May 2009 and since April 2013, most of the reception status is E.

Since the beginning of the data transmission, corrupted data were occasionally transmitted for individual sensors which are referred to as empty. Corrupted data includes both invalid characters in the data string or a number which yields out of range values for the corresponding sensors.

Since November 2014 the data transmission for the total pressure Tp1 often yielded noisy numbers at the upper bound of the measuring range with the corresponding calculated total pressures varying from about 250 kPa to negative values. In addition, the numbers are not stable but very noisy and seem to be an artefact because of the failure of the data logger. The same can be observed for sensor Tp2 since April 2016.

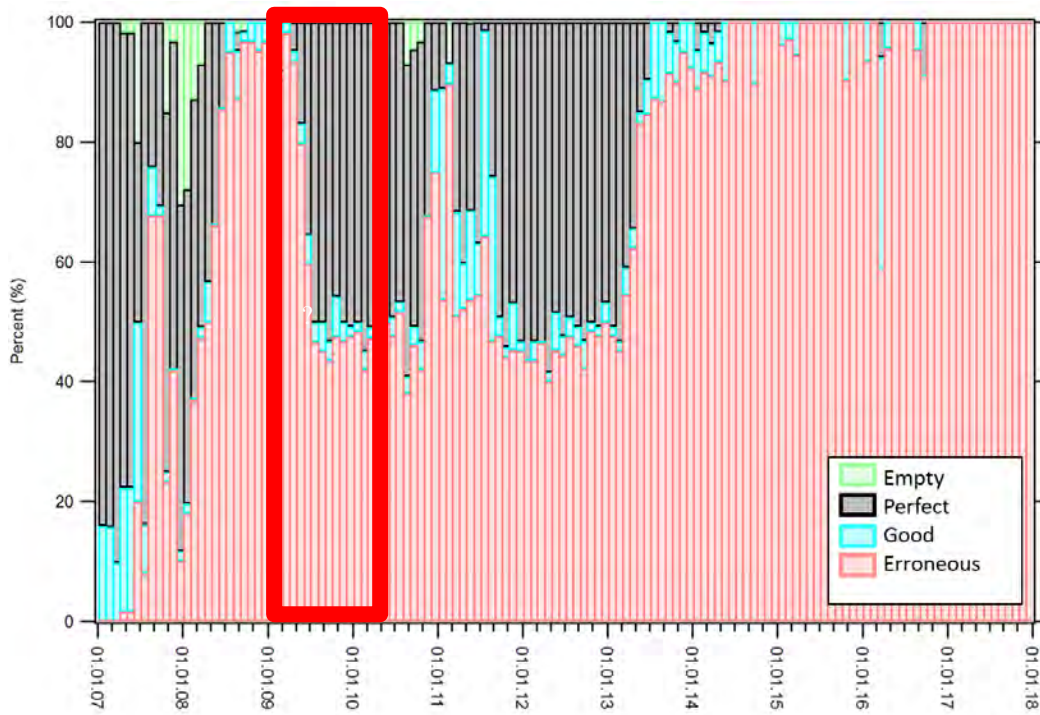


Fig. 6-4: Percentage of P (Perfect), G (Good), and E (Erroneous) messages and empty fields (E) between December 2006 and December 2017

Table 6-2 lists the ‘empty data’ output from the MISL system for each sensor between 2007 and 2017. Until 2012 the volumetric water content sensor Wc2 was mainly affected by invalid values. Since 2013 an increasing number of ‘empty data’ was recorded for all sensors. Since 2016 especially the sensors Tp1 and Tp2 yielded mostly ‘empty data’.

Tab. 6-2: Percent of the ‘empty data’ for all sensors from 2007 to 2017

Sensor	2007	2008	2009	2010	2011	2012	2013	2014	2015	2016	2017
Solexperts_Battery	0.8	0.0	0.3	9.3	12.5	3.1	24.8	58.4	70.8	61.4	51.4
Pp1	0.8	0.1	0.6	9.0	12.3	2.9	23.3	53.6	68.2	58.9	66.1
Pp2	1.5	0.4	0.8	9.9	13.3	2.8	26.8	60.2	77.3	74.7	73.8
Tp1	1.0	0.1	1.1	8.7	11.8	2.9	27.9	62.1	96.6	94.3	99.5
Tp2	1.0	0.4	0.8	9.5	13.0	2.9	27.4	59.5	74.2	61.4	96.2
Wc1	11.4	0.3	0.3	9.2	12.6	3.1	28.2	59.5	74.2	63.9	60.1
Wc2	17.2	6.5	20.7	34.0	46.8	43.9	36.1	65.6	75.1	67.1	66.7
MISL_Battery	9.7	5.2	0.0	1.3	0.3	0.0	0.0	0.0	0.0	0.0	0.5

### 6.1.3 Test data analysis

An overview of the measured data since December 2006 is given in Fig. 6-5. A detailed view of the total pressure cell and water content data measured between 2009 and 2017 is provided in Fig. 6-6 and of the total pressure cell and pore pressure cell data in Fig. 6-7.

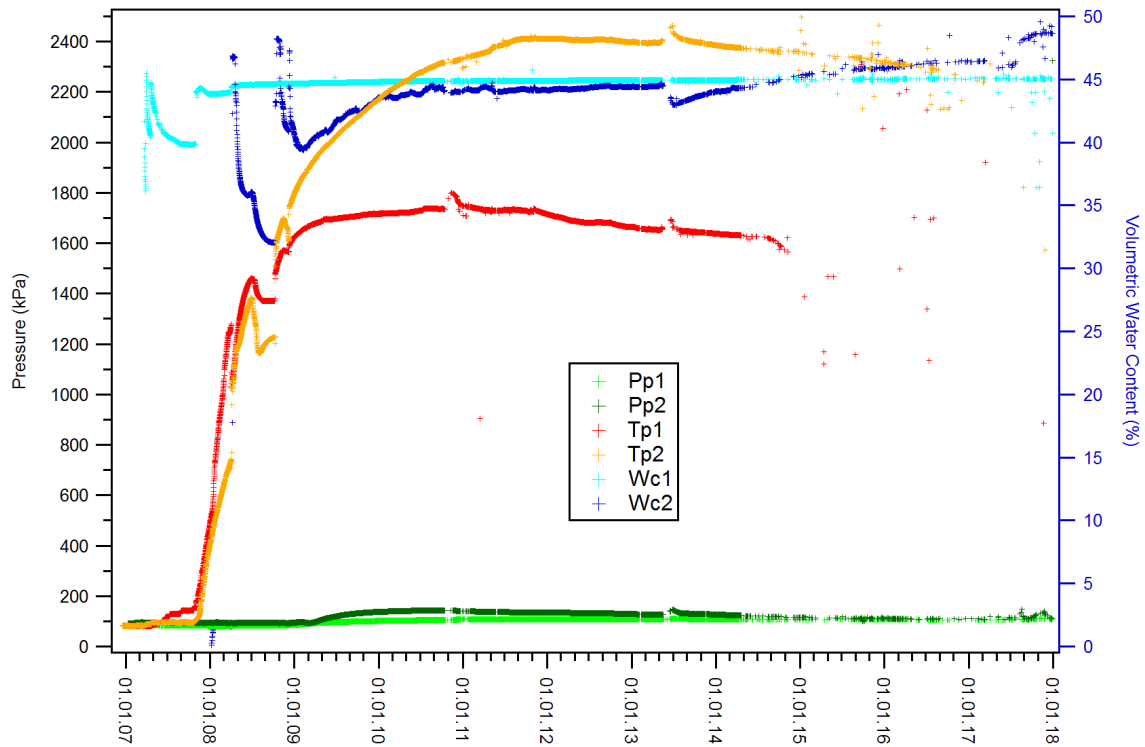


Fig. 6-5: Overview of data between December 2006 to December 2017

Since January 2012, the measurements of the water content sensor Wc1 were stable at 45 % volumetric water content and Wc2 increased to about 49 % volumetric water content. The total pressure Tp1 was slightly decreasing from about 1700 to 1565 kPa in November 2014 and Tp2 from 2400 to 2340 kPa in March 2017, when the sensors stopped to provide reliable measurements. The pressure Pp2 decreased to about 108 kPa with a peak of 146 kPa in June 2013, whereas Pp1 was almost stable at about 108 kPa. Since June 2017, the few reliable and slightly noisy data points still recorded might indicate a slight increase in pore pressure.

The test data generally show that the saturation of the test section is still inhomogeneous. Both the pore pressures and the total pressure were decreasing during the observation period. The values for the pore pressures of 107 and 108 kPa in June 2017 are only slightly higher than atmospheric pressure. The total pressures were still rather high with values above 1500 kPa when the data transmission started to be corrupted. The water content probe Wc1, which is situated at the lower boundary of the test section where saturation probably started, seems to indicate fully saturated conditions with stable data. Wc2 located at the upper boundary of the test section increased to even higher volumetric water contents at the end of 2017 and might also be fully saturated. Generally, it should be considered that the water content probes are not calibrated for this special soil type and might have a higher inaccuracy than given in the technical specifications of the manufacturer.

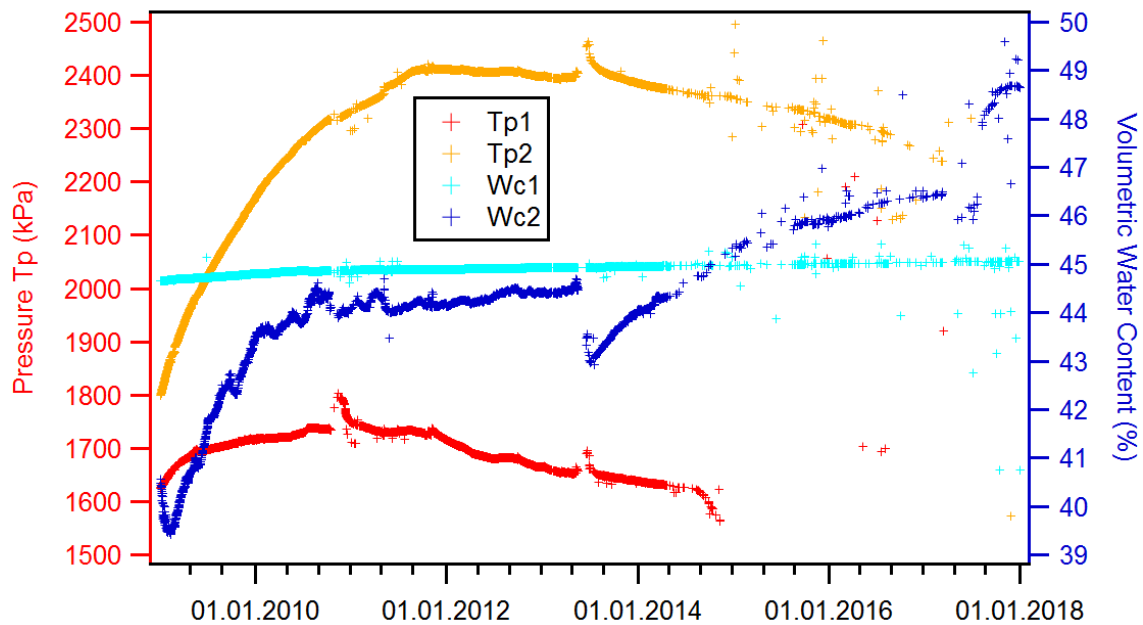


Fig. 6-6: Total pressure cell and water content measurements between 2009 and 2017

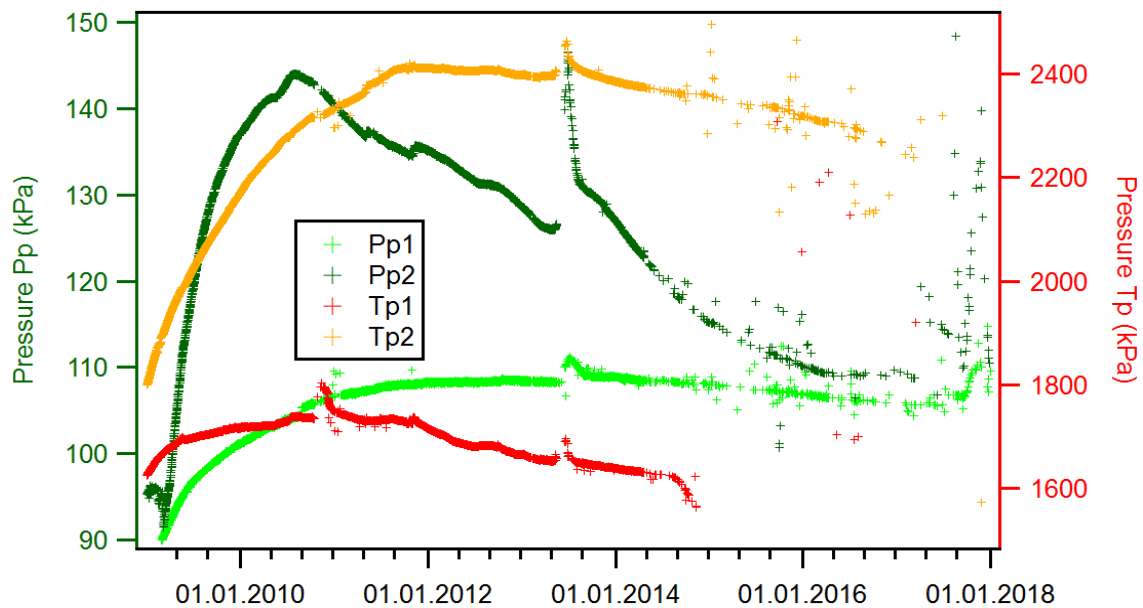


Fig. 6-7: Pore pressure and total pressure cell measurements between 2009 and 2017

#### 6.1.4 Error analysis

Fig. 6-8 and Fig. 6-9 show the parameters from the long error packet. The TYPE\_ERROR message should give the numbers 1 to 5 which were mainly sent between June and July 2007 and August and December 2008. Since May 2013 all parameters are very noisy with values up to 65'535.

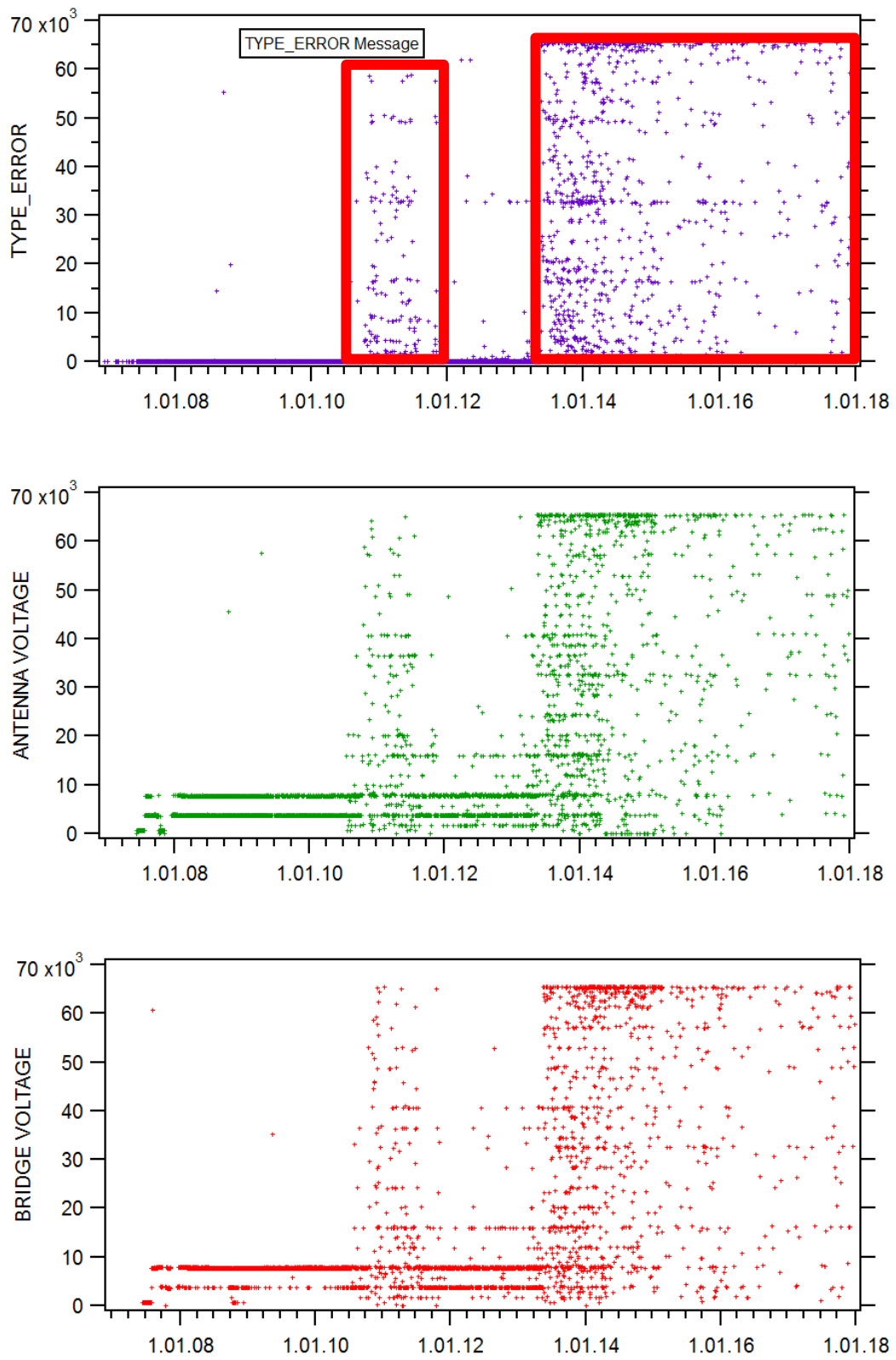


Fig. 6-8: Error type messages and the part of transmitter parameters for reception status E (and partly G) between December 2006 and December 2017

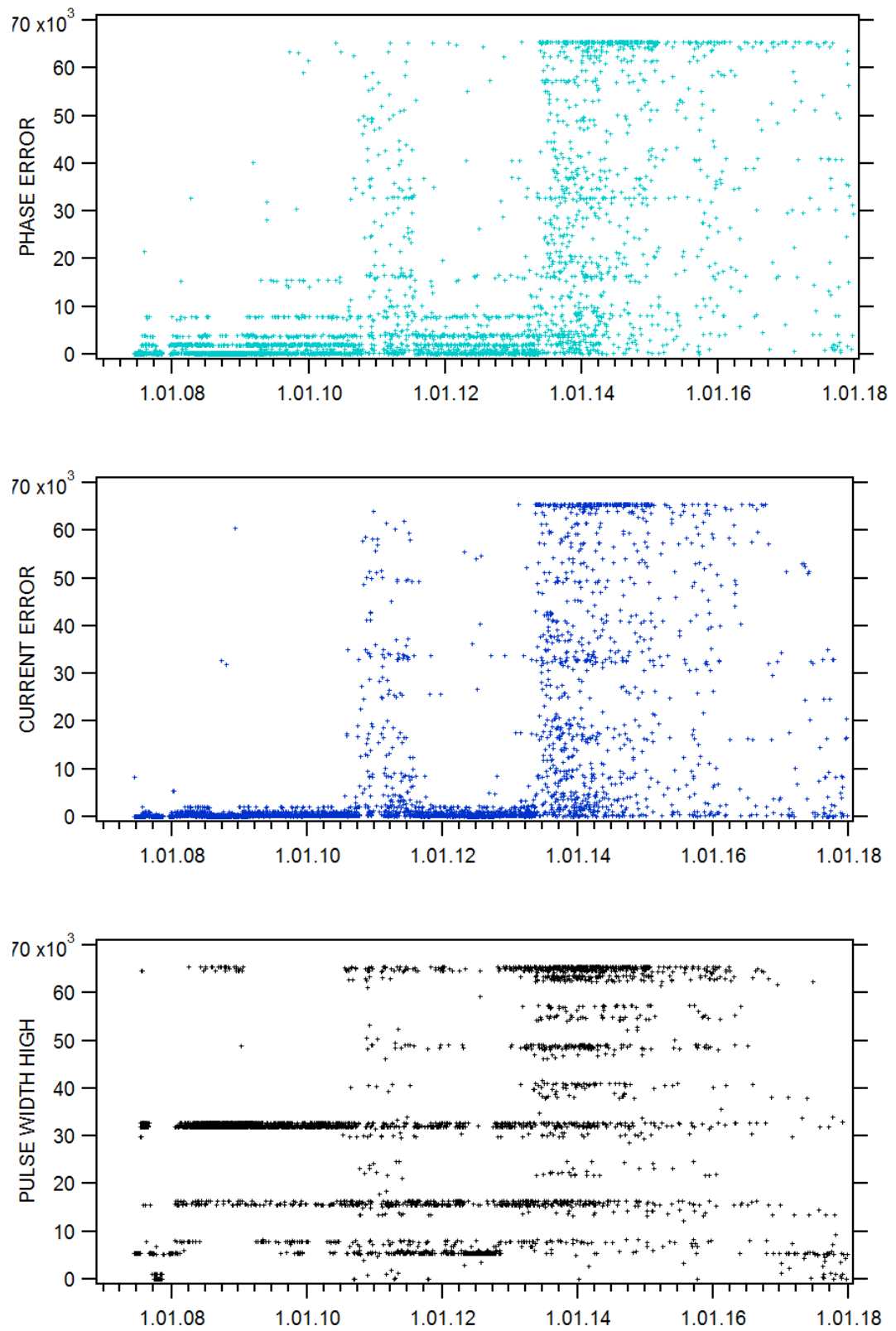


Fig. 6-9: Transmitter parameters for reception status E (and partly G) between December 2006 and December 2017

### 6.2 High-frequency wireless transmission system

Overall data trends of installed HFW sensors can be obtained and compared to the other monitoring systems installed in and around the plug. Fig. 6-10 to Fig. 6-13 depict the values gathered from the HFW nodes until end of 2012. However, this system became unattended after the conclusion of MoDeRn project in 2013. There are evidences of data recorded until November 2014. During the review of the system during start of Modern2020 in 2016 there were no data received anymore, thus no further comparison was possible.

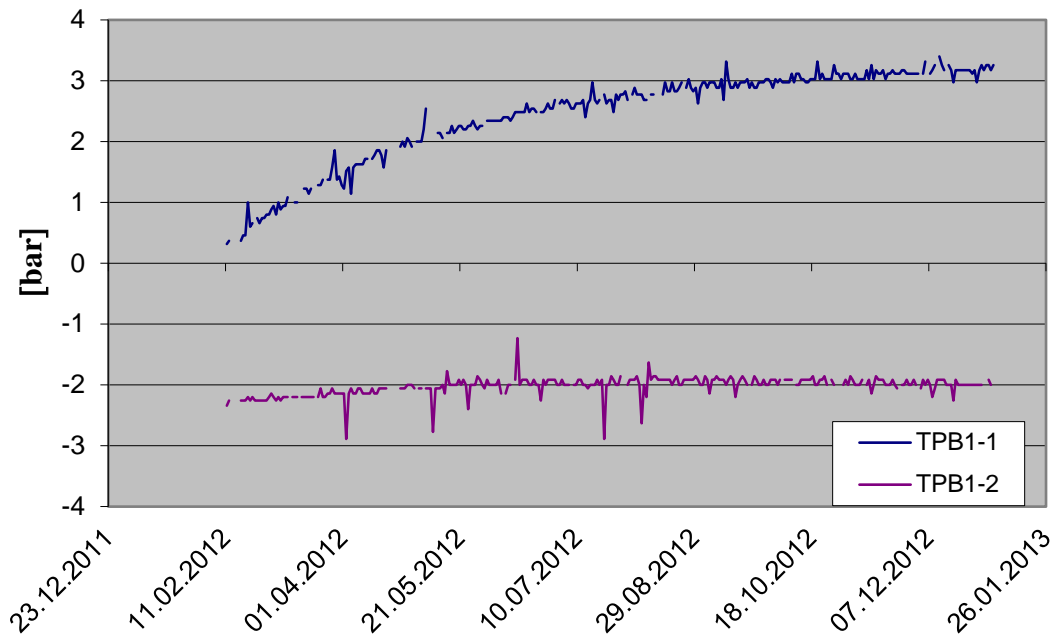


Fig. 6-10 Data of the total pressures (bar) in the buffer gathered from HFW nodes after being installed

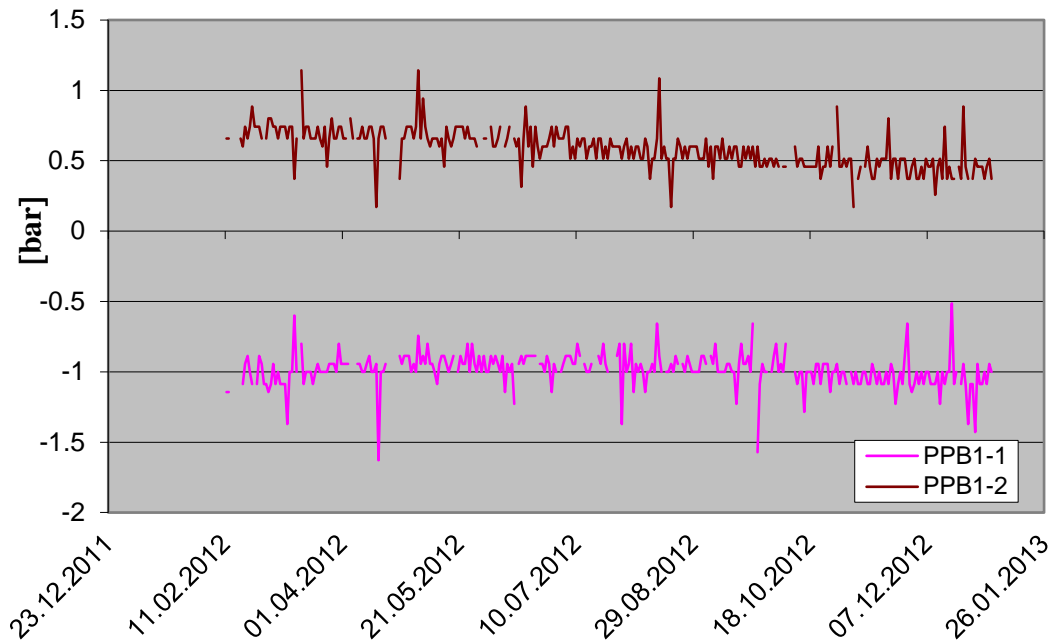


Fig. 6-11: Data of the pore pressures (bar) in the buffer gathered from HFW nodes after being installed

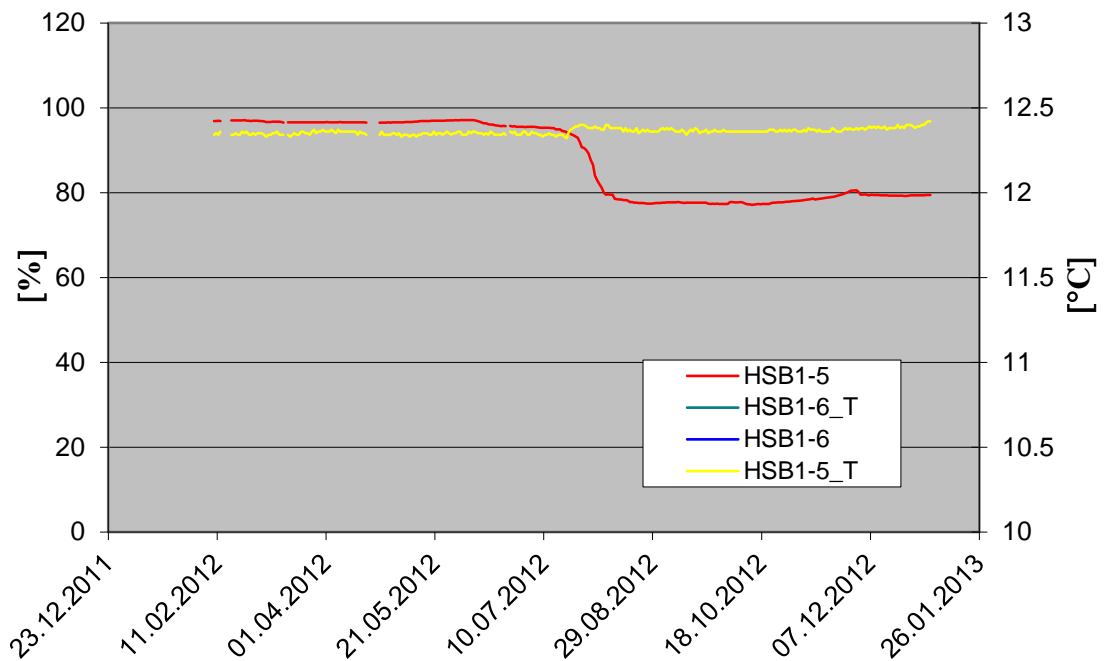


Fig. 6-12: Data of the relative humidity (%; HSB1-5) and temperature (°C; HSB1-5\_T) in the buffer gathered from HFW nodes after being installed

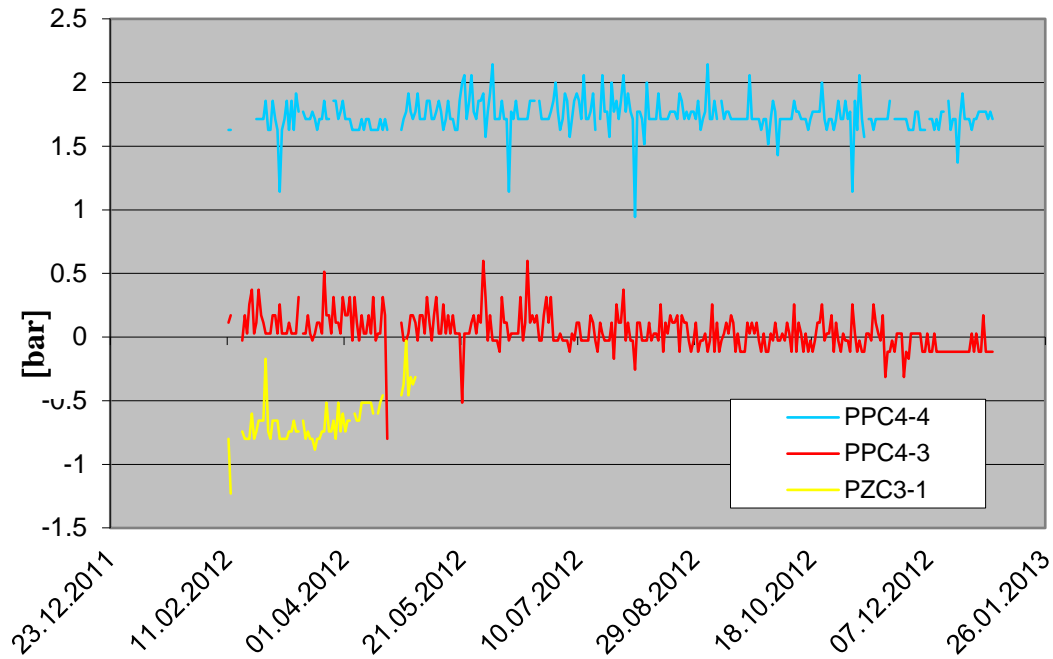


Fig. 6-13: Data of the pore pressure in plug (PPC; bar) and rock (PZC; bar) gathered from HFW nodes after being installed

### 6.3 Cross-hole seismic tomography

The measurements between January 2007 – April 2008 are summarized in Spillmann (2008). Further measurements have not been performed in the course of Modern2020 due to the lack of sufficiently high total pressure of the whole system. For a significant change in seismic velocity field, a total pressure value of 4-5 MPa is desired and the maximum value reached was only about 1.5 MPa throughout the experiment.

## 7 Attempts for buffer pressure increase

### 7.1 Objective

As indicated in the experiment aims one of the main objectives was to increase the water pressure inside the buffer to maximum level, to accelerate the saturation and to break or move the concrete plug. To achieve this objective, it was necessary to continue with the slow hydration of the bentonite buffer initiated in ESDRED and continued in MoDeRn and Modern2020.

### 7.2 System review

The first action was to revise and update the hydration system installed in March 2007, in order to control the water inlet inside the bentonite buffer, Fig. 7-1.

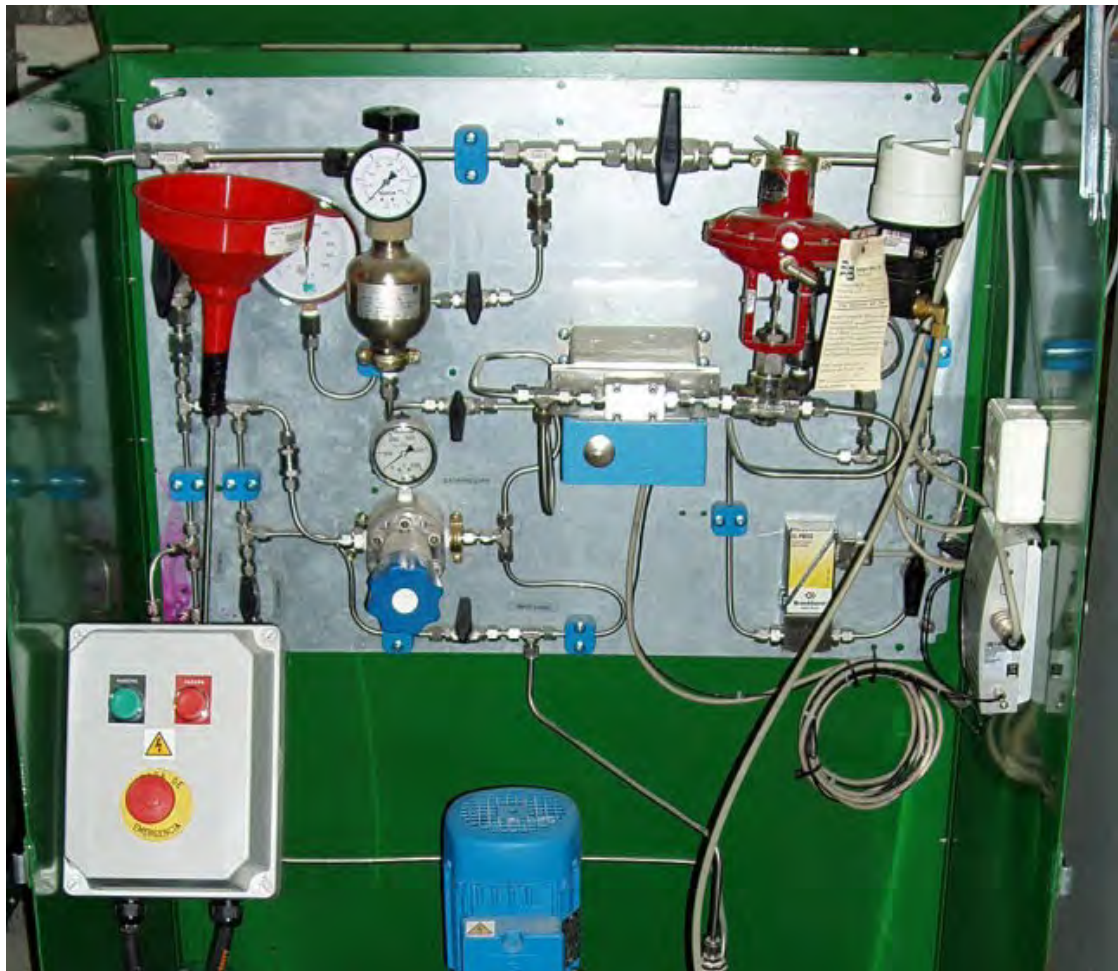


Fig. 7-1: General view of the hydration system control panel

Additionally, the following step have been performed to check update the existing hydration system:

- All signals and devices of the data acquisition system were revised
- All sensor cables were checked, also de sensors conversions
- TP signals were re-wired to eliminate the noise of these signals
- The data logger program was updated
- The SCADA (Fig. 7-2) was improved with new screens and graphs for a better following of the experiment
- The displacement sensors were changed for new ones
- The different wire boxes were revised, and a wiring table was prepared

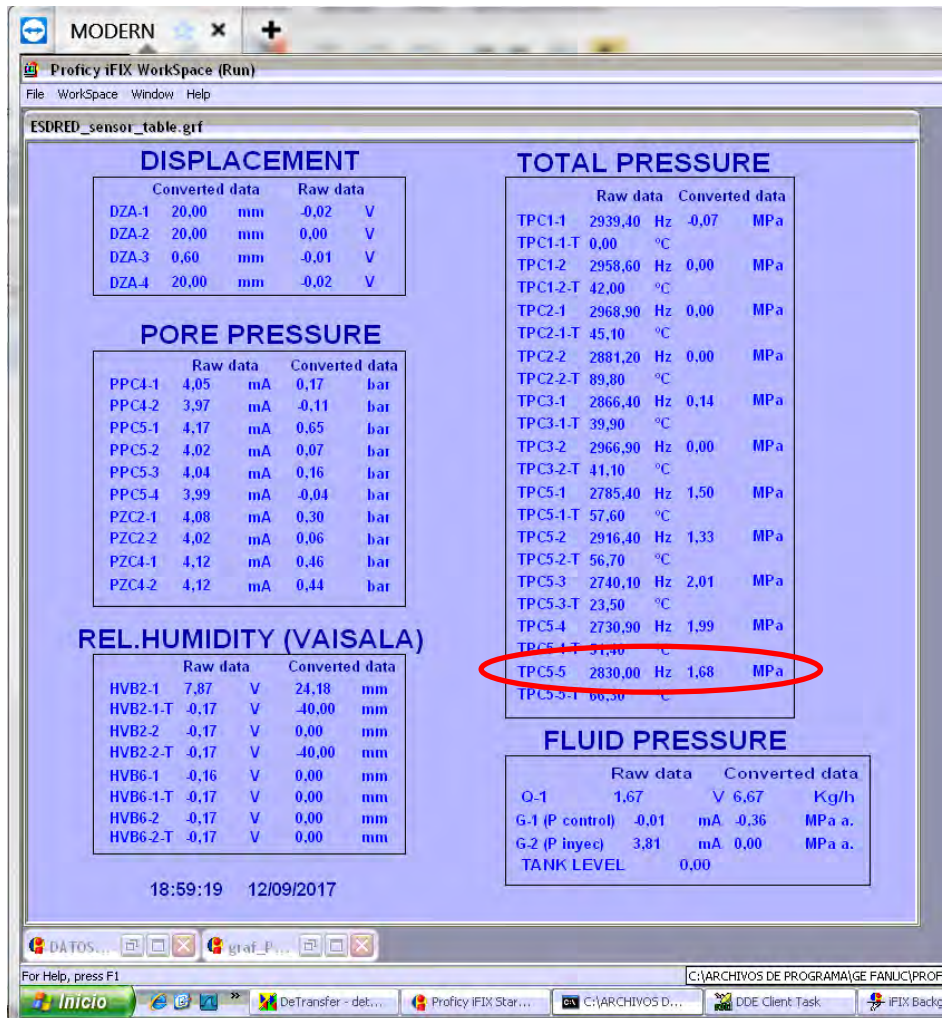


Fig. 7-2: New computer sensor table view

### 7.3 Actions carried out to resume the hydration

The hydration was started on 28 July 2017 but it was stopped again a day later. The system was reviewed “in situ” on 26 September 2017 and it was found a failure on the pressure/controller sensor. It was decided to do a by-pass of the automatic control system in order to start the hydration with a manual control, regulating the pressure with the pressure regulator (Back-Pressure type; Fig. 7-3).

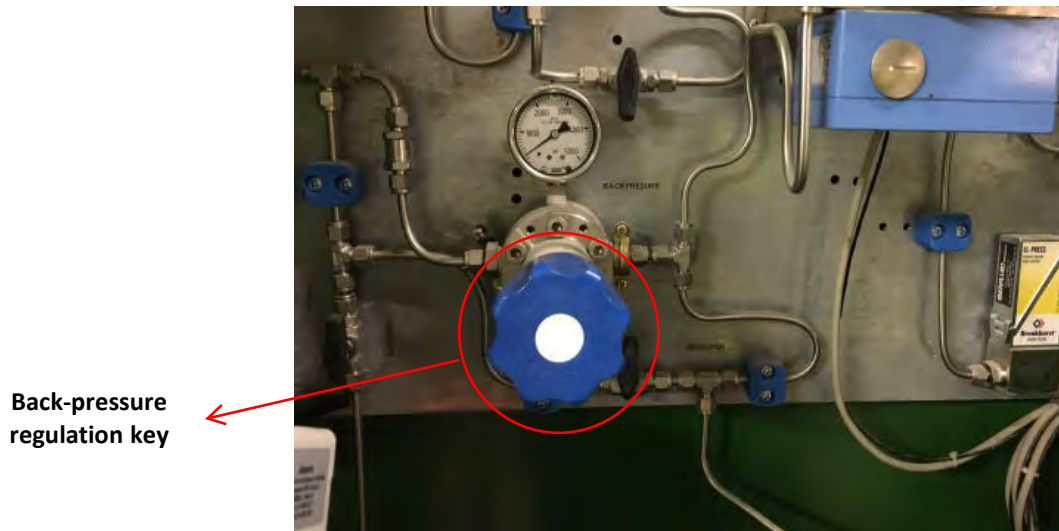


Fig. 7-3: View of the back-pressure regulation key

On 26 September 2017 the hydration was re-started with a value on the injection pressure of 10 bar. Mats 1, 2 and 5 have been opened and the flow rate was 8,6 liter/h. The manometers connected to the mats showed a pressure value of about 4 – 5 bar, see Fig. 7-4.



Fig. 7-4: Mats injection pressure status on 26 September 2017

A bucket was installed to collect the water that comes back along borehole. This is water, which is not reaching the hydration sections. On this specific day, the bucket could be filled in less than 4 hours demonstrating the overall leakage of the hydration system.

On day 28 September 2017, the manometer of mat 1 had a value of zero bar. The mat 2 and mat 5 had values of about 2.5 and 3.5 bar respectively (see Fig. 7-5).



Fig. 7-5: Mats injection pressure status on 28 September 2017

It was decided to close mat 1. The back pressure was regulated again on 10 bar but this pressure was not reached on the remaining mats manometers due to the leak in the system. The mass flow value shows a decreasing trend, probably because the control valve was closing slowly, it can be shown in Fig 7-6 (red line).

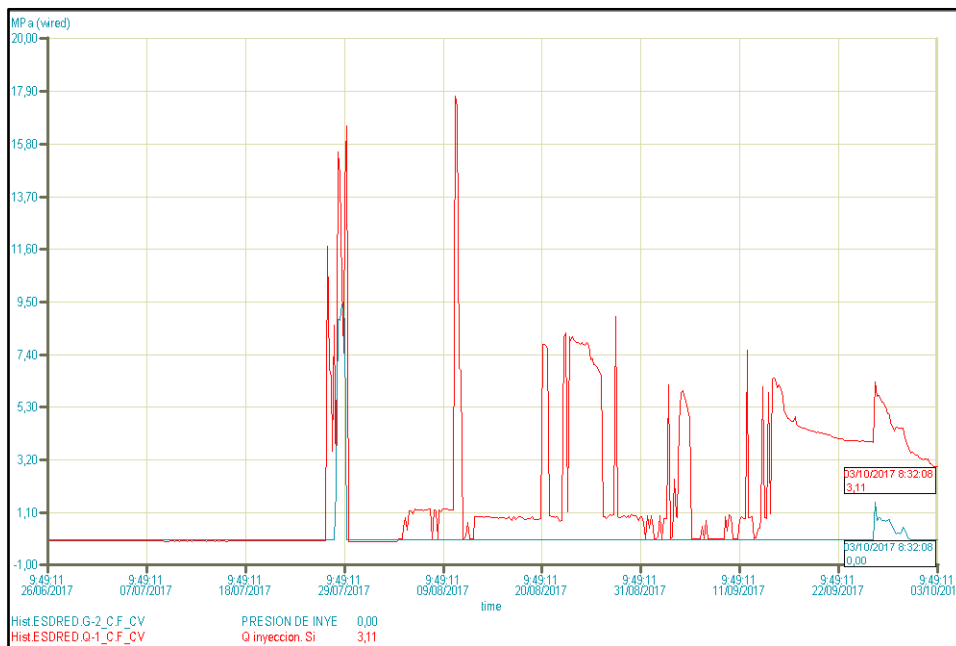


Fig. 7-6: Pressure injection and mass flow values graph on 29 September 2017

The system was checked on 2 October 2017 and the pressure has been dropped to 0 bar. The outflow measured in the bucket was of 0.9 liters in 4 hours.

There was no pressure in the system, all the elements were checked and the problem was found in the water entry valve, which was almost closed, consequently the water inlet to the system could not work properly. It was decided to eliminate this valve, by-passing this line. This work was done by the GTS personnel on 3 October 2017. See Fig. 7-7, with the regulation valve removed. Then, the injection pressure was adjusted to 5 bar, the pressure obtained on the injection mats can be observed in the Fig. 7-8.

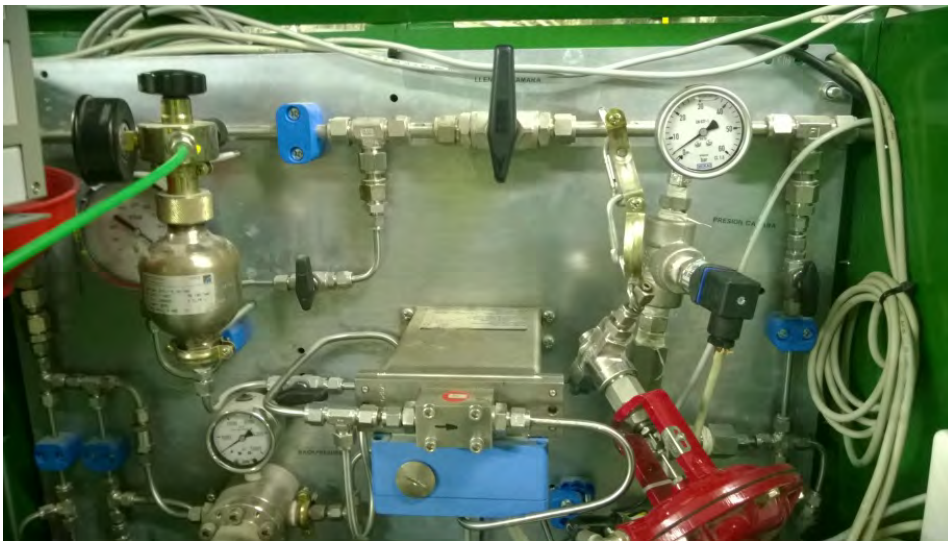


Fig. 7-7: By-pass of the regulation valve



Fig. 7-8: Mat 5 injection pressure status on 3 October 2017

The water with the regulation valve in by-pass mode flowed to hydration sections correctly, but not steadily. See the graph on Fig. 7-9 (red line). The following table (Tab. 7-1) summarizes the different events and are illustrated in the following Fig. 7-10 to 7-14.

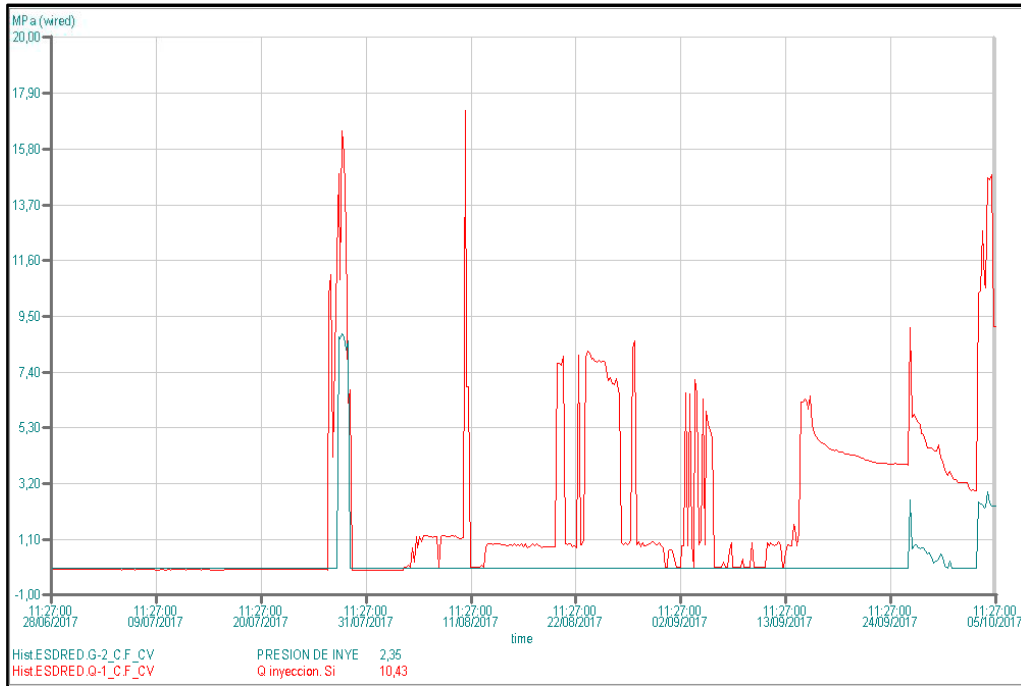


Fig. 7-9: Pressure injection and mass flow values graph on 5 October 2017

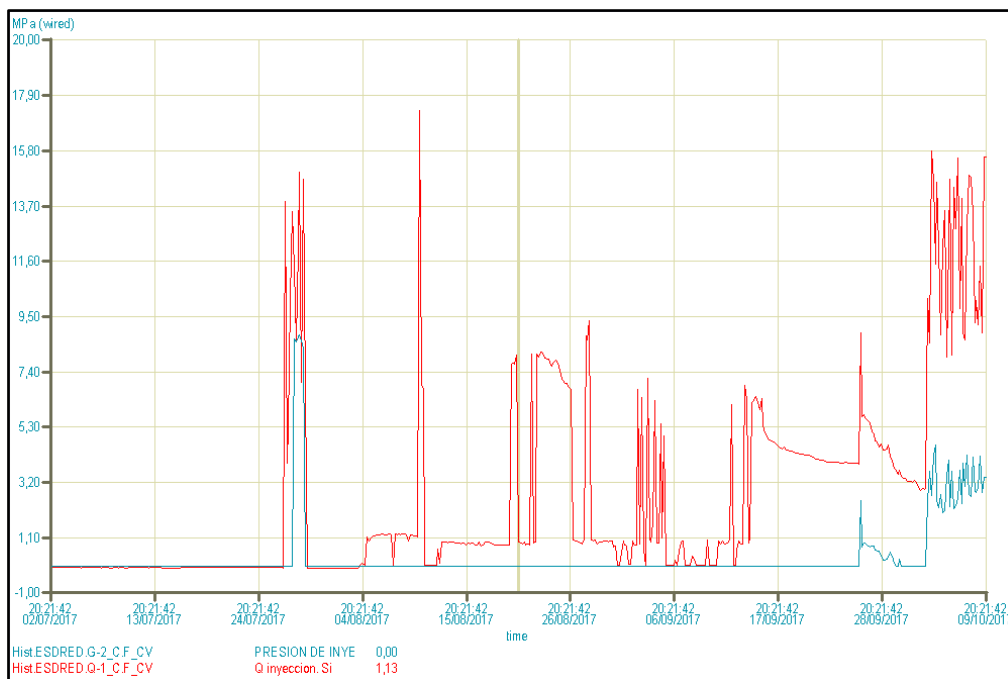


Fig. 7-10: Pressure injection and mass flow values graph on 9 October 2017

Tab. 7-1: Table of events

<b>Date</b>	<b>Event</b>
28/07/2017	Starting of the hydration
29/07/2017	Stopping of the hydration
26/09/2017	Re-Starting of the hydration / Injection pressure of 10 bar / Mats 1, 2 and 5 opened / Pump working in 8,6 liter/h / Manometers showing 4.5 bar of pressure inside the mats
28/09/2017	Mat 1 pressure went down to 0 bar / Mat 2 had a value of 2.5 bar and mat 5 a value of 3.5 bar
29/09/2017	Mat1 was closed
02/10/2017	0 bar of injection pressure reading in the system; It was checked / Outflow at the bottom of the borehole, in the gallery: 10 liters in 2 hours
03/10/2017	By-pass of the regulation valve which was eliminated  Mat 1 and mat 5 pressure: 5 bar / Outflow at the bottom of the borehole, in the gallery: 0.9 liters in 4 hours / Mat 2 was closed
05/10/2017	The valve of Mat number 2 was opened / The injection pressure value: 10 bar (comp. Fig. 7-9) / Regulation of the back pressure was not necessary.
06/10/2017	The injection pressure value: 10 bar / Outflow at the bottom of the borehole, in the gallery: 1.3 liters in 7 minutes / Mat 2 and mat 5 pressure: 5 bar, fluctuating with the rhythm of the pump.
09/10/2017	The injection pressure value: 10.5 bar / Outflow at the bottom of the borehole, in the gallery: 1.2 liters in 7 minutes / Mat 2 and mat 5 pressure: 4.5 bar, fluctuating with the rhythm of the pump (Fig. 7-10).
10/10/2017	The injection pressure value: 10.0 bar / Outflow at the bottom of the borehole, in the gallery: 1.15 liters in 7 minutes / Mat 2 and mat 5 pressure: 4.5 bar, fluctuating with the rhythm of the pump.
11/10/2017	The injection pressure was adjusted to 10.0 bar / Outflow at the bottom of the borehole, in the gallery: 1.2 liters in 7 minutes / Mat 2 and mat 5 pressure: 4.5 bar, fluctuating with the rhythm of the pump (Fig. 7-11).  The SCADA conversion of the injection pressure was checked, this value was 3 bar. It is important considerer that the manometers show absolute pressure and the transducer is reading relative pressure, considering also the error of the manometer readings, these values are consistent.
Between 08 and 10/2017	The increase of PP-C5-3 value was about 0.4 bar / The total pressure values show an increase of about 0.1 bar in section C5 (Fig. 7-12 and Fig. 7-13).
17/10/2017	There was found a leakage in the pulse pump, this drainage was not connected with the water tank and it was diverted to the gallery floor (Fig. 7-14).

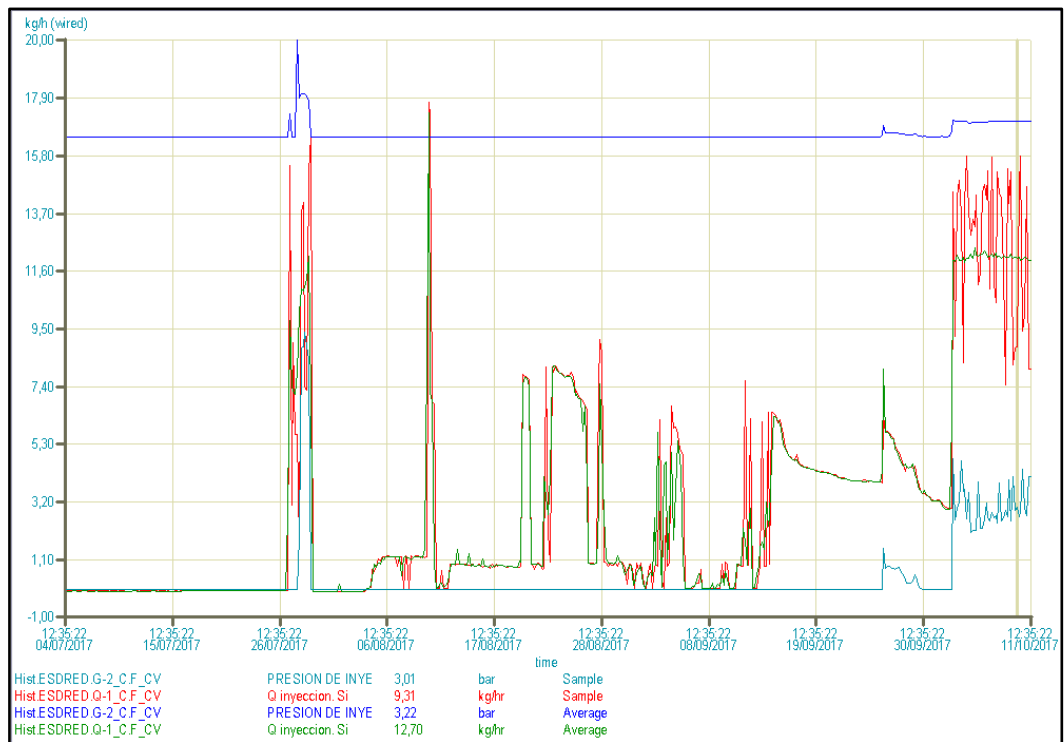


Fig. 7-11: Pressure injection and mass flow values graph on 11 October 2017



Fig. 7-12: Total Pressure and Pore Pressure graph with values on 11 October 2017



Fig. 7-13: Pressure injection and mass flow values graph on 11 October 2017



Fig. 7-14: Pump leakage and injection manometer pressure



Fig. 7-15: Mats pressure on 20 October 2017

The injection pressure was checked again on 20 October 2017, the injection pressure was adjusted to 10.0 bar. The outflow measured in the bucket was of 1.0 liters in 7 minutes.

The manometers of Mat number 2 and 5 had a value of 6 bar, with the pressure fluctuating with the rhythm of the pump (see Fig. 7-15).

The injection pressure was checked on 24 October 2017, the value was 0 bar. A Checking of the injection pressure was done: (close inlet valve, 0 bar open inlet valve). A general review of the system showed this:

- The outflow measured in the bucket was of 0.0 liters in 7 minutes.
- The pump was not working and there was no pressure.
- All the manometers show a value of 0 bar (see Fig. 7-16).
- The laboratory had an electrical shut down and the system will not start automatically.
- The PC, the SCADA and the pump were restarted.

In November 2017 the water level was to low and it was refilled. The injection pressure was checked, and it was adjusted to 10.0 bar. The outflow measured in the bucket was of 0.2 liters in 7 minutes. The pump leaking was increasing. The manometers of Mat number 2 and 5 had a value of 4 bar (see Fig. 7-17).



Fig. 7-16: Mats pressure on 24 October 2017



Fig. 7-17: Mats pressure on 24 November 2017

During December 2017, the pressure was going down, from 4 bar on 1 December 2017 to 2 bar on 4 December 2017, since then the injection pressure did not increase, and the pump was leaking strongly.

Suddenly, there was an attempt of injecting water in the system (19 December 2017) and an outflow of about of 250 ml in 7 minutes was recorded in the access borehole (see Fig. 7-18). The injection pressure was checked, setting the inlet valve to value of 14 bar and reaching 10 bar in the system (Fig. 7-18).



Fig. 7-18: Mats pressure on 19 December 2017

Checking the graphs this day, the pressure went down again. From the backpressure valve the increasing of the pressure is not possible. In the following time period a number of events were detected:

- During January 2018, the injection pressure of the system continues down. It was decided to buy a new water pump.
- The new pump was installed in April 2018. After that, the system reached 10 bar pressure. The system is controlled remotely, a status report was prepared and the graphs were updated.
- On 24 May 2018, the mat number 5 is closed to avoid a leakage of 1 liter in 5 minutes. If mat 5 stays closed the pressure is maintained in the system. Only mat 2 is left for injection.
- On 8 June 2018, the membrane of the pump failed. The hydration was stopped. The membrane of the pump was changed on 15 June 2018 and the pressure of the system was brought back to 10 bar. However, a few hours later the pressure dropped again to 5 bar.
- On 21 June 2018 the hydration system was checked again.
- On 25 June 2018 it is verified that the membrane of the pump is broken again. The hydration was then stopped fully.

Different options to substitute the pump were evaluated but no one was found adequate to combine high flow (at least 10 l/min) with high pressures (up to 3 – 4 MPa) under the given boundary conditions of the inflow lines. Thus the hydration system in its current state could not be reactivated again.

## 8 Results from conventional wired technique sensors

In this chapter the data from conventional wired sensors are shown in graphical form.

### 8.1 Pressure injection and inflow graphs

In the following graphs (Fig. 8-1 to Fig. 8-3) the pressure injection and the according inflow rate are documented for the time period from October 2017 until July 2018.

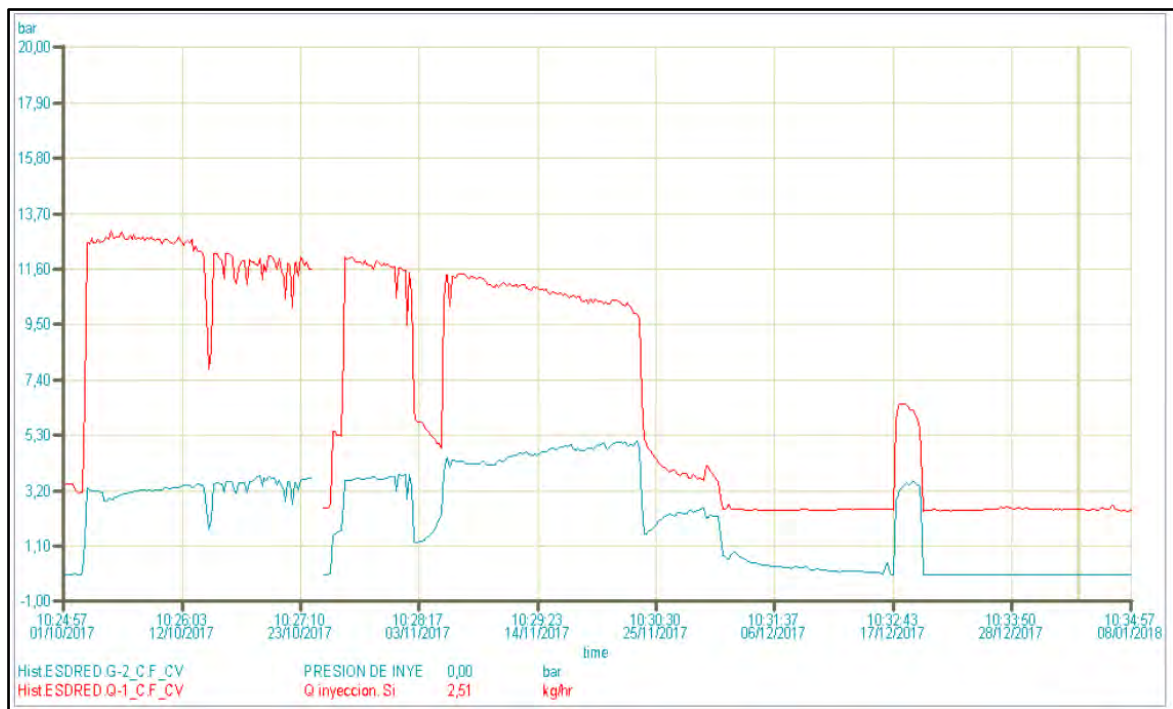


Fig. 8-1: Pressure injection and inflow from 1 October 2017 to 8 January 2018

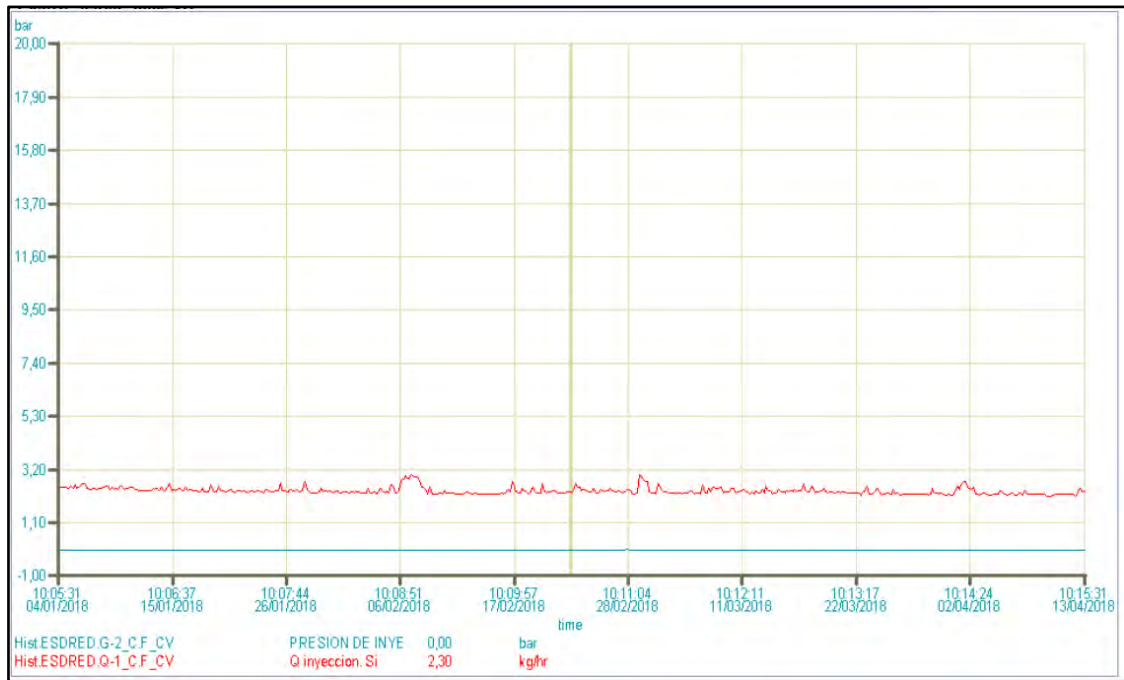


Fig. 8-2: Pressure injection and inflow from 4 January 2018 to 13 April 2018

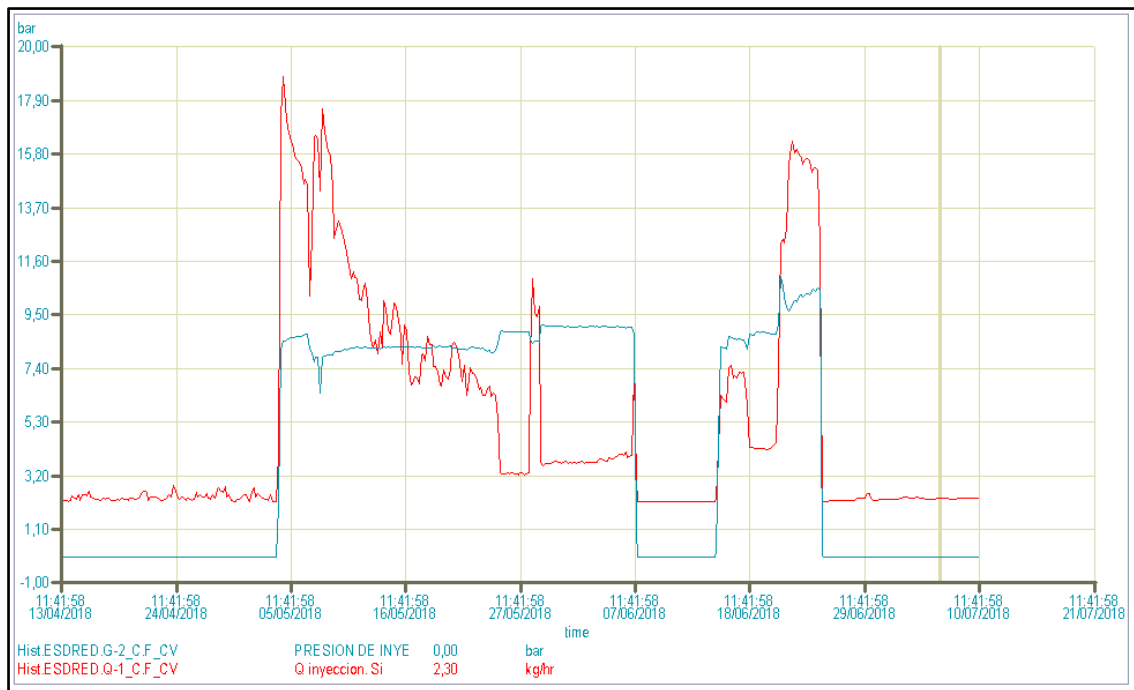


Fig. 8-3: Pressure injection and inflow from 13 April 2018 to 21 July 2018

### 8.2 Total pressure graphs

In the following graphs (Fig. 8-4 to Fig. 8-6) the total pressure values from October 2017 until July 2018 are presented.

The sensor TPC5-4 was not working properly, so it was deleted from the following graphs (Fig. 8-4). The values and status from the following up measurement period at 13 April 2018 (Fig. 8-5) are the same than the system had on 8 January 2018.

The values and status of the total pressure measurements at 22 July 2018 are shown below (Fig. 8-6). The TPC5-4 sensor signal (red line) seems to be recovered from mid of June 2018 on.

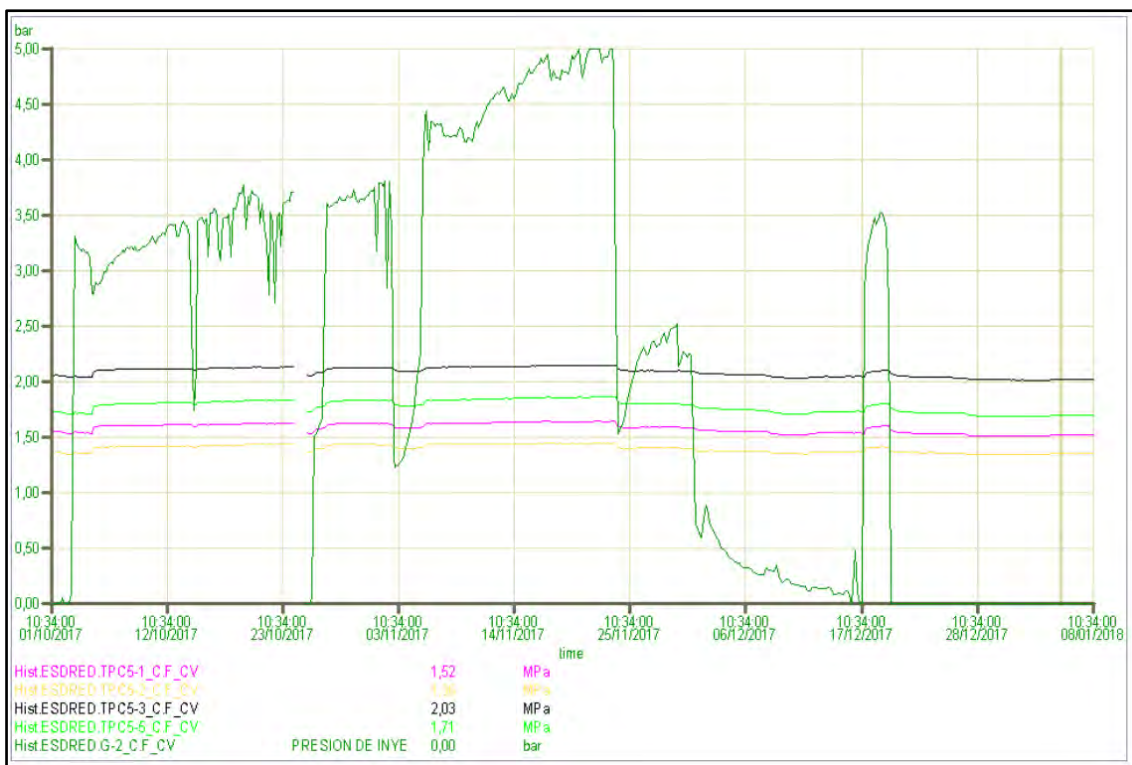


Fig. 8-4: Total pressure trend from 1 October 2017 to 8 January 2018



Fig. 8-5: Total pressure trend from 4 January 2018 to 13 April 2018



Fig. 8-6: Total pressure trend from 14 April 2018 to 22 July 2018

### 8.3 Pore pressure graphs

In the following graphs (Fig. 8-7 and Fig. 8-8) the pore pressure values from October 2017 until April 2018 are presented.

The values and status at 13 April 2018 are the same than the system had on 8 January 2018. No changes could be observed anymore.

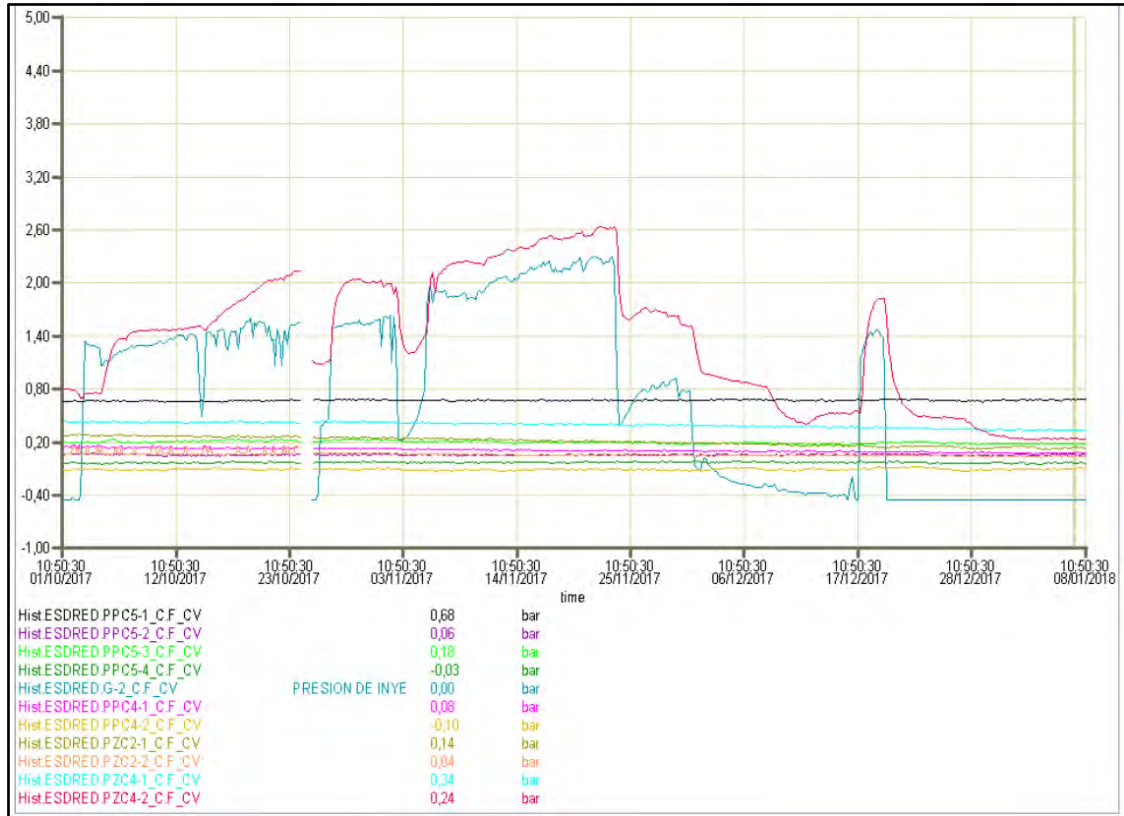


Fig. 8-7: Pore pressure sensors trend from 1 October 2017 to 8 January 2018

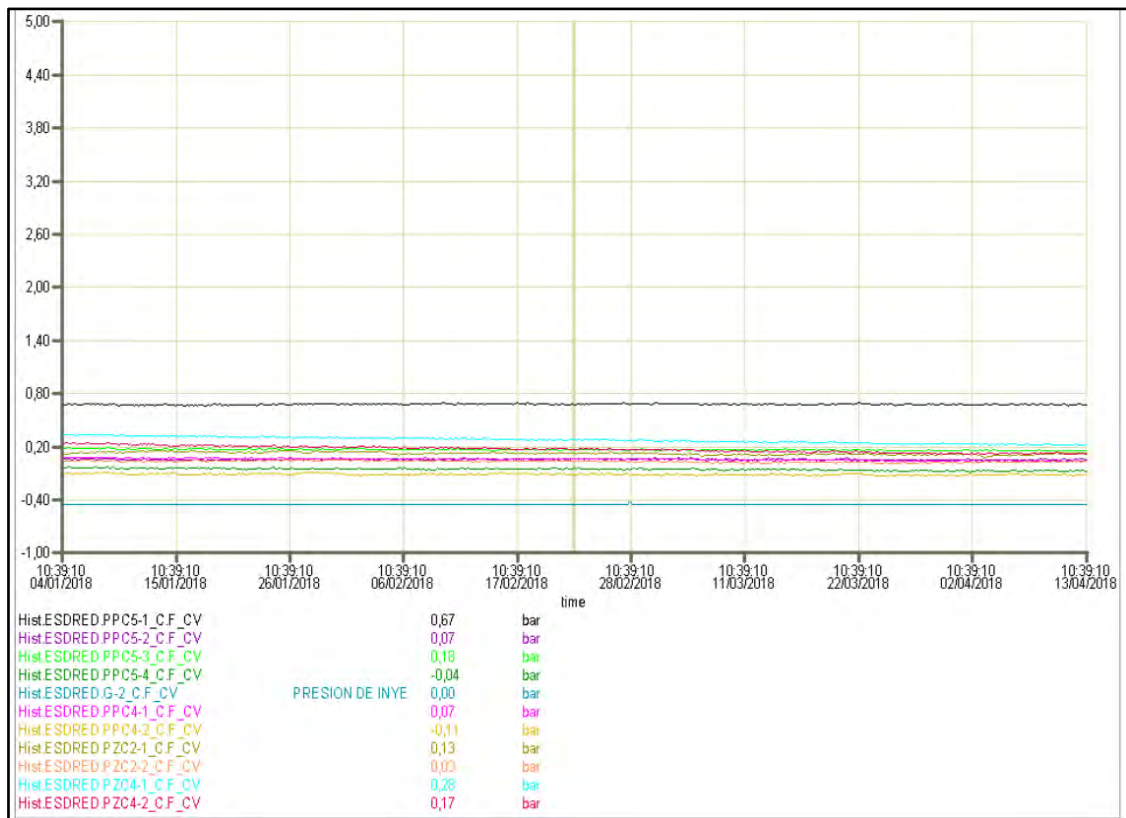


Fig. 8-8: Pore pressure sensors trend from 4 January 2018 to 13 April 2018

#### 8.4 Displacement graphs

The displacement sensors of the plug, namely the extensometers DZA-1, DZA-2 and DZA-4 are mainly out of range and are showing unreasonable values. Only the value from extensometer DZA-3 is constant during the entire measurement period from 2017 and 2018 (Fig. 8-9) showing very little displacement of less than 1 mm.

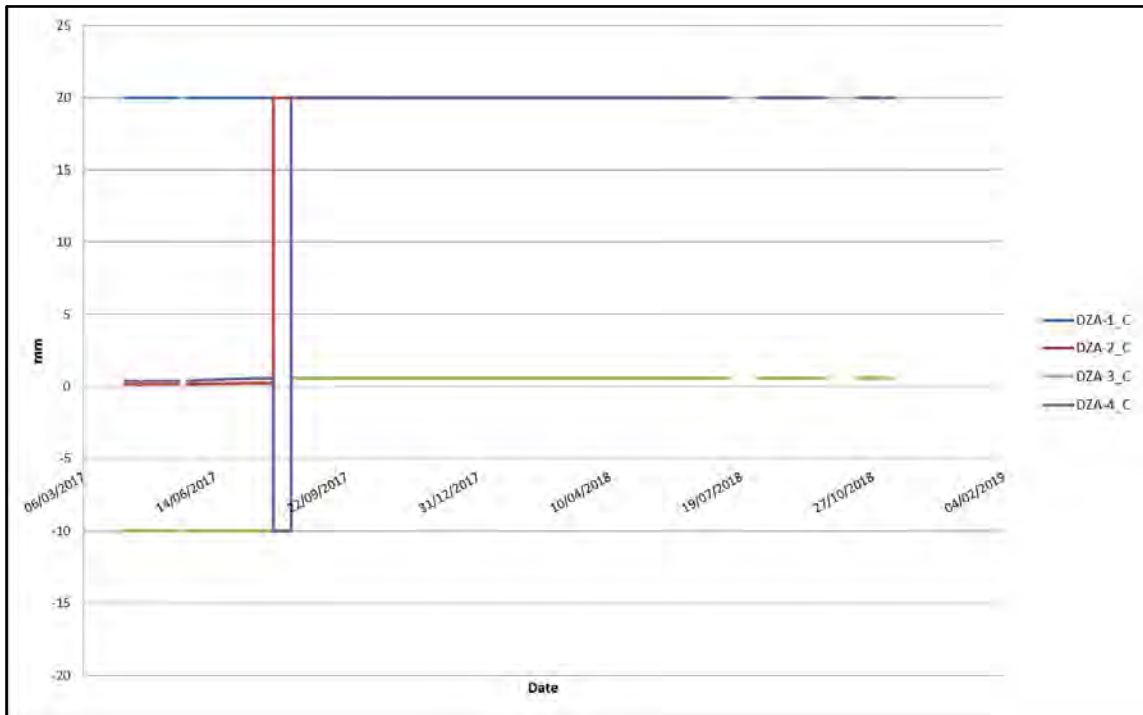


Fig. 8-9: Plug displacement sensors - extensometers trend from March 2017 to February 2019



## 9 Summary, discussion and recommendations

The measurements for the MI wireless monitoring project started in December 2006 (Fig. 9-1). Because of transmission problems, the receiver was moved from the first location in the MI drift to a location near the GMT site at a distance of about 30 m from the transmitter.

Since then, the MISL transmitter continuously provided reliable data for more than six years except for a short period between October 2010 and January 2011. Since May 2013 the transmission status of most data packages had changed to E (error status) and an increased number of missing data packages and of invalid ‘empty’ values was observed. Since May 2014, only occasional valid data could be detected in the transmitted data packages and a great number of data packages were missing.

The transmission status indicate the nearly complete failure of the transmission for most sensors probably related to the near end of the lifetime of MISL transmitter battery and/or of the Solexperts data logger battery.

The magneto-inductive (MI) wireless monitoring experiment system was now working for about eleven years providing good quality data for the given number of sensors and the defined scan rate. The wireless capability has been shown to be reliable for this experiment setup. Improving the transmission quality by the use of even more reliable battery systems is a main issue if the wireless monitoring method will be applied further in other projects.

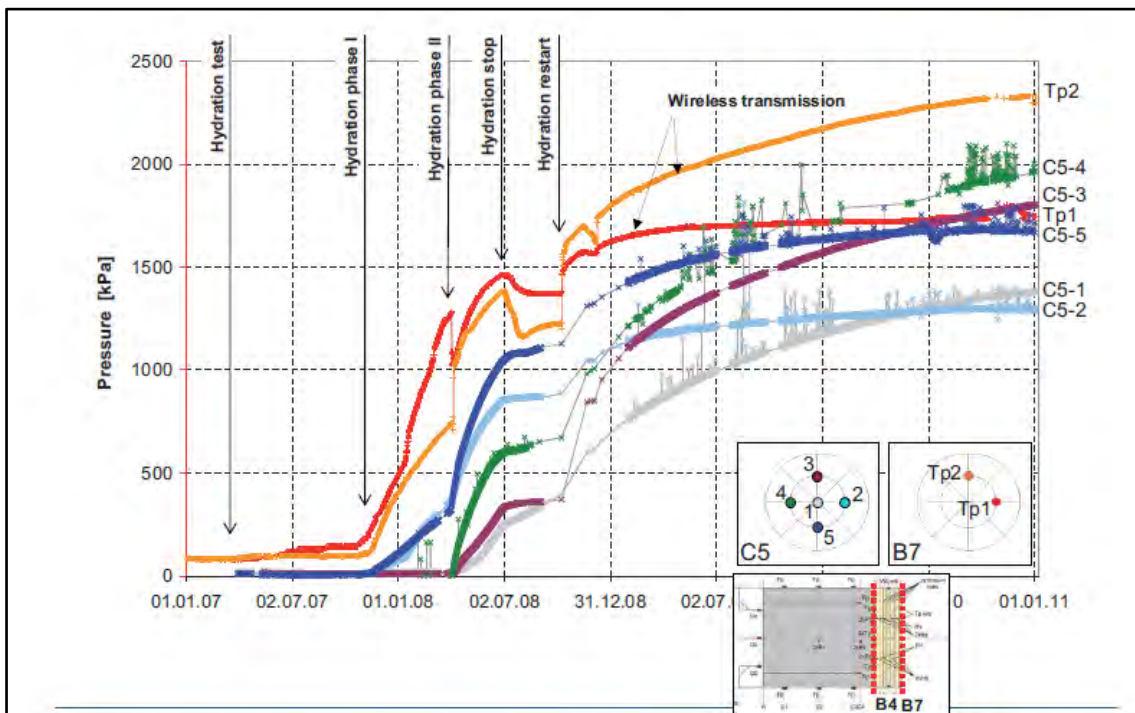


Fig. 9-1: Comparison of wireless and wired monitoring

Although the data provided by the high frequency nodes was too short (this means the life-time of the nodes) for comparison with remaining monitoring systems it is relevant to stress,

that the wireless data transmission in general does not imply any corruption of the gathered data. The messages sent (digital) are controlled at reception about integrity so the only risk is to receive or not the message. However, if the batteries of the wireless unit become too low, the functioning of the sensors used could be affected if this value is not controlled to avoid measurements when below a safety value.

Although several attempts were made, and many components changed, the system for hydrating the buffer of TEM become could not be restored. Most probably this is due to the time passed from the installation date, specially the plastic inflow and outflow lines are leaking so it is very risky to use them for increasing the pressure. Furthermore, the bentonite swelling pressures could not be increased significantly beyond 2 MPa by injecting water in the mats. Either their installed dry density obtained was smaller than planned and calculated or the injected water is not effectively distributed into the bentonite and hydration was incomplete. Thus, the only way to increase the total pressure of the plug will be by increasing the pore pressure up to 2 – 3 MPa. The existing inflow lines cannot be used for performing injections at these pressures.

Because of not being able to increase the pressure in the system resp. the plug significantly during Modern2020 as planned, it makes no sense to perform additional non-intrusive geophysical measurements to make a further assessment. So the already existing comparison of seismic data from the previous Modern- Project (ETH Zürich & NDA, 2013) could not be extended with data from higher pressure levels (see also Fig. 9-2).

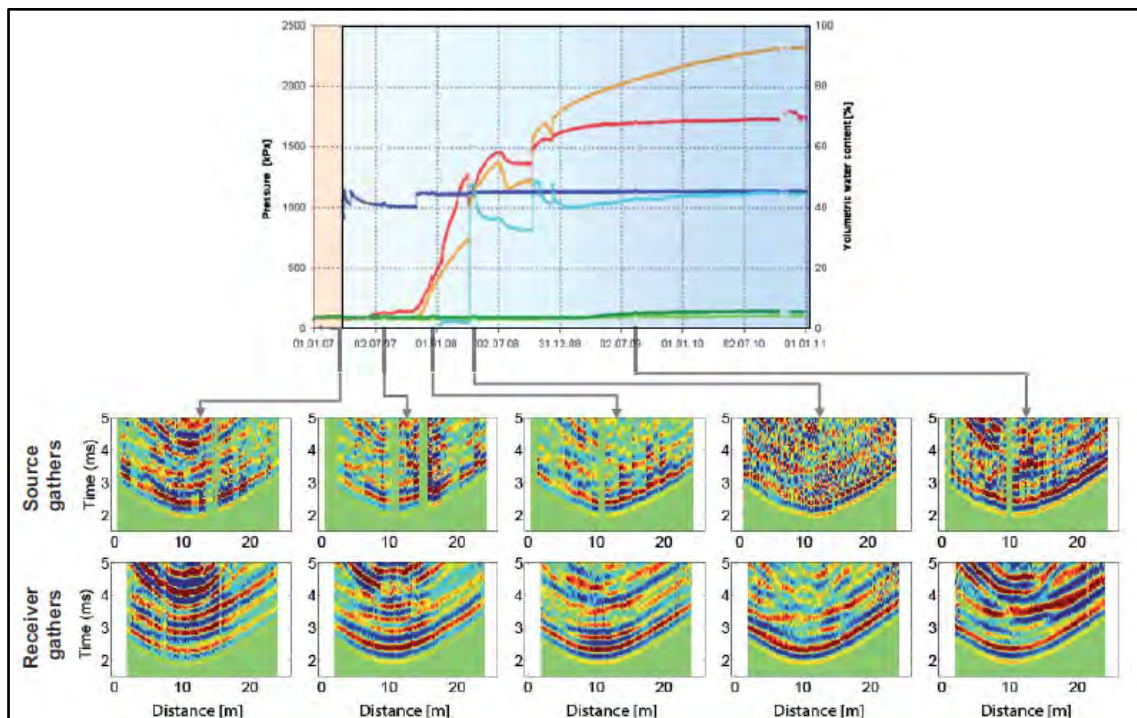


Fig. 9-2: Comparison of seismic data (after Marelli et al., 2010 & Marelli, 2011)

The use of high frequency for data transmission through the EBS components is not recommended as stated in the final report of Modern2020 for task 3.2 of WP3, Deliverable D3.2 “Wireless data transmission systems for repository monitoring” (Schröder et al., 2018).

The Table 4.2 in Schröder et al. (2018) shows both technologies, 169 MHz for the high frequency nodes provided by AITEMIN and 575 Hz for the MISL unit. The wrong frequency selected for the AITEMIN units is evidenced by the change made by Arquimea that afterwards reduced the frequency of these units to 2.2 MHz in LTRBM demonstrator to try overcoming the attenuation suffered in TEM and also in SEALEX experiments, when the buffer saturation progresses.

Furthermore, from the analysis of the results provided in Schröder et al. (2018) versus the used frequencies it is evident that frequencies below 9 KHz are the best choice, the results gathered in TEM just confirm this conclusion.

Finally, it should be stated that the combination of wireless and wired technologies plus promising non-intrusive seismic imaging techniques is the best approach to further develop the required tools to avoid use of cables intersecting the plug in the future monitoring purposes in nuclear waste repositories.

The design, implementation and operation of a experiment like TEM is very costly and difficult so it is desirable and recommendable to try extracting as much relevant information as possible for progressing in the design of the future repository.

TEM comprises several pieces of information that are of interest and not yet gathered:

- The functioning and parametrization of a non-keyed concrete plug that could improve the existing designs for competent rocks (Crystalline rock) usually based on a keyed approach because it is more simple, cheap and fast building one.
- The improvement of a novelty non-intrusive monitoring technique that could provide a complement to the traditional punctual measurement techniques and an alternative for longer operational and post-closure phases.
- The status of the bentonite buffer after being long-time saturated in order to determine if the low swelling pressure reached so far was due to a imperfect saturation using the original wetting system or due to a wrong reached dry density.

Consequently, the continuation of this experiment remains of interest at least to help calibrating the non-intrusive techniques and to demonstrate the load bearing capacity of the non-keyed low-pH concrete plug, which will help to refine the design basis for future use.

In that case, it will be necessary to design and implement a new water inflow system to increase the pore pressure behind the plug (inside the buffer). This could be done by drilling a borehole in the plug up to the buffer to install a water inflow pipe properly sealed and attached to the concrete. Then this pipe could be used to inject water to reach the required pore pressures up to 2 – 3 MPa. The system to provide the water could be the existing one, after repairing the pumps. Alternatively, a pressurized water tank might be used to make the saturation independent from combination of pressure/flow control.



## 10 References

- Barcena, I. & Garcia-Siñeriz, J. L. (2008) : Full scale demonstrator of shotcrete sealing plug under realistic working conditions. - International Conference Underground Disposal Unit Design & Emplacement Processes for a Deep Geological Repository, 16-18 June 2008, Prague.
- Bárcena, I. & García-Siñeriz, J. L. (2009): Report on Full Scale Demonstration of a Shotcrete Plug. - ESDRED, Deliverable D8.3 of Module 4, WP3.2., 23 February 2009; Aitemin.
- Detzner, K. & Spillmann, T. (2011): Modern project: Field report on borehole drilling and sampling. – Nagra Aktennotiz (unpublished).
- ESDRED (2009): Final summary report and global evaluation of the project. – European Commission, ESDRED, Modul 6 (Integration activities), Contract Number F16W-CT-2004-508851, issued by W.K.Seidler, 30 January 2009.
- ETH Zürich & NDA (2013): Seismic Tomography at Grimsel Test Site. - Euratom Research and Training Programme on Nuclear Energy within the 7<sup>th</sup> Framework Programme (2009 – 2013), Deliverable D-No.: 3.2.1, issued 8/1/2013.
- García-Siñeriz, J. L., Barcena, I. Velasco, M., Huertas, F., Alonso, F., Kickmaier, W., Blechschmidt, I., Fries, T. & Fierz, T. (2008): Test Plan for the Full-Scale Demonstration of a Shotcrete Plug. - ESDRED Contract Number: F16W-CT-2004-508851, Deliverable D4.3 of Module 4, WP3.2, 20 May 2008; Aitemin.
- Marelli, S., Manukyan, E., Maurer, H., Greenhalgh, S. A. & Green, A. G. (2010): Appraisal of waveform repeatability and reliability for crosshole and hole-to-tunnel seismic monitoring of radioactive waste repositories. - Geophysics 75, no5, Q21- Q34.
- Marelli, S. (2011): Seismic imaging of temporal changes in underground radioactive waste repositories: surveillance requirements and full-waveform inversion issues. - Doctoral thesis, ETH Zurich, Diss. ETH No. 20040, 1-280 (<http://dx.doi.org/10.3929/ethz-a-006852891>).
- Maurer, H. & Greenhalgh, S.A. (2012): Application of seismic waveform inversions for monitoring radioactive waste repositories and their surroundings: state-of-the-art and future challenges. – Nagra Working Report, NAB 12-46; Wettingen (Nagra).
- NDA, Andra, Aitemin, NRG, Euridice & ETH-Zürich (2010): WP3 Site Plans and Monitoring programmes report. – Modern, Seventh Euratom Framework Programme for Nuclear Research & Training Activities within the 7<sup>th</sup> Framework Programme (2009 - 2013), Contract Number 232598, Deliverable (D-N°:3.1.1), Reporting period 1: 01/05/2009 – 30/10/2010, 26/8/2010.
- NDA, ETH-Zürich, Aitemin, Euridice, NRG & Andra (2013): Monitoring during the staged implementation of geological disposal: Technology Summary Report. – Euratom Research and Training Programme on Nuclear Energy within the 7<sup>th</sup> Framework Programme (2009 – 2013), issued 11/11/2013.
- Rösli, U. (2013): Grimsel GTS Phase VI, Modern MISL Data 1.1.12 – 31.12.12 – Solexperts Data Trend Report. – Nagra Aktennotiz (unpublished).

- Rösli, U. (2012): Grimsel GTS Phase VI, Modern MISL Data 1.1.11 – 31.12.11 – Solexperts Data Trend Report. – Nagra Aktennotiz (unpublished).
- Schröder, T. J. (ed.), E. Rosca-Bocancea, E., García-Siñeriz, J. L., Hermand, G., Abós Gracia, H. L., Mayor Zurdo, J. C., Verstricht, J., Dick, P., Eto, J., Sipilä, M & Saari, J.-M. (2019): Wireless data transmission systems for repository monitoring. - Modern2020 (2016 - 2019) supported by EURATOM, "Development and Demonstration of Monitoring Strategies and Technologies for Geological Disposal", Deliverable D3.2, Work Package 3, Task 2., 29. September 2018.
- Spillmann, T. (2008): Application of wired, wireless and non-intrusive standard monitoring techniques – TEM Project at the Grimsel Test Site – Annual Report. – Nagra Working Report, NAB 08-52; Wettingen (Nagra).